

THE UNIVERSITY of ADELAIDE

Structural behaviour of reinforced and prestressed high performance concrete (HPC) structural elements

by

Mohammad Dhaifallah Alameri

B. (Civil Engineering) & M. Eng. (Civil and Structural)

Thesis submitted in fulfilment of the requirements for the degree of

Doctor of Philosophy

Faculty of Sciences, Engineering and Technology

School of Architecture and Civil Engineering

The University of Adelaide

Australia

-December 2024-

This thesis is dedicated to my mother (Alwa, may Allah bless her), my father (Dhaifallah), my wife (Afrah), and my children (Abdullah and Saud).

TABLE OF CONTENTS

ABSTRACT ..... **iii**

STATEMENT OF ORIGINALITY ..... **v**

LIST OF PUBLICATIONS/MANUSCRIPTS UNDER REVIEW ..... **vi**

ACKNOWLEDGMENTS ..... **vii**

INTRODUCTION AND GENERAL OVERVIEW **1**

CHAPTER 1 ..... **9**

Background **9**

List of Manuscripts **9**

Self-Healing and Mechanical Behaviour of Fibre-Reinforced Ultra-High-Performance Concrete Incorporating Superabsorbent Polymer Under Repeated and Sustained Loadings **12**

CHAPTER 2 ..... **46**

Background **46**

List of Manuscripts **46**

Optimizing GGBS-Based Ultra High-Performance Geopolymer Mortar: An Orthogonal Array Approach **49**

CHAPTER 3 ..... **79**

Background **79**

List of Manuscripts **79**

Optimizing slag-based geopolymer mix design for enhanced strength and durability **81**

CHAPTER 4 ..... **112**

Background **112**

List of Manuscripts **112**

Investigation of UHPC-filled double skin aluminium tubular columns under combined loading conditions **114**

CHAPTER 5 ..... **152**

Background **152**

List of Manuscripts **152**

Investigation of high-performance geopolymer concrete-filled double-skin columns under combined loading conditions **154**

CONCLUSIONS AND FUTURE RECOMMENDATIONS **191**

APPENDIX I (Conference paper) **195**

ABSTRACT

Concrete technology has been advanced in various ways to improve current mix designs based on cementitious materials, or by implementing the geopolymer approach, where waste materials are used as the main binder. The development of existing mix designs has led to the creation of ultra-high-performance concrete (UHPC), which exhibits superior mechanical and durability characteristics. However, UHPC is more susceptible to forming cracks due to autogenous shrinkage. Thus, it is necessary to control the formation of cracks to extend the life cycle of the concrete structural members. Moreover, the technology of geopolymer concrete (GPC) is still under development, and there are many variables in this process that increase the uncertainty of producing GPC. Therefore, this thesis consists of several manuscripts (some of them already published and some under consideration by journals) regarding the improvement of the self-healing performance of UHPC, the optimisation of GPC mix design and the structural applications of UHPC and GPC.

The first chapter investigates the mechanical, durability and self-healing performance of UHPC with a superabsorbent polymer (SAP) under various curing conditions. The SAP-to-binder ratios used in this study were 0.3% and 0.4%. Two approaches were adopted to examine self-healing performance under repetitive loads and sustained tensile loading for up to 28 days. The results show that incorporating an SAP into UHPC enhances the concrete's elastic modulus, flexural strength and tensile strength. Also, the mixes exhibited compressive strength above 120 MPa after 90 days. Furthermore, the load recovery of the prisms under repetitive flexural loads and the prisms under sustained tensile loading demonstrated that the self-healing efficiency of the SAP incorporated into the UHPC mixes was higher than that of the control mixes.

The second chapter presents a study in which GPC was optimised using the Taguchi method, and it details the mix design to produce ultra-high-performance geopolymer concrete (UHPGC). Utilising an L9 orthogonal array, the investigation was structured into two phases, each examining a distinct set of variables across three levels to ascertain their impact on compressive strength. The first phase analysed the water-to-binder (W/B) ratio, silica-fume-to-binder ratio, potassium-silicate-to-potassium-hydroxide ratio and aggregate-to-binder ratio. The second phase explored the effects of the W/B ratio, fibre content, silicon-carbide-to-binder (SiC/B) ratio and superplasticiser-to-binder (SP/B) ratio. The Taguchi method facilitated a meticulous evaluation of 18 unique mix designs and the identification of an optimal mix that significantly elevated the 28-day compressive strength to 126 MPa. This optimal mix was characterised by a W/B ratio of 0.28, a fibre volume of 3%, a SiC/B ratio of 0 and an SP/B ratio of 2%. Furthermore, the study found a robust correlation between the empirical findings of the second phase and the predictions of the developed mathematical model, which substantiates the effectiveness of the Taguchi orthogonal array in enhancing the compressive strength of UHPGC.

The third chapter investigates the mechanical and durability characteristics of fibre-reinforced geopolymer composites (FRGCs). The Taguchi method was employed by using the L9 orthogonal array with four parameters across the three levels of each parameter; the parameters were the percentage of fibre and the W/B, SiC/B and SP/B ratios. The W/B ratio had the most significant impact on the composites' mechanical and durability characteristics. Analysis of variance (ANOVA) with residual fitting was conducted to derive mathematical models for accurately predicting the compressive strength that exhibited a good correlation with the test results.

The fourth chapter studies UHPC-filled double-skin aluminium tube (UHPC-FDAT) columns under combined loading conditions. Four columns under concentric and eccentric loading conditions and a beam were tested. The findings show that increasing the loading eccentricity reduced the ultimate load with an increase in the corresponding mid-height lateral displacement. The specimens tested experimentally were also modelled numerically using the Abaqus software. The numerical results show a very high agreement with the results obtained experimentally. Therefore, a parametric study was conducted by changing one variable among compressive strength, inner tube thickness, outer tube thickness and hollow ratio under the same loading conditions. The outcome of this parametric study shows the dominant influence of the compressive strength of UHPC under axial loading where an increase in the outer tube thickness achieved a higher load while enhancing the loading eccentricity.

The fifth chapter examines FRGC-filled double-skin square steel tube (FRGC-FDST) columns. Four columns under concentric and eccentric loading conditions and a beam were tested. An interaction diagram was plotted experimentally and analytically to assess the capabilities of existing models to predict the results for this kind of column. The findings show good agreement between the experimental and theoretical analyses. Furthermore, finite elements modelling (FEM) was conducted with Abaqus to simulate the constructed columns in the experimental program. The numerical and experimental behaviours of the columns also agreed.

STATEMENT OF ORIGINALITY

I certify that this work contains no material which has been accepted for the award of any other degree or diploma in my name, in any university or other tertiary institution and, to the best of my knowledge and belief, contains no material previously published or written by another person, except where due reference has been made in the text. In addition, I certify that no part of this work will, in the future, be used in a submission in my name, for any other degree or diploma in any university or other tertiary institution without the prior approval of the University of Adelaide and where applicable, any partner institution responsible for the joint- award of this degree.

I acknowledge that copyright of published works contained within this thesis resides with the copyright holder(s) of those works.

I also give permission for the digital version of my thesis to be made available on the web, via the University's digital research repository, the Library Search and also through web search engines, unless permission has been granted by the University to restrict access for a period of time.

02/12/2024

Mohammad Dhaifallah Alameri Date

LIST OF ARTICLES PUBLISHED/UNDER REVIEW/SUBMITTED

JOURNAL PAPERS

Alameri, M., Mohamed Ali, M. S., Elchalakani, M., Sheikh, A., & Fan, R. (2024). Self-Healing and Mechanical Behaviour of Fibre-Reinforced Ultra-High-Performance Concrete Incorporating Superabsorbent Polymer Under Repeated and Sustained Loadings. *Fibers*, 12(11), 95.

Alameri, M., Joseph, J., Mohamed Ali, M. S., Elchalakani, M., & Sheikh, A. H. (2024). Optimising GGBS-based ultra high-performance geopolymer mortar: an orthogonal array approach. *Australian Journal of Structural Engineering*, 1-16.

Alameri, M., Mohamed Ali, M. S., Elchalakani, M., & Sheikh, A. (2024). "Optimizing slag-based fibre reinforced geopolymer mix design for enhanced strength and durability" Submitted to *Journal of Building Engineering* (under review)

Alameri, M., Mohamed Ali, M. S., Elchalakani, M., & Sheikh, A. (2024). "Structural behaviour of UHPC-filled double-skin aluminium tubular columns under combined loads" Submitted to *Journal of Thin-Walled Structures*

Alameri, M., Mohamed Ali, M. S., Elchalakani, M., & Sheikh, A. (2024). "Investigation of high-performance geopolymer concrete-filled double-skin columns under combined loading conditions" Submitted to *Journal of Constructional Steel Research* (under review)

CONFERENCE PAPER

Alameri, M., Sadakkathulla, M. M., Sheikh, A. H., & Elchalakani, M. (2023). Self-healing Behaviour of Ultra-High-Performance Concrete Under Constant Load. In International Symposium of the International Federation for Structural Concrete (pp. 506-513). Cham: Springer Nature Switzerland.).

ACKNOWLEDGEMENTS

In the name of Allah, the Most Gracious, the Most Merciful, I begin by expressing my deepest gratitude to Almighty Allah for granting me the strength, patience, and guidance throughout my academic journey. Without His blessings and mercy, I would not have been able to overcome the challenges and achieve this milestone. I am forever thankful for the wisdom and perseverance that have been bestowed upon me, allowing me to navigate through this complex and rewarding path. Alhamdulillah.

I would like to extend my deepest and heartfelt appreciation to my principal supervisor, Dr. Mohamed Mohamed Sadakkathulla. His unwavering dedication to my progress, combined with his exceptional knowledge and insight, has been fundamental to the completion of this thesis. His constant availability for guidance, thoughtful suggestions, and thorough attention to detail have shaped not only this research but also my personal growth as a scholar. His patience in answering my questions, willingness to challenge me to think critically, and continued encouragement during moments of difficulty have been truly invaluable. I am particularly grateful for his ability to foster an environment where I felt supported and empowered to pursue my ideas, while always steering me in the right direction. His mentorship has left a lasting impact on both my academic journey and my professional development, and for that, I am sincerely thankful. I am also deeply grateful to my co-supervisor, Associate Professor Abdul Sheikh, whose advice and constructive criticism have significantly enhanced the quality of my work. Their dedication, patience, and belief in my abilities have been a constant source of motivation, and I am truly fortunate to have had the privilege of working under their mentorship.

With profound sadness and a heavy heart, I dedicate this thesis to the loving memory of my beloved mother (Alwa), who passed away in 2022. Not a day goes by without me missing her presence, her love, and her unwavering support. Her belief in me, even in times when I doubted myself, gave me the strength to pursue my dreams. Although she is no longer with me in this world, I feel her spirit guiding me every step of the way. This work is a testament to the sacrifices she made and the values she instilled in me. I carry her memory with me always, and her absence is a void that time cannot heal. May Allah grant her the highest place in Jannah and may her soul rest in eternal peace.

To my dearest father (Dhaifallah), whose absence I feel deeply but whose love transcends the miles between us. Though we are separated by distance, I know you have always been with me in spirit, missing me as much as I miss you. Your strength, guidance, and endless prayers have been a silent but powerful force behind every step of this journey. Even when I couldn't see you, I felt the warmth of your support in my heart, reminding me of the values you've instilled in me—perseverance, integrity, and dedication. I long for the day we can be together again, but until then, this accomplishment is as much a tribute to you as it is a reflection of your love and belief in me.

I owe a special debt of gratitude to my beloved wife (Afrah), who has been my steadfast companion and greatest supporter during the seven years we have built our life together in Australia. Her unwavering love, patience, and strength have been my constant source of comfort and motivation throughout this challenging journey. She has gracefully endured the demands

of my academic pursuits, offering me encouragement when I needed it most and standing by me through every challenge, both personal and professional. Her sacrifices, understanding, and faith in me have been nothing short of remarkable, and this achievement is as much hers as it is mine. I am forever grateful for her partnership, which has been a guiding light in both my life and my work.

To my beloved sons, Abdullah and Saud, who have spent much of their young lives while I pursued this PhD. Your boundless energy, infectious smiles, and pure joy have been the light that carried me through even the most challenging days. Every time I felt exhausted, your laughter gave me the strength to keep going. You've both been my greatest motivation and my constant reminder of why this journey is worth it. This achievement is not only for me, but for you as well, and I hope one day it inspires you to pursue your own dreams with the same determination and heart.

To my dear siblings, Hassan, Lama, Abdulaziz, Abdulmajeed, and Samah, who have always welcomed me with open arms during my vacations. Your warmth, love, and hospitality provided me with the much-needed comfort and joy, making every return home a cherished memory. I am deeply grateful for the constant support and encouragement you have given me throughout this journey.

To my father-in-law, Abdullah, and my mother-in-law, Hanan, thank you for your kindness, understanding, and steady belief in me. Your support has meant the world to me.

Lastly, to my friends, who have been by my side through this long and challenging process, your friendship and encouragement have helped me stay grounded and motivated. I am truly blessed to have all of you in my life.

INTRODUCTION AND GENERAL OVERVIEW

Across the globe, there is increased demand for infrastructure due to the rapid growth of the world population, which is expected to increase by 20% in 30 years [1]. One of the preferred cementitious materials used to answer this need for new buildings is concrete, which can be easily made and employed. Therefore, concrete technology has advanced in terms of strength and durability. However, as the main binder for concrete, cement contributes about 7% of greenhouse gas emissions globally [2]. This problem has led to the development of more durable and efficient concrete or the elimination of cement and the production of cementless concrete.

The advancement of concrete technology has resulted in the creation of ultra-high-performance concrete (UHPC), which is known for its superior strength (compression above 120 MPa), efficient durability characteristics and the addition of fibres that make it more ductile than conventional concrete [3]. However, even with these advantages, UHPC is prone to cracks caused by excessive loads in the tension face or autogenous shrinkage due to the low water-to-binder (W/B) ratio used [4]. Consequently, structural elements made of UHPC need to be maintained regularly to avoid any degradation of their structural performance. Many techniques have been developed to meet these maintenance requirements, such as the inclusion of smart materials to hydrate the anhydrous cement particles [5]. This technique is called self-healing, and it can significantly improve the structural elements made of concrete, thus reducing their maintenance requirements. Self-healing increases the durability and sustainability of structural elements.

UHPC uses cement as its main binder, which should be reduced or eliminated to lower the CO_2 emissions caused by producing cement. An alternative to concrete made of cement is

geopolymer concrete (GPC). This cementless concrete is also known as an alkali-activated material. Waste materials, such as slag [6], fly ash [7] and metakaolin [8], which are rich in aluminosilicate, are used as the main binders for this type of concrete, and they can be activated by alkali-activated solutions (AASs), such as sodium hydroxide (NaOH) and sodium silicate (Na2SiO3).

High-performance concrete (HPC) and UHPC can be made without cement through geopolymerisation. Many researchers have obtained high-performance geopolymer concrete (HPGC) or ultra-high-performance geopolymer concrete (UHPGC) [9–11]. However, many variables affect the production of GPC, including the type of binder material, the ratio of the AAS, the molarity of NaOH, the silicate modulus of Na2SiO3, the W/B ratio and the source of the binder materials. Hence, there is a need to optimise the mix design of GPC through statistical approaches (e.g., the Taguchi method [12–14]) to produce HPGC or UHPGC.

Concrete-filled double-skin tube (CFDST) members are built by taking out the central concrete from concrete-filled single-skin tube (CFST) members and replacing it with a hollow steel tube, which slightly improves flexural strength [15]. CFDST members have similar advantages to CFST ones, in addition to being more lightweight and having higher bending stiffness [16]. Different concrete types have been used to construct CFDST columns, such as conventional concrete [17], HPC [18], UHPC [19] and rubberised concrete [20].

Objectives

This thesis has the following objectives:

- Study the effects of a superabsorbent polymer (SAP) on UHPC in terms of mechanical properties, durability characteristics and microstructure. The improvement of self-healing properties obtained by the addition of the SAP will also be studied by applying sustained tensile loads on prisms.

- Optimise and unify a mix design procedure for UHPGC based on the Taguchi method, which is a statistical method to reduce the number of experiments by changing several variables, to achieve the precise production of GPC through an extensive experimental mix design.
- Based on the above-mentioned mix design procedure, produce HPGC and verify its mechanical properties and durability characteristics with the Taguchi method.
- Study UHPC-filled double-skin aluminium tube (UHPC-FDAT) columns experimentally and verify the relevant numerical model with respect to the experimental results.
- Perform a parametric study based on the verified numerical model by changing one variable at a time to measure the effect of each variable.
- Study the fibre-reinforced HPGC-filled double-skin square steel tube (HPGC-FDST) columns experimentally, analytically and numerically.

Thesis Outline

This thesis consists of several manuscripts that have been published or are under review by reputable international journals. Each chapter addresses one of the objectives mentioned above and consists of a manuscript. The chapters have a tripartite structure. First, there is an introductory statement that addresses the main objective of the manuscript; second, the statement of authorship is provided, which explains the contribution of each author; third, the main body of the manuscript is presented.

The first chapter of this thesis focuses on the mechanical responses of UHPC mixed with an SAP under repetitive flexural loads and sustained tensile loading. The SAP-to-binder ratios used in this study were 0.3% and 0.4%; a control UHPC mix was also examined. The mechanical properties of these mixes were investigated under ambient, water and 100% relative humidity (RH) curing conditions. In addition, the mechanical performance of ambient-, water- and 100% RH-cured prismatic specimens (100 mm × 100 mm × 500 mm) under repeated loads

was studied under the same curing conditions. Regarding the sustained tensile loading, prismatic specimens (75 mm × 75 mm × 500 mm) were kept under curing conditions of wet and dry cycles with the applied load for 28 days. The results show that incorporating an SAP into UHPC enhances the cement's elastic modulus, flexural strength and tensile strength. Also, the mixes with SAP exhibited compressive strength above 120 MPa after 90 days. Furthermore, the load recovery of the prisms under repetitive flexural loads and those under sustained tensile loading demonstrated that the self-healing efficiency of the SAP incorporated into the UHPC mixes was higher than that of the control mixes.

The second chapter concentrates on the development of UHPGC based on the compressive strength results. The Taguchi method was used to form an L9 orthogonal array, which involves nine experiments conducted by changing four parameters, with each parameter having three levels. Two trials were conducted based on the provided mix design procedure and the Taguchi method. In the first trial, the variables were the W/B ratio, silica-fume-to-binder ratio, potassium-silicate-to-potassium-hydroxide ratio and aggregate-to-binder ratio. The second trial included the following variables: W/B ratio, percentage of fibre content, silicon-carbide-to-binder (SiC/B) ratio and superplasticiser-to-binder (SP/B) ratio. To measure the impact of the variables, compressive strength was assessed based on the signal-to-noise ratio. The implementation of the Taguchi method facilitated a thorough evaluation of 18 unique mix designs, leading to the identification of an optimal mix that significantly elevated the 28-day compressive strength to 126 MPa. This optimal mix was characterised by a W/B ratio of 0.28, a fibre volume of 3%, a SiC/B ratio of 0 and an SP/B ratio of 2%. Furthermore, the study found a robust correlation between the empirical findings of the second trial and the predictions of the developed mathematical model, which substantiates the effectiveness of the Taguchi orthogonal array in enhancing the compressive strength of UHPGC. This research provides a viable

pathway for mix design optimisation and contributes to the broader goal of advancing construction material technology through methodical parameter analysis.

The third chapter investigates the impact of W/B ratio, percentage of fibre content, SiC/B ratio and SP/B ratio on the performance of fibre-reinforced geopolymer composites (FRGCs) manufactured using high quantities of municipal solid waste. The mechanical and durability characteristics of the developed mixes were assessed using the Taguchi method; each parameter was examined across three levels using an L9 orthogonal array for the experimental setup. This approach facilitated a detailed analysis of the influence of each parameter on the properties of the FRGCs. The experimental program included evaluations of mechanical properties such as compressive, flexural and splitting tensile strength, along with durability properties, which were assessed with porosity and sorptivity tests. The findings show that the W/B ratio had the greatest impact on both mechanical and durability characteristics. Moreover, ANOVA with residual fitting was conducted to derive mathematical models for accurately predicting the compressive strength that exhibited a good correlation with the test results.

The fourth chapter studies UHPC-filled double-skin aluminium tube (UHPC-FDAT) columns under combined loading conditions. Four columns with constant cross-section dimensions and lengths of 1,000 mm were tested experimentally under different levels of loading eccentricity (0 mm, 30 mm, 60 mm and 90 mm). Furthermore, a 1,500 mm long beam was tested under a four-point bending load. The results show that increasing the loading eccentricity led to a reduction in the ultimate load with an increase in the corresponding mid-height lateral displacement. Additionally, the specimens tested experimentally were modelled numerically with the Abaqus software. The numerical findings show a very high agreement with the results obtained experimentally. Therefore, a parametric study was conducted by changing one

variable among compressive strength, inner tube thickness, outer tube thickness and hollow ratio under the same loading conditions. The outcome of this parametric study shows the dominant influence of the compressive strength of UHPC under axial loading where an increase in the outer tube thickness achieved a higher load while enhancing the loading eccentricity.

The fifth chapter investigates double-skin stainless steel tube columns filled with FRGC under concentric, eccentric and flexural loading conditions. Experimental work was conducted to test four short columns under different eccentricities (0 mm, 10 mm, 40 mm and 70 mm) and a beam subjected to three-point flexural bending. An interaction diagram was plotted experimentally and analytically to assess the capabilities of existing models to predict the results for this kind of column. The results show a good agreement between the experimental and theoretical analyses. Furthermore, finite elements modelling (FEM) using Abaqus was conducted to simulate the constructed columns in the experimental program. The numerical and experimental behaviours of the columns also agreed.

The final chapter concludes the thesis by offering important final remarks and suggestions for future research.

References

[1] N. United, World Population Prospects-Population Division-United Nations, UN Department of Economic and Social Affairs Population Division (2024).

[2] E. Benhelal, G. Zahedi, E. Shamsaei, A. Bahadori, Global strategies and potentials to curb CO2 emissions in cement industry, J Clean Prod 51 (2013) 142–161. https://doi.org/https://doi.org/10.1016/j.jclepro.2012.10.049.

[3] J. Li, Z. Wu, C. Shi, Q. Yuan, Z. Zhang, Durability of ultra-high performance concrete–A review, Constr Build Mater 255 (2020) 119296. https://doi.org/https://doi.org/10.1016/j.conbuildmat.2020.119296.

[4] W. Zhang, Q. Zheng, A. Ashour, B. Han, Self-healing cement concrete composites for resilient infrastructures: A review, Compos B Eng 189 (2020) 107892. https://doi.org/10.1016/j.compositesb.2020.107892.

[5] Z. Lv, D. Chen, Overview of recent work on self-healing in cementitious materials, Materiales de Construccion 64 (2014) e034--e034. https://doi.org/10.3989/mc.2014.05313.

[6] M. Albitar, M.S.M. Ali, P. Visintin, Experimental study on fly ash and lead smelter slag-based geopolymer concrete columns, Constr Build Mater 141 (2017) 104–112.

[7] D. Hardjito, S.E. Wallah, D.M.J. Sumajouw, B. V Rangan, Fly Ash-Based Geopolymer Concrete, Australian Journal of Structural Engineering 6 (2005) 77–86. https://doi.org/10.1080/13287982.2005.11464946.

[8] C. Tippayasam, P. Balyore, P. Thavorniti, E. Kamseu, C. Leonelli, P. Chindaprasirt, D. Chaysuwan, Potassium alkali concentration and heat treatment affected metakaolin-based geopolymer, Constr Build Mater 104 (2016) 293–297.

[9] S.M.A. Qaidi, D.S. Atrushi, A.S. Mohammed, H.U. Ahmed, R.H. Faraj, W. Emad, B.A. Tayeh, H.M. Najm, Ultra-high-performance geopolymer concrete: A review, Constr Build Mater 346 (2022) 128495. https://doi.org/https://doi.org/10.1016/j.conbuildmat.2022.128495.

[10] P.S. Ambily, K. Ravisankar, C. Umarani, J.K. Dattatreya, N.R. Iyer, Development of ultra-high-performance geopolymer concrete, Magazine of Concrete Research 66 (2014) 82–89. https://doi.org/https://doi.org/10.1680/macr.13.00057.

[11] S. Xu, P. Yuan, J. Liu, Z. Pan, Z. Liu, Y. Su, J. Li, C. Wu, Development and preliminary mix design of ultra-high-performance concrete based on geopolymer, Constr Build Mater 308 (2021) 125110. https://doi.org/10.1016/j.conbuildmat.2021.125110.

[12] G. Taguchi, S. Chowdhury, Y. Wu, Taguchi's Quality Engineering Handbook, Wiley, Livonia, 2004. https://doi.org/DOI:10.1002/9780470258354.

[13] M. Olivia, H. Nikraz, Properties of fly ash geopolymer concrete designed by Taguchi method, Materials & Design (1980-2015) 36 (2012) 191–198. https://doi.org/10.1016/j.matdes.2011.10.036.

[14] M.N.S. Hadi, N.A. Farhan, M.N. Sheikh, Design of geopolymer concrete with GGBFS at ambient curing condition using Taguchi method, Constr Build Mater 140 (2017) 424–431. https://doi.org/10.1016/j.conbuildmat.2017.02.131.

[15] J.C.M. Ho, C.X. Dong, Improving strength, stiffness and ductility of CFDST columns by external confinement, Thin-Walled Structures 75 (2014) 18–29.

[16] M. Elchalakani, X.-L. Zhao, R. Grzebieta, Tests on concrete filled double-skin (CHS outer and SHS inner) composite short columns under axial compression, Thin-Walled Structures 40 (2002) 415–441.

[17] M. Elchalakani, X.-L. Zhao, R. Grzebieta, Tests on concrete filled double-skin (CHS outer and SHS inner) composite short columns under axial compression, 2002. www.elsevier.com/locate/tws.

[18] B. Zhang, J.G. Teng, T. Yu, Compressive behavior of double-skin tubular columns with high-strength concrete and a filament-wound FRP tube, Journal of Composites for Construction 21 (2017) 04017029.

[19] J.-J. Zeng, Y.-Z. Zheng, Y.-L. Long, Axial compressive behavior of FRP-concrete-steel double skin tubular columns with a rib-stiffened Q690 steel tube and ultra-high strength concrete, Compos Struct 268 (2021) 113912.

[20] M. Elchalakani, M.F. Hassanein, A. Karrech, B. Yang, Experimental investigation of rubberised concrete-filled double skin square tubular columns under axial compression, Eng Struct 171 (2018) 730–746. https://doi.org/10.1016/j.engstruct.2018.05.123.

CHAPTER 1

Background

This chapter focuses on the mechanical responses of UHPC mixed with an SAP under repetitive flexural loads and sustained tensile loading. The SAP-to-binder ratios used in this study were 0.3% and 0.4%; a control UHPC mix was also examined. The mechanical properties, durability characteristics, prisms under repetitive flexural loads and sustained tensile loadings were investigated experimentally to determine the effect of incorporating SAP into UHPC.

List of Manuscripts

Alameri, M., Mohamed Ali, M. S., Elchalakani, M., Sheikh, A., & Fan, R. (2024). Self-Healing and Mechanical Behaviour of Fibre-Reinforced Ultra-High-Performance Concrete Incorporating Superabsorbent Polymer Under Repeated and Sustained Loadings. *Fibers*, 12(11), 95.

Statement of Authorship

Title of Paper	Self-Healing and Mechanical Behaviour of Fibre-Reinforced Ultra-High-Performance Concrete Incorporating Superabsorbent Polymer Under Repeated and Sustained Loadings
Publication Status	☑ Published ☐ Accepted for Publication ☐ Submitted for Publication ☐ Unpublished and Unsubmitted work written in manuscript style
Publication Details	Alameri, M., Mohamed Ali, M. S., Elchalakani, M., Sheikh, A., & Fan, R. (2024). Self-Healing and Mechanical Behaviour of Fibre-Reinforced Ultra-High-Performance Concrete Incorporating Superabsorbent Polymer Under Repeated and Sustained Loadings. Fibers, 12(11), 95.

Principal Author

Name of Principal Author (Candidate)	Mohammad Alameri		
Contribution to the Paper	Conceptualisation, methodology, and manuscript writing and revision		
Overall percentage (%)	65%		
Certification:	This paper reports on original research I conducted during the period of my Higher Degree by Research candidature and is not subject to any obligations or contractual agreements with a third party that would constrain its inclusion in this thesis. I am the primary author of this paper.		
Signature		Date	24-10-2024

Co-Author Contributions

Name of Co-Author	M.S. Mohamed Ali		
Contribution to the Paper	Supervision, conceptualisation, methodology, and manuscript revision (20%)		
Signature		Date	24-10-2024

Name of Co-Author	Mohamed Elchalakani		
Contribution to the Paper	Supervision, conceptualisation, methodology, and manuscript revision (5%)		
Signature		Date	28-10-2024

Name of Co-Author	Abdul Sheikh
Contribution to the Paper	Supervision, conceptualisation, methodology, and manuscript revision (5%)

Signature		Date	29-10-2024

Name of Co-Author	Rong Fan		
Contribution to the Paper	Methodology, data curation, and manuscript writing and revision (5%)		
Signature		Date	12-11-2024

Self-Healing and Mechanical Behaviour of Fibre-Reinforced Ultra-High-Performance Concrete Incorporating Superabsorbent Polymer Under Repeated and Sustained Loadings

Mohammad Alameri[1], M. S. Mohamed Ali[1,*], Mohamed Elchalakani[2], Abdul Sheikh[1] and Rong Fan[3]

[1] *School of Architecture and Civil Engineering, The University of Adelaide, Adelaide, SA 5005, Australia; mohammad.alameri@adelaide.edu.au (M.A.); abdul.sheikh@adelaide.edu.au (A.S.)*

[2] *Department of Civil, Environmental and Mining Engineering, The University of Western Australia, Perth, WA 6009, Australia; mohamed.elchalakani@uwa.edu.au*

[3] *Commonwealth Scientific and Industrial Research Organisation (CSIRO) Mineral Resources, Adelaide, SA 5064, Australia; rong.fan@csiro.au*

**Correspondence: mohamed.mohamedsadakkathulla@adelaide.edu.au*

Abstract

This study investigated the mechanical responses and self-healing capability of incorporating superabsorbent polymer (SAP) particles in Fibre-Reinforced Ultra-High-Performance Concrete (UHPC) mixes under repetitive flexural and sustained tensile loadings. UHPC with SAP addition of 0.3% and 0.4% of the binder ratio were studied along with a control UHPC mix. The methodology included investigating the mechanical properties of these mixes under ambient, water, and 100% of relative humidity (RH) curing conditions. In addition, the mechanical performance of ambient-, water-, and 100% RH-cured prismatic specimens (100 mm × 100 mm × 500 mm) under repeated load was studied under the same curing conditions. Prismatic specimens (75 mm × 75 mm × 500 mm) were kept under cure conditions of wet and dry cycles with applied tensile load for 28 days for the sustained tensile load. The results showed that incorporating SAP into UHPC enhances the elastic modulus, flexural strength, and tensile strength. Also, mixes with SAP have exhibited compressive strength above 120 MPa after 90 days. Furthermore, the load recovery of the prisms under repetitive flexural load and prisms under sustained tensile loading demonstrated the self-healing efficiency of SAP incorporated into the UHPC mixes higher than the control mix specimens.

Keywords: cracks; self-healing; superabsorbent polymer; ultra-high-performance concrete; sustained loadings; mechanical properties; UHPC.

1 Introduction

Ultra-high-performance concrete (UHPC) exhibits excellent ductile characteristics, primarily due to the strain-hardening behaviour provided by steel fibres in the post-cracking stage under tensile loads. It also possesses remarkable mechanical, ductile, and durability features [1,2]. UHPC is widely applied in numerous construction projects, including concrete bridges and offshore towers [3,4]. However, the production of UHPC requires a low water-to-binder ratio (w/b) of up to 0.2. Consequently, a significant amount of unhydrated cement remains within the UHPC matrix, attributed to the limited availability of water for complete hydration [5]. This low w/b ratio is also responsible for high autogenous shrinkage, leading to the development of microcracks [6]. These cracks affect the internal matrix configuration of the concrete and, as they widen due to shrinkage and applied loads, increase the concrete's permeability to aggressive chemicals accelerating concrete deterioration [7]. In response, many codes of practice such as ACI 224R-01 [8], have stipulated crack width limits, especially for elements exposed to alternating wetting and drying cycles.

In light of these challenges, regular inspection, repair, and maintenance become crucial to ensure the durability and extend the serviceable life of existing concrete structures. Given the tedious and costly nature of these processes, there is a growing need to develop in-built repair techniques that involve autogenous healing and closing of cracks by incorporating suitable self-healing agents. For example, nanoclay can be used to release water and hydrate anhydrous cement particles [9]. Additionally, other materials like ground granulated blast furnace slag (GGBS) and fly ash are known to promote the hydration process through the emerging carbonation of calcium hydroxide ($Ca(OH)_2$). Consequently, these innovations enable the healing and sealing of cracks up to 0.1 mm in width [10–12].

Additionally, other healing agents can be utilised to prevent crack formation due to enhanced autogenous shrinkage. These agents function by reserving water and then releasing it later to

internally cure the specimens when cracks occur. Lightweight aggregate (LWA), capable of absorbing between 5% and 25% of its weight in water, can significantly boost the internal curing mechanism. This effectively reduces autogenous shrinkage when the internal relative humidity (IRH) reaches around 96% [13,14]. However, an even more effective method of enhancing the healing mechanism involves incorporating a water-absorbing agent into the concrete mix, such as superabsorbent polymer (SAP), which can absorb water up to 1000 times its volume. The efficacy of SAP as an internal curing agent was investigated by Liu et al. [15], where it was found that SAP particles release water to prevent self-desiccation and enhance the hydration process [16,17]. Therefore, by adding SAP to the mix, the autogenous shrinkage of low w/b ratio mixes decreases and the formation of cracks can be effectively detained.

Superabsorbent polymers (SAPs) have been extensively investigated for their capacity to heal cracks caused by applied loads, as reported in numerous studies. In normal strength concrete (NSC), it was observed that cracks up to 0.3 mm could be sealed by using SAP, although this was associated with a notable decrease in the compressive strength of concrete [18,19]. This decrease occurs because SAP particles, after releasing water to promote the self-healing mechanism, leave behind voids [20]. Furthermore, the self-healing mechanism in high-strength concrete (HSC) with compressive strengths up to 100 MPa, particularly in specimens with added SAP has been examined by Olawuyi [21] indicating that the amount of SAP used in the concrete mix significantly affects mechanical properties, such as a reduction in compressive strength by more than 25% due to the presence of voids caused by SAP. Consequently, subsequent studies by Pourjavadi et al. [22], Savva and Petrou [23], and Kang et al. [24] focused on optimising the SAP dosage to achieve an ideal mix. These investigations revealed that a SAP-to-binder ratio ranging from 0.1% to a maximum of 1% provides an effective balance between maintaining mechanical properties and the healing efficiency of the SAP particles.

Recent investigations primarily concentrated on how SAP influences key properties of UHPC, such as shrinkage [15] and tensile strength [25]. The addition of SAP has been shown to significantly alter the shrinkage characteristics of UHPC, which is crucial for minimising crack formation and ensuring structural integrity [15]. Moreover, the effect of SAP on the tensile strength of UHPC was thoroughly explored, revealing insights into how these polymers can enhance the overall mechanical performance of concrete [26]. This body of research contributes substantially to the development of self-healing UHPC with SAPs, making it a more versatile and robust material for modern construction needs.

Cracking the concrete under tension is inherently difficult as it is brittle which could lead to an immediate failure of the specimens hence compressive tests are performed to initiate cracks; in recent studies, it was observed that the cracks occurred in the interfacial transition zone (ITZ) at around 70% of the compressive strength of the cubes [27–30]. However, adding the steel fibre to the concrete matrix can enhance the ductility and allow the specimens to be cracked in the tension face such as under three- and four-bending tests [31–34], direct tensile strength [35,36], and splitting tensile strength tests [37,38]. Repetitive loads were also introduced to create cracks and evaluate the self-healing mechanism [39–41].

The primary objective of this study was to conduct a comprehensive investigation into the influence of SAP on the mechanical properties of UHPC. Given the limited experimental data available, this research aimed to explain the self-healing mechanisms of UHPC when incorporating a small amount of SAP, whereas previous studies have proved that adding above 1% of SAP will rapidly deteriorate the mechanical performance of concrete. Furthermore, a direct correlation between the microstructural modifications and the macro-behaviour of UHPC mixes was established, both with and without SAP inclusion, to gain deeper insights into how these variations affect the overall performance of the material. A distinctive aspect of this study involved subjecting UHPC specimens containing SAP to sustained tensile loading

for a duration of 28 days, providing a novel approach to assess the healing ability of these materials under continuous stress conditions. By addressing these objectives, this study aimed to contribute significantly to the development of self-healing UHPC, enhancing its versatility and robustness for contemporary construction applications.

2 Experimental Programme

The full experimental programme is illustrated in Figure 1. Three different mixes produced for the purpose of comprehensively evaluating the mechanical performance, durability characteristics, microstructural analysis, and self-healing capabilities under different curing conditions represent the most common curing conditions in real-world scenarios without considering the aggressive conditions.

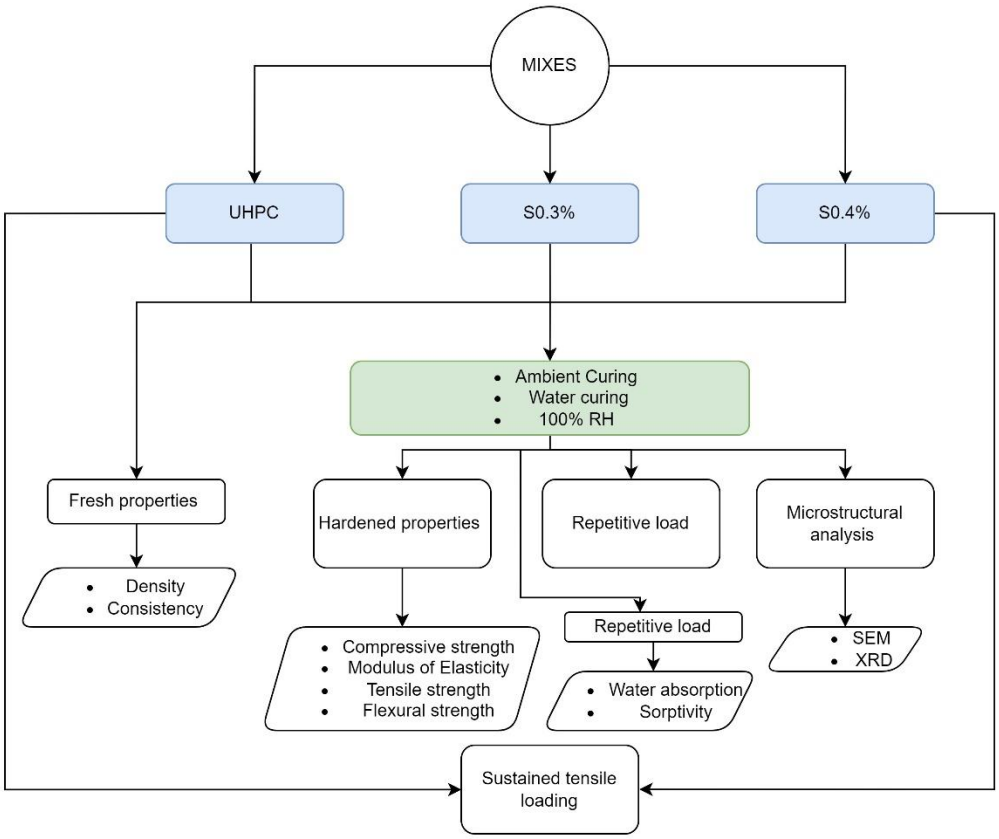


Figure 1. Flow chart of the experimental programme.

2.1 Material Used

The two main binders of this study were Portland cement and ground granulated blast furnace slag (GGBS); silica fume was used as a supplementary binder. The chemical compositions for the binders are summarised in Table 1. Blended and dried sand with high silica contents, sub-angular to rounded grains, and a diameter size ranging from 0.075 mm to 1.18 mm were utilised as fine aggregate. High-range water reducer (HRWR) with 36% solid contents by mass (polycarboxylates superplasticiser (SP), ViscoCrete-10 type, Sika, Sydney, Australia) was used to enhance the workability of the mix. High-strength microsteel fibre with a diameter of 0.2 mm and length of 13 mm with a tensile strength of 2500 MPa was utilised for ductility. The SAP type used in the mix is called Polyacrylate/Polyalcohol Copolymer with a variation in the diameter size between 0.05 mm to 0.5 mm, which can absorb up to 60 g/g.

Table 1. Chemical composition by mass %.

Materials	SiO_2	TiO_2	Al_2O_3	Fe_2O_3	MgO	CaO	Na_2O	K_2O	P_2O_5	SO_3
Cement	19.51	0.26	5.03	2.86	1.59	61.44	0.19	0.37	0.06	2.14
GGBS	35.10	0.57	13.59	0.98	5.36	41.52	0.14	0.33	0.04	0.10
SF	92.35	0.01	0.36	0.78	0.36	0.54	0.19	0.52	0.31	0.04
Quartz sand	93.48	0.04	0.06	0.06	0.03	0.02	0.039	0.02	0.01	0.01

2.2 Mix Proportion and Curing

2.2.1 Mix Procedures

The mixture details of UHPC are summarised in Table 2. The binder consists of OPC and GGBS only where (s/b) represents the fine aggregate-to-binder ratio and w/b represents the water-to-binder ratio, and SAP (%) and SP (%) refer to the percentage of the binder. UHPC denotes the control mix without added SAP, whereas S0.3 and S0.4 denote the concrete mix with a SAP dosage of 0.3% and 0.4% of the binder ratio. Initially, trial mixes with varying water and SP contents were carried out to optimise the workability of the wet mix so that it can be used in the further full-scale batches of the mix. For the mixing procedure, the dry cementitious materials (OPC, GGBS, and SF), sand, and SAP were mixed at room temperature for three minutes. Then, 90% of the water was added for one minute, followed by the SP mixed with the rest of the water and added to the mix. After that, the wet mixing was continued until

the desired consistency was obtained. Finally, the steel fibre was added to the mix for another three minutes to distribute the fibres homogeneously to the mix. Note that the mixing time can vary from the mixes due to the effect of added SAP dosages.

Table 2. Mix proportions.

Mix ID	Binder (%)		Silica Fume (%)s/b	w/b	* Added Water/b	SAP (%)	Steel Fibre (%) (Volume Fraction)	SP (%)
	Cement	GGBS						
UHPC	85	15	25	1.1	0.166	0	0	1.5	4
S0.3						0.0129	0.3		
S0.4						0.0172	0.4		

* The additional water needed to address the absorption of the SAP is calculated based on the SAP's absorption rate.

2.2.2 Curing

The fresh mix was poured into different moulds (cubes, cylinders, and prisms) and then these were cured under three different curing regimes namely: (i) ambient curing in the constant temperature chambers with 25 °C and 50% relative humidity (RH); (ii) water curing in ambient room temperature and humidity conditions; and (iii) 100% RH curing in a fog room. The specimens were demoulded after 24 h; curing commenced immediately and the specimens were cured under the prescribed curing regimes until the day of testing. In the case of reloading experiments, where the prisms were tested under the load again after 28 days, they were placed under the same curing condition after the initial loading stage.

2.3 Methods

2.3.1 Fresh Properties

The consistency test of all fresh mixes was conducted according to ASTM C1437 [42]. The unit weight of fresh concrete was obtained immediately after preparing the mixture by using a cylindrical mould.

2.3.2 Hardened Concrete

An MTS 300 kN closed loop Servo control testing machine with a data acquisition system was used for the flexural and tensile strength tests. After 28 and 56 days, the flexural strength test

was conducted by testing a prismatic specimen (100 mm wide, 100 mm deep, and 500 mm long). The applied load was controlled by using a displacement rate of 0.1 mm/min.

In order to evaluate the tensile strength of the mix, dog bone specimens were prepared as shown in Figure 2, according to the details provided by Singh et al. [43]. The concept of this specimen was to provide two gripping portions at the top and bottom and a shank in the middle. The gripping portions were large enough, which were half the length of the shank, to prevent any premature failure that could happen due to insufficient area. The gripping portions were designed to gradually decrease the width to match the width of the shank. Therefore, the purpose of this test was achieved by failing the specimen in the shank area. Hence, four linear variable differential transformers (LVDTs) (two on each side) were attached to the shank of the specimen to measure the strain and the crack opening. A very low displacement rate control of 0.002 mm/min was utilised to gradually apply the load and ensure that there was no quick and sudden failure in the specimen.

The compressive strength and the modulus of elasticity of the concrete were evaluated using cylindrical specimens (100 mm diameter × 200 mm height) according to the ASTM C39 [44]. The modulus of elasticity test was conducted by bonding four strain gauges to the specimens at their mid-height (two in the longitudinal direction and two in the transverse direction). Moreover, LVDTs were also used on opposite sides to confirm the readings from the axial strain gauges.

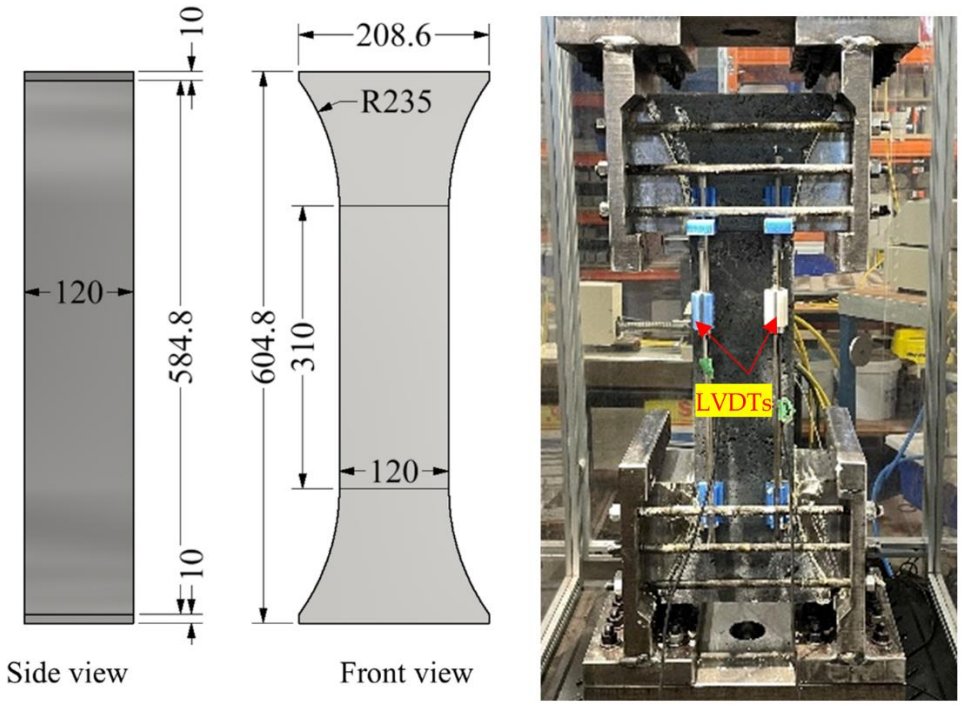


Figure 2. A diagrammatic view of dog bone test and the set-up under uniaxial tensile loading (dimensions in mm).

2.3.3 Durability Properties

Three-disc specimens each with a diameter of 100 mm and a height of 50 mm were cut from a cylindrical specimen to evaluate the effective permeable porosity of each mix according to the guidelines of ASTM C642 [45]. To achieve a constant mass, the specimens were placed in the oven to be dried for 24 h at a temperature of 110 °C. Then, the initial weight (w_i) was measured after placing the specimens at room temperature (25 ± 1 °C); they were then submerged in water for four days to obtain the saturated weight (w_s). The water absorption was calculated by using Equation (1).

$$\text{Water absorption}, \% = \left(\frac{w_s - w_i}{w_i}\right) \times 100 \qquad (1)$$

The sorptivity is an important feature in evaluating the water absorption and transmission via the capillary action of the concrete. The sorptivity test was conducted according to the guidelines of ASTM C1585 [46]. Three cylindrical specimens with a diameter of 100 mm and height of 50 mm were cut from the 28 day-cured cylinder for each mix. The specimens were placed in the oven to be dried for three days at a temperature of 50 °C. Afterwards, the

specimens were left at room temperature (25 ± 1 °C) for 24 h to cool down. Subsequently, they were put in a storage container and left again at room temperature for 15 days. A waterproof tape was used to cover all the peripheral surfaces except the bottom surface to protect the specimens from any flow of water. The base of the specimens was then drowned with a level of water around 3 mm. The specimens were then measured at different intervals up to 8 days. The sorptivity was thus evaluated according to Equation (2).

$$S = \frac{I}{t^{1/2}} \quad (2)$$

where t is the time-lapse in minutes, and I can be calculated from Equation (3) which is the cumulative water absorption (per unit area of inflow surface, mm)

$$I = \frac{\Delta m_t}{a \; x \; d} \quad (3)$$

where Δm_t is the change in mass with time t in grams, a is the exposed area in mm^2 of the specimen, and d is the density of water in g/mm^3.

2.3.4 Load Recovery Under 3-Point Bending Test

It is well-established that the UHPC mainly develops microcracks due to its dense matrix [47]. To effectively quantify and control these cracks, two specific indicators were employed to induce cracking in the specimens. The displacement ratio of the flexural strength test was measured prior to conducting the test at approximately 85% of the expected flexural displacement, the test was intentionally halted and the specimens were returned to their initial curing regime for an additional 28 days. Moreover, post-initial crack formation, each specimen was closely monitored to pre-empt any unforeseen failures. Notably, the presence of steel fibres in UHPC may manifest as curve fluctuations in the observed crack patterns due to the effect of the addition of steel fibres in the mix.

Two specimens were tested to evaluate the self-healing mechanism under repetitive loading. Details of the first specimen along with the testing setup are illustrated in Figure 3. For precise

crack detection, a Crack Mouth Opening Displacement (CMOD) was employed across a notch in this specimen and continuously monitored at a rate of 0.1 mm/min. CMOD was utilised to measure the opening of the cracks inside the notched specimens. The second specimen was unnotched and it was tested similarly to the notched specimen without any CMOD measurement.

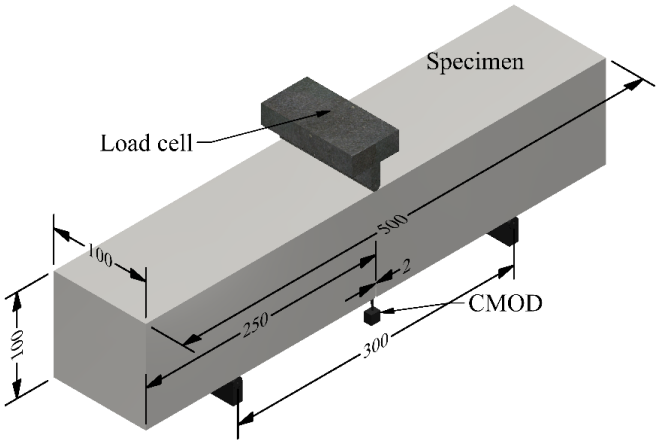


Figure 3. Notched specimens (dimensions in mm).

2.3.5 Microstructural Observations

Backscattered electron (BSE) imaging was utilised to assess the compactness of UHPC with and without SAP particles. The impact of SAP particles on the density of the microstructure including the interfacial transition zone (ITZ) was examined. The healing product and the matrix of the UHPC were also performed at specific points on the samples using energy-dispersive X-ray spectroscopy (EDX). For this, samples were collected from -thenotched specimens after the second loading stage. To halt further cement hydration, these samples were submerged in ethanol alcohol for three days and then oven-dried for an additional three days to ensure complete dryness. Moreover, each sample was enclosed in epoxy resin to create a stable mould and subsequently polished with sandpaper to prepare them for the experiment.

Additionally X-ray diffraction (XRD) analysis was conducted to quantify mineral phases in the mixes. Freshly broken samples were taken from the flexural strength test after 28 days and the notched pre-cracked specimens after 56 days of curing. These samples were ground and

prepared for the experiment. The ambient curing samples from all mixes were selected to be the representative samples in this experiment. It can be argued that ambient curing simulates realistically the condition in the internal parts of concrete elements. XRD patterns were recorded with a PANalytical X'Pert Pro Multi-purpose Diffractometer using Fe-filtered Co Kα radiation, an automatic divergence slit, 2° anti-scatter slit, and fast X'Celerator Si strip detector. The diffraction patterns were recorded in steps of 0.017° 2θ with a 0.5 s counting time per step for an overall counting time of approximately 30 min. Qualitative analysis was performed on the XRD data using in-house XPLOT and High-Score Plus (from PANalytical, Malvern, United Kingdom) search/match software. Furthermore, quantitative analysis was performed on the XRD data using the TOPAS version 6 Rietveld analysis software (from Bruker AXS, Melbourne, Australia).

2.3.6 Prisms Under Sustained Loading

Prismatic specimens with a cross-section of 75 mm × 75 mm and a length of 500 mm were poured and then cured for 28 days under ambient curing conditions. The test set-up is presented in Figure 4 for preparing and testing these specimens. The specimens were kept under sustained tensile loading for 28 days. At the mid-height of the specimen, a groove was made to measure the crack initiated by the applied tensile load. The cracking load was applied for 28 days under wet and dry curing cycles of two days where conditions were continuously altered. A water holder was designed specifically for this experiment to cure the area that cracked. For the purposes of the measurement, two LVDTs were attached on each side near the mid-height of the specimens. Moreover, a strain gauge was bonded to the threaded rod for the purpose of measuring the induced stress in the specimens. These strain values were converted to the equivalent stresses or loads according to the material properties of the threaded rod.

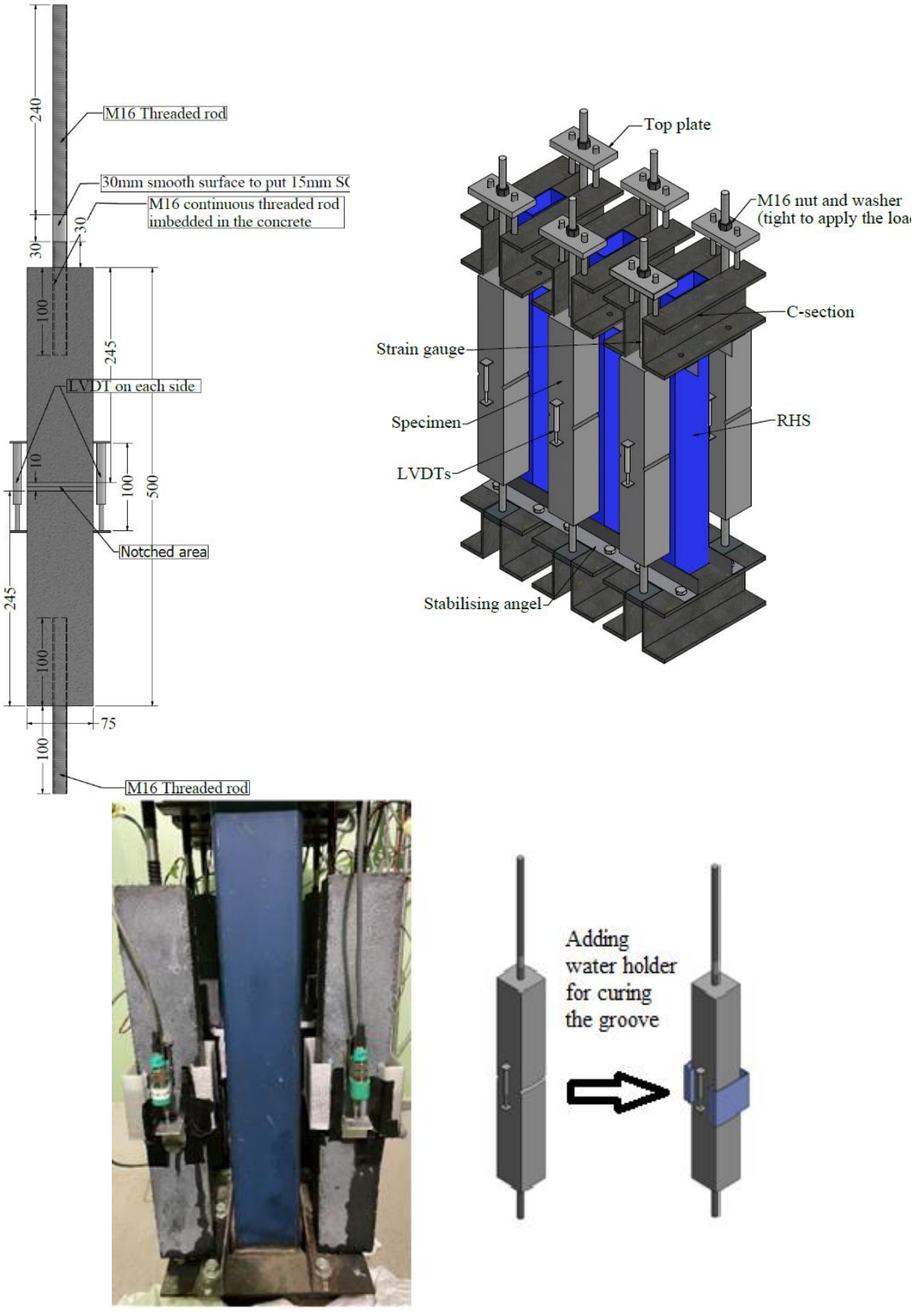


Figure 4. Test set-up of specimens under constant loading (dimensions in mm).

Initially, the specimens were subjected to a steadily increasing applied load until the first crack existed and then it was lowered to 50%, 60%, or 70% of the maximum load according to the results from the tensile strength tests; these reduced loads were sustained for a different period of days. The loads were adjusted manually to avoid any potential premature failure. Table 3 shows the different levels of loads and stresses that have been extracted from the tension test of the threaded rod.

Table 3. Stresses and loads under tensile strength.

	UHPC	**S0.4**
Stress at First crack (MPa)	4.50	3.84
Max. Stress (MPa)	4.62	4.14
Equivalent load for max stress (kN)	24.26	21.74

3 Results and Discussion

3.1 Fresh Properties

Commercially available SAP was procured from a single source in Australia and was mixed in its dry condition without any specific treatment. However, the effect of SAP dosages and w/b ratio on density and consistency of the fresh concrete was investigated in this study. Density is an important indicator of the strength and durability of hardened concrete, whereas consistency improves compatibility consolidation and ease of placement.

Figure 5 illustrates the properties of the fresh concrete for all mixes. It shows that adding SAP with extra free water resulted in a minor reduction in the density, a decrease of 0.86% for S0.3 and 1.15% for S0.4 from the corresponding UHPC control mix. This was due to the absorption of water by SAP during the mixing process as SAP can absorb up to 60 g/g. However, adding extra water to adjust for the water absorbed by SAP to maintain the consistency did not enhance the consistency as can be seen in Figure 5. Note that the control mix had 35% of consistency whereas the mixes S0.3 and S0.4 had a consistency of 33% and 37%, respectively. The main

factor for changing the consistency of each mix was the ability of SAP to absorb the water in the slurry, as reported previously [48].

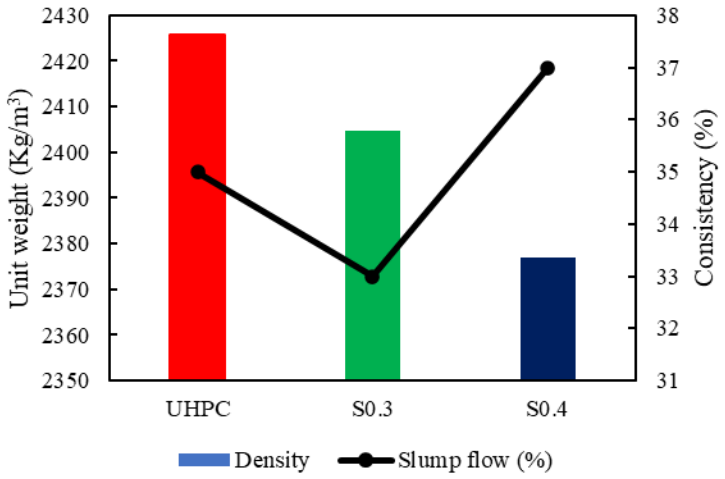


Figure 5. Fresh unit weight and consistency results.

3.2 Hardened Properties

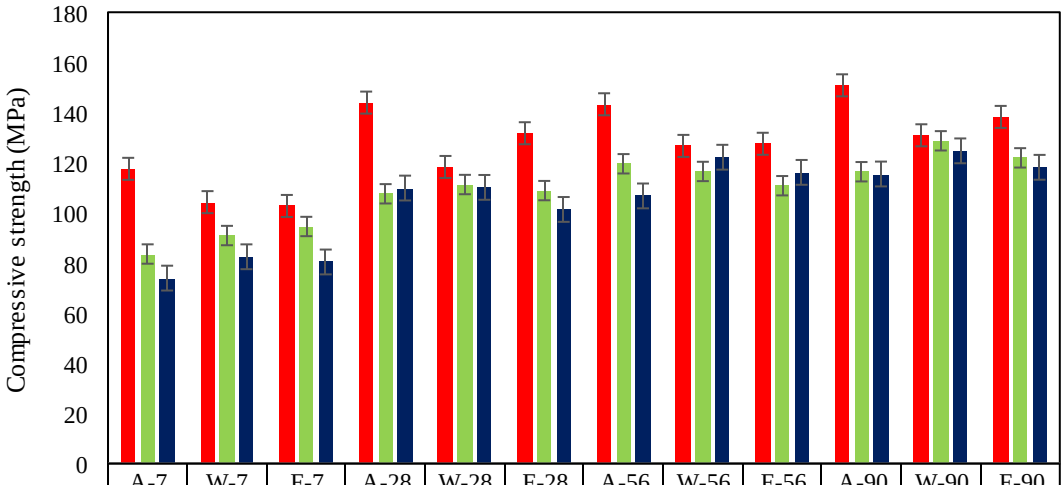
3.2.1 Compressive Strength and Elasticity

Figure 6 presents the compressive strength for all mixes at different time intervals (7, 28, 56, and 90 days) with varying conditions of curing (ambient, water, and 100% RH). UHPC mix with ambient curing had the highest values across all ages. Note that when correlated with the density results shown in Figure 7, the ambient-cured specimens exhibited higher compressive strength values across all ages as the denser the concrete, the better the behaviour under compression. Also, the compressive strength decreased with the increase in SAP dosages, specifically at the early stages. After seven days, the ambient curing mix without SAP had a higher value than S0.3 and S0.4 by 28.8% and 37.3%, respectively. Furthermore, a similar trend was observed for both water-cured and 100% RH curing specimens. For instance, in the case of water curing, the decrease in compressive strength was 12.5% for S0.3 and 21.2% for S0.4 compared to the corresponding control specimens. It can also be seen from Figure 6 that the compressive strength increased gradually with time in all mixes with different curing

conditions. At 28 days, the ambient-cured control specimen had the highest value, whereas the water-cured specimens yielded the best values for UHPC mixes with SAP; the difference between the control mix and S0.3 was 5.9% whilst it was 6.8% for mix S0.4.

Further decline of the difference in compressive strength between UHPC with and without SAP was noticed at 90 days; for example, for mix S0.3, the difference was 1.5% which was negligible. This proved that SAP efficiently assisted in the further hydration of the anhydrous cement particles with the increase in age [49]. On the other hand, the decrease in compressive strength was caused by the voids made by SAP after the desorption of water [50].

Table 4 summarises the modulus of elasticity values for the water-cured specimens at 7 and 28 days along with the corresponding maximum strain. Overall, the specimens with SAP exhibited higher stiffness than the control specimens without SAP. This was in contrast to the compressive strength results, as the modulus of elasticity of S0.3 at 7 days and 28 days showed an increase of 8.7% approximately. Therefore, it can be stated that adding SAP leads to improved modulus of elasticity as adding SAP causes the closure of microcracks and hence the stiffness of the concrete [51].



	A-7	W-7	F-7	A-28	W-28	F-28	A-56	W-56	F-56	A-90	W-90	F-90
UHPC	118	104	103	144	118	132	143	127	128	151	131	138
S0.3	84	91	95	108	111	109	120	117	111	116	129	122
S0.4	74	82	80	110	110	101	107	122	116	115	125	118

Figure 6. Compressive strength for 7, 28, 56, and 90 days for all mixes and different curing conditions (A = ambient, W = water, F = 100% RH).

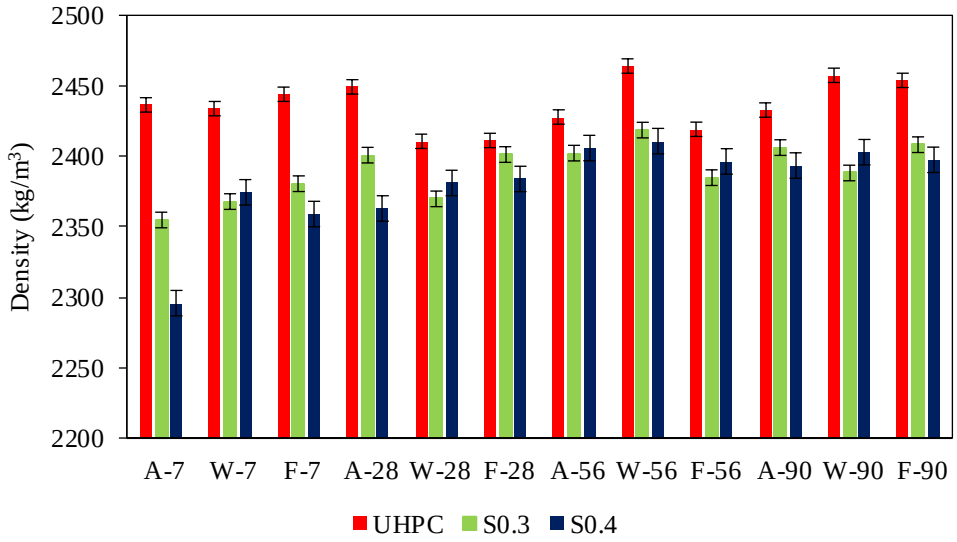


Figure 7. Density at 7, 28, 56, and 90 days for all mixes with different curing conditions (A = ambient, W = water, F = 100% RH).

Table 4. Modulus of elasticity for all mixes for water curing on 7 and 28 days alongside the related mechanical properties, water absorption, and volume of permeable voids.

Mix ID	No. of Days	E_c (GPa)	Max. Stress (MPa)	Max. Strain (με)	Water Absorption (%)	Volume of Permeable Voids (%)
UHPC	7	42.4	108.00	3173		
	28	46.2	125.79	2938	1.34	3.24
S0.3	7	46.3	95.71	2892		
	28	50.6	118.45	2818	2.38	5.46
S0.4	7	48.4	82.97	2385		
	28	47.4	112.40	2830	2.51	5.47

3.2.2 Flexural and Tensile Strength

Figure 8 shows the flexural strength results of all mixes after 28 days and 56 days. For 28 days, S0.3 under water curing had the best results with a flexural strength of 23.46 MPa whilst for the control mix, the best results were recorded for the water-cured specimens. Contrary to the previous results at 28 days, S0.4 had the highest value of flexural strength under 100% RH with 19.65 MPa. For 56 days, the flexural strength of S0.3 was slightly decreased under water curing. However, improved results were observed for ambient and 100% RH curing mixes. For UHPC without SAP, a minor decrease in the flexural strength for the water curing and almost no reduction in strength for the ambient curing was observed. It is interesting to note an increase of 29.7% for the 100% RH-cured specimen. For S0.4, the results fluctuated between an increase

in water and ambient curing and a decrease in the 100% RH curing conditions. The failure of all specimens occurred due to the extensive formation of microcracks; the steel fibres influenced this behaviour as they bridged the cracks, which yielded better strength. Hence, for flexural strength, a combination of SAP and fibre led to better performance of UHPC with SAP which was contrary to the compressive strength behaviour as SAP prevented self-desiccation which decreased internal relative humidity [52]. Consequently, the microcracks could be limited in the mixes with SAP.

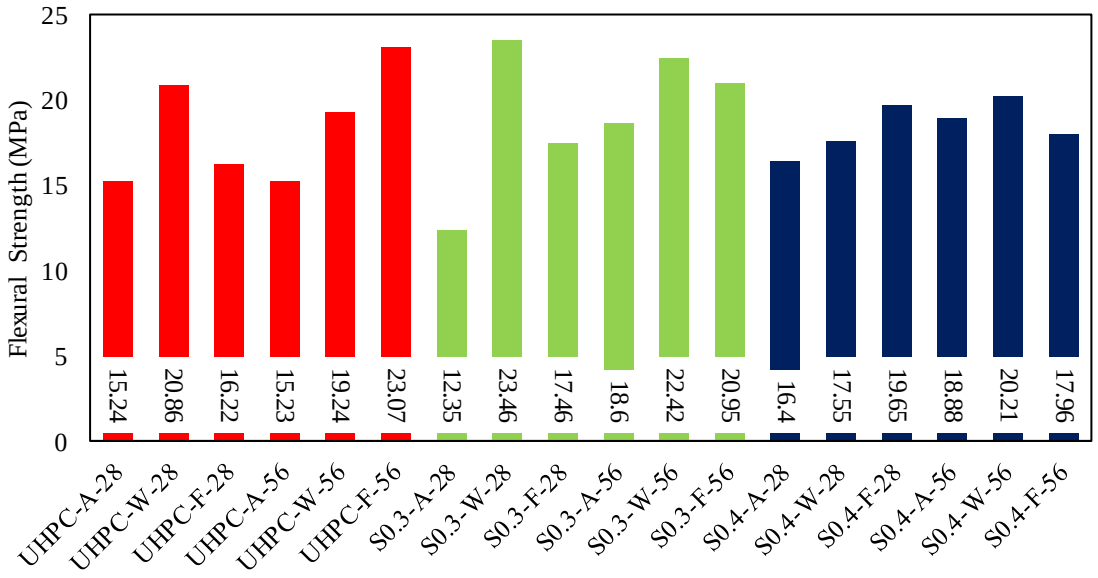


Figure 8. Flexural strength for all mixes at 28 and 56 days with different curing conditions.

The stress/strain relationship under the tensile load for all mixes under ambient curing is shown in Figure 9. The behaviour of specimens under direct tensile load can be classified into three levels: (i) the elastic region with the influence of fibre; (ii) the strain hardening region where the curves fluctuate at the peak strength due to the presence of steel fibres with an increase in the strain; and (iii) the strain softening process. Additionally, the fibre bridging behaviour affects the behaviour regardless of the effect of adding SAP. The SAP effect peaked with S0.3 with elastic behaviour until the peak stress. However, a drop of about 21.5% in the strength happened immediately after the peak stress, which transformed the curve to be in the strain hardening region with another drop to start the softening of the specimen after reaching above

4000 με. Alternatively, UHPC control and S0.4 specimens had lower strength but exhibited similar behaviour throughout. Interestingly, the S0.4 had the best strain hardening behaviour among the specimens and at around 6000 με, it held a higher load. However, a rapid decline in S0.4 happened, whereas the other specimens had a consistent decline. As mentioned previously in the flexural strength behaviour, the benefit of SAP to prevent self-desiccation, which increases the internal curing along with crack-bridging due to steel fibres to bridge the crack, helps in explaining the results of tensile strength. Similar findings have been found in a previous study by Yu et al. [53].

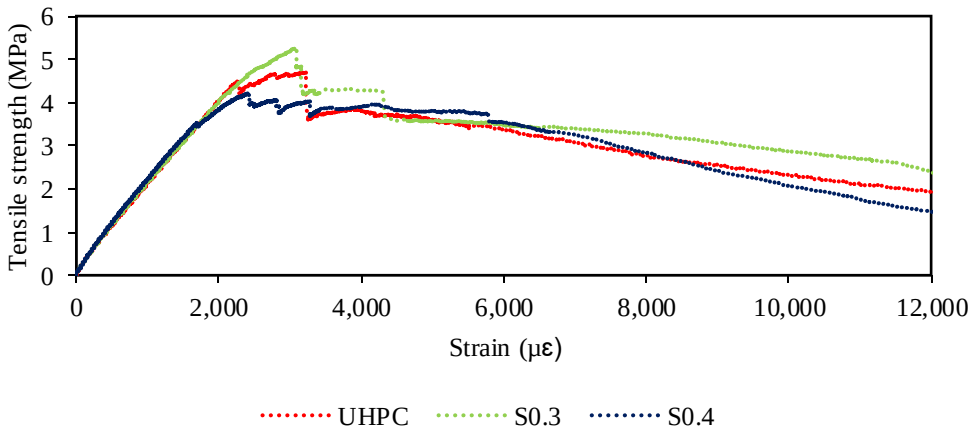
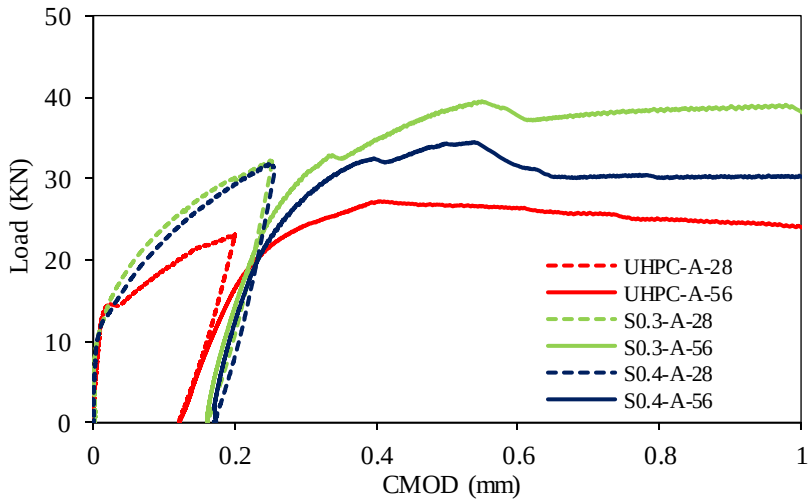


Figure 9. Stress/strain curve for tensile strength for all mixes under ambient curing condition.

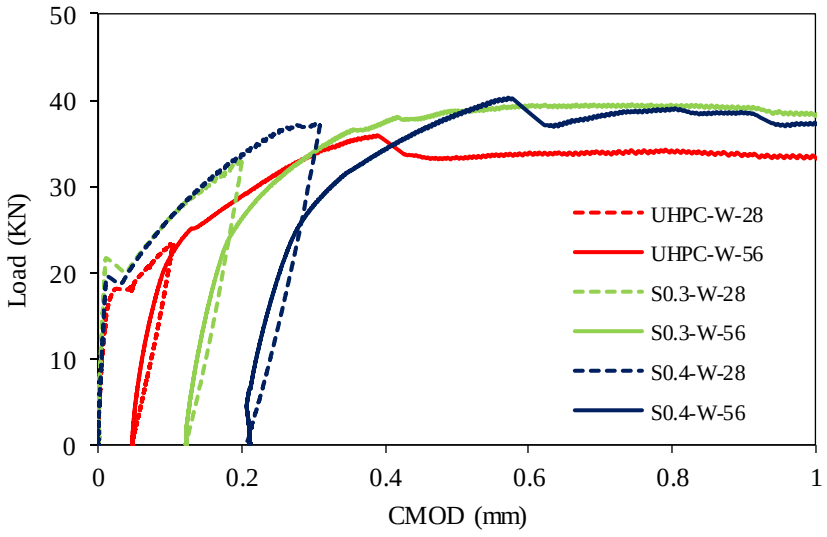
3.3 Mechanism of Self-Healing

The healing mechanism could be understood by applying the flexural load repetitively; for this, the load was initially applied to initiate the cracks and then the specimen was unloaded to subject it to a specific curing condition for a desired age. Figure 10 illustrates the load/CMOD relationship under the three points bending test under different curing regimes. The cracks were initiated by the application of the load. After unloading, the specimens were subjected to the same curing condition for 28 days and then the load was reapplied. During the test, the specimen under load was monitored carefully to prevent premature failure as in some specimens, the crack opening did not attain the desired value for the purpose of this healing study (0.2 mm measured via CMOD). The results of ambient-cured specimens showed that

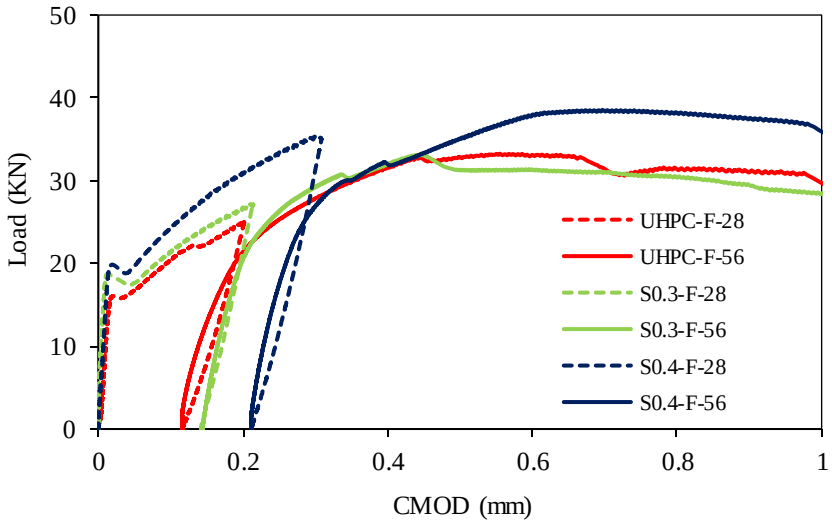
S0.3 and S0.4 had a higher capacity for load recovery after 28 days than the corresponding control specimens. For water-cured specimens, similar behaviour was also observed which confirmed the results found by Qian et al. [54]. Qian et al. found that the recovery of water-cured specimens reached about 105% of the original load. On the contrary, specimens under 100% RH curing showed comparable results between the UHPC control mix and S0.3. However, the S0.4 mix exhibited better performance in terms of load recovery. Hence, it can be concluded that the restoration of load under different curing regimes and healing capacity were maintained by adding SAP.



(**a**)



(**b**)



(c)

Figure 10. Load/CMOD relationship after applied loading until up to 0.2 mm, then reloading after 28 days from the first loading applied. (**a**) Ambient curing; (**b**) water curing; and (**c**) 100% RH curing.

Figure 11 presents the load recovery after the first loading and reloading after 28 days. It can be clearly stated that the UHPC mixed with SAP performed better in the reloading process. UHPC without SAP also increased the stress capacity after the first load. The reason behind this recovery of load for UHPC could be related to two different components: (i) the steel fibre could bridge the crack [51], and (ii) blast furnace slag can limit the crack and improve its durability [55].

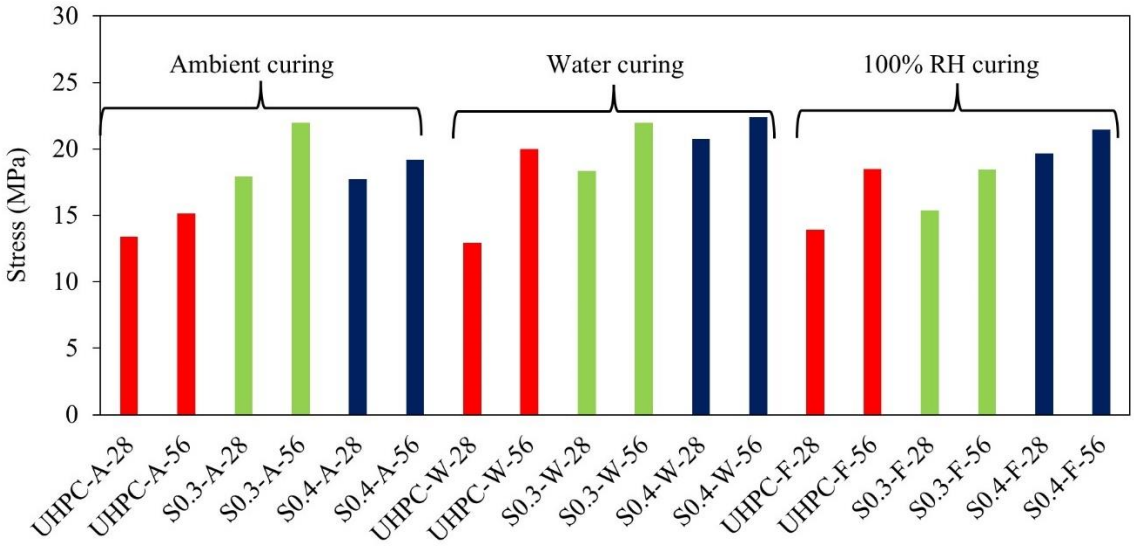


Figure 11. Load recovery for all mixes under different curing conditions.

Furthermore, calcite formation in the cracks was noticed immediately after applying the load for water-cured specimens of S0.3 as shown in Figure 12. This observation signifies the self-healing mechanism due to the presence of SAP particles. The internal curing provided by SAP enhanced the hydration products in the concrete matrix by realising the water that formed $Ca(OH)_2$ internally and reacted with carbon dioxide externally to form the calcium carbonate ($CaCO_3$), which is called calcite, to heal the crack efficiently [56].



Figure 12. Formation of calcite immediately after the cracking load of 28 days (S0.3 with water curing).

3.4 Durability Characteristics

Table 4 shows the results for water absorption and porosity by indicating the volume of permeable voids after 28 days for all mixes. It can be seen that the water absorption was higher in the mixes with SAP and increased with the increased SAP dosages as SAP increased the porosity of UHPC and it was observed by Zhutovsky and Kovler [57] that the very low w/b ratio also involved in this process could increase the porosity.

The absorption rate and sorptivity results are illustrated in Figure 13 which reveals the mechanism of water migration through concrete and the absorption rate of the UHPC control mix had a lower rate among the mixes. This finding correlates well with the results of compressive strength, where UHPC had the highest values regardless of the curing condition. It could be attributed to the capillary mechanism of UHPC, which prevents water movement

within the concrete. For both S0.3 and S0.4, the absorption rate was almost similar whilst the results of sorptivity indicated that the initial absorption was higher with the increase in SAP dosages. On the other hand, the sorptivity attained similar values for all mixes with time. Therefore, it is evident that the outer layers of the specimens for mixes with SAP effectively absorbed the water and then restrained the movement of water within SAP particles or concrete.

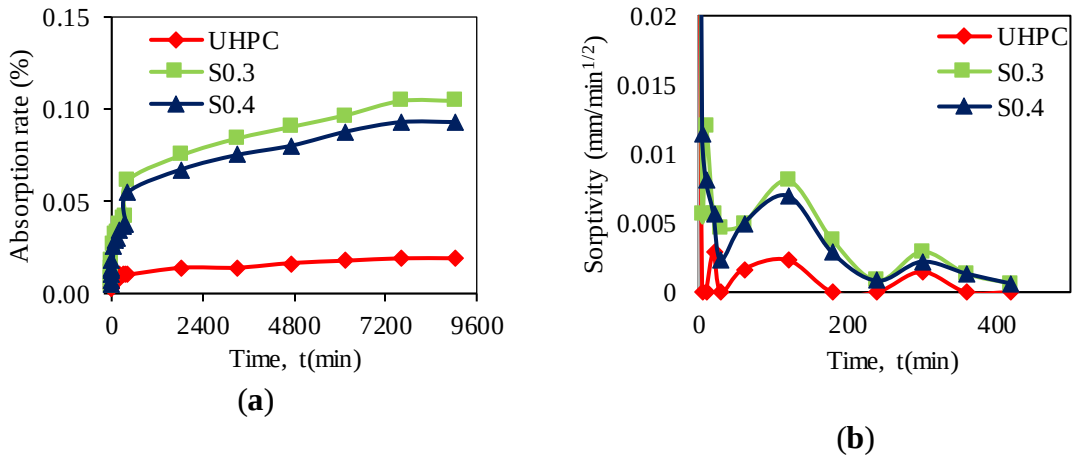


Figure 13. Sorptivity results of all mixes after water curing of 28 days: (**a**) the water absorption; and (**b**) sorptivity.

3.5 Microstructure Investigation

For all mixes, BSE images recorded at 56 days are shown in Figure 14. Additionally, EDX for specific points was plotted. The voids indicated by smooth dark spots are clearly visible for the mixes S0.3 and S0.4 due to SAP particles. These voids will disintegrate the concrete matrix which will correspondingly affect the mechanical strength specifically the compressive strength as it can be observed in the compressive strength results. According to the EDX magnification, SAP had a high amount of element C and the product formed around SAP particles was calcium silicate hydrate (C-S-H) gel. Therefore, it is interesting to see the C-S-H as the main product of healing around the SAP particles which shrunk after the desorption of the water that can be extracted from the size of the SAP voids. Independent of the curing regime, the region around SAP particles consists of $CaCO_3$ and $Ca(OH)_2$ with a minimal gap which differs from the NSC as mentioned in [58]. Thus, SAP particles densify the microstructure by enhancing the hydration products [51,59]. Evidently, SAP creates voids and

weakens the matrix of the UHPC but gradually SAP desorbs water to hydrate the anhydrous cement particles around the voids to make C-S-H gel. Due to the high amount of cementitious materials in the UHPC, SAP yields C-S-H gel as a healing product which was proved to be the best product for the matrix that causes the concrete to gain more strength [60].

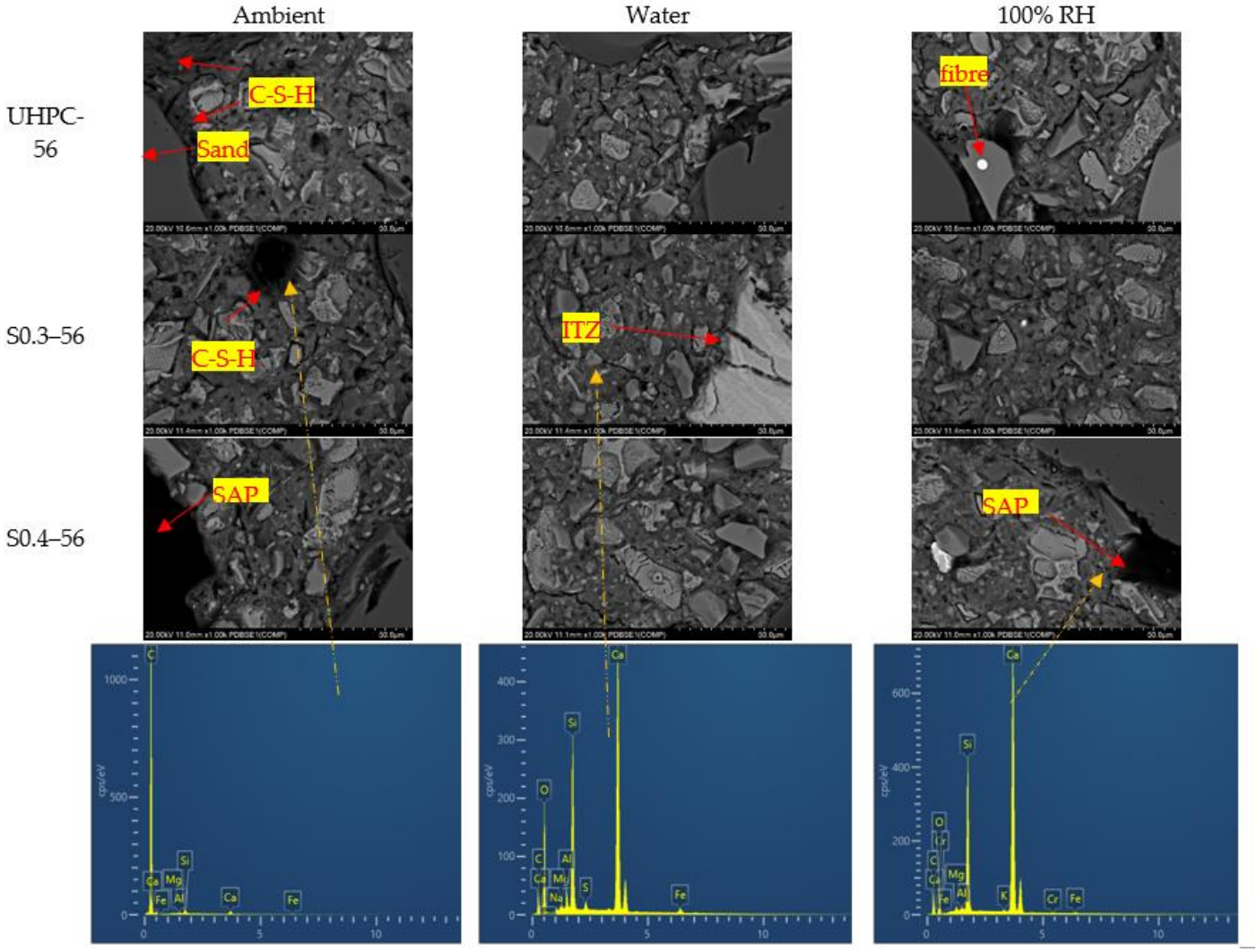


Figure 14. SEM images after 56 days with different curing regimes.

XRD results of the ambient curing of flexural strength test after 28 days and reloaded notched specimens after 56 days are shown in Table 5 and Figure 15. While the amount of SAP differed in each mix, the calculated chemical composition results were very close to each other. However, UHPC-28 days had the highest amount of C_3S composition followed by S0.3–28 and S0.4–28. Therefore, the amount of the hydrated product in mixes with SAP was greater than

that without SAP. Calcite forming $CaCO_3$ product for the healing purposes was also reduced in S0.4 by 20%, S0.3 1%, and UHPC 12%. Therefore, S0.4 after 56 days had produced more $CaCO_3$. Ettringite which is responsible for forming the expansion for the matrix, was seen in the quantitative data of mixes with SAP by Bentz and Jensen [61]. Interestingly, ettringite was also traced in the UHPC-56 days in this study. Furthermore, the lower w/b ratio also led to further hydration of the anhydrous particles.

Table 5. Quantitative XRD results of the matrix of mixes (wt.%).

	UHPC-28	**UHPC-56**	**S0.3–28**	**S0.3–56**	**S0.4–28**	**S0.4–56**
Portlandite	1.0	0.4	0.7	-	-	-
C_3S	18.9	13.5	16.4	12.9	16.4	13.3
Quartz	63.3	69.1	67.9	70.7	64.2	72.0
Calcite	10.5	9.2	9.8	9.7	11.0	8.8
C_4AF	3.5	2.9	3.1	2.6	3.4	2.4
C_2S	1.8	2.4	1.4	1.5	2.4	0.7
C_3A	1.0	0.8	0.8	0.9	1.0	0.7
Ettringite	-	1.8	-	1.8	1.5	1.4
Dolomite	-	-	-	-	-	0.6
SUM (%)	100	100	100	100	100	100

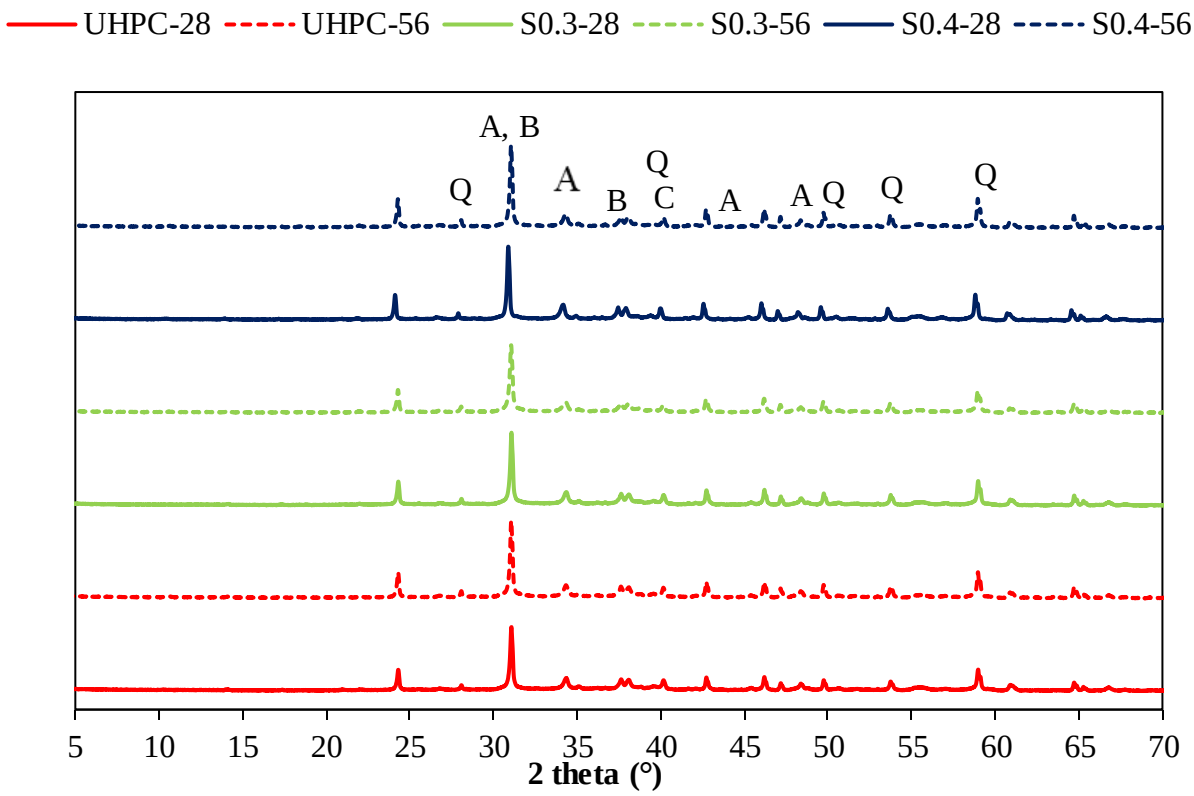


Figure 15. XRD spectra of the mixes after 28 and 56 days [A = alite, B = belite, C = calcite, and Q = quartz].

3.6 Behaviour of the Prisms Under Constant Tensile Load

In Figure 16, the change in the displacement (the opening of the crack at the notched area and average of two LVDTs values) over time is illustrated. For S0.4, the crack in the specimen occurred on day 1 where the stability of the plateau implied there was no dynamic variation in the crack closure. For the UHPC control mix, the crack was triggered on day 9; this is due to the fact that the load was applied slowly to ensure there would not be a premature failure. For all the specimens, the displacement almost remained constant during the whole period except for the UHPC specimen, which raised slightly after day 9. The increase is due to the nature of the load, which was applied periodically to initiate the cracks.

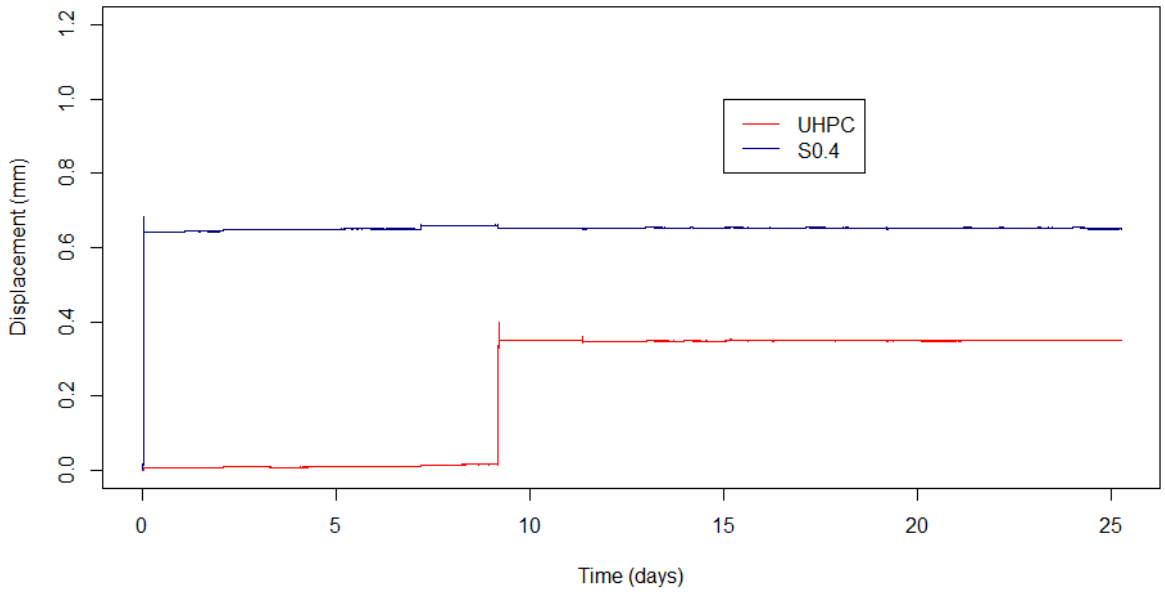


Figure 16. Displacement vs. time for wet and dry cycles.

Figure 17 shows the stress throughout the entire test period. The load was applied recurringly to achieve the cracking load. For S0.4, the stress reached around 8 MPa on day 1 and then it was lowered to 2 MPa, which corresponded to 50% of the load that caused the crack based on the results extracted from the tensile strength experiment in Section 3.2.2. The stress was increased cyclically on days 1, 3, 5, 7, and 9. At day 9, the stress remained at 2 MPa for up to 15 days. It is evident that the stress increased autogenously throughout this interval as the healing capability of S0.4 was demonstrated by the surge in stress rather than a reduction in displacement. For the UHPC control specimen, the load was increased on the same days as S0.4 and the crack was initiated on day 9; the load was adjusted on day 12 to reach 50% of the cracking load. For the next 12 days, the load continued constantly, and it was increased at the end of this period, which caused the failure of the specimen, implying no increase in the capacity of the specimen. Therefore, S0.4 was more effective at healing the cracks and recovering the stiffness at the same displacement reading for both wet and dry cycles.

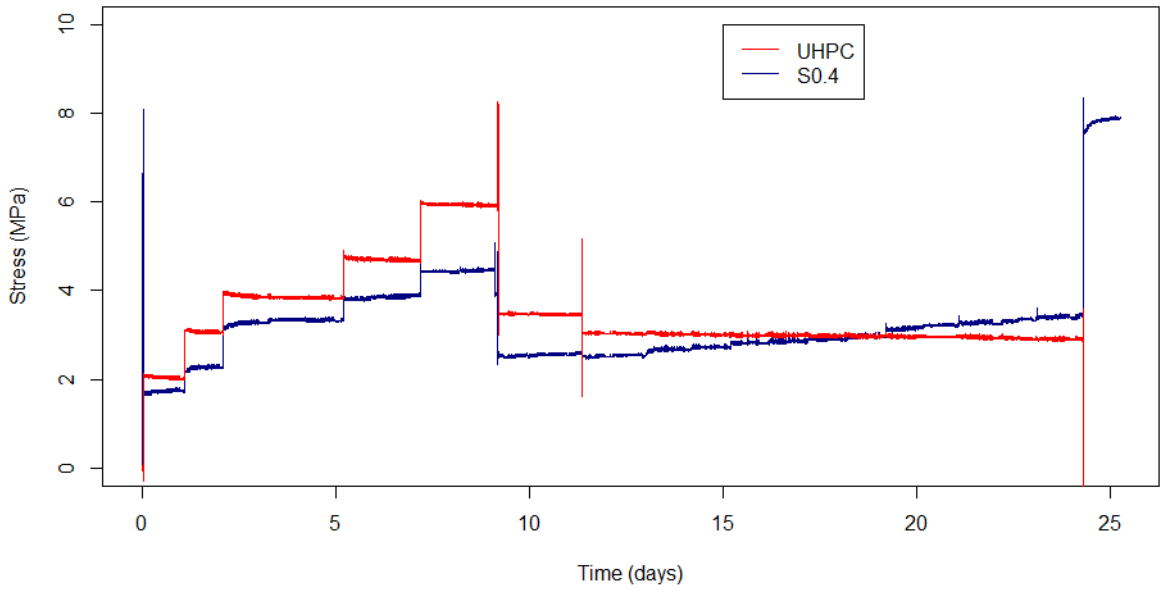


Figure 17. Stress vs. time for wet and dry cycles.

4 Conclusions

This study investigated the effect of incorporating SAP into UHPC mixes on the self-healing performance of different mixes by conducting microstructure, mechanical properties, and durability experiments and also investigating self-healing ability under repeated flexural loads and sustained tensile loads. Two different mixes of UHPC incorporating varying ratios of SAP as well as a control mix without SAP were utilised for this study with three different curing regimes for each mix. The major findings from this study are as follows:

Adding SAP to UHPC required additional water or superplasticiser to maintain the consistency of the mix where the required amount of water depended on the size and absorption capacity of SAP particles.

UHPC mixed with SAP exhibited less compressive strength than the corresponding control mix without SAP, and the compressive strength exceeded above 120 MPa after 90 days for UHPC mixes with SAP. SAP leaves voids in the matrix after releasing the water, which could significantly impact the microstructure of the matrix. However, the release of the water later enhanced the hydration of the UHPC mix and led to the improvement in the strength.

Adding SAP particles improved the modulus of elasticity by closing the microcracks, which led to the improvement in the stiffness.

Regarding flexural and tensile strength results, S0.3 exhibited better results than the mix without SAP in water-cured specimens. There was a decrease in self-desiccation of the internal curing and a reduction in the occurrence of microcracks.

The microstructure of the matrix of UHPC showed the formation of C-S-H gel around SAP voids. Hence, the formation of C-S-H should increase the strength.

Notched specimens of UHPC mixed with SAP had an overall better performance in terms of load recovery and immediate closing of the cracks via the formation of calcite.

Prisms under sustained tensile load for UHPC and S0.4 under wet and dry cycle conditions also confirmed the previous results of self-healing ability after adding SAP. The stress increased for S0.4 with time, indicating that the healing happened with constant displacement readings.

UHPC had better compressive strength due to the dense microstructure in its early stages, and the addition of SAP reduced the compressive strength. However, the addition of SAP showed superior results in tensile and flexural strength tests and also the restoration of the stiffness of the healed concrete. Additionally, mixes with SAP had enhanced the healing process, which could be the cornerstone of more durable and sustainable concrete.

Finally, blending SAP into UHPC seems to have the potential of reduce the maintenance required, reduce the cost-related expenses, and increase the life-span of the buildings. However, Incorporating SAP into UHPC mixes investigation can be further investigated under an aggressive environment such as sulphate attacks. Moreover, the technique of testing the self-healing capability under sustained loadings can be expanded to extend the duration of the sustained loadings.

Acknowledgments:

The authors would like to thank Phillip Visintin for using the test frame of sustained tensile loading experiment as well as Kevin Farries who designed the frame. The research was partially funded by the Australian Research Council grant number [DP 21001425].

References

1. Graybeal, B.A.; Russel, H.G. *Ultra-High Performance Concrete: A State-of-the-Art Report for the Bridge Community*; United States. Federal Highway Administration. Office of Infrastructure Research and Development: McLean, VA, USA, 2013.
2. Xue, J.; Briseghella, B.; Huang, F.; Nuti, C.; Tabatabai, H.; Chen, B. Review of ultra-high performance concrete and its application in bridge engineering. *Constr. Build. Mater.* **2020**, *260*, 119844. https://doi.org/10.1016/j.conbuildmat.2020.119844.
3. Schmitz, G.M. Design and Experimental Validation of 328 ft (100 m) Tall Wind Turbine Towers Utilizing High Strength and Ultra-High Performance Concrete. Ph.D. Thesis, Iowa State University, Ames, IA, USA, 2013; p. 210.
4. Hajar, Z.; Resplendino, J.; Lecointre, D.; Petitjean, J.; Simon, A. Ultra-high-performance concretes: First recommendations and examples of application. In Proceedings of the Fib Symposium 2004—Concrete Structures: The Challenge of Creativity, Avignon, France, 26–28 May 2004; pp. 242–243.
5. Bonneau, O.; Vernet, C.; Moranville, M.; Aïtcin, P.C. Characterization of the granular packing and percolation threshold of reactive powder concrete. *Cem. Concr. Res.* **2000**, *30*, 1861–1867. https://doi.org/10.1016/S0008-8846(00)00300-8.
6. Ji, T.; Chen, C.Y.; Zhuang, Y.Z. Evaluation method for cracking resistant behavior of reactive powder concrete. *Constr. Build. Mater.* **2012**, *28*, 45–49. https://doi.org/10.1016/j.conbuildmat.2011.08.060.
7. Wang, K.; Jansen, D.C.; Shah, S.P.; Karr, A.F. Permeability study of cracked concrete. *Cem. Concr. Res.* **1997**, *27*, 381–393. https://doi.org/10.1016/S0008-8846(97)00031-8.
8. American Concrete Institute. Control of Cracking in Concrete Structures. In *Concrete International*; American Concrete Institute: Farmington Hills, MI, USA, 1980; pp. 35–76. https://doi.org/10.14359/11280.
9. Raza, A.; El Ouni, M.H.; Azab, M.; Khan, D.; Elhadi, K.M.; Alashker, Y. Sustainability assessment, structural performance and challenges of self-healing bio-mineralized concrete: A systematic review for built environment applications. *J. Build. Eng.* **2023**, *66*, 105839. https://doi.org/10.1016/j.jobe.2023.105839.
10. Van Tittelboom, K.; De Belie, N. Self-Healing in Cementitious Materials—A Review. *Materials* **2013**, *6*, 2182–2217. https://doi.org/10.3390/ma6062182.
11. Guo, X.; Liu, X.; Yuan, S. Effects of initial damage on self-healing of fly ash-based engineered geopolymer composites (FA-EGC). *J. Build. Eng.* **2023**, *74*, 106901. https://doi.org/10.1016/j.jobe.2023.106901.
12. Wang, R.; Ding, Z.; Zhang, Y.; Xu, Y. Self-healing of high-performance engineered cementitious materials with crystalline admixture in the seawater environment. *J. Build. Eng.* **2023**, *63*, 105472. https://doi.org/10.1016/j.jobe.2022.105472.
13. Ma, X.; Liu, J.; Shi, C. A review on the use of LWA as an internal curing agent of high performance cement-based materials. *Constr. Build. Mater.* **2019**, *218*, 385–393. https://doi.org/10.1016/j.conbuildmat.2019.05.126.
14. Zhang, Y.; Sun, X. Influence of multi-walled carbon nanotubes on the multi-scale performance of internally cured concrete containing pre-wetted lightweight aggregate. *J. Build. Eng.* **2022**, *58*, 104986. https://doi.org/10.1016/j.jobe.2022.104986.
15. Liu, J.; Farzadnia, N.; Khayat K, Shi, C.; . Effects of SAP characteristics on internal curing of UHPC matrix. *Constr. Build. Mater.* **2021**, *280*, 122530. https://doi.org/10.1016/j.conbuildmat.2021.122530.

16. Wang, F.; Zhou, Y.; Peng, B.; Liu, Z.; Hu, S. Autogenous Shrinkage of Concrete with Super-Absorbent Polymer. *ACI Mater. J.* **2009**, *106*, 123. https://doi.org/10.14359/56458.
17. Liu, K.; Long, Y.; Chen, L.; Ling, X.; Yu, R.; Shui, Z.; Fei, S.; Yu, W.; Li, C.; Ge, K. Mechanisms of autogenous shrinkage for Ultra-High Performance Concrete (UHPC) prepared with pre-wet porous fine aggregate (PFA). *J. Build. Eng.* **2022**, *54*, 104622. https://doi.org/10.1016/j.jobe.2022.104622.
18. Lee, H.X.D.; Wong, H.S.; Buenfeld, N.R. Self-sealing of cracks in concrete using superabsorbent polymers. *Cem. Concr. Res.* **2016**, *79*, 194–208. https://doi.org/10.1016/j.cemconres.2015.09.008.
19. Craeye, B.; Geirnaert, M.; De Schutter, G. Super absorbing polymers as an internal curing agent for mitigation of early-age cracking of high-performance concrete bridge decks. *Constr. Build. Mater.* **2011**, *25*, 1–13. https://doi.org/10.1016/j.conbuildmat.2010.06.063.
20. Mignon, A.; Vagenende, M.; Martins, J.; Dubruel, P.; Van Vlierberghe, S.; De Belie, N. Development of amine-based pH-responsive superabsorbent polymers for mortar applications. *Constr. Build. Mater.* **2017**, *132*, 556–564. https://doi.org/10.1016/j.conbuildmat.2016.12.031.
21. Olawuyi, B.J. The Mechanical Behaviour of High-Performance Concrete with Superabsorbent Polymers (SAP). 2016. Available online: https://doi.org/http://hdl.handle.net/10019.1/98352 (accessed on 15 April 2023).
22. Pourjavadi, A.; Fakoorpoor, S.M.; Khaloo, A.; Hosseini, P. Improving the performance of cement-based composites containing superabsorbent polymers by utilization of nano-SiO_2 particles. *Mater. Des.* **2012**, *42*, 94–101. https://doi.org/10.1016/J.MATDES.2012.05.030.
23. Savva, P.; Petrou, M.F. Highly absorptive normal weight aggregates for internal curing of concrete. *Constr. Build. Mater.* **2018**, *179*, 80–88. https://doi.org/10.1016/J.CONBUILDMAT.2018.05.205.
24. Kang, S.-H.; Hong, S.-G.; Moon, J. Shrinkage characteristics of heat-treated ultra-high performance concrete and its mitigation using superabsorbent polymer based internal curing method. *Cem. Concr. Compos.* **2018**, *89*, 130–138. https://doi.org/10.1016/j.cemconcomp.2018.03.003.
25. Yang, Z., Miao, C., Deng, W., Liu, D., Zhang, J., & Gu, J. . Multi-scale characterization of SAP impact on self-healing behavior in UHPC under varied crack widths and environments. *Constr. and Build. Mater.* **2024**, 421, 135649. https://doi.org/10.1016/j.conbuildmat.2024.135649
26. Ma, X.; Yuan, Q.; Liu, J.; Shi, C. Effect of water absorption of SAP on the rheological properties of cement-based materials with ultra-low w/b ratio. *Constr. Build. Mater.* **2019**, *195*, 66–74. https://doi.org/10.1016/j.conbuildmat.2018.11.050.
27. Samaha, H.R.; Hover, K.C. Influence of microcracking on the mass transport properties of concrete. *ACI Mater. J.* **1992**, *89*, 416–424. https://doi.org/10.14359/2585.
28. Hearn, N. Effect of Shrinkage and Load-Induced Cracking on Water Permeability of Concrete. *ACI Mater. J.* **1999**, *96*, 234–241. https://doi.org/10.14359/450.
29. Grzybowski, M.; Shah, S.P. Shrinkage Cracking of Fiber Reinforced Concrete. *ACI Mater. J.* **1990**, *87*, 138–148. https://doi.org/10.14359/1951.
30. Liu, S.; Bundur, Z.B.; Zhu, J.; Ferron, R.D. Evaluation of self-healing of internal cracks in biomimetic mortar using coda wave interferometry. *Cem. Concr. Res.* **2016**, *83*, 70–78. https://doi.org/10.1016/j.cemconres.2016.01.006.
31. Kan, L.L.; Shi, H.S.; Sakulich, A.R.; Li, V.C. Self-Healing Characterization of Engineered Cementitious Composite Materials. *ACI Mater. J.* **2010**, *107*, 619–626. https://doi.org/10.14359/51664049.
32. Zhang, Z.; Qian, S.; Ma, H. Investigating mechanical properties and self-healing behavior of micro-cracked ECC with different volume of fly ash. *Constr. Build. Mater.* **2014**, *52*, 17–23. https://doi.org/10.1016/j.conbuildmat.2013.11.001.

33. Kanellopoulos, A.; Giannaros, P.; Al-Tabbaa, A. The effect of varying volume fraction of microcapsules on fresh, mechanical and self-healing properties of mortars. *Constr. Build. Mater.* **2016**, *122*, 577–593. https://doi.org/10.1016/j.conbuildmat.2016.06.119.
34. Ma, W.; Xu, Z.; Qin, Y.; Cao, C.; Wang, Y.; Zhou, H. Experimental investigation of nonlinear flow characteristics in cracked polypropylene fibre-reinforced concrete. *Mater. Struct.* **2021**, *54*, 215. https://doi.org/10.1617/s11527-021-01799-3.
35. Nishiwaki, T.; Koda, M.; Yamada, M.; Mihashi, H.; Kikuta, T. Experimental study on self-healing capability of FRCC using different types of synthetic fibers. *J. Adv. Concr. Technol.* **2012**, *10*, 195–206. https://doi.org/10.3151/jact.10.195.
36. Monte, F.L.; Ferrara, L. Tensile behaviour identification in Ultra-High Performance Fibre Reinforced Cementitious Composites: Indirect tension tests and back analysis of flexural test results. *Mater. Struct.* **2020**, *53*, 145. https://doi.org/10.1617/s11527-020-01576-8.
37. Ma, H.; Qian, S.; Zhang, Z. Effect of self-healing on water permeability and mechanical property of Medium-Early-Strength Engineered Cementitious Composites. *Constr. Build. Mater.* **2014**, *68*, 92–101. https://doi.org/10.1016/j.conbuildmat.2014.05.065.
38. Roig-Flores, M.; Pirritano, F.; Serna, P.; Ferrara, L. Effect of crystalline admixtures on the self-healing capability of early-age concrete studied by means of permeability and crack closing tests. *Constr. Build. Mater.* **2016**, *114*, 447–457. https://doi.org/10.1016/j.conbuildmat.2016.03.196.
39. Cuenca, E.; Tejedor, A.; Ferrara, L. A methodology to assess crack-sealing effectiveness of crystalline admixtures under repeated cracking-healing cycles. *Constr. Build. Mater.* **2018**, *179*, 619–632. https://doi.org/10.1016/j.conbuildmat.2018.05.261.
40. Sahmaran, M.; Yildirim, G.; Noori, R.; ÖZBAY, E.; Lachemi, M. Repeatability and pervasiveness of self-healing in engineered cementitious composites. *ACI Mater. J.* **2015**, *112*, 513–522. https://doi.org/10.14359/51687308.
41. Snoeck, D.; De Belie, N. Repeated Autogenous Healing in Strain-Hardening Cementitious Composites by Using Superabsorbent Polymers. *J. Mater. Civil. Eng.* **2016**, *28*, 4015086. https://doi.org/10.1061/(ASCE)MT.1943-5533.0001360.
42. *ASTM C1437-20*; Standard Test Method for Flow of Hydraulic Cement Mortar. ASTM International: West Conshohocken, PA, USA, 2020. https://doi.org/10.1520/C1437-20.
43. Singh, M.; Sheikh, A.H.; Ali, M.S.M.; Visintin, P.; Griffith, M.C. Experimental and numerical study of the flexural behaviour of ultra-high performance fibre reinforced concrete beams. *Constr. Build Mater.* **2017**, *138*, 12–25. https://doi.org/10.1016/j.conbuildmat.2017.02.002.
44. *ASTM C39/C39M-20*; Standard Test Method for Compressive Strength of Cylindrical Concrete Specimens. ASTM International: West Conshohocken, PA, USA, 2020. https://doi.org/10.1520/C0039_C0039M-23.
45. *ASTM C642-21*; Standard Test Method for Density, Absorption, and Voids in Hardened Concrete. ASTM International: West Conshohocken, PA, USA, 2021. https://doi.org/10.1520/C0642-21.
46. *ASTM C1585-20*; Standard Test Method for Measurement of Rate of Absorption of Water by Hydraulic-Cement Concretes. ASTM International: West Conshohocken, PA, USA, 2020. https://doi.org/10.1520/C1585-20.
47. Feng, Z.; Li, C.; Yoo, D.-Y.; Pan, R.; He, J.; Ke, L. Flexural and cracking behaviors of reinforced UHPC beams with various reinforcement ratios and fiber contents. *Eng. Struct.* **2021**, *248*, 113266. https://doi.org/10.1016/j.engstruct.2021.113266.
48. Mechtcherine, V.; Secrieru, E.; Schröfl, C. Effect of superabsorbent polymers (SAPs) on rheological properties of fresh cement-based mortars—Development of yield stress and plastic viscosity over time. *Cem. Concr. Res.* **2015**, *67*, 52–65. https://doi.org/10.1016/j.cemconres.2014.07.003.

49. Liu, J.; Farzadnia, N.; Shi, C.; Ma, X. Shrinkage and strength development of UHSC incorporating a hybrid system of SAP and SRA. *Cem. Concr. Compos.* **2019**, *97*, 175–189. https://doi.org/10.1016/j.cemconcomp.2018.12.029.
50. Snoeck, D.; Schaubroeck, D.; Dubruel, P.; De Belie, N. Effect of high amounts of superabsorbent polymers and additional water on the workability, microstructure and strength of mortars with a water-to-cement ratio of 0.50. *Constr. Build Mater.* **2014**, *72*, 148–157. https://doi.org/10.1016/j.conbuildmat.2014.09.012.
51. Snoeck, D.; Van Tittelboom, K.; Steuperaert, S.; Dubruel, P.; De Belie, N. Self-healing cementitious materials by the combination of microfibres and superabsorbent polymers. *J. Intell. Mater. Syst. Struct.* **2014**, *25*, 13–24. https://doi.org/10.1177/1045389X12438623.
52. Kovler, K. Effect of superabsorbent polymers on the mechanical properties of concrete. In *Application of Super Absorbent Polymers (SAP) in Concrete Construction: State-of-the-Art Report Prepared by Technical Committee 225-SAP*; Springer: Dordrecht, The Netherlands, 2012; pp. 99–114. https://doi.org/10.1007/978-94-007-2733-5_8.
53. Liu, J.; Farzadnia, N.; Khayat, K.H.; Shi, C. Effects of SAP characteristics on internal curing of UHPC matrix. *Constr. Build. Mater.* **2021**, *280*, 122530.
54. Qian, S.Z.; Zhou, J.; Schlangen, E. Influence of curing condition and precracking time on the self-healing behavior of Engineered Cementitious Composites. *Cem. Concr. Compos.* **2010**, *32*, 686–693.
55. Darquennes, A.; Olivier, K.; Benboudjema, F.; Gagné, R. Self-healing at early-age, a way to improve the chloride resistance of blast-furnace slag cementitious materials. *Constr. Build. Mater.* **2016**, *113*, 1017–1028. https://doi.org/10.1016/j.conbuildmat.2016.03.087.
56. Jensen, O.M.; Hansen, P.F. Water-entrained cement-based materials—I. Principles and theoretical background. *Cem. Concr. Res.* **2001**, *31*, 647–654. https://doi.org/10.1016/S0008-8846(01)00463-X.
57. Zhutovsky, S.; Kovler, K. Durability aspects of internally cured high performance concrete. In Proceedings of the International RILEM Conference on Use of Superabsorbent Polymers and Other New Additives in Concrete, Lyngby, Denmark, 15–18 August 2010; pp. 15–18.
58. Sun, B.; Wu, H.; Song, W.; Li, Z.; Yu, J. Hydration, microstructure and autogenous shrinkage behaviors of cement mortars by addition of superabsorbent polymers. *Front. Struct. Civ. Eng.* **2020**, *14*, 1274–1284. https://doi.org/10.1007/s11709-020-0656-x.
59. Snoeck, D.; Dewanckele, J.; Cnudde, V.; De Belie, N. X-ray computed microtomography to study autogenous healing of cementitious materials promoted by superabsorbent polymers. *Cem. Concr. Compos.* **2016**, *65*, 83–93. https://doi.org/10.1016/j.cemconcomp.2015.10.016.
60. Sun, J.; Shi, H.; Qian, B.; Xu, Z.; Li, W.; Shen, X. Effects of synthetic C-S-H/PCE nanocomposites on early cement hydration. *Constr. Build. Mater.* **2017**, *140*, 282–292. https://doi.org/10.1016/j.conbuildmat.2017.02.075.
61. Bentz, D.P.; Jensen, O.M. Mitigation strategies for autogenous shrinkage cracking. *Cem. Concr. Compos.* **2004**, *26*, 677–685. https://doi.org/10.1016/S0958-9465(03)00045-3.

CHAPTER 2

Background

This chapter concentrates on the development of UHPGC based on the compressive strength results. The Taguchi method was used to form an L9 orthogonal array, which involves nine experiments conducted by changing four parameters, with each parameter having three levels. Two trials were conducted based on the provided mix design procedure and the Taguchi method.

List of Manuscripts

Alameri, M., Joseph, J., Mohamed Ali, M. S., Elchalakani, M., & Sheikh, A. H. (2024). Optimising GGBS-based ultra high-performance geopolymer mortar: an orthogonal array approach. *Australian Journal of Structural Engineering*, 1-16.

Statement of Authorship

Title of Paper	Optimising GGBS-based ultra high-performance geopolymer mortar: an orthogonal array approach
Publication Status	☑ Published ☐ Accepted for Publication ☐ Submitted for Publication ☐ Unpublished and Unsubmitted work written in manuscript style
Publication Details	Alameri, M., Joseph, J., Mohamed Ali, M. S., Elchalakani, M., & Sheikh, A. H. (2024). Optimising GGBS-based ultra high-performance geopolymer mortar: an orthogonal array approach. Australian Journal of Structural Engineering, 1-16.

Principal Author

Name of Principal Author (Candidate)	Mohammad Alameri		
Contribution to the Paper	Conceptualisation, methodology, and manuscript writing and revision		
Overall percentage (%)	60%		
Certification:	This paper reports on original research I conducted during the period of my Higher Degree by Research candidature and is not subject to any obligations or contractual agreements with a third party that would constrain its inclusion in this thesis. I am the primary author of this paper.		
Signature		Date	24-10-2024

Co-Author Contributions

Name of Co-Author	Jovan Joseph		
Contribution to the Paper	Methodology, data curation, and manuscript writing (20%)		
Signature		Date	25/10/2024

Name of Co-Author	M.S. Mohamed Ali		
Contribution to the Paper	Supervision, conceptualisation, methodology, and manuscript revision (10%)		
Signature		Date	24-10-2024

Name of Co-Author	Mohamed Elchalakani
Contribution to the Paper	Supervision, conceptualisation, methodology, and manuscript revision (5%)

Signature		Date	28-10-2024

Name of Co-Author	Abdul Sheikh		
Contribution to the Paper	Supervision, conceptualisation, methodology, and manuscript revision (5%)		
Signature		Date	29-10-2024

Optimizing GGBS-Based Ultra High-Performance Geopolymer Mortar: An Orthogonal Array Approach

Mohammad Alameri[1,*], Jovan Joseph[1], M.S. Mohamed Ali[1], Mohamed Elchalakani[2], Abdul Sheikh[1]

[1] *School of Architectural and Civil Engineering, The University of Adelaide, Adelaide, Australia*

[2] *Department of Civil, Environmental and Mining Engineering, The University of Western Australia, Perth, Australia*

[*] *Correspondence: Mohammad.alameri@adelaide.edu.au*

Abstract

This study emphasizes the optimization of compressive strength in ultra high-performance geopolymer mortar by employing the Taguchi method's orthogonal array design. Recognizing the critical need for enhanced compressive strength in construction materials, the research focuses on identifying and adjusting key mix design parameters through a systematic experimental approach. Utilizing an L9 orthogonal array, the investigation was structured into two phases, each examining a distinct set of variables across three levels to ascertain their impact on compressive strength. The first phase analysed the water-to-binder ratio (W/B), silica fume-to-binder ratio (SF/B), potassium silicate-to-potassium hydroxide ratio (PS/PH), and aggregate-to-binder ratio. The second phase shifted focus to explore the effects of W/B ratio, fibre content, silicon carbide to binder ratio (SiC/B), and superplasticiser to binder ratio (SP/B). The adoption of the Taguchi method facilitated a meticulous evaluation of 18 unique mix designs, leading to the identification of an optimal mix that significantly elevated the 28-day compressive strength to 126 MPa. This optimal mix was characterized by a W/B ratio of 0.28, a fibre volume of 3%, a SiC/B of 0, and a SP/B ratio of 2%. Additionally, the study underscored a robust correlation between the empirical findings of the second phase and the predictions of a developed mathematical model, substantiating the effectiveness of the Taguchi orthogonal array in enhancing the compressive strength of UHPGC. This research not only provides a viable pathway for mix design optimization but also contributes to the broader goal of advancing construction material technology through methodical parameter analysis.

Keywords: Mix design, Compressive strength, Taguchi method, Optimization, Parameter analysis, L9 orthogonal array, W/B ratio, Fibre content, UHPGC.

1 Introduction

Since the mid-20th century, cement production has seen a dramatic increase, reaching an unprecedented peak of up to 5000MT/year by 2018 [1]. This growth has not come without environmental consequences; it contributes to approximately 8% of the global CO_2 emissions, a figure that is alarmingly significant [2]. This escalation in cement production not only emphasizes the immense scale of modern construction activities but also brings to light the urgent need for more sustainable practices in the construction industry. The environmental footprint of cement production is a major concern, prompting a critical re-evaluation of traditional building materials and methods.

In response to these environmental challenges and demands, the construction sector has seen the initiation of ultra high-performance concretes (UHPC). UHPC is renowned for its compressive strengths exceeding 120 MPa and enhanced ductility, attributed to a dense microstructure [3]. These properties enable the creation of more slender structural elements, reducing maintenance requirements [4]. However, the production of UHPC involves a substantial use of cement and fine aggregates, about two to three times more than traditional concrete. This factor, while contributing to UHPC's superior performance, adversely impacts environmental sustainability and increases the carbon footprint of construction materials.

In the wake of heightened environmental sustainability concerns, there has been a rising interest within structural engineering research and development towards the creation of ultra high-performance geopolymer concrete (UHPGC). This interest is driven by the potential to replace cement with supplementary cementitious materials (SCMs), using industrial waste by-products like slag, metakaolin, and fly ash. These materials, abundant in alumina-silicate compounds, can be effectively activated using alkaline solutions. The integration of UHPGC in construction,

especially in the design of slender structural elements, offers significant environmental advantages. By embracing UHPGC, the construction industry can make substantial strides towards achieving more environmentally sustainable practices, a necessity in the current ecological climate [5].

Geopolymer concretes are known by various names, including “geo-polymer,” “alkali-activated materials,” and “alkali-bonded materials,” all denoting a range of concrete types rich in alumina-silica compounds. These compounds are activated using an alkali/silicate solution, as detailed by Singh et al. [6]. The manufacturing process of geopolymer concrete (GPC) involves replacing cement with industrial by-products. This substitution leads to the formation of continuous sialate monomers (-Si-O-Al-O-) upon activation, a key factor in GPC's environmentally sustainable attributes. In comparison to ordinary portland cement concrete (OPCC), GPC demonstrates superior performance characteristics, including enhanced chemical resistance, reduced corrosion of steel reinforcements, and improved fire resistance [7–9]. These advantages, along with its sustainability benefits, have significantly bolstered the case for GPC, culminating in the construction of the first major GPC structure in Australia in 2013 [10].

Building on the advancements in geopolymer concretes, the production UHPGC necessitates a deep understanding of the formation of a densely packed concrete matrix. This formation is primarily driven by the chemical activation of active alumina-silica constituents and the incorporation of inactive constituents like fine aggregates. The development of UHPGC heavily relies on the type and proportion of SCMs employed, which include ground granulated blast furnace slag (GGBS), fly ash (FA), silica fume (SF), and metakaolin (Mk) [11–15]. Additionally, the alkaline activators used, predominantly sodium or potassium-based, and their varying molarities, along with the incorporation of different percentages of steel fibres, play a critical role in determining the performance of the resulting concrete [16]. The effect of varying molarities of sodium-based alkaline activators, especially when coupled with high-temperature

curing (over 40°C) for periods of 24, 48, and 72 hours, is also crucial in understanding the polymeric matrix formation in UHPGC [17]. Furthermore, factors like the amorphous nature of the constituents, particle shape, size distribution, and Hydration Modulus (HM), Eq. (1), are instrumental in the effective polymerization of the alumina silicates when activated in an alkaline solution. These factors also correlate significantly with the strength development of UHPGC [18,19].

$$HM = \frac{CaO + MgO + Al_2O_3}{SiO_2} \quad (1)$$

The high HM value of GGBS was 1.87 compared to FA which was 0.84 indicate the use of GGBS as a main Alumina-silicate constituent in the polymerisation process of the concrete mix to maximise the early strength [20]. Moreover, Na_2O content in the alkali activators solution (AAS) is a significant term often used to categorise design mixes, even as it is the cations (Na^+/K^+) that ideally partake in the polymerisation of the alumina-silicates. Therefore, Gao et al. [21] have employed 5.6% Na_2O content to the total binder mass and an activator modulus (Ms, SiO_2/Na_2O molar mass) of 1.4 to produce optimal performance results. However, adding limestone to GGBFS and FA-based geopolymers creates new nucleation sites that vary the percentage of polymeric molecules in the matrix along with the amounts of chemically and physically bound water [21–23]. Hence, these studies provide important information on the stoichiometry of the polymer molecules such as – Sodium Aluminate Silicate Hydrate (N-A-S-H), Calcium Aluminate Silicate Hydrate (C-A-S-H), Calcium Silicate Hydrate (C-S-H), and their subsequent combinations, which can in turn help unravel the long-term behavioural aspects such as creep, shrinkage, and strength development.

To efficiently investigate a multitude of variables with a minimal number of experiments, researchers employ the Taguchi method. This method is a type of fractional factorial design that utilizes a special set of arrays, known as orthogonal arrays (OA) [24]. The Taguchi method's design of experiments, which employs OA, is notably more efficient compared to

traditional experimental design techniques. It significantly minimizes the influence of uncontrolled parameters and reduces the total number of required experiments. For example, while a classic factorial design approach would necessitate 81 trials for examining four parameters at three levels each, the Taguchi method accomplishes this with only nine trials. A key feature of this method is the utilization of the signal-to-noise (S/N) ratio. The S/N ratio is instrumental in optimizing variables, assisting in data analysis, and predicting optimal outcomes. It serves as the objective function for optimization [25]. The use of OA in the Taguchi method ensures a well-balanced set of experiments. The major advantages of employing the Taguchi method include its resilience, efficiency, cost-effectiveness, and the simplicity it brings to interpreting experimental outcomes.

The production of GPC is influenced by numerous variables within the constituent mix, each playing a pivotal role in determining the concrete's overall performance. Given this complexity, the Taguchi method emerges as a highly effective tool for developing an optimal design mix for high strength GPC. This methodology, already proven successful in the design of normal GPC mixes, offers a structured approach to handling the multifaceted interactions of various mix components. Table 1 provides a concise summary of the variables employed in each study that utilizes the Taguchi methods, offering a clear overview of how this approach has been applied in different contexts.

Table 1 Geopolymer's variables changed in Taguchi method in different studies

References	Binders' variables					Aggregate content	Activator variables						Superplasticizer	Curing variables				Fibre %
	GGBS wt%	Fly Ash wt%	OPC content wt%	W/B	Binder content		NaOH concentration (M/L)	The ratio of alkaline solution	AAS/Binder ratio	Alkali/Aluminium ratio	Type of Alkali	Silicon Content in the solution		Oven curing (C°)	Time of curing (hrs)	Water curing	Steam curing	
Nazari et al. (2012) [26]							×	×	×					×	×	×		
Olivia and Nikraz (2012) [27]						×		×	×								×	
Bagheri and Nazari (2014) [28]	×						×							×	×			
Panagiotopoulou et al. (2015) [29]										×	×	×						
Mehta et al. (2017) [30]			×				×							×				
Hadi et al. (2017) [31]					×		×	×	×									
Prusty and Pradhan (2020) [32]	×			×	×		×	×										
Dave et al. (2021)					×		×	×					×					
Karthik and Mohan (2021) [33]					×		×	×					×					
Raj et al. (2021) [34]				×			×	×	×					×	×			
Rawat et al. (2022) [35]	×	×	×	×														×

2 Research Significance:

This study aims to utilize the Taguchi method with an L9 OA for optimizing the mix proportion of UHPGC. The primary focus is on assessing the compressive strength as a key indicator of the effectiveness of the variables in the mix. This research will compare these outcomes with an existing strength factor model, ensuring a robust validation of the results derived from the Taguchi method. In this process, the selected variables for the UHPGC mix will undergo a detailed filtering process through a novel mix design approach developed specifically for this study.

3 Methodology

3.1 Mix design process:

A novel approach has been developed in this study to synthesise the mix process of geopolymer based on Taguchi method. Fig. 1 illustrates the development of the mix design process which starts with finding the most significant factors affecting the geopolymer mix design according to the previously published research. The types of materials and the total amount formed in this step is then used to find the total water to binder ratio (W/B). W/B depends on multiple factors (potassium silicate (K_2SiO_3) "which will be called throughout this paper as PS" ratio to potassium hydroxide (KOH) "which will be called throughout this paper as PH", PH molarity, dosage of superplasticiser (SP), and the free water). All quantities must conform to the following Eq. (2) for balancing between the Si/Al ratio and K/Al ratio which will influence the setting time, the workability, and the compressive strength [36]. These ratios play a critical role in the chemical composition of the geopolymer concrete, therefore, in this study, the aim is to set the Si/Al double the ratio of K/Al.

$$\frac{\frac{Si}{Al}}{1+\frac{K}{Al}} \geq 1.1 \tag{2}$$

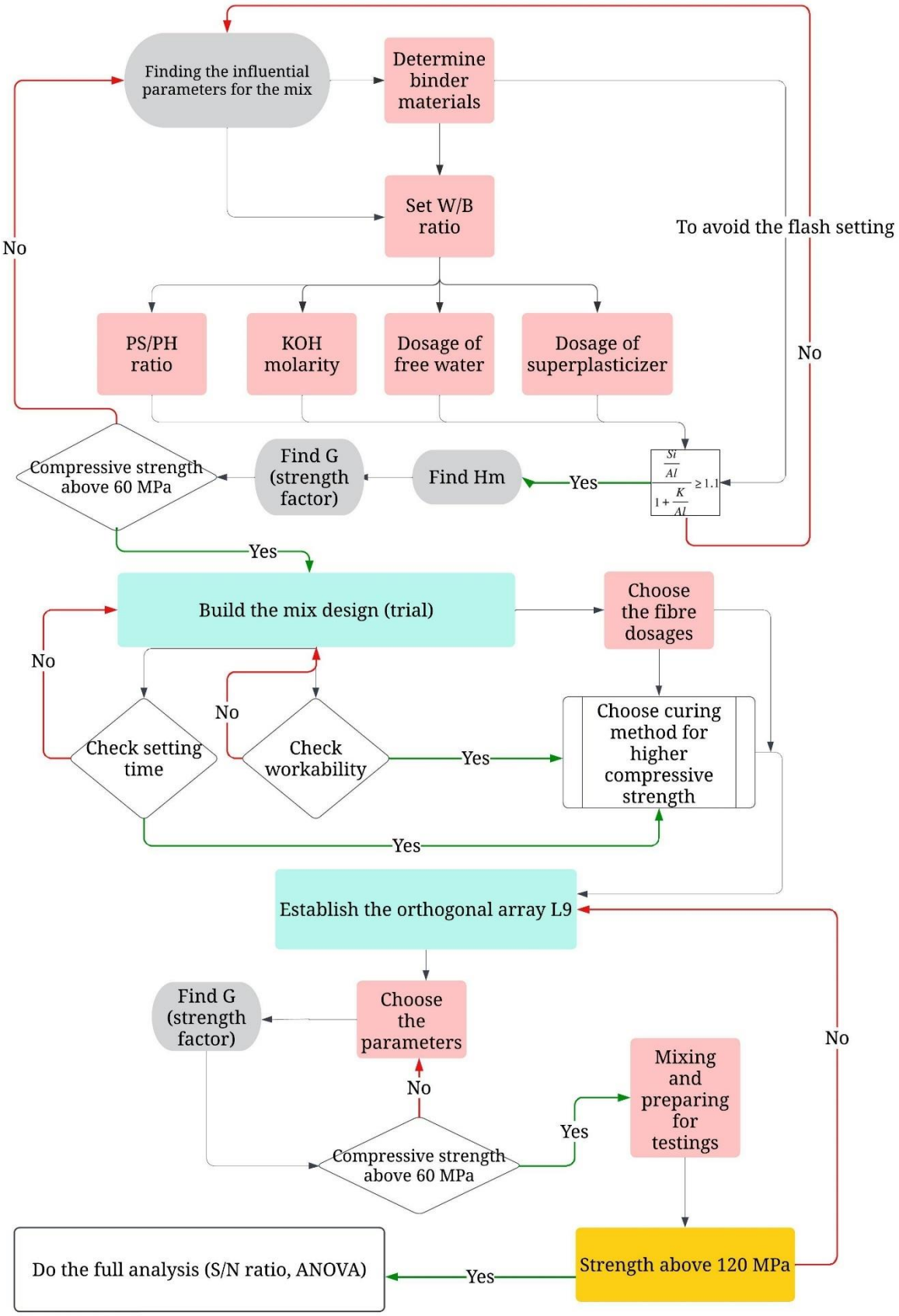


Fig. 1 Suggested mix design process

The process is continued by finding the HM according to Eq. (1), followed by the strength factor (G) as per Eq. (3), which will indicate the expected compressive strength according to Eq. (4) by Elchalakani et al. [37] to predict the geopolymer mortar compressive strength.

$$G = \frac{HM \times \left(\frac{PS}{PH}\right)}{\left(\frac{W}{B}\right)} \quad (3)$$

$$f_c' = 4.3G + 22.9 \quad (4)$$

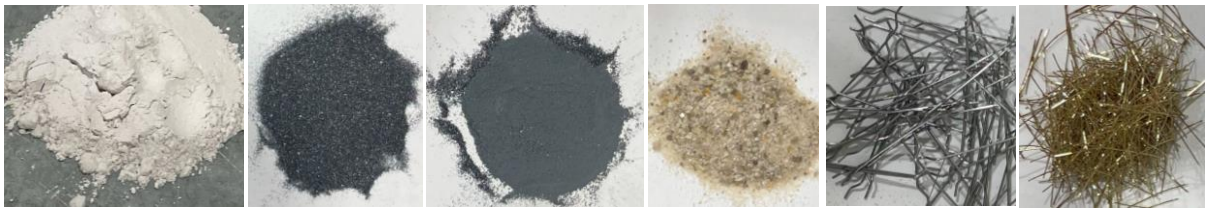
In this study, multiple trial mixes have been formed with the addition of fibre with varying types and dosages. All trial mixes were tested for workability, setting time, and compressive strength after 7 days. Then, the Taguchi method setup was established once we reached a compressive strength above 60 MPa with a workable mix that possess at least 15 minutes of initial setting time. Consequently, the OA is established by varying parameters according to the trials.

In the Taguchi method, the predicted compressive strength must be checked for all mixes to ensure a systematic output for the compressive strength. If the predicted compressive strength exceeds 60 MPa, the process continues after finalising the OA. After each mix trial in the OA, the total binder content will be optimised based on the average density after 7 and 14 days to obtain a dense microstructure, which will increase the probability of acquiring a higher compressive strength. After analysing the first one, the Taguchi method was repeated to change the variables to reach above 120 MPa of compressive strength. It should be noted that the parameters between the first and the second trial were adjusted by using the mix process flowchart shown in Fig. 2.

3.2 Materials used:

The main binder materials used in this study to produce the geopolymer mortar comprised GGBS, SF, and silicon carbide (SiC). The fine aggregate is quartz sand with high silica content, a sub-angular to round shape, and varied diameter size of (0.075 mm to 1.18 mm). Table 2 is

presented the chemical composition of the dry constituents which was analysed using X-ray fluorescence (XRF) to identify the major and minor oxide components, following the guidelines provided by ASTM C114 [38]. Alkaline Activator material (AAM) solution consists of potassium hydroxide with a molarity of 13.95, and potassium silicate (Silicate modulus (Ms), SiO_2/K_2O = 1.5). The AAM solution has been supplied in a liquid condition by Ace Chemicals Australia. Demineralised water was used as a free water with the High-range water reducer (HRWR) (polycarboxylates superplasticiser (SP), ViscoCrete-10 type, Sika, Australia) was utilised which has 41.7% solid contents by mass. The mixes used two different types of steel fibre (straight fibre, D=0.2 mm and L=13 mm) and (hooked end fibre, D=0.55 mm and L=35 mm). Liu et al [39] indicated that increasing the length of the steel fibre and decreasing its diameter delays the progression of micro and macro cracks. Therefore, in this study, two types of steel fibres with small diameters and different lengths were utilised to improve compressive strength. The tensile strength for the 0.2D fibre and 0.55D fibre are 2850 MPa and 1350 MPa, respectively. The materials can be visualised in Fig. 2.



a) b) c) d) e) f)

Fig. 3 a) GGBS, b) SiC, c) SF, d) Quartz sand, e) Steel fibre (0.55D), and f) Steel fibre (0.2D)

Table 2 Chemical composition of the dry materials

	SiO_2	TiO_2	Al_2O_3	Fe_2O_3	MgO	CaO	Na_2O	K_2O	P_2O_5	SO_3
GGBS	35.10	0.57	13.59	0.98	5.36	41.52	0.14	0.33	0.04	0.10
SiC	96.03	0.02	0.25	0.83	0.31	0.02	0.04	0.29	0.03	0.06
SF	92.35	0.01	0.36	0.78	0.36	0.54	0.19	0.52	0.31	0.04
Quartz sand	93.48	0.04	0.06	0.06	0.03	0.02	0.039	0.02	0.01	0.01

3.3 Details of mix design based on the Taguchi method:

The Taguchi method [24] was used to maximise the output by finding the optimum mix design. The main aim is to reach above 120 MPa of compressive strength. To achieve the goal of this study, the Taguchi method array was repeated twice with different variables by analysing the first array to find the significant variables then establish the new array accordingly.

In the first array, four main parameters (W/B, silica fume to binder ratio (SF/B), PS/PH, and fine aggregate to binder ratio (Agg/B)) with three levels of each parameter were studied in the mix design (Table 3 and Table 4). The L9 OA from the Taguchi method was used to prepare nine different mix designs. The detailed mix designs are given in Table 5. The binder contained one change by varying the SF ratio to the total binder ratio which also has GGBS. The W/B ratio was also changed by including the free water, the water amount of AAS, and the water in the SP. The molarity of the PH was kept constant for this trial at 13.95. The AAS to binder ratio (AAS/B) ratio was also kept constant at 0.6. The output of compressive strength at 7-and 28-day was Analysed from this array to find the most significant variables and establish a new optimised array by changing the variables accordingly.

The second array contains four main parameters (W/B, fibre content (Fibre%), SiC to binder ratio by percentage (SiC/B), and SP/B) with three levels for each parameter (Table 3 and Table 4). Table 5 presents the mix design. Based on the trials, W/B was selected again to be used in this array which includes the free water and the amount of water in the AAS and SP. Furthermore, the SP/B ratio was varied by maintaining the required W/B ratio. One variable related to the binder, SiC, has been changed with the GGBS contents in this array. Repeatedly, the L9 orthogonal array was utilised. The fibre percentage as a volume fraction was also selected as a variable in this array due to its efficient influence on the strength of the UHPGC [40–42]. The aim of this study to reach a compressive strength of 120 MPa has been achieved after conducting the second array.

The optimum results were predicted by using the S/N ratio. For the compressive strength, higher results are required; therefore, the larger is better equation of the S/N ratio will be applied to find the optimum parameters, Eq. (5). Furthermore, the results were Analysed by finding the most contributed factor to the output (compressive strength) in each array through the analysis of variance (ANOVA). ANOVA is a statistical analysis that predicts the contribution of each parameter as a percentage by finding the sum squares of each parameter to the total sum of squares [25].

$$S/_N = -10 \log \frac{1}{n} \sum_{n}^{1} \frac{1}{y_i^2} \quad (5)$$

Where n is the number of experiments, y_i is the response output (compressive strength results) for the i^{th}.

Table 3 L9 Orthogonal array

Trial 1/Trial 2	A	B	C	D
M1	1	1	1	1
M2	1	2	2	2
M3	1	3	3	3
M4	2	1	2	3
M5	2	2	3	1
M6	2	3	1	2
M7	3	1	3	2
M8	3	2	1	3
M9	3	3	2	1

Table 4 Factors and levels used in Taguchi experiment design.

	Factor	Level 1	Level 2	Level 3
Trial 1	A-W/B	0.36	0.37	0.38
	B-SF/B	0	0.15	0.30
	C-PS/PH	2	2.5	3
	D-Agg/B	1.3	1.4	1.5
Trial 2	A-W/B	0.30	0.29	0.28
	B-Fibre%	2	2.5	3
	C-SiC/B	0	0.1	0.2
	D-SP/B	2%	2.5%	3%

Table 5 Mixture designs

Mix	GGBS kg/m³	SF kg/m³	SiC kg/m³	Fine Agg. kg/ m³	AAS/B	PS/ PH	W/B ratio	SP kg/ m³	Fibre kg/m³	
									0.55D*	0.2D*
T1M1	701.9	0	78	1014	0.6	2	0.36	35.9	157	78.5
T1M2	561.4	112.3	74.8	1048	0.6	2.5	0.36	35.9	157	78.5
T1M3	431.4	215.7	71.8	1078.4	0.6	3	0.36	35.9	157	78.5
T1M4	658.4	0	73.2	1097.4	0.6	2.5	0.37	36.6	157	78.5

T1M5	575.3	115.1	76.8	997.3	0.6	3	0.37	35.3	157	78.5
T1M6	442.8	221.4	73.8	1033.1	0.6	2	0.37	35.4	157	78.5
T1M7	674.1	0	75	1048.6	0.6	3	0.38	36	157	78.5
T1M8	541.4	108.3	72.2	1082.9	0.6	2	0.38	36.1	157	78.5
T1M9	453.4	226.7	75.6	982.4	0.6	2.5	0.38	34.8	157	78.5
T2M1	591.4	197.1	0	1104	0.38	3	0.3	37.9	104.7	52.3
T2M2	503.1	193.5	77.4	1083.5	0.38	3	0.3	46.4	130.8	65.4
T2M3	418	190	152	1063.9	0.38	3	0.3	54.7	157	78.5
T2M4	504.4	194	77.6	1086.4	0.38	3	0.29	55.9	104.7	52.3
T2M5	430.2	195.6	156.4	1095.2	0.38	3	0.29	37.5	130.8	65.4
T2M6	583.5	194.5	0	1089.1	0.38	3	0.29	46.7	157	78.5
T2M7	431.1	196	156.8	1097.5	0.38	3	0.28	47	104.7	52.3
T2M8	584.5	194.8	0	1091.1	0.38	3	0.28	56.1	130.8	65.4
T2M9	511.1	196.6	78.6	1100.7	0.38	3	0.28	37.7	157	78.5

*: Volume fraction

3.4 Mixing procedures, curing and testings:

The mixing process is illustrated in Fig. 4 and adapted based on the suggestion by Denarie [43]. All materials were prepared before the first step of mixing. The dry constituents which contain GGBS, SF, SiC, and fine aggregate, were mixed for three minutes to obtain a homogenous mixture. 90% of demineralised water with SP were then added for ten minutes. The fibre was added and mixed for up to two minutes. Finally, the AAS that includes PS and PH was mixed with 10% of the demineralised water and added to the mix for two more minutes.

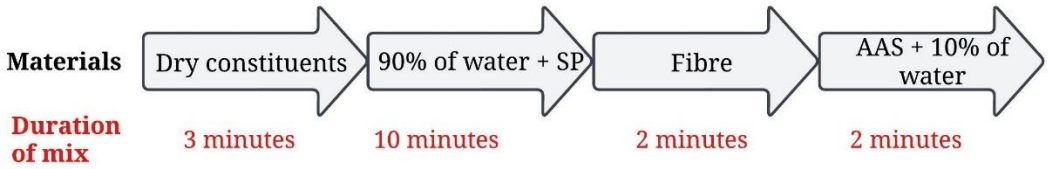


Fig. 4 Mixture procedure

The mortar was immediately poured into the cylindrical moulds that has a height of 200 mm and diameter of 100 mm for curing and testing. The specimens were cast in a prepared steel mould, cleaned, and oiled. The mortar was poured into the mould in three layers; each layer was packed 25 times by a steel rod. On the day of testing, the specimens were grounded from the top to make an even surface.

The curing regime was unified for all specimens. The lid was used to cover the cylindrical moulds for the purpose of immersing the mould in the hot water tank. The mould has been

placed inside the hot water tank for 24 hours with a temperature of 100 ℃. Following the hot curing condition, the specimens were kept in the fog room under 100% of relative humidity (RH) until the day of the testing.

The compressive strength at 7-and 28-day experiments were evaluated in this study according to the ASTM C39 [44]. The dimensions of the cylinders were measured, and then a Seidner machine with a capacity of 3000 kN was utilised to load the specimen at a rate of 20 MPa/min until the failure of the specimen.

4 Results and discussion:

4.1 Compressive strength

The evaluation of all mixes in this study was carried out by the compressive strength experiment at 7 and 28 days. The compressive strength results at 7 and 28 days for all trials are shown in Fig. 5. The results showed that the highest 7-day compressive strength for trial 1 was achieved by T1M8 with 67 MPa, and for the 28-day compressive strength, T1M9 achieved 83 MPa. In trial 2, the highest 7-day compressive strength was achieved by T2M9 with 98 MPa, and the highest 28-day compressive strength was also achieved by T2M9 with 126 MPa. Generally, trial 2 has better performance in terms of higher compressive strength. Therefore, the optimisation after each mix to make a dense microstructure has led to this improvement.

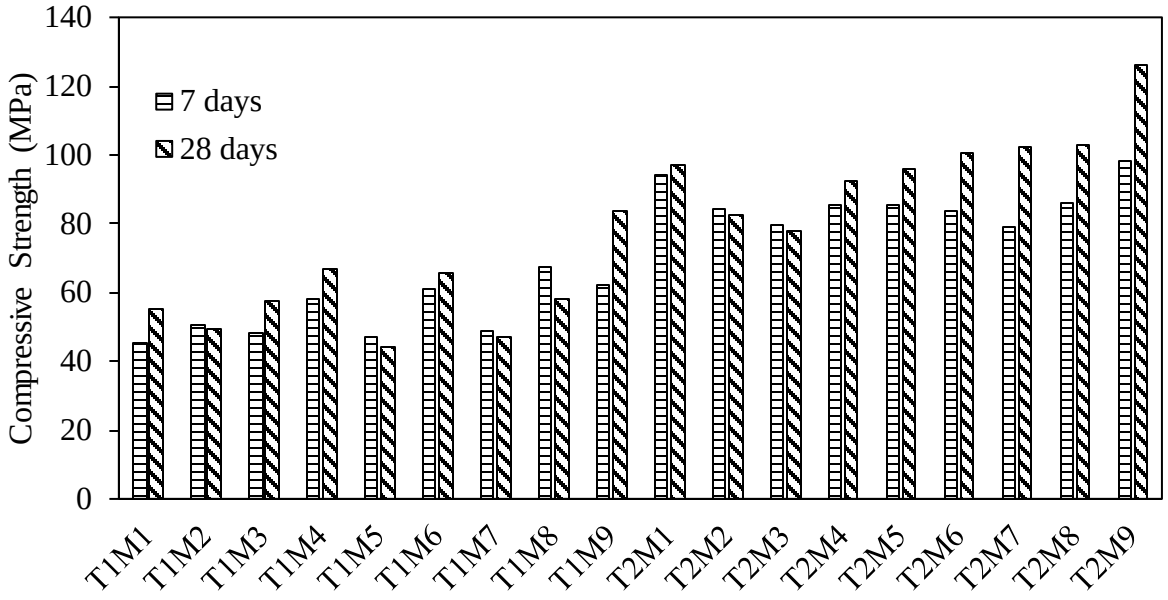


Fig. 5 Compressive strength at 7-and 28-day for all mixes

4.2 Taguchi output

The results from the compressive strength were converted statistically to the S/N ratio according to Eq. (5). The Taguchi method analysis was done using Minitab 19.00 software [45]. The mean responses and S/N ratios were calculated for each trial variable. The mean responses are the raw average compressive strength data for all results in the same variable level. The difference between the highest and lowest mean results was calculated, and then the variables' impacts were ranked according to the highest difference, called delta in this study. Moreover, the S/N ratios have been treated similarly to classify the most effective variable based on the highest delta.

4.2.1 Trial 1: 7-day compressive strength analysis

Table 6 and Table **7** show the mean responses and S/N ratio for 7-day compressive strength results, respectively. It can be observed that the W/B parameter has the highest impact on the strength in the short term. It is well known that for the conventional concrete, the W/B ratio massively affects the strength of the composites. Therefore, a lower W/B ratio results in a compact microstructure with reduced voids and enhances the chemical reaction due to the improved contact between the binder particles and the AAM [46]. The second most influential

parameter was the PS/PH ratio. Finally, The SF/B and Agg/B parameters have almost equivalent effects on the 7-day compressive strength.

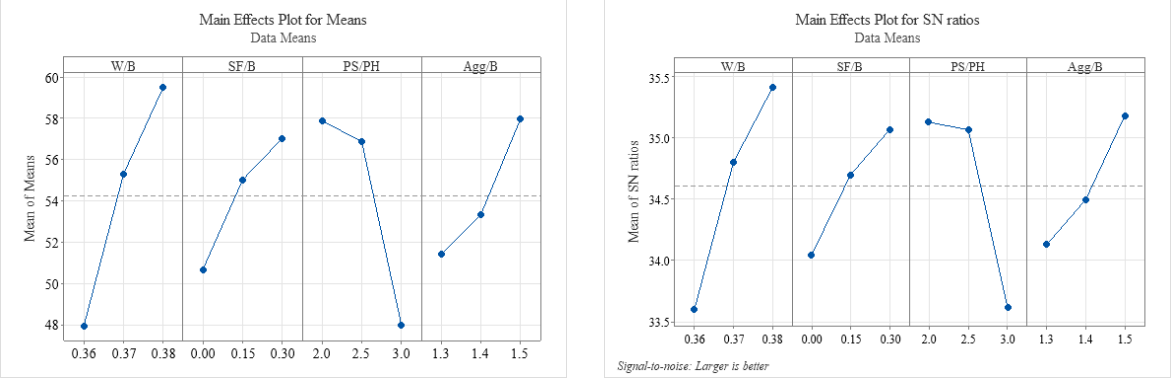
The results were plotted in Fig. 6 to visualise the trend of each parameter. Increasing the W/B ratio from 0.36 to 0.38 has shown the best results for 7-day compressive strength. Consequently, it can be said that there is more room for an extra geopolymerization process in these mixes where the water assists in increasing the polymerization. However, the optimum level for PS/PH is 2 where at a ratio of 3, the strength has decreased drastically. Agg/B ratio of 1.5 and SF/B ratio of 0.3 were the optimum parameters.

Table 6 Trial 1, mean response for 7-day compressive strength

Level	W/B	SF/B	PS/PH	Agg/B
1	47.93	50.68	57.89	51.42
2	55.31	55.03	56.89	53.35
3	59.52	57.05	47.97	57.99
Delta	11.59	6.37	9.92	6.57
Rank	1	4	2	3

Table 7 Trial 1, S/N ratio for 7-day compressive strength

Level	W/B	SF/B	PS/PH	Agg/B
1	33.60	34.05	35.13	34.13
2	34.80	34.70	35.07	34.50
3	35.41	35.07	33.62	35.18
Delta	1.81	1.02	1.51	1.05
Rank	1	4	2	3



a) b)

Fig. 6 7-day compressive strength a) mean responses b) S/N ratio

4.2.2 Trial 1: 28-day compressive strength analysis

The mean responses and S/N ratios for 28-day compressive strength are shown in Table 8 and Table 9, respectively. The parameter SF/B ratio has considerably affected the 28-day compressive along with the PS/PH ratio which has been ranked following the SF/B ratio. The SF enhances the compactness of the geopolymer composite matrix and fills the voids [47]. Therefore, the ultrafine particles of SF could enhance the compressive strength.

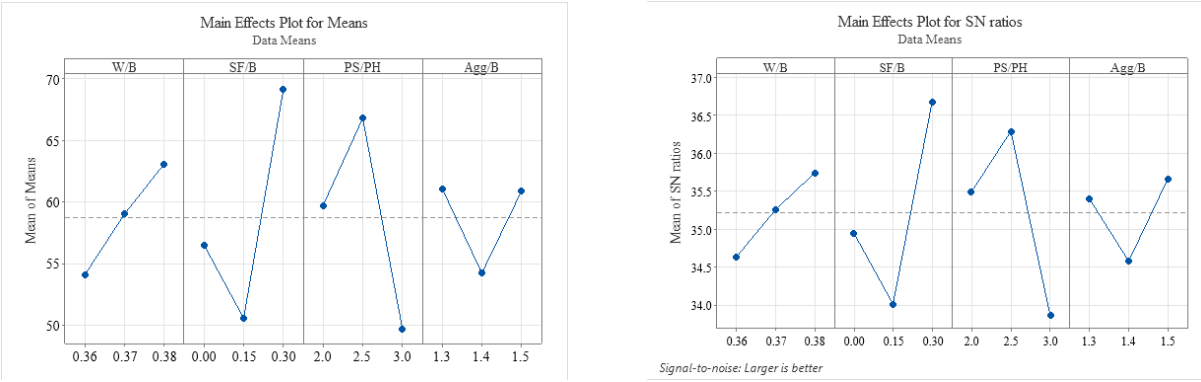
Furthermore, the mean responses and S/N ratio were plotted in Fig. 7. The best combination can be determined; accordingly, the W/B ratio has the same effect as in 7-day compressive strength, as well as the SF/B ratio which has the best outcome at 0.3 level. It is evident that the higher ratio of SF exhibits higher compressive strength. However, the change happened in the PS/PH ratio, where the 28-day compressive analysis by Taguchi method showed that the 2.5 ratio has a better outcome than the 2 ratio which was the best ratio for 7-day compressive strength results. The Agg/B ratio also changed its impact in the 28-day compressive strength results analysis where the ratio of 1.5 was equaled with 1.3.

Table 8 Trial 1, mean response for 28-day compressive strength

Level	W/B	SF/B	PS/PH	Agg/B
1	54.07	56.51	59.70	61.06
2	59.00	50.55	66.78	54.20
3	63.07	69.09	49.67	60.88
Delta	8.99	18.54	17.11	6.86
Rank	3	1	2	4

Table 9 Trial 1, S/N ratio for 28-day compressive strength

Level	W/B	SF/B	PS/PH	Agg/B
1	34.64	34.95	35.50	35.40
2	35.26	34.02	36.29	34.58
3	35.75	36.68	33.87	35.67
Delta	1.11	2.66	2.43	1.08
Rank	3	1	2	4

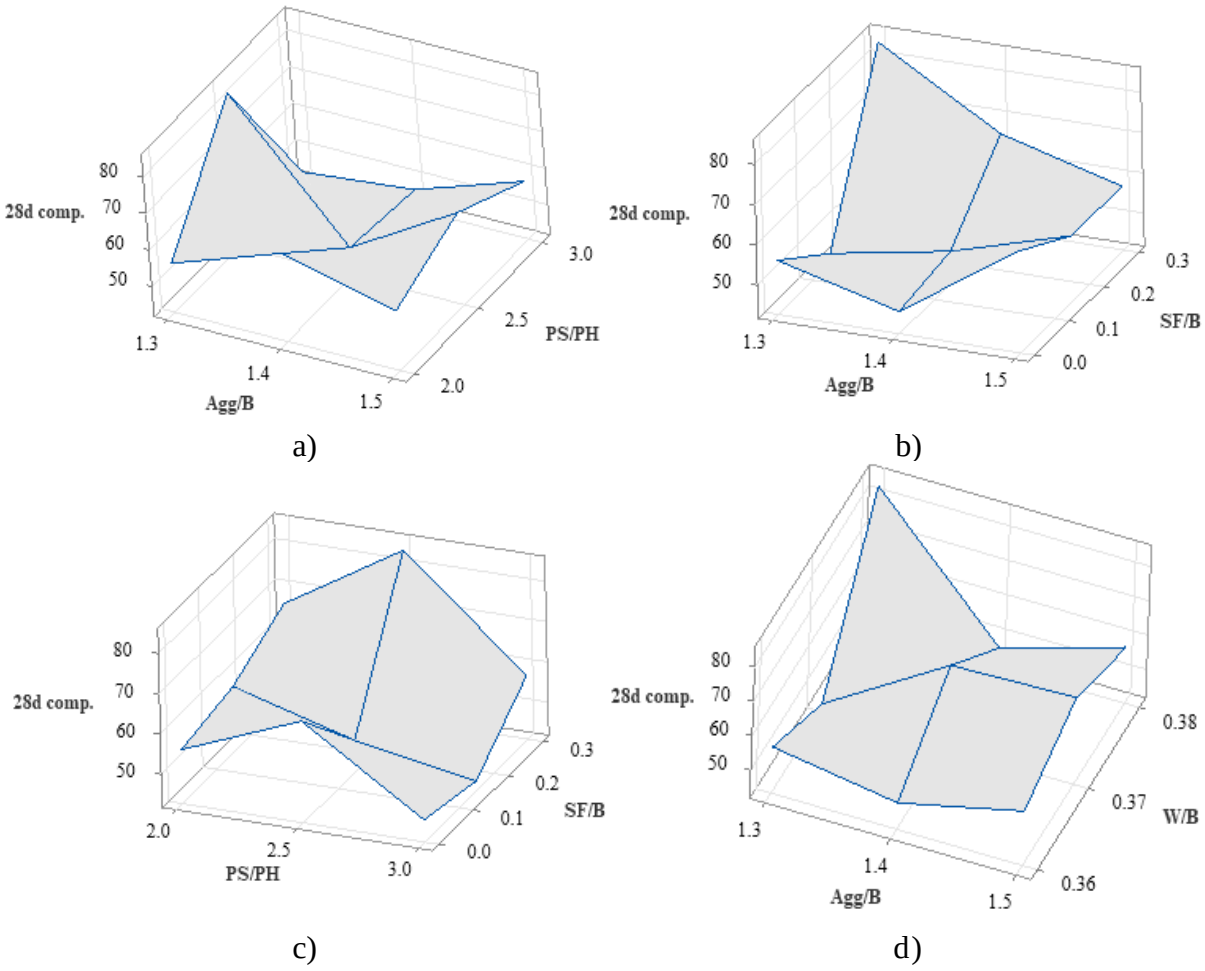


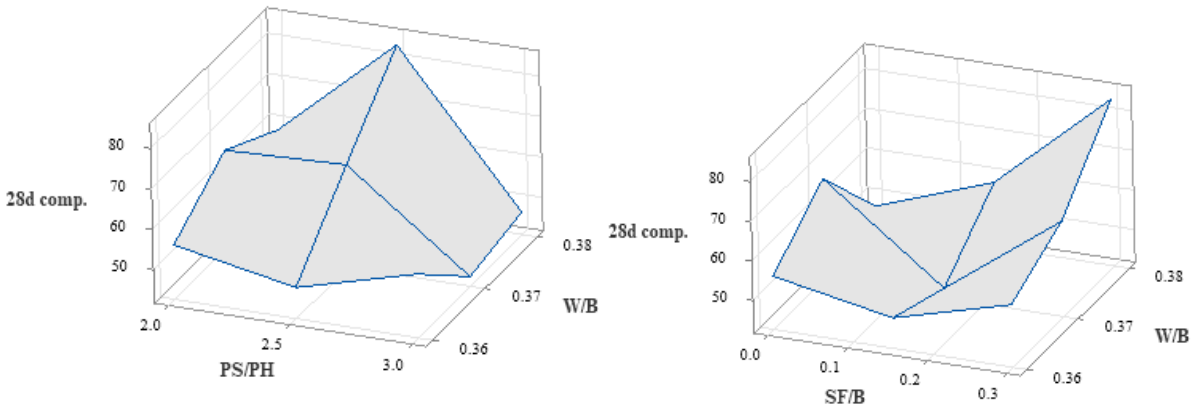
a) b)

Fig. 7. 28-day compressive strength a) mean responses b) S/N ratio

Fig. 8 shows the dependency of the parameters and their level on the 28-day compressive strength results for trial 1. The highest compressive strength above 80 MPa can be achieved by ratio of 1.3 for the Agg/B parameter, PS/PH ratio of 2.5, and SF/B ratio of 0.3, Fig. 8(a). Also, the SF/B ratio of 0.3 and the Agg/B ratio of 1.3 have achieved around 70 MPa of compressive strength, as shown in Fig. 8(b). Furthermore, the SF/B ratio of 0 with PS/PH ratio of 2.5 has

achieved an acceptable result above 70 MPa. Fixing the Agg/B ratio of 1.3 with a W/B ratio of 0.38 will obtain the highest compressive strength for this series of mixes, Fig. 8(d). Additionally, Fig. 8(e) illustrates that increasing the level W/B ratio almost linearly increases the compressive strength with a PS/PH ratio of 2.5. These results confirm that the proposed method comprehensively assesses building a mix design with a minimum of 45 MPa compressive strength results of all mixes in trial 1.





e) f)

Fig. 8 Effect of parameters and their levels on 28-day compressive strength for trial 1

4.2.3 Trial 2: 7-day compressive strength analysis

Following a trial-and-error procedure after trial 1 to carefully choose the most appropriate parameters, the parameters and their associated levels have been picked, and the outcome of 7- and 28-day compressive strength has been Analysed according to the Taguchi method.

Table 10 and Table 11 show the mean responses and the S/N ratios for 7-day compressive strength of trial 2, respectively. It can be deduced that the most significant parameter is the SP/B ratio, followed by the SiC/B ratio. The W/B ratio and Fibre% parameters have approximately similar impacts.

The trend of the parameters relating to each level has been plotted in Fig. 9. Increasing the SP/B ratio from 2% to 2.5% has led to a substantial decrease of 12% in compressive strength. Thus, the level of the SP/B negatively impacted the compressive strength due to the role of the superplasticizer in covering the binder particles with layer which could significantly affect the geopolymerization level [48]. Subsequently, leaving un-reacted binder particles in short term or may be even in long term. However, the increase in SiC/B ratio from 0.1 to 0.2 also has a considerable negative effect of 9% in the compressive strength. Lastly, it can be noticed that the parameters W/B ratio and Fibre% have negligible impact on 7-day compressive strength.

Table 10 Trial 2, mean response for 7-day compressive strength

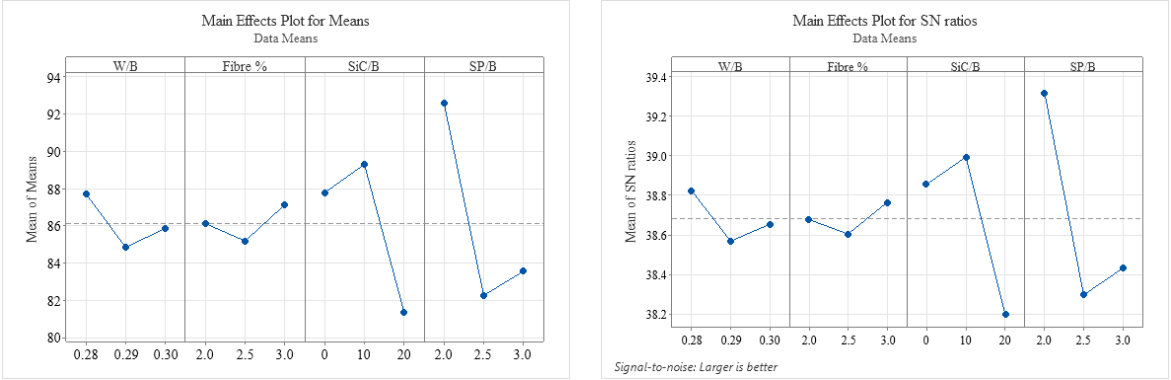
Level	W/B	Fibre %	SiC/B	SP/B

Table 11 Trial 2, S/N ratio for 7-day compressive strength

Level	W/B	Fibre %	SiC/B	SP/B

1	87.71	86.12	87.77	92.61
2	84.83	85.18	89.30	82.25
3	85.87	87.12	81.35	83.55
Delta	2.88	1.95	7.95	10.36
Rank	3	4	2	1

1	38.83	38.68	38.86	39.32
2	38.57	38.61	39.00	38.30
3	38.66	38.77	38.20	38.43
Delta	0.26	0.16	0.79	1.02
Rank	3	4	2	1



a) b)

Fig. 9 7-day compressive strength a) mean responses b) S/N ratio

4.2.4 Trial 2: 28-day compressive strength analysis

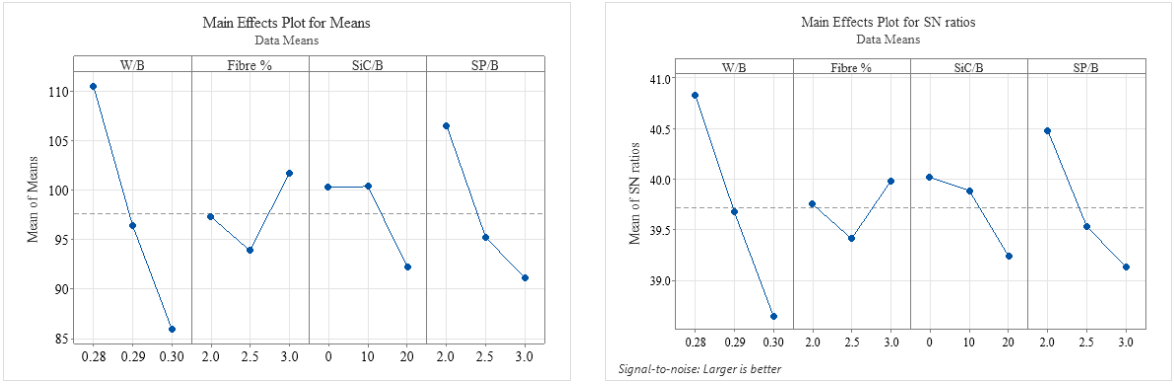
The 28-day compressive strength analysis for mean responses and S/N ratios are shown in Table 12 and Table 13, respectively. The W/B ratio and the SP/B ratio have the most influential impact on the compressive strength. However, it can be deduced that the SiC/B ratio and Fibre% have a lower impact on the compressive strength based on the Taguchi method analysis. Fig. 10 shows each level's positive and negative parameters' effects on the compressive strength. Increasing the level of W/B from 0.28 to 0.29 and 0.3 led to a significant decrease in the compressive strength of 13% and 23%, respectively. This is contrary to the W/B ratio of trial 1, which has shown that a higher W/B ratio improves compressive strength. Therefore, as reported in previous literature [49], the lower W/B ratio is foreseeable to be combined with SF and obtain the desired compressive strength for UHSGC. A higher W/B reduces the cohesion of the particle-to-particle interaction and weakens the intensity of the C-S-H gel which is responsible for the strength of the concrete. Similarly, the SP/B ratio did to the mixes. However, Fibre% of 3% has the highest compressive strength, as well as the SiC/B ratio of 0 and 0.10.

Table 12 Trial 2, mean response for 28-day compressive strength

Level	W/B	Fibre %	SiC/B	SP/B
1	110.48	97.30	100.25	106.52
2	96.40	93.87	100.36	95.22
3	85.96	101.68	92.23	91.10
Delta	24.52	7.81	8.13	15.42
Rank	1	4	3	2

Table 13 Trial 2, S/N ratio for 28-day compressive strength

Level	W/B	Fibre %	SiC/B	SP/B
1	40.82	39.75	40.02	40.48
2	39.68	39.41	39.89	39.53
3	38.65	39.98	39.24	39.14
Delta	2.18	0.57	0.78	1.34
Rank	1	4	3	2



a) b)

Fig. 10 28-day compressive strength a) mean responses b) S/N ratio

Fig. 11 presents the dependent relationship for the parameters and their levels on the 28-day compressive strength. It can be deduced that the best combination for the higher compressive strength can be achieved by a SiC/B ratio of 0.10 and Fibre% of 3%, as shown in Fig. 11(a). Additionally, W/B ratio of 0.28 and SP/B of 2% as illustrated in Fig. 11(f), have the highest outcome of 28-day compressive strength above 120 MPa. Increase the SP/B ratio from 2% to 3% with a constant 3% of Fibre% has a linear descent which substantially reduces the compressive strength from above 120 MPa to around 80 MPa. Therefore, an excessive amount of SP can lead to the weakening of the GPC matrix cohesion; hence, the SP/B ratio must be optimised with the W/B ratio. However, increasing the Fibre% from 2% to 3% with a constant W/B ratio increased the compressive strength by 20% Fig. 11(d). The combination of the small diameter which can positively influence the compressive strength and the end hooked fibre can increase the compressive strength [50].

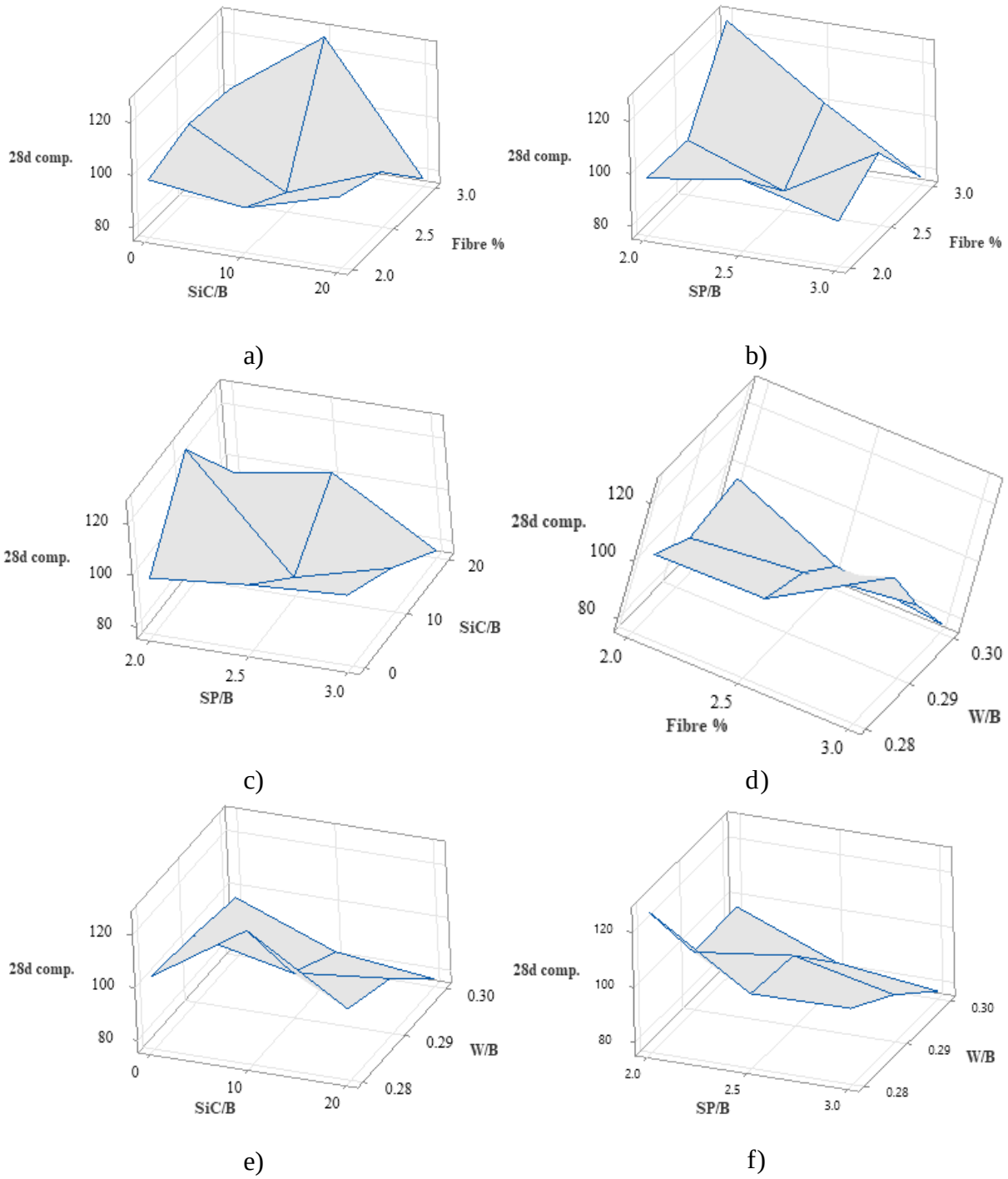


Fig. 11 Effect of parameters and their levels on 28-day compressive strength for trial 2

4.3 ANOVA for 28-day compressive strength for Trial 1 & 2

ANOVA quantifies the quality of GPC and determines the significance of the parameters. It presents the most contributed parameter on the GPC. ANOVA results obtained for trial 1 and trial 2 for 28-day compressive strength are shown in Table 14 and Table 15, respectively. It was found that trial 1 is notably affected by the SF/B ratio, followed by the PS/PH ratio with

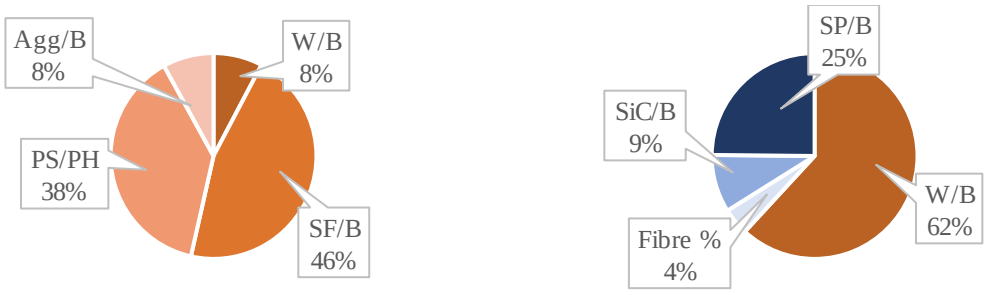
45.8% and 38.5%, respectively. The W/B ratio and Agg/B ratio have less impact on the outcome for a combined contribution of 15.7%. However, in trial 2, the parameters were changed according to the mix design process, and it was found that the W/B ratio has the most significant contribution of 61.9%, followed by the SP/B ratio which has a contribution of 24.8%. The SiC/B ratio and Fibre% have less effect on the trial 2 output with a 9% and 4.2% contribution, respectively. For GPC, the optimum amount of liquid in the mix is necessary to control the compressive strength by forming a dense microstructure.

Table 14 Trial 1, ANOVA of 28-day compressive strength

Factor	DF	Sum of Squares	Mean of Squares	% Contribution
W/B	2	1.84	0.92	7.71
SF/B	2	10.94	5.47	45.81
PS/PH	2	9.19	4.59	38.46
Agg/B	2	1.91	0.95	8
Total	8	23.88		100

Table 15 Trial 2, ANOVA of 28-day compressive strength

Factor	DF	Sum of Squares	Mean of Squares	% Contribution
W/B	2	7.10	3.55	61.85
Fibre %	2	0.48	0.24	4.23
SiC/B	2	1.04	0.52	9.07
SP/B	2	2.85	1.42	24.84
Total	8	11.48		100



a) b)

Fig. 12 The contribution of each parameter on the trials a) trial 1; and b) trial 2

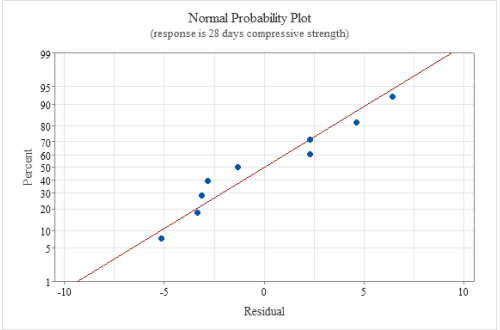
4.4 Modelling

In this study, a predictive mathematical model for the 28-day compressive strength outcome for trial 1 and trial 2 has been developed by linear regression analysis. The 28-day compressive strength without any made transformation as a function of (for trial 1: W/B, SF/B, PS/PH, and Agg/B; for trial 2: W/B, Fibre%, SiC/B, and SP/B). The equations predicted from the linear regression analysis are presented in Eqs. (6 and 7).

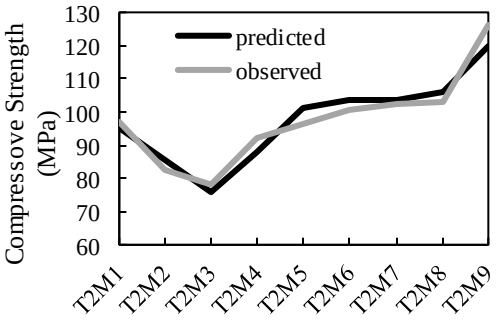
$$28d\ Comp.strength = -88 + 450\frac{W}{B} + 41.9\frac{SF}{B} + 10\frac{PS}{PH} - 0.9\frac{Agg}{B} \quad (R^2 = 42.69\%) \tag{6}$$

$$28d\ Comp.strength = 484.8 - 1226\frac{W}{B} - 4.38Fibre\% - 0.4\frac{PS}{PH} - 15.42\frac{SP}{B} \quad (R^2 = 91.44\%) \tag{7}$$

The R^2 value, known as the coefficient of determination, ranges from 0% to 100%. Values near 100% indicate a strong fit between the independent and dependent variables. However, it's important to note that the level of confidence, typically expressed as a 95% confidence level, is related to the precision of the estimation, and this level has been utilised in this study. The developed regression models for both trials have values of 42.69% and 91.44% for trial 1 and trial 2, respectively. It can be deduced that trial 2 has a higher value indicating the variables' significance on the outcome. Furthermore, Fig. 13 shows the correlation between the experimental data and their corresponding output from the model. It can be observed that the developed mathematical model for determining the compressive strength at 28-day agrees well with the compressive strength results output from the experimental program.



a)



b)

Fig. 13 28-day compressive strength trial 2 a) Normal probability plot; b) Confirmation of the predicted and observed results

4.5 Geopolymer strength factor

For further clarification of the significance of this approach, the geopolymer strength factor (G) as mentioned in Eq. (3) with its predicted compressive strength, as shown in Eq. (4), along with the experimental test results are plotted and presented in Fig. 14. G is based on the fundamental understandings of the HM and can be used for future mix designs to predict compressive strength. As it can be seen for trial 2, a satisfactory correlation between G and 28-day compressive strengths was attained. Interestingly, all results for trial 2 have achieved higher compressive strengths than Eq. (4). Therefore, this factor is beneficial to be included in the mixing process for better estimation of the GPC mortar as well. However, in addition to what was mentioned earlier for the effect of the W/B ratio on the GPC, the first trial has more W/B ratio; therefore, the trial 1 is less scattered compared to the trial 2, which has less W/B ratio. Moreover, the compressive strength predictions of trial 1 are mostly higher than the experimental results.

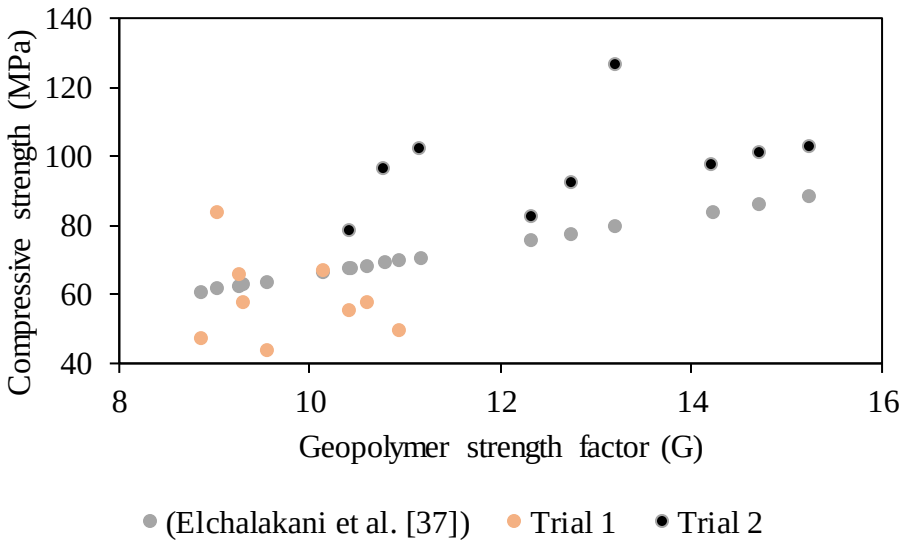


Fig. 14 28-day compressive strengths of the trials and the proposed equation against the geopolymer strength factor

5 Conclusion

This study has assessed a new approach for the mix design process of GPC based on the Taguchi method. This study investigated two trials with four parameters per trial and three levels of each parameter. Following are the conclusions made from observing the experimental data and analysing the Taguchi method.

- For trial 1, the optimum mix for the highest 28-day compressive strength includes W/B ratio of 0.38, SF/B ratio of 0.3, PS/PH ratio of 2.5 and Agg/B ratio of 1.5. However, the highest compressive strength was 83.85 MPa which is not considered a UHPGC.
- For trial 2, a combination of a W/B ratio of 0.28, Fibre% of 3%, SiC/B of 0, and SP/B of 2% has achieved the highest 28-day compressive strength of 126 MPa, which is considered the optimum mixture design for UHPGC according to the proposed method.
- The analysis of the L9 orthogonal array based on the Taguchi method has attained a valid prediction of the development of the GPC mix design. The analysis showed that the most contributed parameters that affected the trials were SF/B with 45.8% and W/B with 61.8% for trial 1 and trial 2, respectively.
- The mathematical model for both trials has been extracted from the regression analysis. It was a good fit for the model between the predicted 28-day compressive strength and the experimental results of trial 2.
- Both experimental results from both trials aligned closely with the predicted 28-day compressive strength derived from the geopolymer strength factor. Remarkably, trial 2 exhibited better performance within the experimental program and surpassed the predictions based on the geopolymer strength factor.

Acknowledgement

The authors would like to acknowledge the financial support from the Australian Research Council (DP 21001425) for undertaking this research.

References

[1] R.M. Andrew, Global CO 2 emissions from cement production, 1928–2018, Earth Syst Sci Data 11 (2019) 1675–1710. https://doi.org/https://doi.org/10.5194/essd-11-1675-2019, 2019.

[2] R.M. Andrew, Global CO 2 emissions from cement production, 1928–2018, Earth Syst Sci Data 11 (2019) 1675–1710. https://doi.org/https://doi.org/10.5194/essd-11-1675-2019, 2019.

[3] O.T. Sanya, J. Shi, Ultra-high-performance fiber reinforced concrete review: constituents, properties, and applications, Innovative Infrastructure Solutions 8 (2023) 188.

[4] M.H. Akeed, S. Qaidi, H.U. Ahmed, R.H. Faraj, A.S. Mohammed, W. Emad, B.A. Tayeh, A.R.G. Azevedo, Ultra-high-performance fiber-reinforced concrete. Part IV: Durability properties, cost assessment, applications, and challenges, Case Studies in Construction Materials 17 (2022) e01271.

[5] M. Abdellatief, M. Mortagi, M. Abd Elrahman, A.M. Tahwia, A.E. Alluqmani, H. Alanazi, Characterization and optimization of fresh and hardened properties of ultra-high performance geopolymer concrete, Case Studies in Construction Materials 19 (2023) e02549.

[6] M. Abdellatief, M.A. Elrahman, H. Alanazi, A.A. Abadel, A. Tahwia, A state-of-the-art review on geopolymer foam concrete with solid waste materials: components, characteristics, and microstructure, Innovative Infrastructure Solutions 8 (2023) 230.

[7] S. Luhar, D. Nicolaides, I. Luhar, Fire resistance behaviour of geopolymer concrete: An overview, Buildings 11 (2021) 82. https://doi.org/https://doi.org/10.3390/buildings11030082.

[8] P. Pradhan, S. Dwibedy, M. Pradhan, S. Panda, S.K. Panigrahi, Durability characteristics of geopolymer concrete - Progress and perspectives, Journal of Building Engineering 59 (2022) 105100. https://doi.org/https://doi.org/10.1016/j.jobe.2022.105100.

[9] S. Singh, S.K. Sharma, M.A. Akbar, Evaluation of mechanical and durability properties along with flexural fatigue life of pavement quality geopolymer concrete, Innovative Infrastructure Solutions 9 (2024) 4.

[10] Geopolymer Institute, (2023). https://www.geopolymer.org/ (accessed September 20, 2022).

[11] H.Y. Leong, D.E.L. Ong, J.G. Sanjayan, A. Nazari, The effect of different Na2O and K2O ratios of alkali activator on compressive strength of fly ash based-geopolymer, Constr Build Mater 106 (2016) 500–511. https://doi.org/https://doi.org/10.1016/j.conbuildmat.2015.12.141.

[12] J. Wu, Z. Zhang, Y. Zhang, D. Li, Preparation and characterization of ultra-lightweight foamed geopolymer (UFG) based on fly ash-metakaolin blends, Constr Build Mater 168 (2018) 771–779. https://doi.org/https://doi.org/10.1016/j.conbuildmat.2018.02.097.

[13] M. Abdellatief, M. Abd Elrahman, A.A. Abadel, M. Wasim, A. Tahwia, Ultra-high performance concrete versus ultra-high performance geopolymer concrete: Mechanical performance, microstructure, and ecological assessment, Journal of Building Engineering 79 (2023) 107835.

[14] D. Hardjito, S.E. Wallah, D.M.J. Sumajouw, B. V Rangan, Fly Ash-Based Geopolymer Concrete, Australian Journal of Structural Engineering 6 (2005) 77–86. https://doi.org/10.1080/13287982.2005.11464946.

[15] K. Suresh, Muthukannan, K. Arun, G. Chithambar, D. Kanniga, Influence of incinerated biomedical waste ash and waste glass powder on the mechanical and flexural properties of reinforced geopolymer concrete, Australian Journal of Structural Engineering 23 (2022) 254–268. https://doi.org/10.1080/13287982.2022.2044613.
[16] P.S. Ambily, K. Ravisankar, C. Umarani, J.K. Dattatreya, N.R. Iyer, Development of ultra-high-performance geopolymer concrete, Magazine of Concrete Research 66 (2014) 82–89. https://doi.org/https://doi.org/10.1680/macr.13.00057.
[17] C.D. Atiş, E.B. Görür, O. Karahan, C. Bilim, S. İlkentapar, E. Luga, Very high strength (120 MPa) class F fly ash geopolymer mortar activated at different NaOH amount, heat curing temperature and heat curing duration, Constr Build Mater 96 (2015) 673–678. https://doi.org/10.1016/j.conbuildmat.2015.08.089.
[18] H.Y. Leong, D.E.L. Ong, J.G. Sanjayan, A. Nazari, Suitability of Sarawak and Gladstone fly ash to produce geopolymers: A physical, chemical, mechanical, mineralogical and microstructural analysis, Ceram Int 42 (2016) 9613–9620. https://doi.org/https://doi.org/10.1016/j.ceramint.2016.03.046.
[19] L.N. Assi, E.E. Deaver, P. Ziehl, Effect of source and particle size distribution on the mechanical and microstructural properties of fly Ash-Based geopolymer concrete, Constr Build Mater 167 (2018) 372–380. https://doi.org/https://doi.org/10.1016/j.conbuildmat.2018.01.193.
[20] M. Dong, W. Feng, M. Elchalakani, G.K. Li, A. Karrech, E.F. May, Development of a high strength geopolymer by novel solar curing, Ceram Int 43 (2017) 11233–11243. https://doi.org/https://doi.org/10.1016/j.ceramint.2017.05.173.
[21] X. Gao, Q.L. Yu, H.J.H. Brouwers, Reaction kinetics, gel character and strength of ambient temperature cured alkali activated slag–fly ash blends, Constr Build Mater 80 (2015) 105–115. https://doi.org/https://doi.org/10.1016/j.conbuildmat.2015.01.065.
[22] S. Zhang, Z. Li, B. Ghiassi, S. Yin, G. Ye, Fracture properties and microstructure formation of hardened alkali-activated slag/fly ash pastes, Cem Concr Res 144 (2021) 106447. https://doi.org/https://doi.org/10.1016/j.cemconres.2021.106447.
[23] X. Dai, S. Aydin, M.Y. Yardimci, R.E.N. Qiang, K. Lesage, G. De Schutter, Rheology, early-age hydration and microstructure of alkali-activated GGBFS-Fly ash-limestone mixtures, Cem Concr Compos 124 (2021) 104244. https://doi.org/https://doi.org/10.1016/j.cemconcomp.2021.104244.
[24] G. Taguchi, S. Chowdhury, Y. Wu, Taguchi's Quality Engineering Handbook, Wiley, Livonia, 2004. https://doi.org/DOI:10.1002/9780470258354.
[25] G. Taguchi, S. Chowdhury, Y. Wu, Taguchi's Quality Engineering Handbook, Wiley, Livonia, 2004. https://doi.org/DOI:10.1002/9780470258354.
[26] A. Nazari, H. Khanmohammadi, M. Amini, H. Hajiallahyari, A. Rahimi, Production geopolymers by Portland cement: Designing the main parameters' effects on compressive strength by Taguchi method, Mater Des 41 (2012) 43–49. https://doi.org/10.1016/j.matdes.2012.04.045.
[27] M. Olivia, H. Nikraz, Properties of fly ash geopolymer concrete designed by Taguchi method, Materials & Design (1980-2015) 36 (2012) 191–198. https://doi.org/10.1016/j.matdes.2011.10.036.
[28] A. Bagheri, A. Nazari, Compressive strength of high strength class C fly ash-based geopolymers with reactive granulated blast furnace slag aggregates designed by Taguchi method, Materials & Design (1980-2015) 54 (2014) 483–490. https://doi.org/10.1016/j.matdes.2013.07.035.

[29] C. Panagiotopoulou, S. Tsivilis, G. Kakali, Application of the Taguchi approach for the composition optimization of alkali activated fly ash binders, Constr Build Mater 91 (2015) 17–22. https://doi.org/10.1016/j.conbuildmat.2015.05.005.
[30] A. Mehta, R. Siddique, B.P. Singh, S. Aggoun, G. Łagód, D. Barnat-Hunek, Influence of various parameters on strength and absorption properties of fly ash based geopolymer concrete designed by Taguchi method, Constr Build Mater 150 (2017) 817–824. https://doi.org/10.1016/j.conbuildmat.2017.06.066.
[31] M.N.S. Hadi, N.A. Farhan, M.N. Sheikh, Design of geopolymer concrete with GGBFS at ambient curing condition using Taguchi method, Constr Build Mater 140 (2017) 424–431. https://doi.org/10.1016/j.conbuildmat.2017.02.131.
[32] J.K. Prusty, B. Pradhan, Multi-response optimization using Taguchi-Grey relational analysis for composition of fly ash-ground granulated blast furnace slag based geopolymer concrete, Constr Build Mater 241 (2020) 118049. https://doi.org/https://doi.org/10.1016/j.conbuildmat.2020.118049.
[33] S. Karthik, K.S.R. Mohan, A taguchi approach for optimizing design mixture of geopolymer concrete incorporating fly ash, ground granulated blast furnace slag and silica fume, Crystals (Basel) 11 (2021) 1279. https://doi.org/https://doi.org/10.3390/cryst11111279.
[34] S.R. Raj, P.G. Arulraj, N. Anand, K. Balamurali, G. Gokul, Influence of various design parameters on compressive strength of geopolymer concrete: A parametric study by taguchi method, International Journal of Engineering 34 (2021) 2351–2359. https://doi.org/https://doi.org/10.5829/ije.2021.34.10a.16.
[35] S. Rawat, Y.X. Zhang, C.K. Lee, Multi-response optimization of hybrid fibre engineered cementitious composite using Grey-Taguchi method and utility concept, Constr Build Mater 319 (2022) 126040. https://doi.org/10.1016/j.conbuildmat.2021.126040.
[36] S. Yaseri, G. Hajiaghaei, F. Mohammadi, M. Mahdikhani, R. Farokhzad, The role of synthesis parameters on the workability, setting and strength properties of binary binder based geopolymer paste, Constr Build Mater 157 (2017) 534–545.
[37] M. Elchalakani, M. Dong, A. Karrech, G. Li, M.S. Mohamed Ali, T. Xie, B. Yang, Development of fly ash-and slag-based geopolymer concrete with calcium carbonate or microsilica, Journal of Materials in Civil Engineering 30 (2018) 4018325. https://doi.org/https://doi.org/10.1061/(ASCE)MT.1943-5533.0002527.
[38] ASTM C114-18, Standard Test Methods for Chemical Analysis of Hydraulic Cement, ASTM International, 2018. https://doi.org/10.1520/C0114-18.
[39] Y. Liu, Z. Zhang, C. Shi, D. Zhu, N. Li, Y. Deng, Development of ultra-high performance geopolymer concrete (UHPGC): Influence of steel fiber on mechanical properties, Cem Concr Compos 112 (2020) 103670. https://doi.org/10.1016/j.cemconcomp.2020.103670.
[40] Y. Liu, C. Shi, Z. Zhang, N. Li, D. Shi, Mechanical and fracture properties of ultra-high performance geopolymer concrete: Effects of steel fiber and silica fume, Cem Concr Compos 112 (2020) 103665. https://doi.org/10.1016/j.cemconcomp.2020.103665.
[41] Z. Wu, C. Shi, W. He, L. Wu, Effects of steel fiber content and shape on mechanical properties of ultra high performance concrete, Constr Build Mater 103 (2016) 8–14. https://doi.org/10.1016/j.conbuildmat.2015.11.028.
[42] S.H.G. Mousavinejad, M. Sammak, Strength and chloride ion penetration resistance of ultra-high-performance fiber reinforced geopolymer concrete, Structures 32 (2021) 1420–1427. https://doi.org/10.1016/j.istruc.2021.03.112.

[43] E. Denarié, SAMARIS D25b-guidance for the use of UHPFRC for rehabilitation of concrete highway structures, (2006).
[44] ASTM C39/C39M-20, Standard Test Method for Compressive Strength of Cylindrical Concrete Specimens, ASTM International, West Conshohocken, PA, 2020. https://doi.org/10.1520/C0039_C0039M-10.
[45] Minitab, (2023).
[46] L.N. Tchadjie, S.O. Ekolu, Enhancing the reactivity of aluminosilicate materials toward geopolymer synthesis, J Mater Sci 53 (2018) 4709–4733.
[47] F.N. Okoye, J. Durgaprasad, N.B. Singh, Effect of silica fume on the mechanical properties of fly ash based-geopolymer concrete, Ceram Int 42 (2016) 3000–3006. https://doi.org/https://doi.org/10.1016/j.ceramint.2015.10.084.
[48] Y. Alrefaei, Y.-S. Wang, J.-G. Dai, Q.-F. Xu, Effect of superplasticizers on properties of one-part Ca (OH) 2/Na2SO4 activated geopolymer pastes, Constr Build Mater 241 (2020) 117990.
[49] A. Wetzel, B. Middendorf, Influence of silica fume on properties of fresh and hardened ultra-high performance concrete based on alkali-activated slag, Cem Concr Compos 100 (2019) 53–59. https://doi.org/10.1016/j.cemconcomp.2019.03.023.
[50] Y. Liu, Z. Zhang, C. Shi, D. Zhu, N. Li, Y. Deng, Development of ultra-high performance geopolymer concrete (UHPGC): Influence of steel fiber on mechanical properties, Cem Concr Compos 112 (2020) 103670. https://doi.org/10.1016/j.cemconcomp.2020.103670.

Chapter 3

Background

This chapter explores the development of FRGC based on the mechanical and durability assessments. The Taguchi method was used to form an L9 orthogonal array, which involves nine experiments conducted by changing four parameters, with each parameter having three levels. Moreover, ANOVA analysis accompanied by residual fitting was conducted to derive mathematical models for accurately predicting the compressive strength exhibiting good correlation with the test results.

List of Manuscripts

Alameri, M., Mohamed Ali, M. S., Elchalakani, M., & Sheikh, A. (2024). "Optimizing slag-based fibre reinforced geopolymer mix design for enhanced strength and durability" Submitted to *Journal of Building Engineering* (under review)

Statement of Authorship

Title of Paper	Optimizing slag-based fibre reinforced geopolymer mix design for enhanced strength and durability
Publication Status	☐ Published ☐ Accepted for Publication ☑ Submitted for Publication ☐ Unpublished and Unsubmitted work written in manuscript style
Publication Details	Alameri, M., Mohamed Ali, M. S., Elchalakani, M., & Sheikh, A. (2024). "Optimizing slag-based fibre reinforced geopolymer mix design for enhanced strength and durability" Submitted to Journal of Building Engineering (under review)

Principal Author

Name of Principal Author (Candidate)	Mohammad Alameri		
Contribution to the Paper	Conceptualisation, methodology, and manuscript writing and revision		
Overall percentage (%)	80%		
Certification:	This paper reports on original research I conducted during the period of my Higher Degree by Research candidature and is not subject to any obligations or contractual agreements with a third party that would constrain its inclusion in this thesis. I am the primary author of this paper.		
Signature		Date	24-10-2024

Co-Author Contributions

Name of Co-Author	M.S. Mohamed Ali		
Contribution to the Paper	Supervision, conceptualisation, methodology, and manuscript revision (10%)		
Signature		Date	24-10-2024

Name of Co-Author	Mohamed Elchalakani		
Contribution to the Paper	Supervision, conceptualisation, methodology, and manuscript revision (5%)		
Signature		Date	28-10-2024

Name of Co-Author	Abdul Sheikh		
Contribution to the Paper	Supervision, conceptualisation, methodology, and manuscript revision (5%)		
Signature		Date	29-10-2024

Optimizing slag-based geopolymer mix design for enhanced strength and durability

Mohammad Alameri[1,*], M.S. Mohamed Ali[1], Mohamed Elchalakani[2], Abdul Sheikh[1]

[1] *School of Architecture and Civil Engineering, The University of Adelaide, Adelaide, Australia*

[2] *Department of Civil, Environmental and Mining Engineering, The University of Western Australia, Perth, Australia*

[*] *Corresponding author E-mail: Mohammad.alameri@adelaide.edu.au*

Abstract

This study explores the impact of water to binder ratio (W/B), fibre content (fibre%), silica carbide to binder ratio (SiC/B), and superplasticizer to binder ratio (SP/B) on the performance of fibre-reinforced geopolymer composite (FRGC). Utilizing the Taguchi method, the mechanical and durability characteristics of the developed mixes were assessed, by examining each parameter across three levels using an L9 orthogonal array for the experimental setup. This approach facilitated a detailed analysis of the influence of each parameter on the properties of FRGC. The experimental program included evaluations of mechanical properties such as compressive, flexural, and splitting tensile strengths, along with durability properties assessed through porosity and sorptivity tests. It was found that the W/B ratio has the most significant impact on both mechanical and durability characteristics. Moreover, ANOVA analysis accompanied by residual fitting was conducted to derive mathematical models for accurately predicting the compressive strength exhibiting good correlation with the test results.

Keywords: Taguchi method, Mechanical properties, Geopolymer, Fibre-reinforced geopolymer composites, and durability.

1 Introduction

In recent years, the pursuit of cleaner, more sustainable construction materials has led to a surge in interest in geopolymer concrete (GPC) as a greener alternative to Ordinary Portland Cement (OPC) concrete. OPC contributes to about 5-7% of global greenhouse gas emissions which underscores the urgent need for more environmentally friendly options [1]. The main precursor of GPC is sourced from municipal solid wastes (MSW) which includes industrial waste such as slag, fly ash, and metakaolin. The annual generation of only metal waste is around 80.4 million tons globally which is projected to increase by about 60% in 2050 with the increase of the population [2]. Therefore, addressing the urgent need to adequately manage the waste materials has led the researchers to incorporate them into the production of concrete by partially replacing the cement [3] or adopting the manufacturing of the GPC [4]. GPC emerged as a promising solution, offering not only strength and durability equivalent to conventional concrete but also a lower carbon footprint due to its production process [5,6].

The adoption of GPC in mainstream construction practices has been slow. This hesitation is attributed to the complexity of its mix design, which involves navigating a vast array of variables to optimize the mechanical properties and durability of GPC. The mix design of Geopolymer Concrete (GPC) remains an attractive area of research, with its composition primarily consisting of two critical components: a binder rich in silica and alumina, and alkaline activator materials (AAM) [7]. Initially, AAM dissolves the binder, releasing silicon (Si) and aluminium (Al) ions into the solution. Subsequently, the addition of water promotes the hydrolysis process which breaks down the molecular structure enabling the formation of links between SiO_4 and AlO_4 tetrahedral units. This sets the stage for the polymerization process wherein SiO_4 and AlO_4 units are interconnected through shared oxygen atoms forming a robust three-dimensional (3D) polymeric network [8]. The process can be described by the following empirical chemical formulae [9]:

$$Si(OH)_4 + Al(OH)^{4-} \rightarrow (-Si-O-Al-O-)_n + 4H_2O$$

Therefore, the geopolymer synthesis is affected by many factors such as water to binder ratio (W/B), Si/Al ratio, alkaline activator solutions (AAS), the molarity of AAS and the curing regime conditions.

The discussion surrounding the impact of various variables on the production of GPC and its fresh properties, strength, and durability characteristics are extensively documented in the published literature [10–15]. Consequently, achieving the target mix proportions necessitates multiple iterations of trial-and-error experiments. Numerous factors contribute to shaping GPC production influencing both its fresh and hardened properties. For instance, binder content such as ground granulated blast slag (GGBS) has been observed to decrease porosity while potentially rendering the product prone to sulfuric acid attack [16]. However, GGBS-based GPC has demonstrated the capability to achieve high strength that reduces the reliance on heat curing which is a necessity in fly ash (FA) based GPC for strength enhancement [17]. Nonetheless, combining GGBS and FA has been found to decrease the final setting time [18]. Another critical variable studied is the alkali-activated slag (AAS) to binder ratio (AAS/B); it was found that an increase in sodium hydroxide (NaOH) content leads to an enhanced compressive strength [19]. This underscores the complicated interplay of variables in optimizing GPC mix designs for achieving desired properties and performance. Furthermore, fibre reinforced GPC has been studied to improve ductility [20]. However, it is important to consider the combined effect of these variables which may pose challenges that require further investigation.

Compiling an extensive database from previous studies will greatly assist in developing a consistent mix design procedure for GPC similar to the OPC concrete. These databases have been collected and statistically analysed in several studies [21–25]. Xia et al. [21] assembled

1756 mix designs from 111 studies to construct a unified mix design based on reactive modulus. This analysis revealed that twelve factors significantly impact the mechanical properties of GPC such as W/B ratio, AAS/B ratio and curing regime conditions which indicate the complexity of achieving a consistent mix design. These factors are vastly diverse that a single study cannot collectively review them using the same materials for each mix. Moreover, Li et al. [22] have evaluated various GPC design methods and highlighted the predominance of the strength-oriented method in designing GPC mixes. However, focusing solely on strength could compromise the durability of the mix which is an essential attribute of concrete performance. Furthermore, Ansari et al. [26] suggested that the statistics-based approach could save time in developing a mix design and recommended the adoption of the Taguchi method which can be easily applied to minimise the experiments.

Note that the Taguchi method is a statistical approach that depends on the design of experiment (DoE) which is organized by a special set of arrays called orthogonal arrays (OA) to examine the highest number of variables with minimum number of experiments [27]. For example, consider an experimental scenario involving five variables (each divided into four levels); the conventional way of DoE requires 4^5 or 1024 experiments while the Taguchi method requires only 16 experiments. Additionally, the Taguchi method enhances the analysis by employing the signal-to-noise ratio (S/N) which focuses on optimizing performance characteristics against the variance to ensure the robustness of the system and simplifies how the results are interpreted [27].

This method was employed in studying the GPC for optimization purposes in previous investigations [28–37]. A summary of these studies along with the type of OA used the three major input parameters (binder parameters, AAS parameters and fibres), and the output field (strength and durability) are illustrated in Table 1. This compilation highlights the capability of the Taguchi method in efficiently designing experiments for GPC by accommodating a

broad array of variables. Moreover, this method allows for a detailed examination of the interplay between various variables across multiple levels, showcasing its utility in optimizing the complex mix design of GPC. Through this strategic analysis, the Taguchi method proves instrumental in enhancing both the performance and sustainability of GPC addressing the critical aspects of strength and durability accurately.

Table 1 Previously published studies of GPC adopting the Taguchi method

Reference	OA used	Parameters considered	Output considered
Dave et al. [28]	L9	Binder (Binder content); AAS (Na_2SiO_3/NaOH ratio, dosage of superplasticizer, NaOH Molarity)	Strength (compressive strength 7 days); Durability (resistance of corrosion and acid resistance)
Prusty and Pradhan [38]	L16	Binder (GGBS replacement ratio, W/B ratio, and Binder content); AAS (Molarity of NaOH, and Na_2SiO_3/NaOH)	Strength (compressive strength 7 and 28 days); Microstructural analysis.
Hadi et al. [29]	L9	Binder (Binder content); AAS (Na_2SiO_3/NaOH, AAS/B, Molarity)	Strength (compressive strength at 7 and 28 days)
Dave and Bhogayata [30]	L9	Binder (Binder content); AAS (Na_2SiO_3/NaOH ratio, dosage of superplasticizer, NaOH Molarity)	Strength (compressive and tensile strength at 7 days)
Nasir et al. [31]	L16	Binder (GGBS replacement ratio, and Sand/B ratio) AAS (AAS/B, Na_2SiO_3/NaOH, NaOH Molarity)	Strength (compressive strength at 3, 7 and 28 days)
Kanagaraj et al. [32]	L18	Binder (GGBS replacement ratio) AAS (Na_2SiO_3/NaOH, NaOH Molarity)	Strength (compressive strength at 28 days)
Onoue and Bier [33]	L18	Binder (GGBS replacement ratio); AAS (Molarity of NaOH, and Na_2SiO_3/NaOH); Mixing regime and time; Curing temperature; and Cumulative temperature)	Strength (compressive and flexural strengths at 1, 7, 28, 56, 91 days); Durability (sulfuric acid resistance)
Kan et al. [34]	L9	Binder (Metakaolin/B ratio); Curing condition; and Fibre ratio	Strength (compressive strength at 3, 7 and 28 days, tensile and flexural strengths at 7 and 28 days)

Chokkalingam et al. [35]	L18	Binder (Binder content, and GGBS replacement ratio); AAS (AAS/B, Na_2SiO_3/NaOH, NaOH Molarity)	Strength (compressive strength at 1, 7 and 28 days); Durability (water absorption, abrasion test, mass losses, and sorptivity)
Olivia and Nikraz [36]	L9	Binder (AAS/B); AAS (Na_2SiO_3/NaOH); Curing condition (heat curing)	Strength (compressive strength at 1, 7 and 28 days); Durability (mass loss, sorptivity, and absorption ratio)
Panagiotopoulou et al. [37]	L16	AAS (alkali/Al ratio, alkali species, and silicon content in the AAS)	Strength (compressive strength at 7 days)
Mohebi et al. [39]	L9	AAS (Na_2SiO_3/NaOH, AAS/B, and NaOH molarity); Curing condition	Strength (compressive strength at 28 days); Durability (abrasion test, and mass loss)

In this study, it is proposed to employ the Taguchi method for the development of a durable and environmentally sustainable fibre-reinforced geopolymer composite (FRGC). By employing the Taguchi method, the current study seeks to identify the optimal mix design for FRGC by focusing specifically on the key parameters such as water/binder (W/B) ratio, silica carbide to binder ratio (SiC/B), superplasticizer to binder ratio (SP/B) and fibre volume percentages (fibre%). These parameters are selected based on their potential impact on the mechanical and durability properties of the composite which will provide a comprehensive understanding of the performance of the mix design mechanism. The analysis will be conducted using the signal-to-noise ratio (S/N) to statistically determine the most effective combination of parameters for optimizing both the strength and durability characteristics of the geopolymer concrete. The successful optimization of FRGC mix design through this systematic approach will significantly contribute to the development of sustainable construction materials and eco-friendly building solutions.

2 Experimental setup

2.1 Materials used

In this study, the primary binding materials utilized to create the geopolymer mortar included GGBS, Silica Fume (SF), and (SiC) and it is shown in Table 2. The fine aggregate consisted of quartz sand that is characterized by its high silica content, a shape ranging from sub-angular to round and a variety of diameters between 0.075 mm and 1.18 mm. The Alkaline Activator Material (AAM) solution is composed of potassium hydroxide (PH) with a molarity of 13.95 and potassium silicate (PS), which has a Silicate Modulus (Ms) of SiO2/K2O = 1.5. Demineralized water was added to the mix along with a high-range water reducer (polycarboxylate superplasticizer (SP)) of the ViscoCrete-10 type from Sika, Australia which contains 41.7% solid content by mass. The mixtures incorporated two types of steel fibres namely, straight fibres with a diameter of 0.2 mm and length of 13 mm (0.2D) and hooked-end fibres with a diameter of 0.55 mm and length of 35 mm (0.55D). The tensile strengths of the 0.2D fibres and 0.55D fibres are 2850 MPa and 1350 MPa respectively.

Table 2 Chemical composition of the dry materials

	SiO_2	TiO_2	Al_2O_3	Fe_2O_3	MgO	CaO	Na_2O	K_2O	P_2O_5	SO_3
GGBS	35.10	0.57	13.59	0.98	5.36	41.52	0.14	0.33	0.04	0.10
SiC	96.03	0.02	0.25	0.83	0.31	0.02	0.04	0.29	0.03	0.06
SF	92.35	0.01	0.36	0.78	0.36	0.54	0.19	0.52	0.31	0.04
Quartz sand	93.48	0.04	0.06	0.06	0.03	0.02	0.039	0.02	0.01	0.01

2.2 Details of mix design based on the Taguchi method:

To develop the Taguchi analysis in this study, L9 orthogonal array (OA) was utilised which features four primary parameters (W/B, fibre content (fibre%), SiC/B and SP/B); with each of these parameters having three levels as detailed in Table 3 and Table 4 and the full mix design details summarised in Table 5.

The optimum results were predicted by using the S/N ratio. For the compressive strength, tensile strength and flexural strength higher results are required; therefore, the larger is better equation of the S/N ratio will be applied to find the optimum parameters as shown in Eq. (1). Furthermore, smaller is better S/N ratio was used for water absorption (WA) and apparent volume of permeable voids (AVPV) as shown in Eq. (2). Thus, the analysis of the results was conducted by identifying the factor that most significantly influenced the output within the array by using the statistical tool Analysis of Variance (ANOVA) which quantifies the contribution of each parameter in terms of a percentage, this is achieved by calculating the sum of squares for each parameter relative to the total sum of squares, thereby providing a predictive measure of each parameter's impact on the overall outcome.

Table 3 L9 Orthogonal array

Trial	A	B	C	D
M1	1	1	1	1
M2	1	2	2	2
M3	1	3	3	3
M4	2	1	2	3
M5	2	2	3	1
M6	2	3	1	2
M7	3	1	3	2
M8	3	2	1	3
M9	3	3	2	1

Table 4 Factors and levels used in Taguchi experiment design.

Factor	Level 1	Level 2	Level 3
A-W/B	0.30	0.29	0.28
B-Fibre%*	2	2.5	3
C-SiC/B	0	0.1	0.2
D-SP/B	0.02	0.025	0.03

* Volume fraction

Table 5 Mix proportions

Mix	Binder			Fine Agg. kg/ m^3	AAS/ B	PS/PH	W/B ratio	SP kg/ m^3	Fibre%	
	GGBS kg/m^3	SF kg/m^3	SiC kg/m^3						0.55D	0.2D
M1	590	194	0	1098	0.38	3	0.3	0.02	0.133	0.067
M2	510	194	80	1098	0.38	3	0.3	0.025	0.167	0.083
M3	430	194	160	1098	0.38	3	0.3	0.03	0.200	0.100
M4	510	194	80	1098	0.38	3	0.29	0.03	0.133	0.067
M5	430	194	160	1098	0.38	3	0.29	0.02	0.167	0.083
M6	590	194	0	1098	0.38	3	0.29	0.025	0.200	0.100
M7	430	194	160	1098	0.38	3	0.28	0.025	0.133	0.067

M8	590	194	0	1098	0.38	3	0.28	0.03	0.167	0.083
M9	510	194	80	1098	0.38	3	0.28	0.02	0.200	0.100

$$S/N = -10 \log \frac{1}{n} \sum_{n}^{1} \frac{1}{y_i^2} \quad (1)$$

$$S/N = -10 \log \frac{1}{n} \sum_{n}^{1} y_i^2 \quad (2)$$

where n is the number of experiments, y_i is the mean response output (such as the compressive strength results).

2.3 Mixing procedures, curing and testings

2.3.1 Mix procedures

The mixing process is illustrated in Fig. 1 and it is commenced by mixing GGBS, SF, SiC and fine aggregate for two minutes to achieve a uniform mixture then 90% of the demineralized water and SP were added and mixed thoroughly for a further ten minutes. The fibres were then introduced to the mixture and mixed for an additional two minutes to ensure even distribution. In the final step, the AAM mixed with the remaining 10% of the demineralized water was added to the mixture for two more minutes of mixing. The purpose of adding the AAM at the final step is to avoid any flash setting that could happen with a prolonged time of mixing. This detailed sequence of steps ensured a consistent and well-blended mix optimized for its intended application. The mortar was thoroughly mixed and immediately poured into the clear and oiled moulds for curing and testing. Note that, the mortar was poured into the mould in three layers; each layer was compacted 25 times by a steel rod.

2.3.2 Curing

The curing process for all samples was standardized to ambient room-temperature conditions except for the specimens used for compressive strength testing at 28 days. Three specimens were taken from each mix were immersed in a hot water tank for 24 hours under 100 ºC.

Subsequently, these specimens were stored with other specimens under ambient conditions for 27 days as shown in Fig. 2.

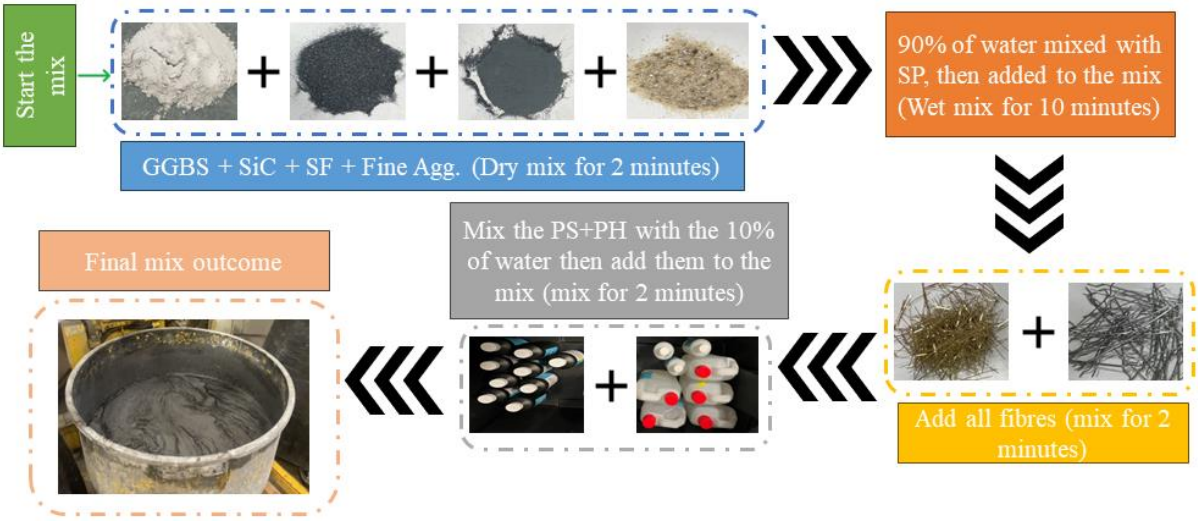


Fig. 1 Mixture procedure



a) b)

Fig. 2 a) room temperature curing condition; b) specimens immersed in hot water tank.

2.3.3 Tests for mechanical properties

The compressive strength of the cylindrical specimens (200 mm high x 100 mm diameter) was assessed in accordance with AS 1012.9 [40]. These evaluations were conducted at two intervals: 7 and 28 days post-curing for specimens cured at room temperature, and only at 28 days for those specimens subjected to hot water curing. A universal testing machine with a capacity of 3000 kN facilitated these tests. The same machine was also employed to evaluate

the splitting tensile strength as outlined by AS 1012.10 [41] and determine the flexural strength in alignment with AS 1012.11 [42]. The values for the mechanical properties were obtained by taking the average of three test results.

2.3.4 Tests for water absorption

The water absorption rate was estimated according to the method prescribed by ASTM 642-21 [43]. Three-disc specimens were cut from a cylindrical specimen having a thickness of 50 mm and a diameter of 100 mm. These discs were then dried in the oven for 24 hours at 110 ºC to attain a constant mass and they subsequently were immersed in water for four days to obtain the saturated weight. Following the evaluation of the water absorption rate, the specimens were used to evaluate the apparent volume of permeable voids (AVPV). The bulk density of the discs was evaluated before and after immersing the specimens in boiling water for 5 hours.

2.3.5 Sorptivity tests

Sorptivity was evaluated according to ASTM 1585-20 [44], and the test setup is shown in Fig. 3. It assists in quantifying the durability of the concrete by measuring the amount of absorbed water in a period of up to 8 days to calculate the quantify of cumulative water absorption. Three-disc specimens were cut from cylindrical specimens having a thickness of 50 mm and a diameter of 100 mm. These specimens were then put in the oven for three days at 50 ºC to achieve a constant mass; they were then placed in a container for 15 days at a room temperature of (25 ± 2) ºC. Note that, to ensure that the water absorption occurs only from the base, the peripheral surfaces of the discs were sealed with waterproofing tape. The water absorption process commenced 30 seconds after immersing in a water level of 3 mm, with measurements taken continuously for the first hour at intervals of five minutes for the first ten minutes then every ten minutes up to one hour then every hour up to eight hours and finally every day up to eight days.

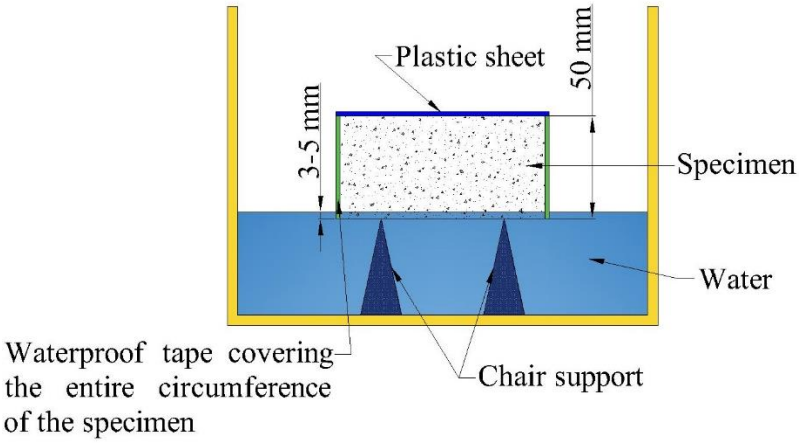


Fig. 3 Schematic representation of sorptivity test [44]

3 Results and discussion:

3.1 Compressive strength

The Taguchi method was used to construct mix designs which were then assessed through compressive strength tests at two intervals: 7 and 28 days under ambient curing and 28 days under hot water curing. Fig. 4 presents the outcomes of all compressive strength test results. The highest compressive strength was achieved for all the mixes subjected to hot water curing conditions at 28 days. Notably, the hot curing process has improved the compressive strength outcomes primarily due to the enhancement of the matrix compactness and higher reactivity ratio leading to the accelerated form of the calcium silicate hydrated (CSH) gel [45].

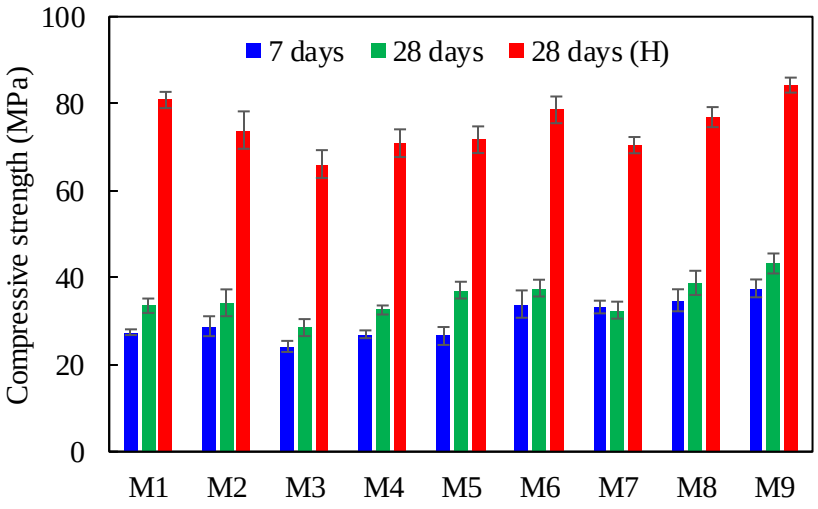


Fig. 4 Compressive strength for the 7-,28- and 28(H)-day.

Table 6 presents the analysis of the S/N ratio for the 7-day compressive strength where Delta is the calculated value of the highest variation among each parameter's values and the four major parameters were then ranked in descending order based on the Delta value. Based on the rankings, the W/B ratio has the most significant impact on the 7-day compressive strength. The presence of water during the chemical reaction of aluminosilicate materials affects the concentration of the AAS which could hinder the geopolymerization process. This suggests that macro pores form within the microstructure of the mortar matrix due to the presence of water as indicated by the tests conducted by Park and Pour-Ghaz [46]. Additionally, the SiC/B ratio is identified as the second most influential parameter on the 7-day compressive strength. This is attributed to the ability of SiC to reinforce the geopolymer matrix [47], Which leads to the increase pf the strength.

Table 6 S/N ratio for 7-day compressive strength

Level	**W/B**	**Fibre%**	**SiC/B**	**SP/B**
1	30.95	29.21	30.05	29.62
2	29.29	29.59	29.82	30.08
3	28.49	29.94	28.87	29.04
Delta	2.46	0.73	1.18	1.04
Rank	1	4	2	3

Fig. 5 illustrates the impact of each parameter on the 7-day compressive strength based on the analysis of mean responses. These responses were derived from the average results obtained for each parameter. For example, the mean value of the 7-day compressive strength of the W/B parameter at a level of 0.28 has been extracted from three different mixes (M7, M8 and M9). Note that, the W/B level increase from 0.28 to 0.3 results in a 25% decrease in compressive strength. On the other hand, increasing the fibre% from 2% to 3% in increments of 0.5 shows a consistent trend of approximately 5% strength increase from one level to the next. The SiC/B parameter demonstrates optimal results at a 0 level beyond which a decreasing trend is observed. Hence, the excessive amount of Si content seems to negatively affect the compressive strength at ambient curing conditions. Conversely, the SP/B parameter shows that

increasing the level from 0.02 to 0.025 boosts the 7-day compressive strength, but further increases lead to a decline in results. Thus, it is concluded that the optimum levels for maximizing the 7-day compressive strength are 0.28 for W/B, 3% for fibre%, 0 for SiC/B, and 0.025 for SP/B.

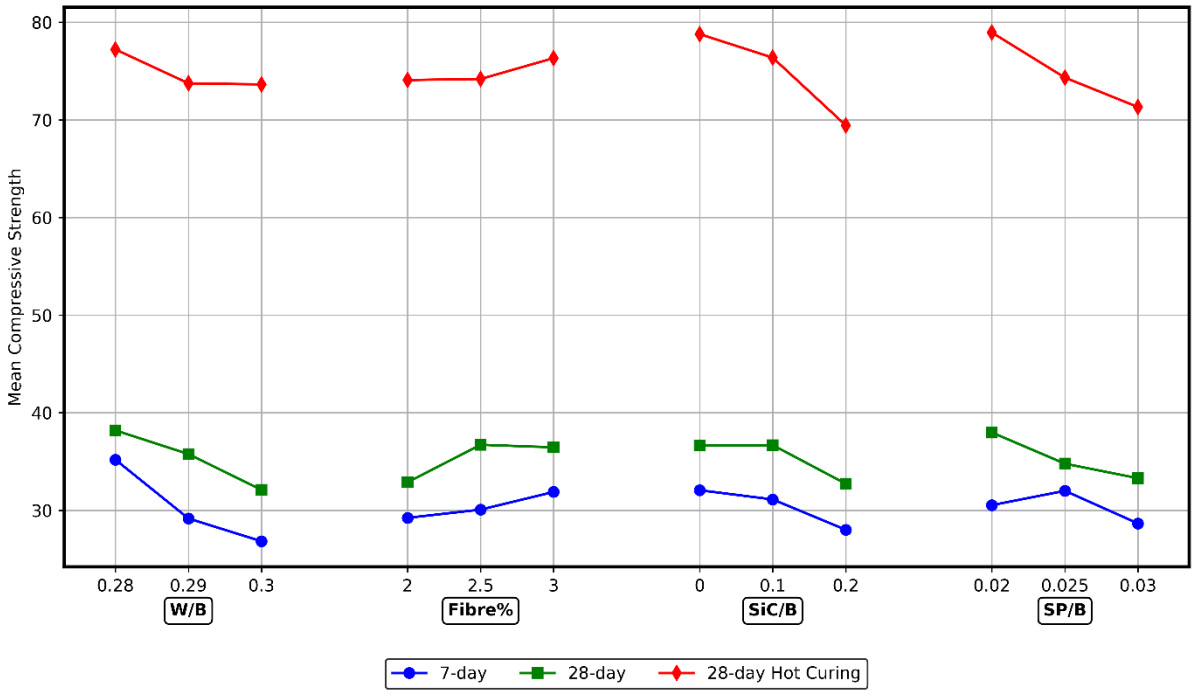


Fig. 5 Mean responses for 7-,28- and 28(H)-day compressive strength

The S/N ratio results for the 28-day compressive strength are presented in Table 7 and it indicates that the W/B ratio has the most significant influence on the 28-day outcomes similar to the 7-day compressive strength. However, the SP/B ratio now exhibits nearly the same impact on the 28-day compressive strength as the SiC/B ratio. The fibre% has the least effect on the 28-day results. Thus, the progression of the 28-day compressive strength generally follows the trend observed in the 7-day results with a minor adjustment in the influence between the SiC/B and SP/B parameters.

Table 7 S/N ratio for 28-day compressive strength

Level	W/B	Fibre %	SiC/B	SP/B
1	31.62	30.46	31.35	31.55
2	31.11	31.27	31.22	30.87
3	30.17	31.17	30.33	30.48
Delta	1.45	0.81	1.02	1.07
Rank	1	4	3	2

Fig. 5 displays the trend of each parameter based on the mean responses of 28-day compressive strength results where the W/B ratio at a level of 0.28 showcases the highest average value of 32.5 MPa whilst at 0.3 level, there is a corresponding reduction of 16% in the 28-day compressive strength. Note that, the corresponding reduction in the 7-day compressive strength value for W/B = 0.3 was 25% indicating the continuation of the geopolymerization process. Regarding the fibre% parameter, the lowest compressive strength is observed at the 2% level whilst a 10% increase is noted for a fibre% of 2.5% and there is no further increase in the 28-day compressive strength value when the fibre% was increased to 3%. The marginal impact of fibre% is attributed to utilising hybridisation of the fibre% (33% of short fibre and 67% of end-hooked fibre) for enhancing both tensile and flexural strengths. Furthermore, the SiC/B parameter achieves the maximum 28-day compressive strength at the zero level showing a downward trend similar to the 7-day compressive strength indicating that zero is the optimum level of SiC/B, which means increasing the content of Si content in the GGBS-based GPC could have a negative impact. Finally, the SP/B parameter exhibits a downward trend starting from the 0.02 level which presents the highest compressive strength results at 28 days. Thus, the optimum level for the SP/B parameter is 0.02 for 28-day compressive strength confirming that a lower liquid ratio benefits the GPC mix design by increasing its strength. Therefore, the optimum levels for achieving the highest compressive strength are W/B = 0.28, fibre% = 2.5%, SiC/B = zero and SP/B = 0.02.

Table 8 displays the S/N ratio for the 28-day compressive strength under hot water curing conditions. The SiC/B ratio emerges as the most significant parameter primarily due to its contribution to increasing the silicon content in the mix which in combination with the associated high temperature leads to an increase in compressive strength [48]. Amongst the remaining parameters, SP/B has a significant effect whilst W/B and fibre% have the least impact on the compressive strength of hot water cured.

Table 8 S/N ratio for 28-day compressive strength (H)

Level	W/B	Fibre %	SiC/B	SP/B
1	37.71	37.37	37.95	37.93
2	37.37	37.42	37.63	37.41
3	37.32	37.61	36.81	37.05
Delta	0.39	0.24	1.14	0.89
Rank	3	4	1	2

Fig. 5 illustrates the effectiveness of each parameter on the hot water cured 28-day compressive strength. The W/B parameter shows little variation as does the fibre%. A significant drop in compressive strength with increasing SiC/B level is noted. Therefore, Zhuang et al [48] have mentioned that increasing Si content with associated high temperature enhances compressive strength. Hence, the addition of SiC/B has reduced the highest compressive strength due to the excessive amount of Si content in the mix, also a massive decrease has ensured there is an optimum level of Si content in the mix. For the SP/B, the optimum level to achieve the highest compressive strength is 0.02. To conclude, the optimum level for each parameter is 0.28 for W/B, 3% for fibre%, 0 for SiC/B, and 0.02 for SP/B.

3.2 Flexural and splitting tensile strength

Flexural strength results for the FRGC are presented in Fig. 6. Flexural strength is a critical mechanical characteristic that ensures the matrix can resist the formation of cracks and with the introduction of steel fibre, the crack can be bridged. In this study, the maximum value of flexural strength was 13 MPa which was obtained from the mixes that have a fibre% of 2.5% and 3%. The minimum value obtained was 8 MPa for mix M2 having a fibre% of 2.5%. Note that whilst M2 and M8 have the same fibre%, M8 yield 60% flexural strength higher than M2 therefore, the increase can be attributed to the higher W/B of M2. It can be deduced that the fibre is not the only parameter that enhances the flexural strength, its benefit is more pronounced in bridging the cracks in the tension area of the composite [49].

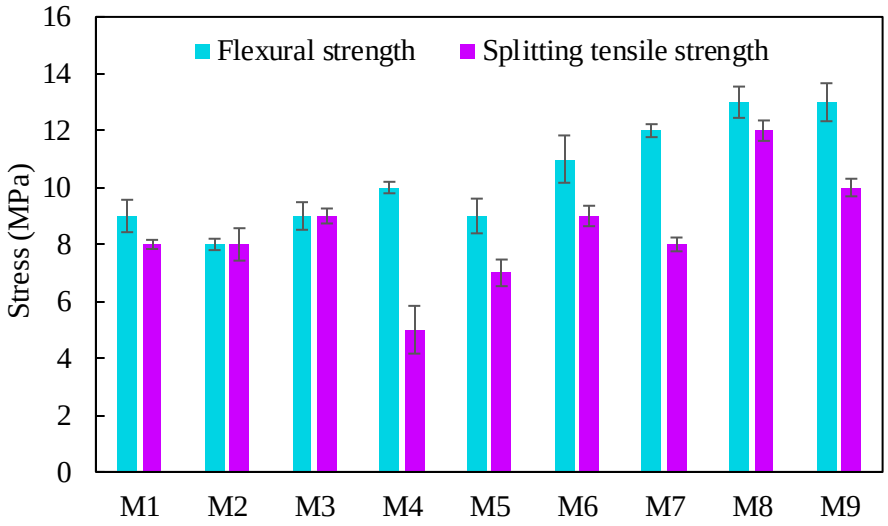


Fig. 6 Flexural and splitting tensile strength

Table 9 illustrates the S/N ratio results and the parameter rankings affecting the flexural strength. The W/B ratio has the most significant impact on this property mainly due to water release leading to voids in the FRGC matrix which weakens its structure. This is similar to the study by Wang et al. [50] which found that an increase of W/B ratio correlates with a reduction in GPC strength. Additionally, the fibre% emerges as the second most influential parameter on flexural strength followed by the SiC/B and SP/B ratios.

Table 9 S/N ratio for Flexural strength

Level	W/B	Fibre%	SiC/B	SP/B
1	22.05	20.22	20.73	20.15
2	19.97	19.81	20.11	20.16
3	18.74	20.73	19.92	20.45
Delta	3.3	0.92	0.81	0.31
Rank	1	2	3	4

Fig. 7 displays the mean responses of flexural strengths of different parameters and their associated levels. The W/B ratio emerges as a critical factor consistently achieving the highest flexural strength of 12.8 MPa at a level of 0.28 with a subsequent reduction of 31% to 8.8 MPa at a level of 0.3. This underscores the pronounced impact of water addition on the flexural strength. In contrast, the other parameters exhibit negligible variation between the mean flexural strength with an average low of 10 MPa and a high of 11 MPa. To conclude, the

optimal levels determined for maximizing flexural strength are a W/B ratio of 0.28, a fibre% of 3%, SiC at 0 and SP/B ratio of 0.03.

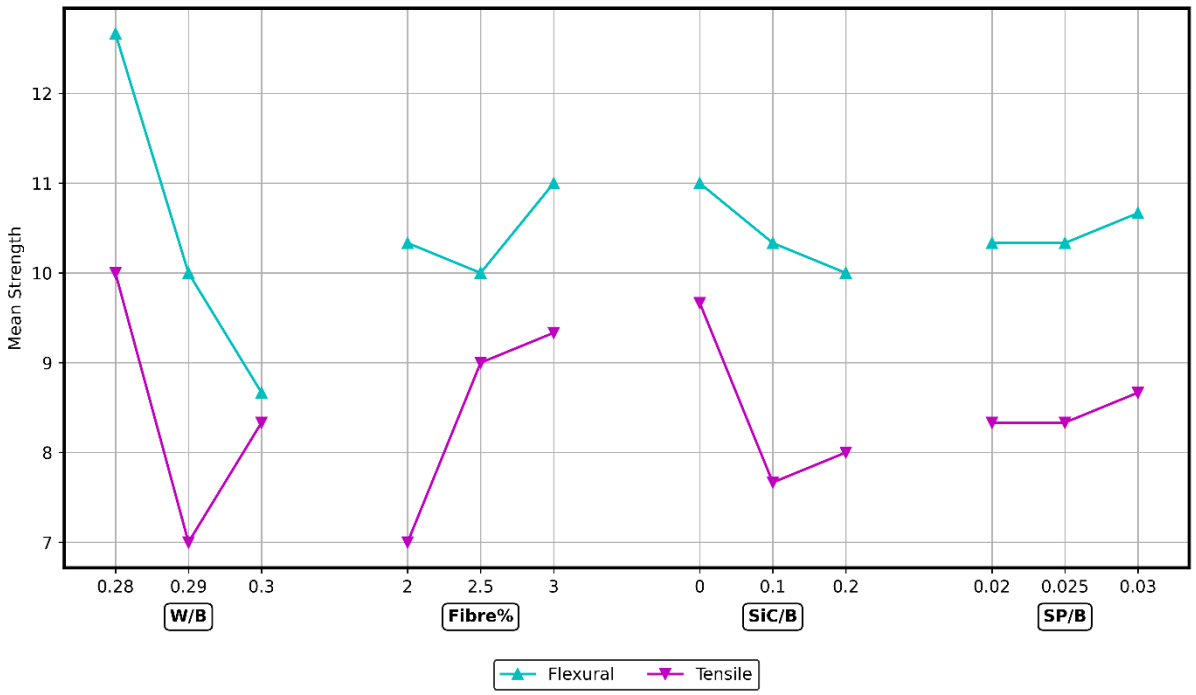


Fig. 7 Mean responses for flexural and tensile strength

Fig. 6 also displays the splitting tensile strength values for all the mixes, wherein mix M8 achieved the maximum value while mix M4 yielded the minimum value. This variation underscores the significant impact of the fibre% on the splitting tensile strength as the fibre% of M8 was 2.5% and for M2 was 2%.

Table 10 displays S/N ratio results and the parameter rankings affecting the splitting tensile strength where the W/B ratio is the most critical factor indicating that the geopolymerization process significantly influences the strength of FRGC. This suggests that excessive addition of water could detrimentally affect the strength of the material. Subsequently, fibre% ranks second in terms of influence followed by the SiC/B parameter.

Table 10 S/N ratio for splitting tensile strength

Level	W/B	Fibre%	SiC/B	SP/B
1	19.88	16.7	19.58	18.32
2	16.66	18.85	17.35	18.4
3	18.4	19.39	18.02	18.22

Delta	3.23	2.69	2.23	0.19
Rank	1	2	3	4

Fig. 7 illustrates the trend of mean responses for parameters and their levels impacting the splitting tensile strength. The highest average splitting tensile strength of 10 MPa was observed at the 0.28 W/B level. The values dropped upon increasing the W/B ratio resulting in the lowest strength of 7.5 MPa at the 0.29 level followed by a slight increase to 8.4 MPa at the 0.3 level. This pattern marks a variation from other strength outcomes where the 0.28 level of the W/B parameter consistently yielded the highest averages for both compressive and flexural strengths suggesting a unique optimal level for splitting tensile strength. Moreover, the fibre% parameter demonstrated a significant upward trend enhancing the splitting tensile strength from 7 MPa at a 2% level to 9 MPa at 2.5%, with further increases noted at a 3% level. This indicates that incorporating fibre into the FRGC notably strengthens the tension-bearing capacity of the matrix. Consequently, the optimal levels to maximize splitting tensile strength are identified as 0.28 for W/B, 3% for fibre%, 0 for SiC/B and 0.03 for SP/B.

3.3 Porosity and sorptivity

Durability is a major characteristic of geopolymer concrete, essential for its longevity and performance of absorbing liquids. This study quantifies the durability of FRGC via sorptivity and porosity indicators specifically examining the effective permeable porosity through WA and AVPV tests and the results obtained are shown in Fig. 8. The mix M7 that had a W/B of 0.28, fibre% of 2%, SiC/B of 0.2 and SP/B at 0.025 yielded the maximum value of WA equal to 7.73%. On the contrary, the mix M2 showed better absorption characteristics at 6.42% with a decrease of 17% and it had a W/B of 0.3, fibre% of 2.5%, SiC/B of 0.1 and SP/B of 0.025, also it possessed the minimum value of AVPV of 4.45% suggesting enhanced durability characteristics for this mix M2. These outcomes are a paradox to the strength properties outcomes where the lower the W/B the higher the strength obtained.

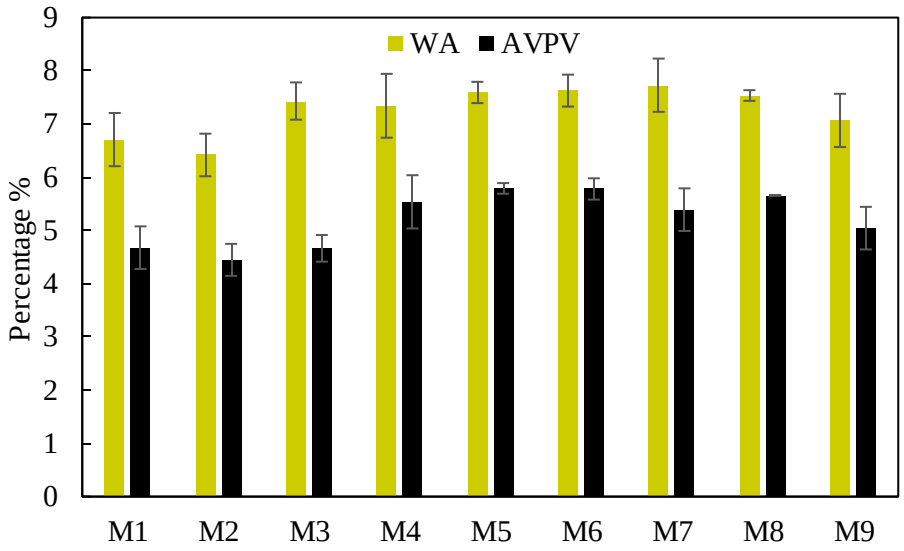


Fig. 8 The water absorption rate % (WA) and apparent volume for permeable voids % (AVPV)

Table 11 displays the S/N ratio results for WA along with the factor rankings impacting durability where the W/B ratio emerges as the paramount factor influencing durability suggesting that while water presence is crucial for the geopolymerization process, excessive water can lead to increased porosity by creating voids within the mortar matrix.

Table 11 S/N ratio for WA

Level	W/B	Fibre%	SiC/B	SP/B
1	-17.43	-17.20	-17.24	-17.04
2	-17.52	-17.10	-16.82	-17.19
3	-16.70	-17.35	-17.60	-17.43
Delta	0.82	0.25	0.78	0.38
Rank	1	4	2	3

Fig. 9 shows mean responses for parameters affecting WA in FRGC. Notably, the higher W/B ratio significantly affects WA with an optimal level of 0.3 whilst a lower W/B yielded the highest strength values. This contrasts with the findings by Wang et al. [50] and Guo et al. [51] that found lower W/B ratios lead to reduced WA values. This difference can be due to the addition of extra water aiding the geopolymerization process by filling voids and potentially enhancing durability although it does not necessarily improve the strength of the mix. Therefore, the optimal levels are determined to be W/B of 0.3, fibre% of 2.5, SiC/B of 0.1 and SP/B of 0.02, highlighting the balance between durability and structural integrity.

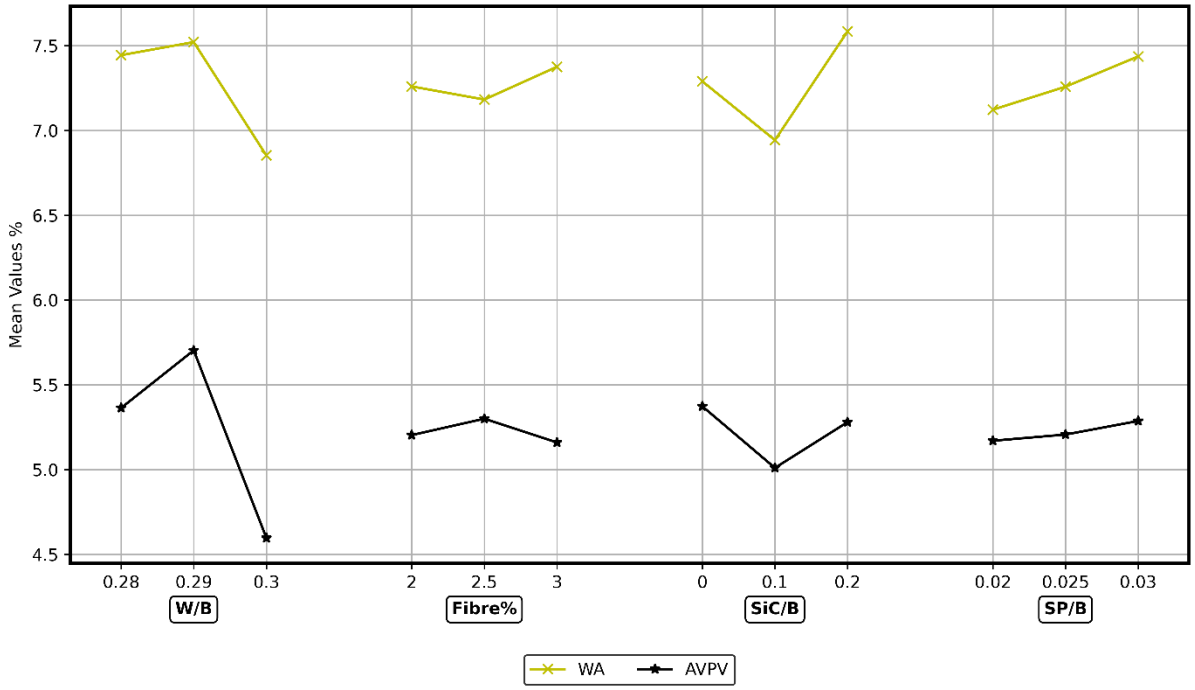


Fig. 9 Mean responses for the WA and AVPV

Table 12 shows the ranking of S/N ratio analysis of the parameters affecting the AVPV. The W/B was found to be the most influential parameter affecting the AVPV of FRGC. It is evident that the W/B play a crucial role in developing the GPC and the optimum level could significantly change the mechanism of the geopolymerization.

Table 12 S/N ratio for AVPV

Level	W/B	Fibre%	SiC/B	SP/B
1	-14.58	-14.30	-14.57	-14.24
2	-15.12	-14.43	-13.96	-14.28
3	-13.25	-14.22	-14.42	-14.43
Delta	1.87	0.21	0.60	0.2
Rank	1	3	2	4

Fig. 9 illustrates the optimum levels for each parameter which is similar to the trends observed in WA where the lowest percentage of voids was observed at the 0.3 level of the W/B parameter. This underscores that water presence not only sustains the geopolymerization process but also helps fill the voids. Hence, water acts as a catalyst in the geopolymerization reaction facilitating the dissolution of aluminosilicate precursors and the subsequent reorganization into a dense geopolymer matrix and this process is essential for developing the

internal structure of the geopolymer matrix. Thus, the optimum parameter levels are identified as 0.3 for W/B, 2.5% for fibre%, 0.1 for SiC/B and 0.02 for SP/B.

Fig. 10 Fig. 10 illustrates the water absorption rates for the mixes after 28 days of ambient curing, shedding light on the mechanisms of water transport within the matrix. Analysing these rates provides crucial insights into porosity and permeability, which are vital for assessing the durability and sustainability of the composite matrix. Notably, the water transport within the matrix decreases with a reduced W/B ratio, as evidenced by mixes M7, M8, and M9 that exhibited the lowest cumulative water absorption. This reduction in water uptake after a time-lapse of 100 minutes indicates the impact of lower W/B ratios on capillary action, effectively restricting water ingress. Consequently, the mixes with lower W/B ratios demonstrate enhanced durability and sustainability by limiting water access, thereby showcasing their superior performance in terms of durability and structural integrity.

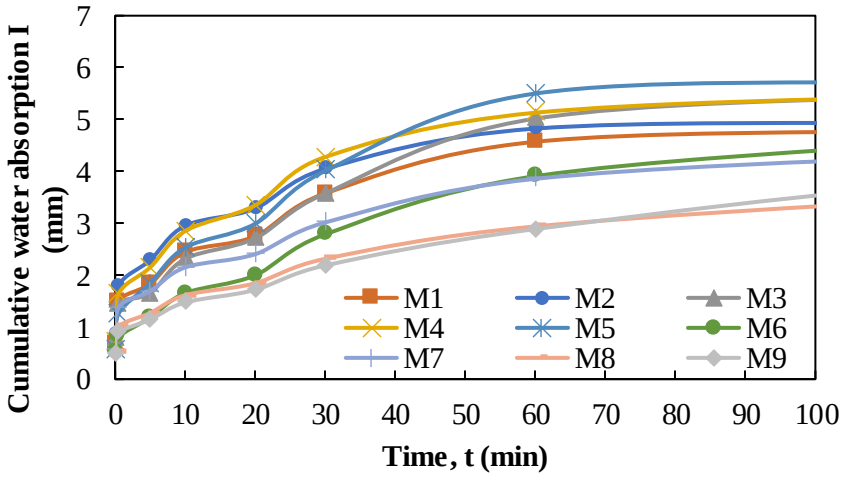


Fig. 10 Cumulative water absorption rate per time for all mixes

3.4 ANOVA for mechanical properties and durability

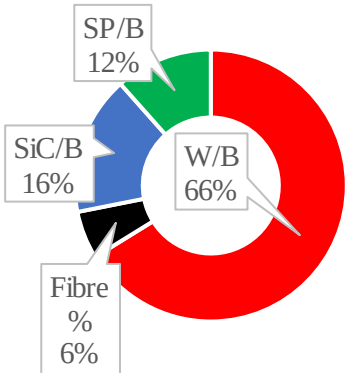
ANOVA obtains the contribution of the process parameters on the output characteristics. Table 13 shows the ANOVA analysis performed on the output characteristics and Fig. 11 presents the contribution of each parameter on the output characteristics. According to the results of ANOVA, the W/B parameter has the most significant influence on the 7-day compressive

strength at 66%, 28-day compressive strength at 40%, flexural strength at 87%, splitting tensile strength at 44%, WA at 50%, and AVPV at 89%. However, the SiC/B parameter significantly affects the 28-day compressive strength of hot-cured specimens with a contribution of 57%. Moreover, the SiC/B parameter has a significant quantum of influence after the W/B parameter for 28-day compressive strength and WA. Furthermore, the fibre% has been noted to affect the splitting tensile strength output. It can be briefly said that the W/B parameter has a dominant effect on the FRGC's output mechanical and durability characteristics.

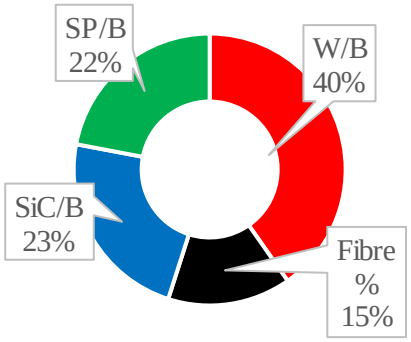
Table 13 ANOVA for all outputs

	Parameter	Degree of freedom	Sum of squares	% contribution
7-day compressive strength	W/B	2	9.41	66.18
	Fibre %	2	0.81	5.70
	SiC/B	2	2.35	16.55
	SP/B	2	1.64	11.56
	Total	8	14.22	100.00
28-day compressive strength	W/B	2	3.25	40.27
	Fibre %	2	1.18	14.67
	SiC/B	2	1.86	23.05
	SP/B	2	1.78	22.02
	Total	8	8.08	100.00
28-day compressive strength (hot curing)	W/B	2	0.27	7.35
	Fibre %	2	0.10	2.72
	SiC/B	2	2.07	57.10
	SP/B	2	1.19	32.84
	Total	8	3.62	100.00
Flexural strength	W/B	2	16.73	86.82
	Fibre %	2	1.28	6.64
	SiC/B	2	1.08	5.60
	SP/B	2	0.18	0.94
	Total	8	19.27	100.00
Splitting tensile strength	W/B	2	15.65	43.85
	Fibre %	2	12.14	34.00
	SiC/B	2	7.85	22.00
	SP/B	2	0.05	0.15
	Total	8	35.69	100.00
WA	W/B	2	1.22	49.67
	Fibre %	2	0.10	3.92

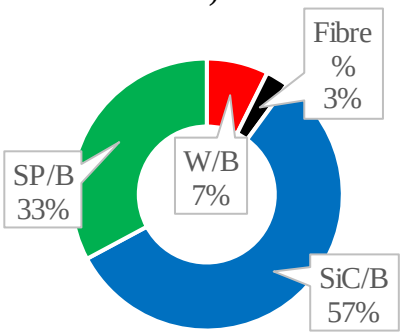
	SiC/B	2	0.91	37.18
	SP/B	2	0.23	9.22
	Total	8	2.45	100.00
AVAV	W/B	2	5.58	88.52
	Fibre %	2	0.07	1.04
	SiC/B	2	0.60	9.44
	SP/B	2	0.06	1.01
	Total	8	6.31	100.00



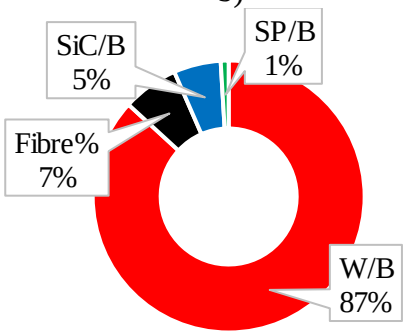
a)



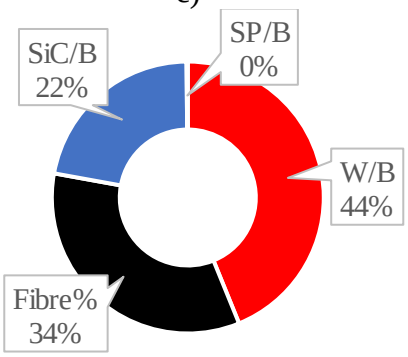
b)



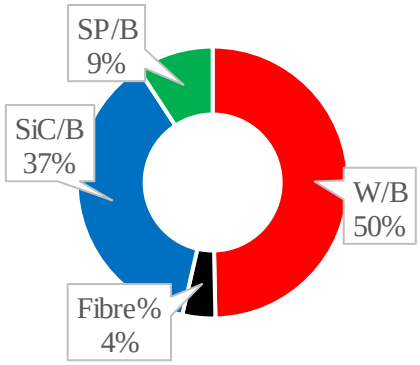
c)



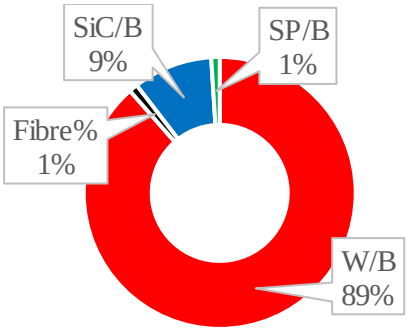
d)



e)



f)



g)

Fig. 11 Contribution of the parameters on each output a) 7-day compressive strength; b) 28-day compressive strength; c) 28-day compressive strength (hot curing); d) Flexural strength; e) Splitting tensile strength; f) Water absorption; and g) Apparent volume for permeable voids

4 Mathematical modelling for compressive strength

For developing a mathematical model for estimating the compressive strength of FRGC, the integration of residual fitting of the compressive strength results and previous ANOVA will be utilised. This methodology enables to precisely quantify the influence of different process parameters on compressive strength, ensuring a high degree of model accuracy and reliability. The careful examination of residuals played a crucial role in this process that assists in identifying any variances between the observed values and those predicted by the current model with the residual fitting for compressive strength shown in Fig. 12. However, ANOVA analysis was instrumental in evaluating the statistical significance of each parameter showing their individual and combined effects on compressive strength. A notable outcome of this analytical endeavour was the determination R-squared (R^2) value of the model which indicates how well the input variables explain the variation in compressive strength affirming the effectiveness of the model in predicting material performance under varied conditions. The R^2 value ranging between zero and one signifies that a value closer to one indicates a better fit between the independent and dependent variables. The predictive equations for the compressive strength

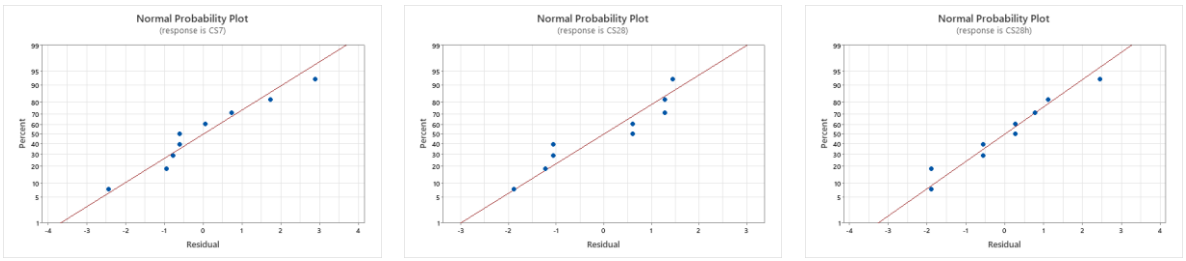
at different intervals and curing methods are illustrated in Eqs (3), (4), and (5) 7-,28- and 28(H)-day compressive strength respectively.

$$f'_{c,7-day} = 155.6 - 433.3\ W/B + 3\ Fibre\% - 20\ SiC/B - 200\ SP/B \quad (R^2 = 88.62\%) \tag{3}$$

$$f'_{c,28-day} = 127.1 - 300\ W/B + 3.33\ Fibre\% - 20\ SiC/B - 433\ SP/B \quad (R^2 = 90.17\%) \tag{4}$$

$$f'_{c,28-day\ (hot-cured)} = 141.4 - 166.7\ W/B + 2.33\ Fibre\% - 48.33\ SiC/B - 767\ SP/B \quad (R^2 = 94.15\%) \tag{5}$$

The developed regression models for the outputs have high R^2 values: 88.62% for 7-day compressive strength, 90.17% for 28-day compressive strength and 94.17% for 28-day compressive strength under hot curing. Moreover in Fig. 12 the linearity of the residual plots is also utilised for verifying the significance of the coefficients in the model. The linearity of the 28-day compressive strength with a hot curing plot can be observed more clearly in Fig. 12(c).



a) b) c)

Fig. 12 The residual plot for the a) 7-day compressive strength; b) 28-day compressive strength; and c) 28-day compressive strength (hot curing)

5 Conclusion

This study explores the impact of four parameters namely W/B, fibre%, SiC/B and SP/B on the performance of FRGC. The Taguchi method was employed to assess the mechanical and durability characteristics of the developed mixes. Each parameter was examined across three different levels using an L9 OA for the experimental setup. This methodical approach allowed for a detailed analysis of the influence of every parameter on the properties of FRGC, leading

to the identification of optimal mix compositions for improved performance. The following conclusions are made based on the obtained results:

- The Taguchi method can be widely used to minimize the number of experiments, specifically for the design of GPC mix which has many variables.
- The W/B ratio was found to be the most effective parameter impacting the mechanical and durability characteristics. For the mechanical properties, the lower W/B ratio mixes exhibited higher strengths. However, the higher W/B ratio has the lowest WA and AVPV values which in turn indicates better results. Therefore, finding a break-even point for the W/B ratio is necessary for optimizing the best mix.
- SiC/B parameter has the most significant impact on the 28-day compressive strength under hot water curing conditions as it boosted the geopolymerization which has enabled it to approximately double the results of the 28-day compressive strength of the ambient curing conditions for all mixes.
- The fibre% has been found more effective in enhancing the splitting tensile strength with an optimum level of 2.5%.
- ANOVA analysis has confirmed the predominant contribution of W/B for all the mixes. Furthermore, the contribution of every parameter on every output has been found in detail.
- A mathematical method for the compressive strength results was developed based on ANOVA analysis and the residual fitting with a coefficient of determination around 90%.

Acknowledgement

The authors would like to acknowledge the financial support from the Australian Research Council (DP 21001425) for undertaking this research. The authors also thank Longhui Li, Chenchen Fan, Di Wu and Shanshan Feng who assisted in the lab work.

References

[1] E. Benhelal, G. Zahedi, E. Shamsaei, A. Bahadori, Global strategies and potentials to curb CO2 emissions in cement industry, J Clean Prod 51 (2013) 142–161.
[2] The world Bank, Trends in Solid Waste Management, (2018). https://datatopics.worldbank.org/what-a-waste/trends_in_solid_waste_management.html.
[3] R. Rithuparna, V. Jittin, A. Bahurudeen, Influence of different processing methods on the recycling potential of agro-waste ashes for sustainable cement production: A review, J Clean Prod 316 (2021) 128242.
[4] A. Danish, T. Ozbakkaloglu, M.A. Mosaberpanah, M.U. Salim, M. Bayram, J.H. Yeon, K. Jafar, Sustainability benefits and commercialization challenges and strategies of geopolymer concrete: A review, Journal of Building Engineering 58 (2022) 105005.
[5] S.E.A. Sawan, M.F. Zawrah, R.M. Khattab, A.A. Abdel-Shafi, In-situ formation of geopolymer foams through addition of silica fume: Preparation and sinterability, Mater Chem Phys 239 (2020) 121998.
[6] M.F. Zawrah, H.A. Badr, R.M. Khattab, H.E.H. Sadek, S.E.A. Sawan, A.A. El-Kheshen, Fabrication and characterization of non-foamed and foamed geopolymers from industrial waste clays, Ceram Int 47 (2021) 29320–29327.
[7] J. Davidovits, Geopolymers: inorganic polymeric new materials, J Therm Anal Calorim 37 (1991) 1633–1656.
[8] P. Duxson, A. Fernández-Jiménez, J.L. Provis, G.C. Lukey, A. Palomo, J.S.J. van Deventer, Geopolymer technology: the current state of the art, J Mater Sci 42 (2007) 2917–2933.
[9] K.A. Komnitsas, Potential of geopolymer technology towards green buildings and sustainable cities, Procedia Eng 21 (2011) 1023–1032.
[10] C. Zhang, H. Khorshidi, E. Najafi, M. Ghasemi, Fresh, mechanical and microstructural properties of alkali-activated composites incorporating nanomaterials: A comprehensive review, J Clean Prod 384 (2023) 135390.
[11] A. Hassan, M. Arif, M. Shariq, Use of geopolymer concrete for a cleaner and sustainable environment–A review of mechanical properties and microstructure, J Clean Prod 223 (2019) 704–728.
[12] M. Lahoti, K.H. Tan, E.-H. Yang, A critical review of geopolymer properties for structural fire-resistance applications, Constr Build Mater 221 (2019) 514–526.
[13] M. Alhawat, A. Ashour, G. Yildirim, A. Aldemir, M. Sahmaran, Properties of geopolymers sourced from construction and demolition waste: A review, Journal of Building Engineering 50 (2022) 104104.
[14] M.S.T. Masoule, N. Bahrami, M. Karimzadeh, B. Mohasanati, P. Shoaei, F. Ameri, T. Ozbakkaloglu, Lightweight geopolymer concrete: A critical review on the feasibility, mixture design, durability properties, and microstructure, Ceram Int 48 (2022) 10347–10371.
[15] N. Asim, M. Badiei, N.A. Samsudin, M. Mohammad, H. Razali, D. Hui, Clean technology option development for smart and multifunctional construction materials: sustainable geopolymer composites, Journal of Building Engineering (2024) 109932.
[16] A. Saptamongkol, V. Sata, A. Wongsa, W. Kroehong, J. Ekprasert, P. Chindaprasirt, Hybrid geopolymer paste from high calcium fly ash and glass wool:

Mechanical, microstructure, and sulfuric acid and magnesium sulfate resistance characteristics, Journal of Building Engineering 76 (2023) 107245. https://doi.org/https://doi.org/10.1016/j.jobe.2023.107245.
[17] X. Ji, Z. Wang, H. Zhang, X. Wang, J. Huo, T. Zhang, Optimization design and characterization of slag cementitious composites containing carbide slag and desulfurized gypsum based on response surface methodology, Journal of Building Engineering 77 (2023) 107441. https://doi.org/https://doi.org/10.1016/j.jobe.2023.107441.
[18] A. Rafeet, R. Vinai, M. Soutsos, W. Sha, Guidelines for mix proportioning of fly ash/GGBS based alkali activated concretes, Constr Build Mater 147 (2017) 130–142.
[19] M.U. Salim, C. Moro, Towards sustainable construction: Performance evaluation of slag-cenosphere geopolymers under different NaOH concentrations, Journal of Building Engineering 91 (2024) 109605.
[20] N. Pattanayak, H.K. Behera, S.S. Das, Mix design strategy and optimization considering characteristic evaluation of geopolymer concrete, Journal of Building Engineering 91 (2024) 109557. https://doi.org/https://doi.org/10.1016/j.jobe.2024.109557.
[21] T. Xie, P. Visintin, X. Zhao, R. Gravina, Mix design and mechanical properties of geopolymer and alkali activated concrete: Review of the state-of-the-art and the development of a new unified approach, Constr Build Mater 256 (2020) 119380.
[22] N. Li, C. Shi, Z. Zhang, H. Wang, Y. Liu, A review on mixture design methods for geopolymer concrete, Compos B Eng 178 (2019) 107490. https://doi.org/10.1016/j.compositesb.2019.107490.
[23] C. Gunasekara, P. Atzarakis, W. Lokuge, D.W. Law, S. Setunge, Novel analytical method for mix design and performance prediction of high calcium fly ash geopolymer concrete, Polymers (Basel) 13 (2021) 900.
[24] W. Lokuge, A. Wilson, C. Gunasekara, D.W. Law, S. Setunge, Design of fly ash geopolymer concrete mix proportions using Multivariate Adaptive Regression Spline model, Constr Build Mater 166 (2018) 472–481.
[25] P. Zhang, Y. Mao, W. Yuan, J. Zheng, S. Hu, K. Wang, A critical review on modeling and prediction on properties of fresh and hardened geopolymer composites, Journal of Building Engineering 88 (2024) 109184. https://doi.org/https://doi.org/10.1016/j.jobe.2024.109184.
[26] M.A. Ansari, M. Shariq, F. Mahdi, Geopolymer concrete for clean and sustainable construction–A state-of-the-art review on the mix design approaches, in: Structures, Elsevier, 2023: pp. 1045–1070.
[27] G. Taguchi, S. Chowdhury, Y. Wu, Taguchi's Quality Engineering Handbook, Wiley, Livonia, 2004. https://doi.org/DOI:10.1002/9780470258354.
[28] S. V Dave, A. Bhogayata, N.K. Arora, Mix design optimization for fresh, strength and durability properties of ambient cured alkali activated composite by Taguchi method, Constr Build Mater 284 (2021) 122822. https://doi.org/10.1016/j.conbuildmat.2021.122822.
[29] M.N.S. Hadi, N.A. Farhan, M.N. Sheikh, Design of geopolymer concrete with GGBFS at ambient curing condition using Taguchi method, Constr Build Mater 140 (2017) 424–431. https://doi.org/10.1016/j.conbuildmat.2017.02.131.
[30] S. V Dave, A. Bhogayata, The strength oriented mix design for geopolymer concrete using Taguchi method and Indian concrete mix design code, Constr Build Mater 262 (2020) 120853.

[31] M. Nasir, M.A.M. Johari, A. Adesina, M. Maslehuddin, M.O. Yusuf, M.J.A. Mijarsh, M. Ibrahim, S.K. Najamuddin, Evolution of room-cured alkali-activated silicomanganese fume-based green mortar designed using Taguchi method, Constr Build Mater 307 (2021) 124970.
[32] B. Kanagaraj, N. Anand, U.J. Alengaram, B. Praveen, K. Tattukolla, Performance evaluation on engineering properties and sustainability analysis of high strength geopolymer concrete, Journal of Building Engineering 60 (2022) 105147.
[33] K. Onoue, T.A. Bier, Optimization of alkali-activated mortar utilizing ground granulated blast-furnace slag and natural pozzolan from Germany with the dynamic approach of the Taguchi method, Constr Build Mater 144 (2017) 357–372. https://doi.org/10.1016/j.conbuildmat.2017.03.189.
[34] L. Kan, W. Wang, W. Liu, M. Wu, Development and characterization of fly ash based PVA fiber reinforced Engineered Geopolymer Composites incorporating metakaolin, Cem Concr Compos 108 (2020) 103521.
[35] P. Chokkalingam, H. El-Hassan, A. El-Dieb, A. El-Mir, Development and characterization of ceramic waste powder-slag blended geopolymer concrete designed using Taguchi method, Constr Build Mater 349 (2022) 128744.
[36] M. Olivia, H. Nikraz, Properties of fly ash geopolymer concrete designed by Taguchi method, Materials & Design (1980-2015) 36 (2012) 191–198. https://doi.org/10.1016/j.matdes.2011.10.036.
[37] C. Panagiotopoulou, S. Tsivilis, G. Kakali, Application of the Taguchi approach for the composition optimization of alkali activated fly ash binders, Constr Build Mater 91 (2015) 17–22. https://doi.org/10.1016/j.conbuildmat.2015.05.005.
[38] J.K. Prusty, B. Pradhan, Multi-response optimization using Taguchi-Grey relational analysis for composition of fly ash-ground granulated blast furnace slag based geopolymer concrete, Constr Build Mater 241 (2020) 118049. https://doi.org/https://doi.org/10.1016/j.conbuildmat.2020.118049.
[39] R. Mohebi, K. Behfarnia, M. Shojaei, Abrasion resistance of alkali-activated slag concrete designed by Taguchi method, Constr Build Mater 98 (2015) 792–798.
[40] AS 1012.9, Methods of testing concrete - Compressive strength tests — Concrete , mortar and grout specimens, Australian Standards (2014) 1–13.
[41] AS 1012.10, Australian Standard 1012.10: Methods of testing concrete - Determination of indirect tensile strength of concrete cylinders (`Brazil' or splitting test), Australian Standards (2000) 9.
[42] AS 1012.11, Methods of testing concrete -Determination of the modulus of rupture, Australian Standards (2000) 1–9.
[43] ASTM C642-21, Standard Test Method for Density, Absorption, and Voids in Hardened Concrete, ASTM International, West Conshohocken, PA, 2021. https://doi.org/10.1520/C0642-21.
[44] ASTM C1585-20, Standard Test Method for Measurement of Rate of Absorption of Water by Hydraulic-Cement Concretes, ASTM International, West Conshohocken, PA, 2020. https://doi.org/10.1520/C1585-20.
[45] S. Vediyappan, P.K. Chinnaraj, B.B. Hanumantraya, S.K. Subramanian, An experimental investigation on geopolymer concrete utilising micronized biomass silica and GGBS, KSCE Journal of Civil Engineering 25 (2021) 2134–2142.
[46] S. Park, M. Pour-Ghaz, What is the role of water in the geopolymerization of metakaolin?, Constr Build Mater 182 (2018) 360–370.
[47] Y. Shi, Q. Zhao, C. Xue, Y. Jia, W. Guo, Y. Zhang, Y. Qiu, Preparation and curing method of red mud-calcium carbide slag synergistically activated fly ash-

ground granulated blast furnace slag based eco-friendly geopolymer, Cem Concr Compos 139 (2023) 104999.
[48] X.Y. Zhuang, L. Chen, S. Komarneni, C.H. Zhou, D.S. Tong, H.M. Yang, W.H. Yu, H. Wang, Fly ash-based geopolymer: clean production, properties and applications, J Clean Prod 125 (2016) 253–267.
[49] T. Ji, C.Y. Chen, Y.Z. Zhuang, Evaluation method for cracking resistant behavior of reactive powder concrete, Constr Build Mater 28 (2012) 45–49. https://doi.org/10.1016/j.conbuildmat.2011.08.060.
[50] W. Wang, C. Fan, B. Wang, X. Zhang, Z. Liu, Workability, rheology, and geopolymerization of fly ash geopolymer: Role of alkali content, modulus, and water–binder ratio, Constr Build Mater 367 (2023) 130357. https://doi.org/https://doi.org/10.1016/j.conbuildmat.2023.130357.
[51] T. Guo, G. Zhang, F. Ma, P. Shen, R. Wang, W. Song, L. Wang, P. Han, X. Bai, Mechanical properties and microstructure of red mud-coal metakaolin geopolymer concrete based on orthogonal tests, Journal of Building Engineering 79 (2023) 107789.

Chapter 4

Background

This study aims to investigates the ultra-high-performance concrete filled double-skin aluminium tubes (UHPC-FDAT) columns under combined loading conditions. Five specimens under concentric, eccentric and flexural loads were tested. Additionally, the specimens tested experimentally were modelled numerically in ABAQUS software package. After that, a parametric study established by changing one variable under the same loading conditions including the compressive strength, inner tube thickness, outer tube thickness, and hollow ratio.

List of Manuscripts

Alameri, M., Mohamed Ali, M. S., Elchalakani, M., & Sheikh, A. (2024). "Structural behaviour of UHPC-filled double-skin aluminium tubular columns under combined loads" Submitted to *Journal of Thin-Walled Structures*

Statement of Authorship

Title of Paper	Structural behaviour of UHPC-filled double-skin aluminium tubular columns under combined loads
Publication Status	☐ Published ☐ Accepted for Publication ☑ Submitted for Publication ☐ Unpublished and Unsubmitted work written in manuscript style
Publication Details	Alameri, M., Mohamed Ali, M. S., Elchalakani, M., & Sheikh, A. (2024). "Investigation of UHPC-filled double skin aluminium tubular columns under combined loading conditions" Submitted to Journal of Thin-Walled Structures

Principal Author

Name of Principal Author (Candidate)	Mohammad Alameri		
Contribution to the Paper	Conceptualisation, methodology, and manuscript writing and revision		
Overall percentage (%)	80%		
Certification:	This paper reports on original research I conducted during the period of my Higher Degree by Research candidature and is not subject to any obligations or contractual agreements with a third party that would constrain its inclusion in this thesis. I am the primary author of this paper.		
Signature		Date	24-10-2024

Co-Author Contributions

Name of Co-Author	M.S. Mohamed Ali		
Contribution to the Paper	Supervision, conceptualisation, methodology, and manuscript revision (10%)		
Signature		Date	24-10-2024

Name of Co-Author	Mohamed Elchalakani		
Contribution to the Paper	Supervision, conceptualisation, methodology, and manuscript revision (5%)		
Signature		Date	28-10-2024

Name of Co-Author	Abdul Sheikh		
Contribution to the Paper	Supervision, conceptualisation, methodology, and manuscript revision (5%)		
Signature		Date	29-10-2024

Structural behaviour of UHPC-filled double-skin aluminium tubular columns under combined loads

Mohammad Alameri[1,*], M.S. Mohamed Ali[1], Abdul Sheikh[1], Mohamed Elchalakani[2],

[1] *School of Architectural and Civil Engineering, The University of Adelaide, Adelaide, Australia*

[2] *Department of Civil, Environmental and Mining Engineering, The University of Western Australia, Perth, Australia*

[*] *Corresponding author E-mail: Mohammad.alameri@adelaide.edu.au*

Abstract

Concrete-filled double-skin tubular columns are highly valued in modern construction for their outstanding load capacity, reduced self-weight, and excellent ductility. Replacing the steel tubes with lightweight aluminium alloys further enhances the strength-to-weight ratio and corrosion resistance. This study investigates both experimentally and numerically the axial and flexural behaviour of ultra-high performance concrete-filled double-skin aluminium circular tube columns. Five specimens were fabricated having a constant cross section with an outer diameter of 203.2 mm and an inner diameter of 80 mm. Four columns have been loaded under axial compression with varying eccentricities from 0 mm to 90 mm and a beam has been tested under four-point bending. The axial load capacity, failure pattern, load-deflection relationships, and load-strain relationships observed from the experimental program are reported. The finite element model (FEM) was developed and validated against the test results, and it was utilised to perform a parametric study examining the effect of concrete compressive strength, inner and outer tube thicknesses, and hollow ratio on the structural performance of the composite columns.

Keywords: UHPC-filled aluminium tubes; composite columns; finite element analysis; Circular hollow sections; Experimental investigation.

1 Introduction

Concrete-filled double-skin steel tubes (CFDSST) members as schematically illustrated in Fig. 1, are composite columns comprising inner and outer steel tubes confining the sandwiched concrete. The inner and outer tubes provide higher confinement for the sandwiched concrete, which enhances its bearing capacity and ductility. Therefore, these members have gained growing popularity due to their higher strength-to-weight ratio due to the removal of the core concrete, ease of construction, good corrosion resistance, and ease of service installation through the inner void such as installing pipes without compromising the structural performance [1,2] Moreover, utilising the inner and outer tubes as a permanent formwork result in saving both cost and time in the construction sector.

Different types of steel such as steel carbon [3] and stainless steel [4] have been adopted mostly to confine the sandwiched concrete. Further enhancements can be made to CFDSST by replacing the steel with aluminium due to their lightweight as its density is only one-third that of steel [5]. The aluminium tubes also enhance the aesthetical appearance and corrosion resistance. Therefore, many studies have considered the utilisation of the aluminium tubes and explore their structural performance [6–9].

The seismic performance of concrete-filled double-skin aluminium tube (CFDAT) columns is significantly enhanced, primarily attributed to their relatively lower strength-to-weight ratio. [10] . Despite these advantages, the CFDAT structural performance has not been thoroughly investigated [11–14]. Zhou and Young [15] explored the structural performance of CFDAT columns under concentric axial compression load by varying the concrete strength and geometrical dimension. Design equations were proposed to predict the squash load capacity accurately. Furthermore, other scholars have investigated the CFDAT subjected to in-plane bending loading conditions [5] and axial loading for CFDAT slender columns [6]. However,

the above-mentioned studies have considered only utilising the normal strength concrete (NSC).

The rising public demand for resilient structures has driven the need for stronger and more durable materials. Thus, ultra-high-performance concrete (UHPC), with its densely packed matrix, plays a vital role in providing compressive strength exceeding 120 MPa [16]. Furthermore, it possesses a higher tensile strength of up to 15 MPa with better post-cracking ductility behaviour due to the incorporation of steel fibres [17]. Moreover, its durability characteristics are improved due to the dense matrix, resulting in fewer permeability voids than NSC [18]. The use of UHPC in CFDAT columns remains an unexplored area of study. However, the use of UHPC in CFDSST has been scarcely studied [19]. The utilisation of UHPC infill leads to reduce the cross-section due to its higher strength, improves the ductility and energy absorption, which enhances the seismic performance, and the composite columns can sustain higher load post failure of the composite [20].

There is still a lack of understanding of the structural performance of CFDAT under different loading conditions, such as eccentric compressive loading. However, multiple studies have provided design recommendations based on steel tube double-skin columns investigation, which could lead to conservative estimation [11,21–23].

Combining UHPC and aluminium tubes offers higher structural performance and resistance to corrosion required for long-term durability and structural integrity, particularly in harsh marine and coastal environments. This study aims to experimentally investigate the structural performance of short UHPC-filled double-skin aluminium tube (UHPC-FDAT) columns under concentric load, eccentric load with varying load eccentricity of (30 mm, 60 mm, and 90 mm), and bending. This will give a comprehensive overview of completing the P-M diagram of the UHPC-FDAT columns. Additionally, Finite element model (FEM) will be developed and verified by the experimental results reported in this study to examine the influence of concrete

compressive strength, inner and outer tube thicknesses, and hollow ratio on the structural performance of UHPC-FDAT columns.

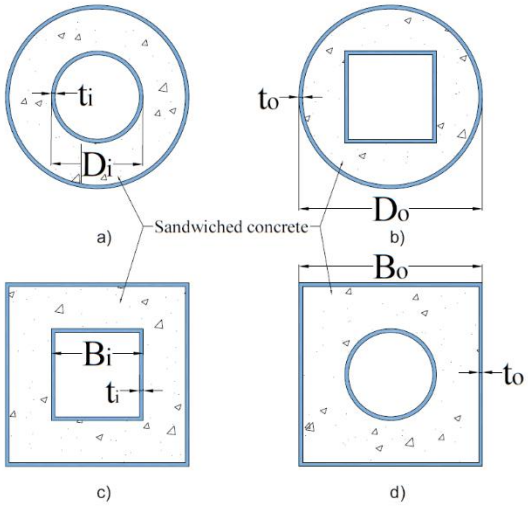


Fig. 1 Cross sections of most common CFDT a) Circular hollow section (CHS) inner and outer skins; b) CHS outer skin and square hollow section (SHS) inner skin; c) SHS outer and inner skins; and d) SHS outer and CHS inner skins

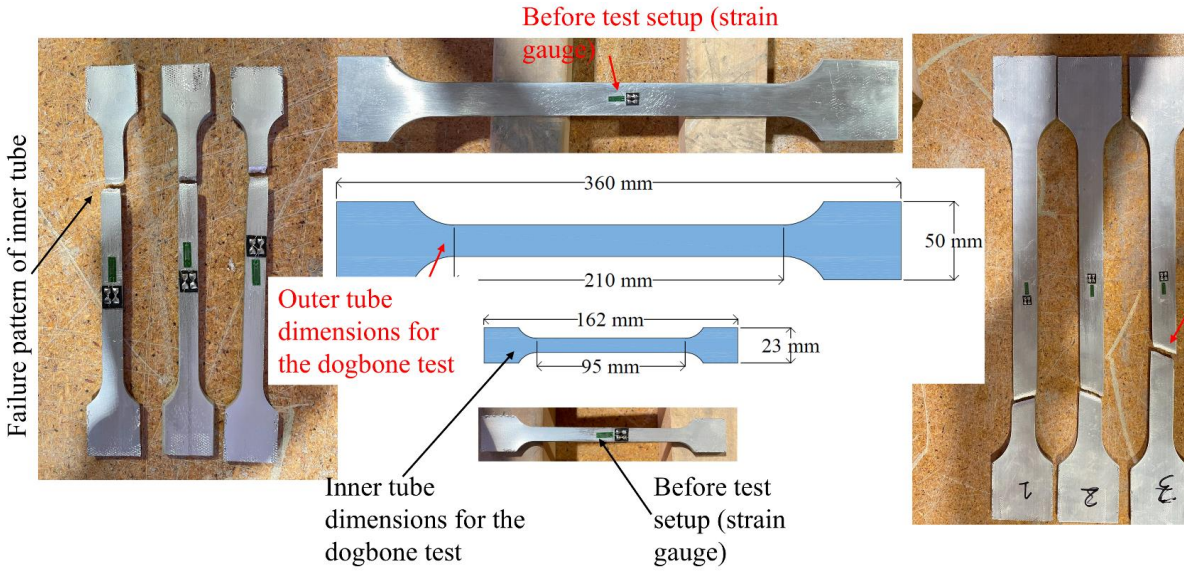
2 Experimental Programme

This section describes the material properties of both aluminium tubes and UHPC, the details and fabrication of the columns and beams, the test variables, instrumentation, and test procedures.

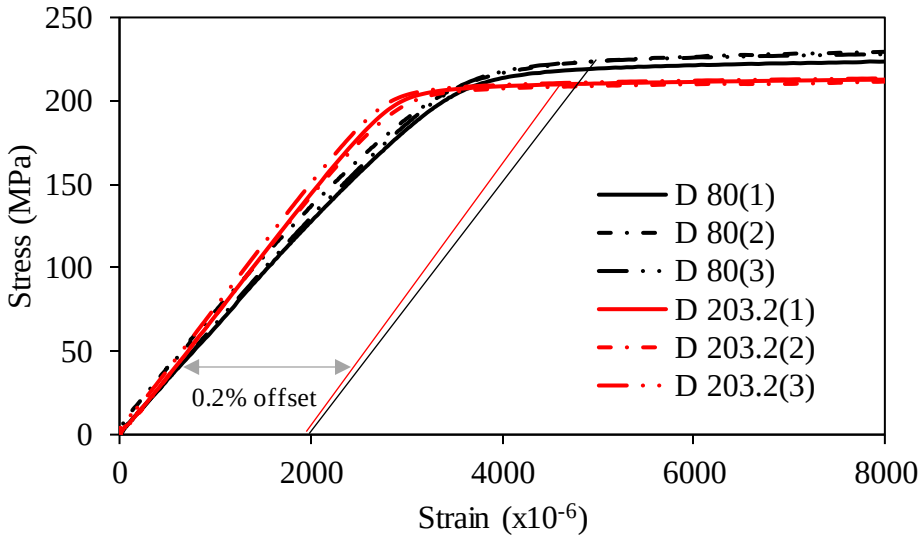
2.1 Material properties

2.1.1 Aluminium tubes

The aluminium tubes comprised two different diameters, 80 mm for the inner tube and 203.2 mm for the outer tube, with a consistent thickness of 3 mm for both tubes. Both tubes were fabricated according to the guidelines of ASTM B221aluminium alloy grade 6063 [24]. Three coupons were tested per tube to extract the mechanical properties such as the ultimate strength, the yield strength, and the elongation of the aluminium tubes according to the guidelines provided by ASTM E8 [25], as shown in Fig. 2 and Table 1.



a)



b)

Fig. 2 a) the mechanical properties test for aluminium tubes preparation and failure patterns; and b)Stress-strain curve for the aluminium alloy tubes (inner tubes in black and outer tubes in red) (D is the diameter of the tube)

Table 1 Mechanical properties of aluminium alloy tubes

Section	$f_{y,o}/f_{y,i}$ (MPa)	$\varepsilon_{y,o}/\varepsilon_{y,i}$ ($\mu\varepsilon$)	$f_{u,o}/f_{u,i}$ (MPa)	$\varepsilon_{u,o}/\varepsilon_{u,i}$ ($\mu\varepsilon$)	Modulus of elasticity E_a (GPa)	Elongation (%)
	209.59	2386	234.16	27201	71.81	11.58
Outer tube	208.05	2306	232.32	15196	72.03	11.81
	210.26	2332	234.17	10486	73.88	12.23
Average	209.30		233.55		72.57	
Standard deviation	1.13		1.06		1.14	
Inner tube	219.23	3123	236.12	8016	62.97	11.79

	220.35	3126	243.11	6710	61.19	12.63
	221.31	3013	242.11	10694	63.72	14.03
Average	220.30		240.45		62.63	
Standard deviation	1.04		3.78		1.30	

Note: $f_{y,o}$ = yield strength of outer tube; $f_{y,i}$ = yield strength of inner tube; $\varepsilon_{y,o}$ = yield strain of outer tube; $\varepsilon_{y,i}$ = yield strain of inner tube; $f_{u,o}$ = ultimate strength of outer tube; $f_{u,i}$ = ultimate strength of inner tube; $\varepsilon_{u,o}$ = ultimate strain of outer tube; and $\varepsilon_{u,i}$ = ultimate strain of inner tube.

2.1.2 UHPC

UHPC mix design is presented in Table 2. The target compressive strength for this mix was 120 MPa. The dry constituents were mixed for three minutes to ensure the materials were homogeneously mixed. The water was then added with the superplasticiser for up to 15 minutes. The steel fibres were then incorporated into the mix for a further three minutes so that the fibres can be distributed evenly.

Table 2 mix proportions

Mix ID	**Binder (%)**		**Silica fume (%)**	**s/b**	**w/b**	**Steel Fibre (%) (volume fraction)**	**SP/b**
	Cement	**Slag**					
UHPC	85	15	25	1.1	0.166	1.5	0.04

Note: b = binder; s = fine aggregate; w = water; and SP = superplasticiser.

Cylinders with a diameter of 100 mm and height of 200 mm were tested on the same day of column tests according to AS1012.9 [26] used to determine the compressive strength and the results of the ultimate compressive strength f_c', the average compressive strength $f_{c,avg}'$, and the modulus of elasticity (E_c) are presented in Table 3, and the stress-strain relationship is illustrated in Fig. 3.

Table 3 Compressive strength results of each column and beam

Specimen ID	$f_c'(MPa)$	$f_{c\ avg}'(MPa)$	**Standard deviation**	**E_c (GPa)**
C1-1	120.30			
C1-2	127.31	121.94	4.76	45.23
C1-3	118.22			
C2-1	133.59			
C2-2	123.03	127.18	5.63	46.57
C2-3	124.93			
C3-1	130.43			
C3-2	122.36	128.69	5.67	45.91
C3-3	133.29			
C4-1	124.33	128.55	5.32	46.72
C4-2	134.52			

C4-3	126.81			
B-1	123.00			
B-2	132.28	128.57	4.91	46.68
B-3	130.34			

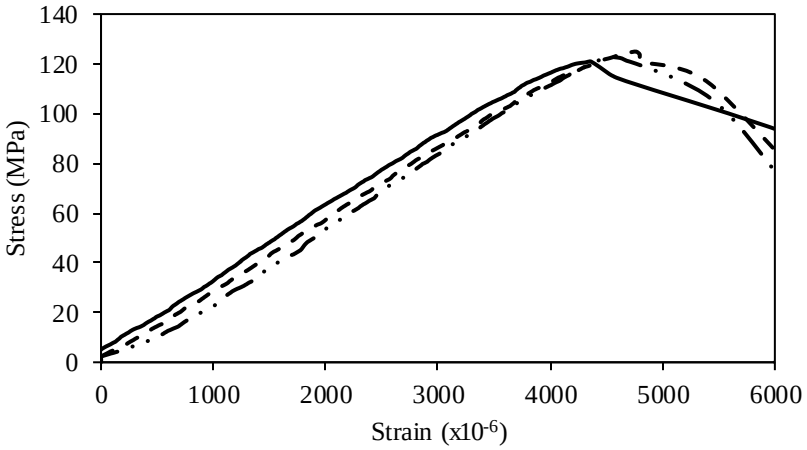


Fig. 3 Typical stress-strain relationship of the cylinders under compression test

2.1.3 Test Specimens

Four columns of UHPC-FDAT with a height of 1000 mm were constructed and prepared to be tested under concentric and eccentric axial compressive loads as summarised in Table 4. The cross-section details are depicted in Fig. 4. A 1500 mm long beam having the same cross-section as the columns was also cast and tested under a four-point bending load. The UHPC for the specimens were poured vertically in increments of 200 mm, and it was compacted diligently to distribute the mortar between the aluminium tube skins evenly. These were cured under ambient conditions at a temperature of 24 ℃ and RH of 55% for 28 days.

Table 4 Specimens details (all dimensions in mm)

Specimen ID	Column/Beam	D_o x t_o	D_i x t_i	L	Eccentricity (mm)
C1	Column	203.2 x 3	80 x 3	1000	0
C2	Column	203.2 x 3	80 x 3	1000	30
C3	Column	203.2 x 3	80 x 3	1000	60
C4	Column	203.2 x 3	80 x 3	1000	90
B	Beam	203.2 x 3	80 x 3	1500	-

2.1.4 Instrumentations

All columns were instrumented with linear variable displacement transducers (LVDTs) and longitudinal strain gauges as shown in Fig. 4. Seven LVDTs were used for each column; of these three LVDTs were utilised to measure the lateral deflection of the columns for continuous

generating the deflection profile at an interval of 175 mm above and below the mid-height of the column. Furthermore, two LVDTs were mounted vertically to determine any abnormal deviation perpendicular to the applied load. The remaining two LVDTs were used to measure the axial shortening of the columns. Moreover, four longitudinal strain gauges (one on each face of the aluminium tube surface) were attached at the mid-height of the columns for continuous recording of strains.

For the beam, the test set-up is illustrated in Fig. 4(c), wherein three laser-based LVDTs were inserted underneath the middle of the beam to measure the deflection. Moreover, seven strain gauges were horizontally attached on half of the beam starting from top which called strain gauge 1 (SG1); the strain gauges were distributed equally and attached at the perimeter face where SG1 at the top, SG7 at the bottom and other strain attached in ascending order. These SGs will assist in providing more insights about the strain profile of the beam and other behaviours.

2.1.5 Test Procedures

The four UHPC-FDAT columns were tested under monotonically increasing axial compression load at a load rate of 30 kN/minute with a varying eccentricity of 0 mm (for measuring squash load), 10 mm, 40 mm and 70 mm, and the loading was terminated when the columns failed completely. For the beam, a universal test machine was used which has a capacity of 5000 kN and the load rate was 5 kN/m.

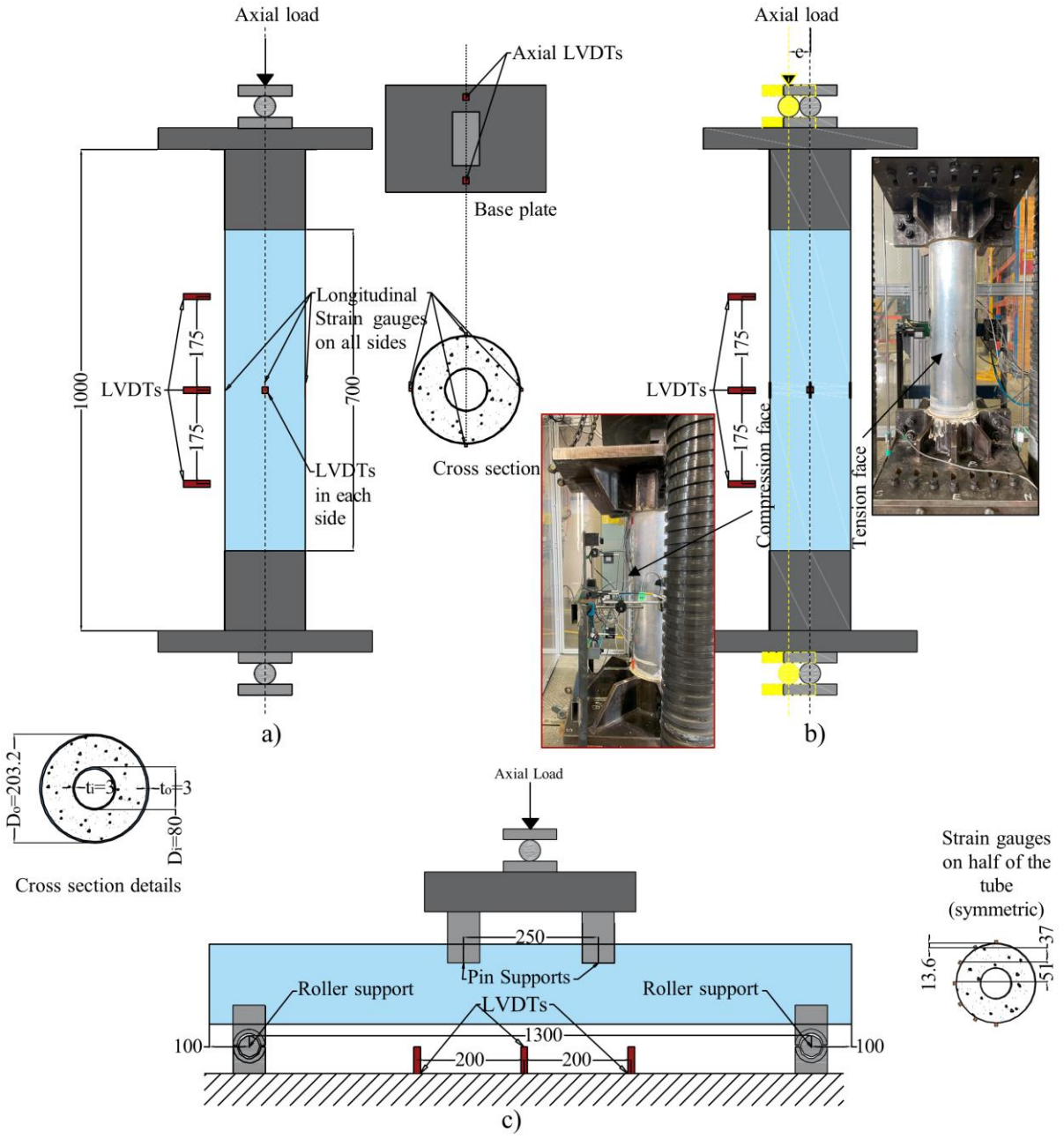


Fig. 4 Test set-up for a) the concentric column (with cross-section illustrated); b) under eccentric load; and c) under a three-point bending scenario of the beam (dimensions in mm)

3 Results

All columns and the beam were loaded until the specimens failed. The following parameters were recorded and are summarised in Table 5; the ultimate load (P_u) and the corresponding moment (M_u), axial strain (ε_u) and axial displacement ($\Delta_{u,axial}$), eccentricity, the mid-height lateral deflection at P_u ($\Delta_{u,mid}$), failure location from the middle of the specimen (where (0) is at the mid-height, (+) indicates above the mid-height, and (-) indicates below the mid-height),.

Table 5 Test results for all UHPC-FDAT columns and the beam

Specimen	e (mm)	P_u (kN)	$\Delta_{u,mid}$ (mm)	M_u (kN.m)	Failure location (mm)	Failure mode	ε_u	$\Delta_{u,axial}$ (mm)
C1	0	3431	1.17	0.00	0 to +50	LB	0.00309	4.69
C2	30	2212	3.22	73.48	0 to +50	LB in C and R in T	0.00225	3.83
C3	60	1400	12.74	101.89	+100 to +150	LB in C and R in T	0.00558	4.15
C4	90	848	21.68	94.71	0 to +50	LB in C and R in T	0.00761	4.75
B	-	95.3	28.34	50.01	+100 to -100	R in T	0.02162	17.92

LB = local buckling; R = rupture; C= compression face; and T = tension face

3.1 Failure modes and ultimate bearing capacity

Fig. 5(a) shows the failure pattern of the concentrically loaded column at a peak load of 3431 kN due to local buckling around the mid-height of the specimen in the outer tube; the concrete also failed by crushing in the same region due to the axial shortening of the column without outward bending. However, the other columns (C2, C3 & C4) failed in the mid-span region in the same fashion wherein there was local buckling of the outer tube and crushing of concrete accompanied with fracture of UHPC in the tension face as shown in Fig. 5(b).

The failure pattern of the beam tested under four-point bending is shown in Fig. 5(c) due to the occurrence of rupturing on the outer skin on the tension face between the applied loads and associated with the widening of the crack in the surrounding UHPC. This failure was preceded by the extensive sagging of the beam and also the local buckling in the outer aluminium tube on the compression face of the beam.

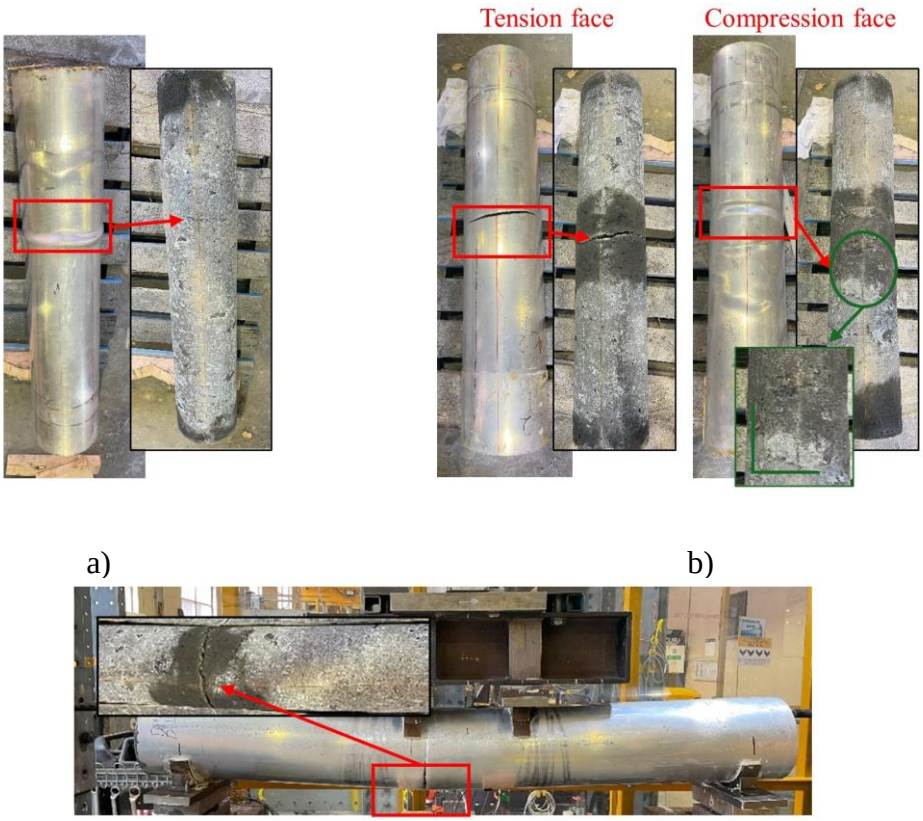


Fig. 5 Failure pattern of UHPC-FDAT for: a) C1 under concentric load; b) typical failure patterns for C2-C4 under different eccentricities; and c) failure of the beam

3.2 Load-deformation relationship

The ultimate axial load-average axial shortening relationship for all columns is plotted in Fig. 6. It can be seen that increasing the eccentricity of the applied load decreases the ultimate load by 28%, 58% and 75% for columns C2, C3 and C4, respectively, when compared with column C1 with zero eccentricity. The deflection magnitudes for all the columns increased linearly with the increasing applied load up to the ultimate load. Note that in the case of column C1 with concentrically applied load, the load dropped abruptly after the squash load, whereas column C4 with the large eccentricity of 90 mm exhibited a beam-like behaviour wherein the peak load was sustained with increasing deflection before the load started to drop-off.

Fig. 7 shows the mid-height displacement of the columns with the corresponding applied axial load. The flexural stiffness defined by the slope of the curve's ascending (elastic) branch has been significantly decreased due to the increased eccentricity. C1 and C2 with the low

eccentricity of 0 mm and 30 mm, respectively, have shown a significant enhancement of flexural stiffness compared to other columns.

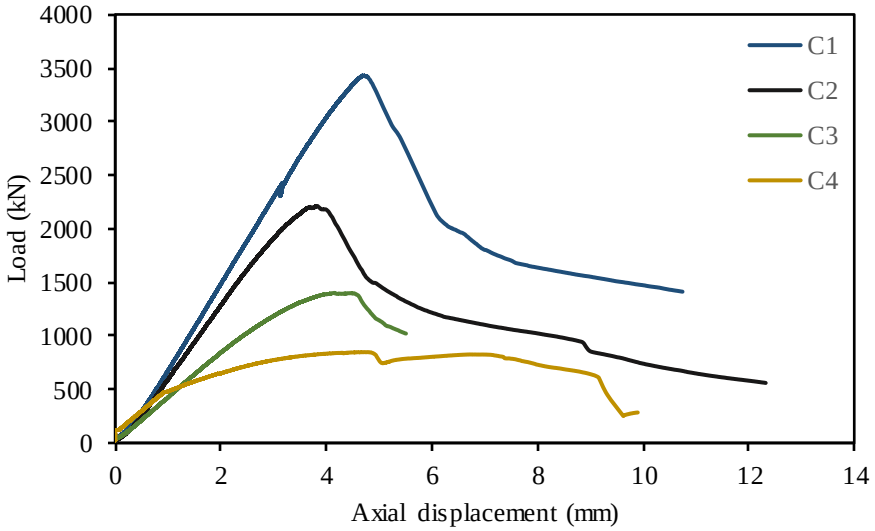


Fig. 6 Axial load vs axial displacement

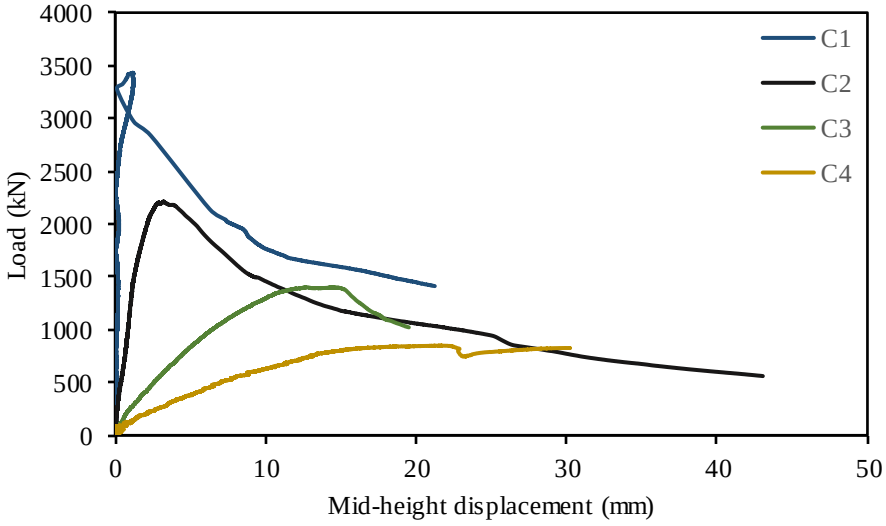
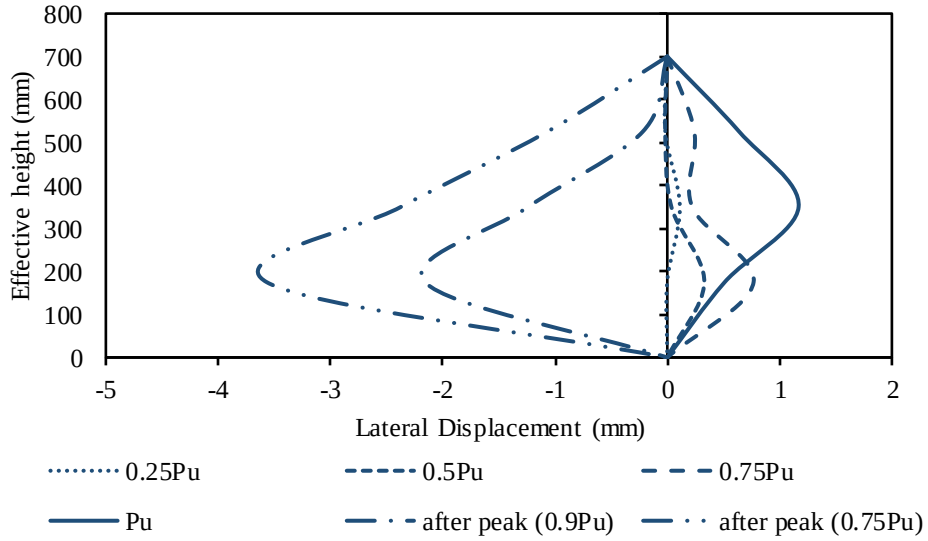


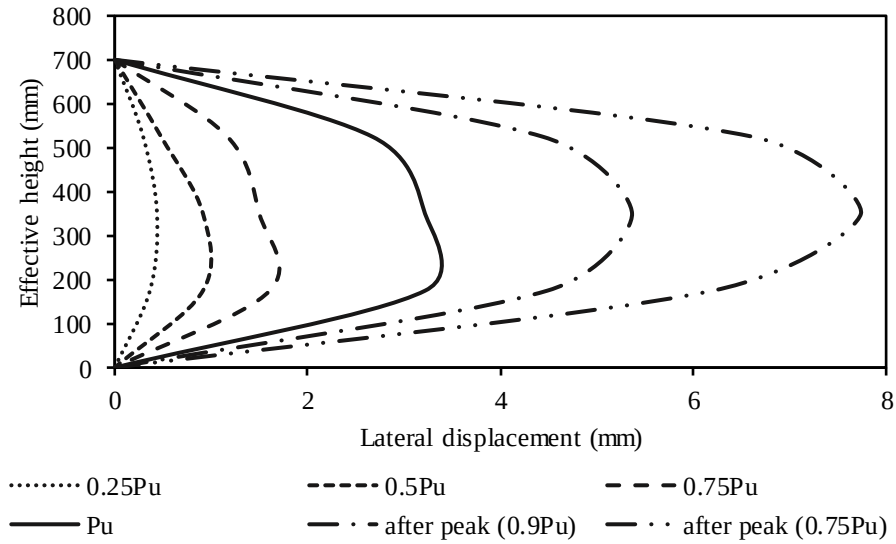
Fig. 7 Axial load vs mid-height displacement of the columns

The lateral displacement profiles of the columns at significant axial load intervals along the different lateral LVDT locations are illustrated in Fig. 8; note that these LVDTs locations were illustrated in Fig. 4(a) where 0 mm deflection considered at the two ends of the effective length which is 700 mm. It is worth noting that the global buckling of columns increases with the increase in eccentricities. Moreover, the columns exhibit similar behaviours, with the

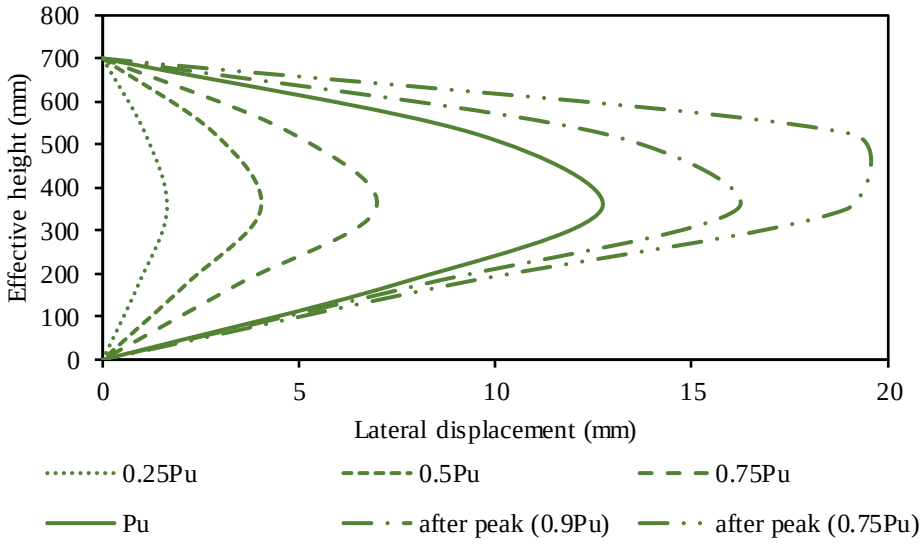
maximum lateral displacement occurring at the mid-height of the column. Therefore, it can be deduced that the aluminium tubes controlled and confined the concrete to allow for a significant increase in the lateral displacement eliminating abrupt failure of test specimens, thus assisting in increasing the ductility and enhancing the structural performance.



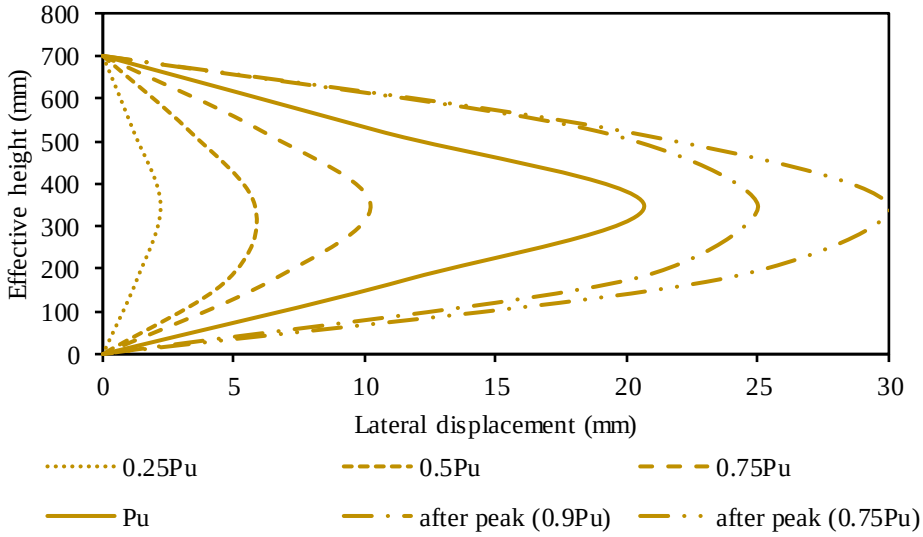
a)



b)



c)



d)

Fig. 8 Deflection profile along the effective height of the column a) C1; b) C2; c) C3; and d) C4

The load-midspan displacement relationship is plotted in Fig. 9. Notably, the yield point was achieved at 65.96% of the ultimate load. The beam exhibited a strain-hardening behaviour up to the ultimate load and then strain strain-softening behaviour until the specimen failed. After the ultimate load, the load dropped significantly, and then the rupture happened in the outer tube and sandwiched concrete. Furthermore, the rate of dropping the load decreased when it reached 42.55% of the ultimate load with a corresponding displacement of 21.91 mm due to the inner tube and steel fibre in the concrete, preventing the beam from total failure. Moreover,

the deflection profile of the beam at different intervals of the ultimate load along the length of the beam is illustrated in Fig. 10. It can be observed that there is a massive increase in the deflection after 80% of the ultimate load, which explained as the start of the soft-hardening region.

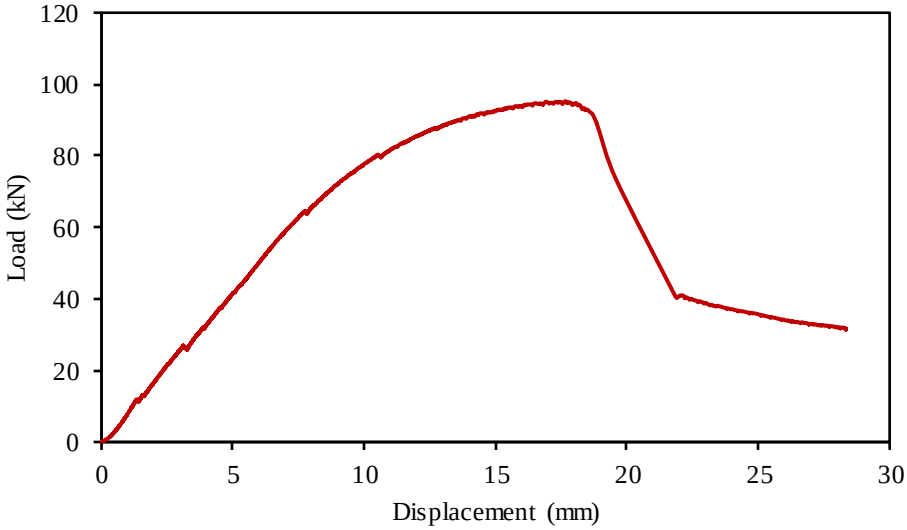


Fig. 9 Load vs displacement of the beam in the middle

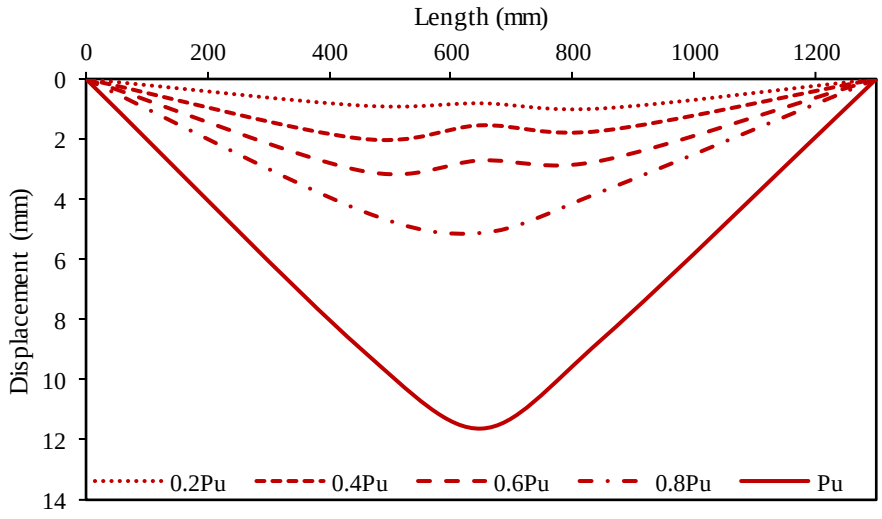


Fig. 10 Deflection profile of the beam at different interval of loads

3.3 Load-strain relationships

The axial strain magnitudes both at compression and tension faces for all columns were recorded continuously, as shown in Fig. 11. For C1, the failure occurred due to the local buckling of the outer tube due to the crushing of the concrete, which is indicated by the abrupt

drop in the load near the yield strain. Applying the load eccentrically enhances the flexural behaviour due to the influence of the aluminium tubes by mitigating the rapid failure after the failure of the concrete. On the contrary, it can be inferred from Fig.11 that the aluminium tube enhances the failure pattern in eccentrically loaded columns and fails smoothly without an abrupt drop in applied axial load after attaining the peak load. Note that even for the column C2 with the least load eccentricity of 30 mm, the load drop after the ultimate load is only 11.85%, and the load start to decrease steadily with the strain increase in both compression and tension faces whilst for the concentrically loaded column C1 the corresponding drop in peak load is 57.78%. Furthermore, the columns C3 and C4 with 60 mm and 90 mm eccentricities, respectively, exhibited different failure behaviours in the outer tube, where the ultimate load was achieved beyond the yield point.

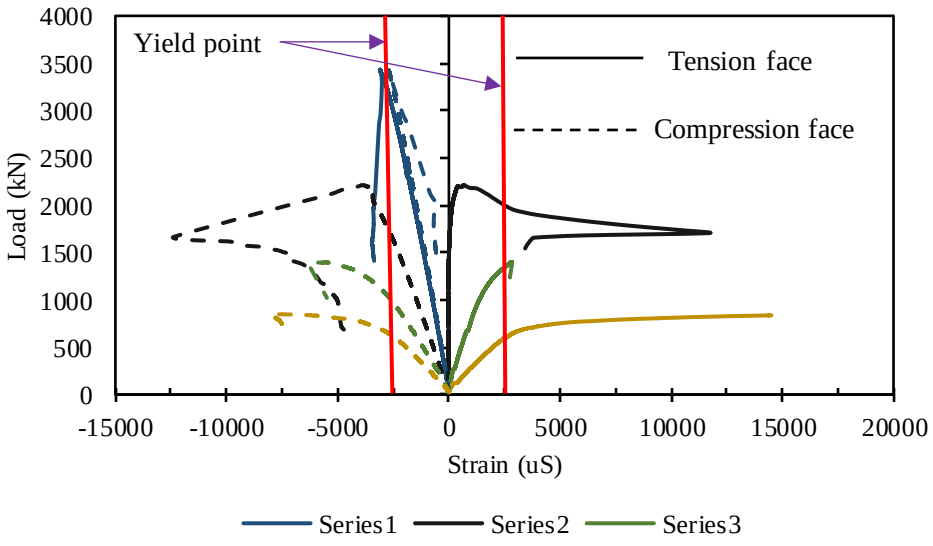


Fig. 11 Axial load vs the axial strain on compression and tension faces

The axial strain values as percentages at different intervals of the ultimate load on all faces are plotted in Fig. 12 to observe how the axial strain of the outer tube was affected by the variation of the axial load eccentricities. Notably, the column under concentric load C1 has an almost equal distribution of the strain around the perimeter of the column where the yielding happened nearly at the ultimate load on all the faces. However, applying the load eccentrically changed the strain pattern as indicated in Fig. 12(b), where the strain gauges SG1 and SG3 have not

yielded at the ultimate load and SG4 on the compression face exhibited strain beyond the yield point. Therefore, increasing the eccentricity compressed the columns more on the compression face and stretched them more on the tension face, as shown in Fig. 12(c) and Fig. 12(d). However, under different eccentricities except for the concentrically loaded column, the axial strain on SG1 and SG3 have not yielded at the ultimate load. Hence, it is worth mentioning that the aluminium tubes have enhanced the structural performance of CFDAT columns under eccentrically applied loads.

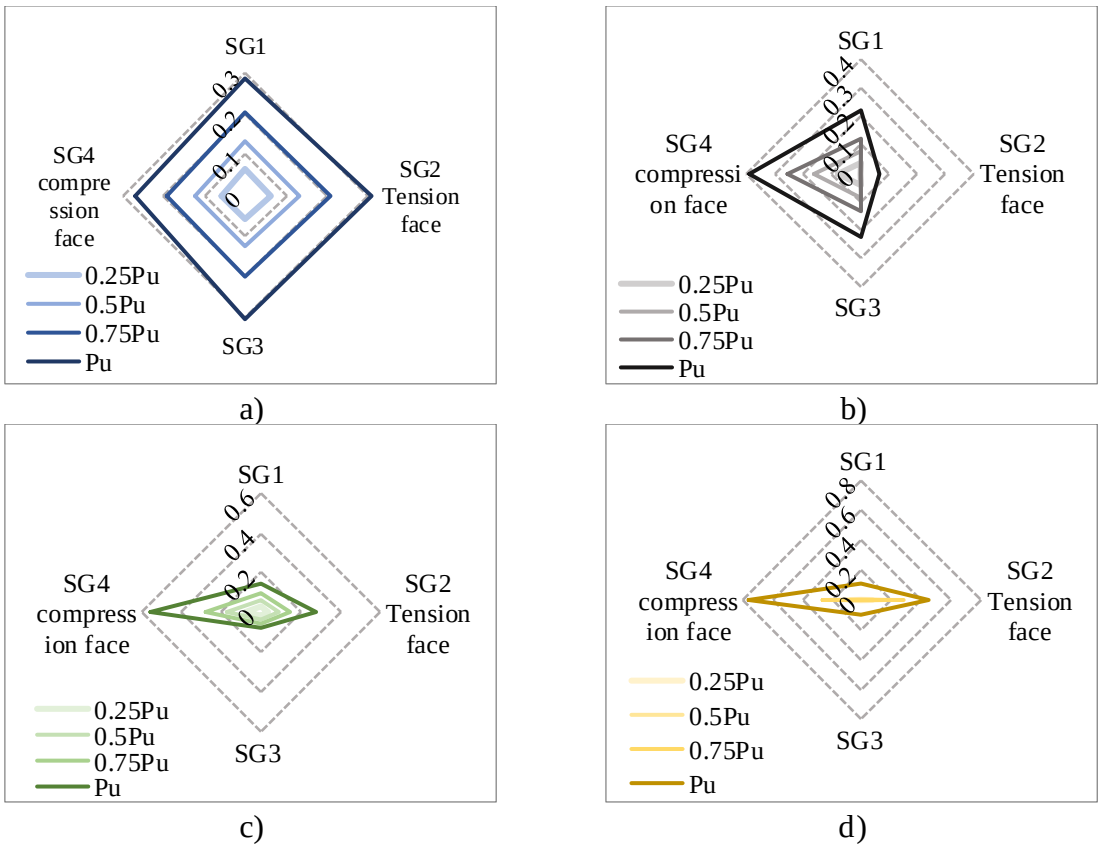


Fig. 12 The reading of the axial strain at different intervals of the ultimate load on four sides of the column at the mid-height: a) C1; b) C2; c) C3; and d) C4

The behaviour of the beam in terms of the strain values at different intervals of the ultimate load is illustrated in Fig. 13, which was obtained from seven strain gauges attached to the beam on the middle along half of the beam from the top (compression face) up to the bottom (tension face). The strain values up to 60% of the ultimate load exhibited linear elastic behaviour on both faces. However, at 80% of the ultimate load, the strain values below the neutral axis

demonstrated a nonlinear increase with the highest value achieved on the tension face of 10000 micro-strain. Beyond 80% of the ultimate load, the beam started to deform rapidly until the failure point after the ultimate load. The failure occurred on the tension face due to the rupture of the outer tube and flexural cracks of the sandwiched concrete as mentioned in section 3.1.

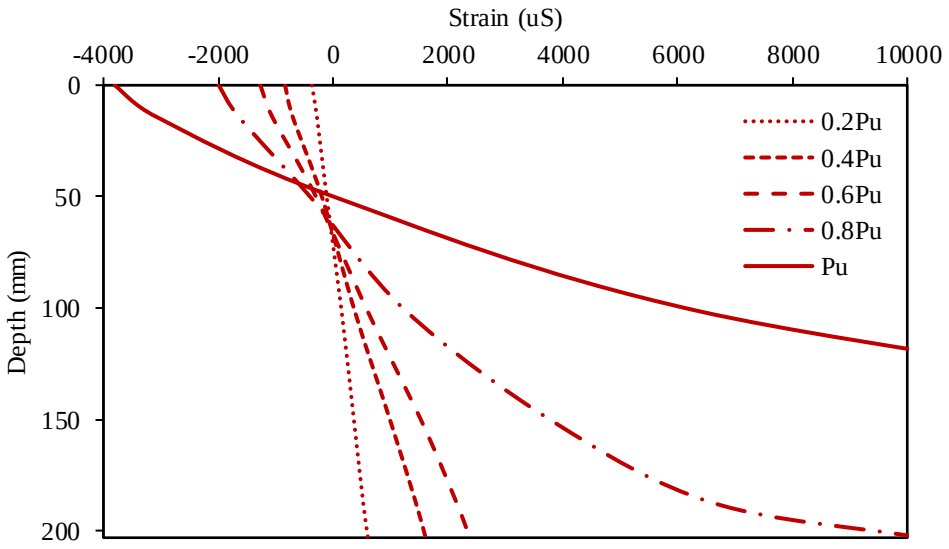


Fig. 13 Strain profile of the beam at different stages of the load along the depth of the beam where the 0 mark in the y-axis indicates the top of the beam

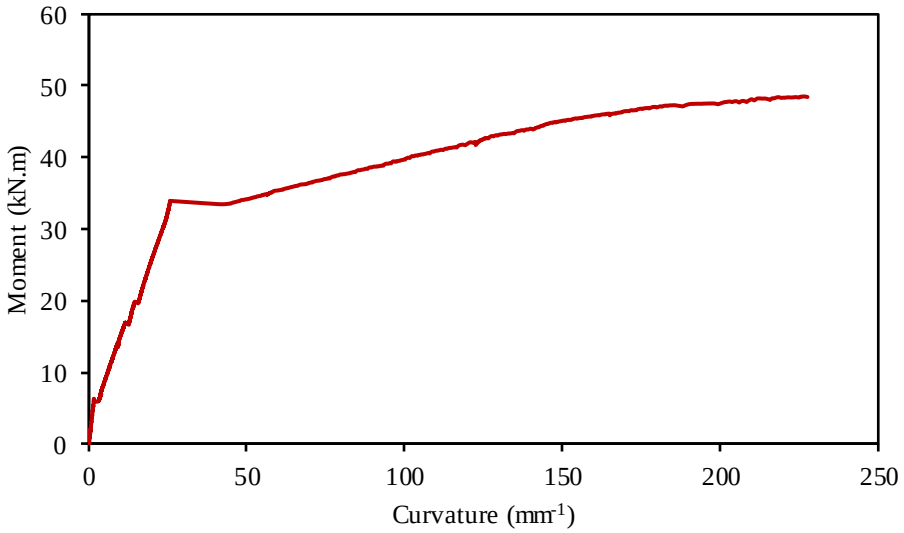


Fig. 14 Moment-curvature relationship of the beam

Fig. 14 shows the moment-curvature relationship of the beam. The curve was extracted from the attached strain gauges on the beam at the middle of the length. Initially, the curvature exhibited a linear increase, demonstrating a steady increase in the flexural stiffness of the

elastic region. The moment was increased gradually with a rapid increase in the curvature after reaching the yield point, indicating the plastic region with ductility and energy absorption. After that, the moment increased slowly, which indicates the strain hardening region before the specimen failed.

4 Finite-element modelling (FEM)

All experimental specimens are numerically constructed. Abaqus [27] was used as the finite element modelling (FEM) package to numerically analyse the results and establish a parametric study after accurately validating the obtained FEM results by the experimental results obtained in this study. Different studies have utilised this package to analyse the composite columns numerically and achieved remarkable precision [28–31]. The ultimate axial load and associated axial displacement are estimated using a comprehensive nonlinear analysis. Additionally, a comparison is made between the failure pattern seen in the experimental programme and the corresponding columns simulated by the model. Aspects such as meshing, boundary conditions, loads, constituent modelling of the materials, and component interactions are all considered when developing the models in Abaqus.

4.1 Geometry of the model

Fig. 15 displays the meshing and model geometry for a column created in Abaqus, along with the steel caps attachments at each column's two ends used to load the column. Each model component was made independently before being assembled during the assembly phase. The inner tube, outer tube and sandwiched concrete compose the actual column components. Steel caps have been employed at the ends of the columns to appropriately contain the load so that it can be securely transmitted at both the top and bottom of the column without causing damage during the experimental testing. Additionally, a more realistic model of the experimental program has been created for these caps. The steel plates utilised at either end of the steel caps, which assisted in adjusting the eccentricity of loading in the experimental work, have also been

taken into account by the model. Since these plates functioned elastically, they are simply processed as elastic components in order to reduce computing effort while maintaining column responsiveness and failure modes.

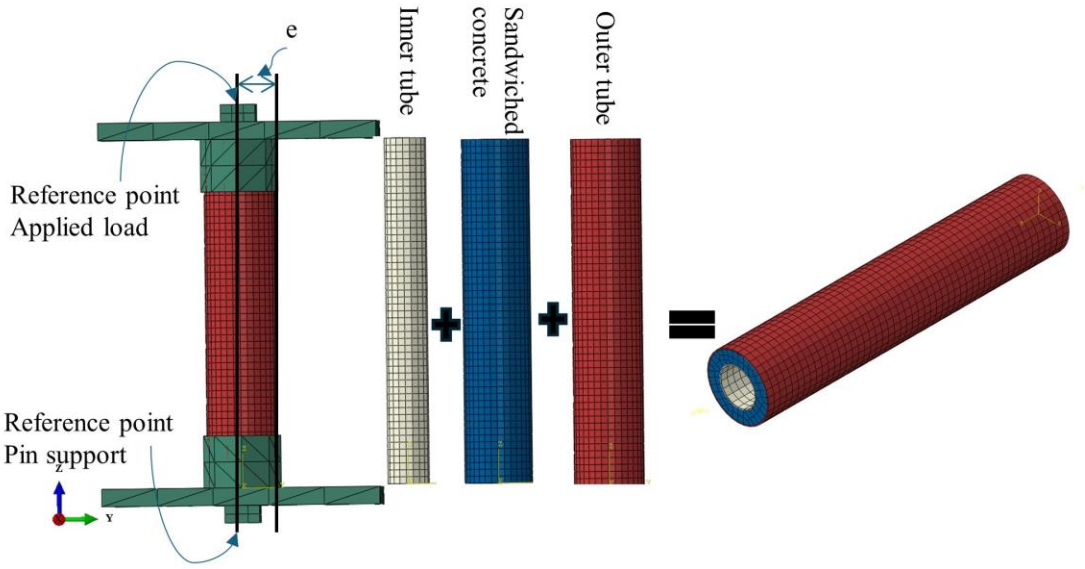


Fig. 15 Model set-up in Abaqus

4.2 Constitutive material models

4.2.1 Aluminium alloy material

The material properties of the aluminium alloy were extracted based on the experimental results, as mentioned in section 2.1.1. The stress-strain curve was regenerated according to the Eqs (1 and 2) provided by Ramberg and Osgood [32] and improved by Hill [33].

$$\varepsilon = \frac{f}{\mathrm{E}} + 0.002\left(\frac{f}{f_{0.2}}\right)^{n} \tag{1}$$

$$n = \frac{ln\,2}{ln\left(\frac{f_{0.2}}{f_{0.1}}\right)} \tag{2}$$

where f is the tensile strength, ε is the tensile strain, E is the modulus of elasticity, $f_{0.2}$ is the 0.2% proof stress, $f_{0.1}$ is the 0.1% proof stress, and n is the exponent of strain hardening. The regenerated stress-strain curve and the plotted curves from the experimental data are shown in Fig. 16.

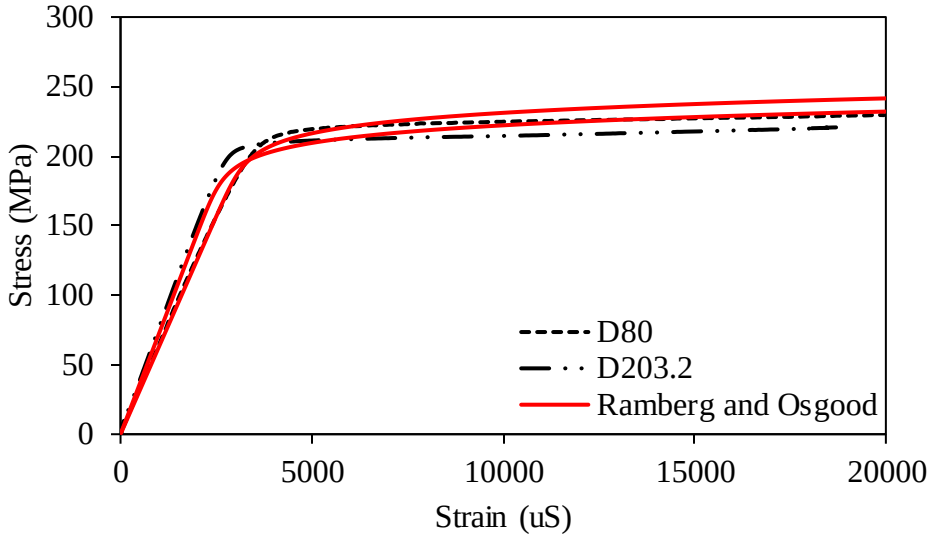


Fig. 16 Regenerated stress-strain relationship for inner and outer aluminium tubes

4.2.2 UHPC

The constitutive response of the UHPC was simulated by utilising the concrete damage plasticity (CDP) model [34]. The CDP model incorporates the effects of damage and plasticity to replicate the irreversible permanent deformations of this concrete-based material and the degradation of stiffness caused by micro-cracking, where the material behaves differently under tension and compression loading regimes. Lee and Fenves made further improvements in the model [35], which are available in Abaqus. These features enable precise capture of the nonlinear inelastic behaviour of concrete-based materials, making the CDP model highly popular. The CDP model includes elastic properties that account for the response of elastic materials. Additionally, it features a pressure-dependent yield surface, reflecting the pressure-sensitive yielding behaviour commonly exhibited by concrete-based materials. The model employed a non-associated flow rule with a plastic potential distinct from the yield surface to replicate the dilation response of these pressure-sensitive materials. Both compressive and tensile stress states are captured by a single yield function, which contributes to the robustness of iteratively based computational algorithms. The yield surface (F) and plastic potential (G) are represented by the following functions, which are expressed as follows:

$$F = \frac{1}{1-\alpha}\left(\bar{q} - 3\alpha\bar{p} + \beta\left(\tilde{\varepsilon}^{pl}\right)\left(\hat{\bar{\sigma}}_{max}\right) - \gamma\left(-\hat{\bar{\sigma}}_{max}\right)\right) - \bar{\sigma}_c\left(\tilde{\varepsilon}_c^{\,pl}\right) \leq 0 \quad (3)$$

$$G = \sqrt{(\zeta\sigma_{t0}\tan\varphi)^2 + \bar{q}^2} - \bar{p}\tan\varphi \quad (4)$$

$$\alpha = \frac{\frac{\sigma_{bo}}{\sigma_{co}} - 1}{2 \times \frac{\sigma_{bo}}{\sigma_{co}} - 1}; \quad 0 \leq \alpha \leq 0.5 \quad (5)$$

$$\beta = \frac{\bar{\sigma}_c\left(\tilde{\varepsilon}_c^{pl}\right)}{\bar{\sigma}_t\left(\tilde{\varepsilon}_t^{pl}\right)}(1-\alpha) - (1+\alpha) \quad (6)$$

$$\gamma = \frac{3(1-k_c)}{2k_c - 1} \quad (7)$$

Where $\bar{q}$ is the von Mises effective stress, $\bar{p}$ is the hydrostatic pressure, $\hat{\bar{\sigma}}_{max}$ is the maximum principle stress, $\bar{\sigma}_c$ and $\bar{\sigma}_t$ are the equivalent compressive and tensile stresses with their associated with the accumulated plastic strain $\left(\tilde{\varepsilon}_c^{\,pl}\right)$ and $\left(\tilde{\varepsilon}_t^{pl}\right)$, respectively, ζ is the deviation from the curve and taken as 0.1 in this model, σ_{t0} is the initial tensile strength, φ is the dilation angle (which is taken as 56° in this model), σ_{bo} and σ_{co} are the initial yield stress extracted from the bi-axial and uniaxial compression test, respectively, γ is a function that depends on k_c and it impacts the yield surface, k_c is the ratio of the second stress invariant on the tensile and compressive meridians at initial stress and is taken as 0.66 in this model and $\frac{\sigma_{bo}}{\sigma_{co}}$ is biaxial stress ratio and set at 1.05 in this model according to previous studies [36].

The stress-strain curve was constructed following the typical uniaxial stress-strain curve extracted from the compression and tension tests experiments. The strains are classified into elastic strains (ε_{0c}^{el}, ε_{0t}^{el}) for compression and tension, inelastic strain and cracking strain (ε_c^{in}, ε_t^{ck}), and plastic strain ($\tilde{\varepsilon}_c^{pl}$, $\tilde{\varepsilon}_t^{pl}$). The strains are composed based on the following equations.

$$\varepsilon_c^{in} = \varepsilon_c - \varepsilon_{0c}^{el} = \varepsilon_c - \frac{\sigma_c}{E_0} \quad (8)$$

$$\varepsilon_t^{ck} = \varepsilon_t - \varepsilon_{0t}^{el} = \varepsilon_t - \frac{\sigma_t}{E_0} \quad (9)$$

$$\tilde{\varepsilon}_c^{pl} = \varepsilon_c^{in} - \frac{d_c}{(1 - d_c)} \frac{\sigma_c}{E_0} \quad (10)$$

$$\tilde{\varepsilon}_t^{pl} = \varepsilon_t^{ck} - \frac{d_t}{(1 - d_t)} \frac{\sigma_t}{E_0} \quad (11)$$

The damage parameters are calculated based on the following equations for compression and tension (d_c, d_t) respectively

$$d_c = 1 - \left[\frac{\frac{\sigma_c}{E_0}}{0.2\varepsilon_c^{in} + \frac{\sigma_c}{E_0}} \right] \quad (12)$$

$$d_t = 1 - \frac{\sigma_t}{f_t} \quad (13)$$

Note that the damage variable varies from zero to one, where zero represents no damage and one represents total damage.

4.3 Steps, interaction, boundary conditions, and mesh elements

An explicit dynamic step was employed in this model to avoid the iterations made by the static steps due to the complexities of the material behaviour. The dynamic step has been recognised by multiple literatures to generate accurate results [37,38]. The benefit of using explicit dynamics is that the model will complete the results after each step and then start a new step. The amplitude was also introduced in the model to progressively apply the load according to the defined step, which was set to ten; therefore, the applied load will be divided equally (in our model, it is displacement control). Hence, the applied displacement for the columns is 10 mm, and the steps are 20 seconds, meaning the increment of steps will be 0.5 mm/second.

All contacts were introduced in the initial step. General contact was utilised for the whole model. The contact property options were defined, including tangential behaviour with a plenty friction coefficient of 0.3 and normal behaviour with hard contact with the choice of allowing the separation after the contact. The interaction between the UHPC and the aluminium tubes

was also defined as surface-to-surface contact. Furthermore, two reference points were constructed near the ends of the steel cap, and the coupling interaction was used to connect the reference points to the end plates, as shown in Fig. 15. Therefore, the boundary conditions are applied through the reference points. Two boundary conditions are defined in this model; the first is to be used as a pin support to prevent the column from any translation movements. The other boundary condition is set to apply the load through it, which has been allowed to move in one direction, and it can rotate as well to follow the bending of the column. The load was applied through a displacement control approach of 10 mm in one direction to mimic the axial load for all columns except for the beam which has about 25 mm of displacement at the ultimate load in the experimental results.

The element type used in this model for all parts is a solid with eight-node elements and reduced integration, as suggested by multiple studies (C3D8R) [39–41]. Usually, Shell elements are used to simulate the aluminium material (e.g. S4R). However, previous studies by Elchalakani et al. and Hassanein et al. [42,43] have demonstrated that the use of shell elements affected the interaction between the concrete and the steel tube, which may also be applicable in this study to the use of solid elements for aluminium tubes to improve the interactions. After that, each part was meshed separately, with a mesh size of 20 mm.

4.4 Results of FEM and validations

In order to validate the suggested numerical model, the load-axial displacement relationship obtained numerically from all specimens was compared to the experimental results, as shown in Fig. 17. Generally, there is a high agreement between the numerical and experimental results and the minor differences can be attributed to factors such as the imperfections of the experimental specimens. Furthermore, Table 6 compares the obtained experimental and numerical results of the ultimate load (P_u) and ultimate moment (M_u). The ratio average was introduced between the experimental and numerical results with an average of 0.99 for P_u and 0.94 for M_u. Additionally, a standard deviation (SD) of 0.016 and 0.112 for P_u and M_u were

determined, respectively, which indicates a very high correlation between the experimental results and FEM.

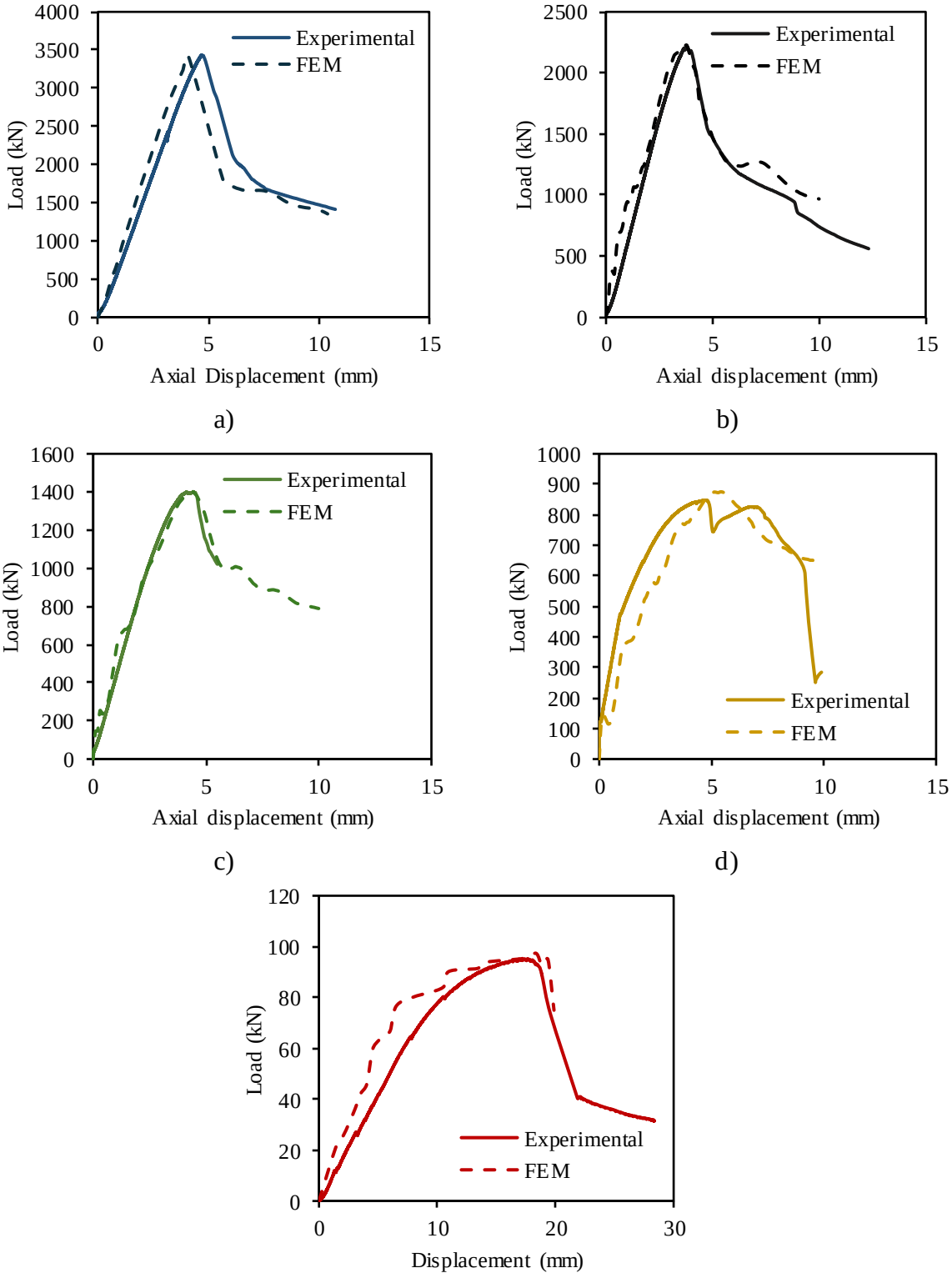
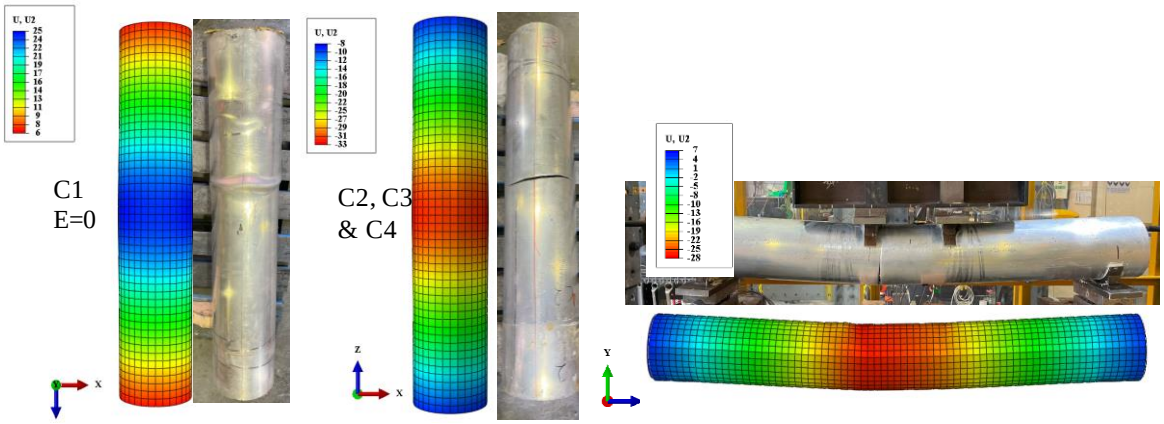


Fig. 17 Load-axial displacement for a) C1; b) C2; c) C3; d) C4; and e) B

It is also worth noting that the failure pattern and mode can be accurately predicted by FEM analysis as can be seen in Fig. 18(a), where the FEM failure pattern is juxtaposed with the experimental ones. A similar inference can also be stated for the case of the beam tested in this study.

Table 6 Summary and comparison of experimental and numerical results

Specimen ID	e (mm)	Ultimate load (experimental) $P_{u,exp}$ (kN)	Ultimate load (Numerical) $P_{u,FEM}$ (kN)	$P_{u,exp}/P_{u,FEM}$	Ultimate moment (experimental) $M_{u,exp}$ (kN.m)	Ultimate moment (Numerical) $M_{u,FEM}$ (kN.m)	$M_{u,exp}/M_{u,FEM}$
C1	0	3430.69	3413.12	1.01	4.01	5.26	0.76
C2	30	2212.17	2231.98	0.99	73.49	80.86	0.91
C3	60	1400.67	1404.09	1.00	101.88	97.77	1.04
C4	90	848.04	875.45	0.97	94.71	92.71	1.02
B	-	95.25	97.83	0.97	50.01	51.36	0.97
Average				0.99			0.94
SD				0.016			0.112



a) b)

Fig. 18 Comparison of failure patterns between numerical and experimental results for a) columns under concentric load and typical failure of eccentrically loaded columns; and b) beam

The load-moment interaction diagram (P-M) is generated based on the test results is compared with its counterpart generated from FEM results in Fig.19, which shows an excellent correlation between test and numerical results. Note that the axial load represents the maximum load carried by the columns, and the corresponding moment was calculated based on the loading eccentricity and the second-order effect due to the mid-height lateral displacement.

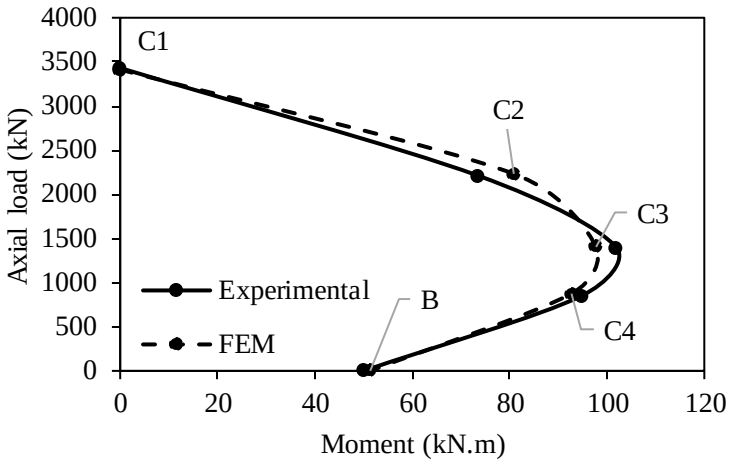


Fig. 19 P-M interaction diagram comparison of experimental results and numerical model

4.5 Parametric study

As the FEM results exhibited accurate correlation with test results, it was decided to perform an extensive parametric study by simulating numerically forty different specimens to investigate the influence of different variables such as concrete compressive strength and the skin dimensions on the structural performance of the UHPC-FDAT columns. Table 7 shows the dimensions and material properties of the control group, which are the same as those of the tested specimens experimentally and validated numerically in the present study. Moreover, the columns were categorised into four groups for numerical simulations by changing one parameter for each group. Each group is divided into two sub-groups, and each sub-group will be compared to the original columns in the control group in terms of the load-axial displacement relationship. The P-M interaction diagrams will also be formulated to compare the numerical model results with the control group for each variable.

The first group includes columns with different UHPC compressive strengths by changing the compressive strength to 90 MPa in the first sub-group and 60 MPa in the second sub-group, whereas the control group has a compressive strength of 125 MPa on average. This parameter is set to investigate how the strength of the concrete could change the performance of the columns under different eccentricities, while it is known that under pure axial compressive loads, the concrete strength influences the results significantly.

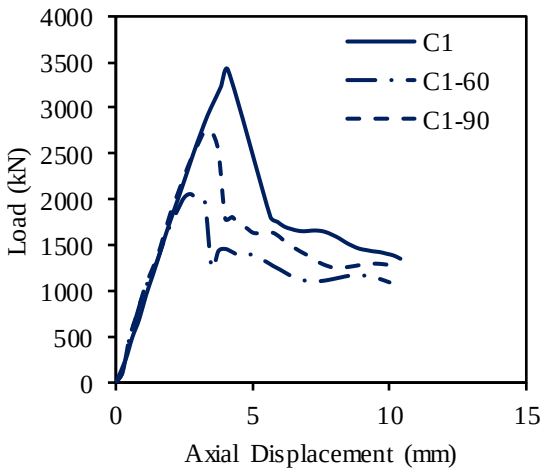
For studying the effect of the stiffness of the outer and inner tubes on the confinement of the concrete, for the second and third groups, the primary variable was the thickness of the outer tube (t_o) and the inner tube (t_i), which were set at 6 mm and 9 mm, whilst for the control group, it was 3 mm or both outer and inner tubes. Therefore, these parameters could give more insights into t.

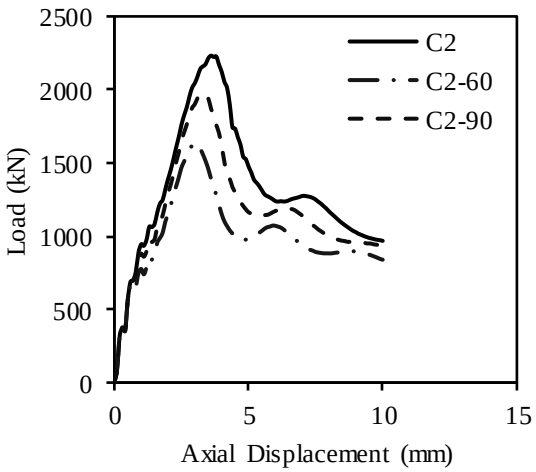
The last group will include the changes in the diameter of the inner tube, which will be changed from 80 mm in the control group to 40 mm and 120 mm. Hence, the hollow ratio variation will impact the concentrically loaded specimen, influencing the concrete area, which will vary the axial load capacity. However, this group aims to investigate the impact of the hollow ratio under different eccentricities for the aluminium columns.

Table 7 Dimensions and mechanical properties of the control group of the columns and parametric study

Specimen ID	Eccentricity (mm)	Outer tube				Inner tube				f'_c (MPa)	Length (mm)
		D_o (mm)	t_o (mm)	D_o/t_o	$f_{y,o}$ (MPa)	D_i (mm)	t_i (mm)	D_i/t_i	$f_{y,i}$ (MPa)		
Control group											
C1	0	203.2	3	67.73	210	80	3	26.67	219	125	1000
C2	30	203.2	3	67.73	210	80	3	26.67	219	125	1000
C3	60	203.2	3	67.73	210	80	3	26.67	219	125	1000
C4	90	203.2	3	67.73	210	80	3	26.67	219	125	1000
B	-	203.2	3	67.73	210	80	3	26.67	219	125	1500
Group 1											
C1-90	0	203.2	3	67.73	210	80	3	26.67	219	90	1000
C2-90	30	203.2	3	67.73	210	80	3	26.67	219	90	1000
C3-90	60	203.2	3	67.73	210	80	3	26.67	219	90	1000
C4-90	90	203.2	3	67.73	210	80	3	26.67	219	90	1000
B-90	-	203.2	3	67.73	210	80	3	26.67	219	90	1500
C1-60	0	203.2	3	67.73	210	80	3	26.67	219	60	1000
C2-60	30	203.2	3	67.73	210	80	3	26.67	219	60	1000
C3-60	60	203.2	3	67.73	210	80	3	26.67	219	60	1000
C4-60	90	203.2	3	67.73	210	80	3	26.67	219	60	1000
B-60	-	203.2	3	67.73	210	80	3	26.67	219	60	1500
Group 2											
C1-t_o6	0	203.2	6	33.87	210	80	3	26.67	219	125	1000
C2-t_o6	30	203.2	6	33.87	210	80	3	26.67	219	125	1000
C3- t_o6	60	203.2	6	33.87	210	80	3	26.67	219	125	1000

C4- t_o6	90	203.2	6	33.87	210	80	3	26.67	219	125	1000
B- t_o6	-	203.2	6	33.87	210	80	3	26.67	219	125	1500
C1- t_o9	0	203.2	9	22.58	210	80	3	26.67	219	125	1000
C2- t_o9	30	203.2	9	22.58	210	80	3	26.67	219	125	1000
C3- t_o9	60	203.2	9	22.58	210	80	3	26.67	219	125	1000
C4- t_o9	90	203.2	9	22.58	210	80	3	26.67	219	125	1000
B- t_o9	-	203.2	9	22.58	210	80	3	26.67	219	125	1500
					Group 3						
C1-t_i6	0	203.2	3	67.73	210	80	6	13.33	219	125	1000
C2- t_i6	30	203.2	3	67.73	210	80	6	13.33	219	125	1000
C3- t_i6	60	203.2	3	67.73	210	80	6	13.33	219	125	1000
C4- t_i6	90	203.2	3	67.73	210	80	6	13.33	219	125	1000
B- t_i6	-	203.2	3	67.73	210	80	6	13.33	219	125	1500
C1- t_i9	0	203.2	3	67.73	210	80	9	8.89	219	125	1000
C2- t_i9	30	203.2	3	67.73	210	80	9	8.89	219	125	1000
C3- t_i9	60	203.2	3	67.73	210	80	9	8.89	219	125	1000
C4- t_i9	90	203.2	3	67.73	210	80	9	8.89	219	125	1000
B- t_i9	-	203.2	3	67.73	210	80	9	8.89	219	125	1500
					Group 4						
C1-D_i120	0	203.2	3	67.73	210	120	3	40.00	219	125	1000
C2-D_i120	30	203.2	3	67.73	210	120	3	40.00	219	125	1000
C3-D_i120	60	203.2	3	67.73	210	120	3	40.00	219	125	1000
C4-D_i120	90	203.2	3	67.73	210	120	3	40.00	219	125	1000
B-D_i120	-	203.2	3	67.73	210	120	3	40.00	219	125	1500
C1-D_i40	0	203.2	3	67.73	210	40	3	13.33	219	125	1000
C2-D_i40	30	203.2	3	67.73	210	40	3	13.33	219	125	1000
C3-D_i40	60	203.2	3	67.73	210	40	3	13.33	219	125	1000
C4-D_i40	90	203.2	3	67.73	210	40	3	13.33	219	125	1000
B-D_i40	-	203.2	3	67.73	210	40	3	13.33	219	125	1500





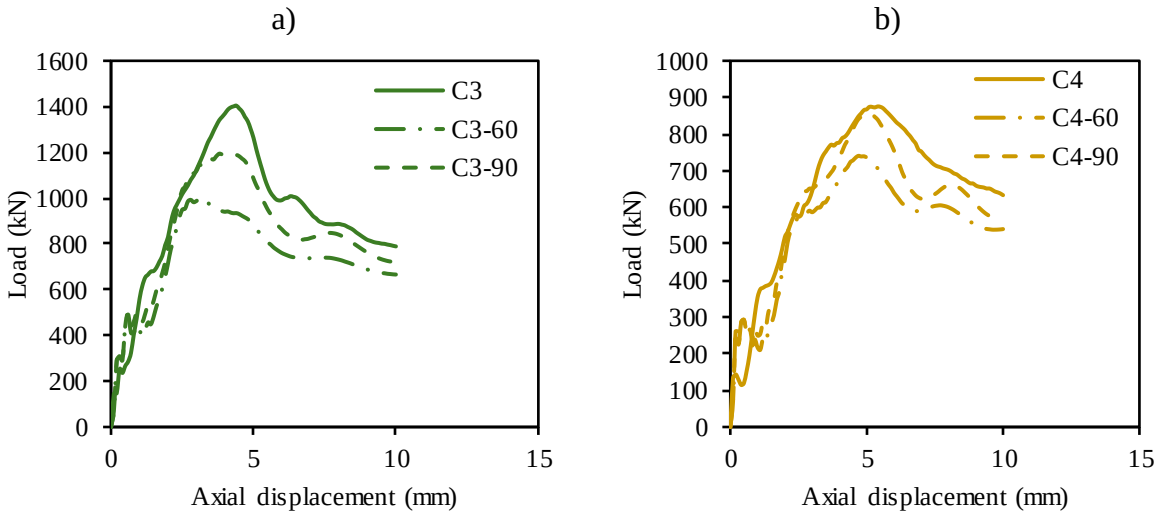
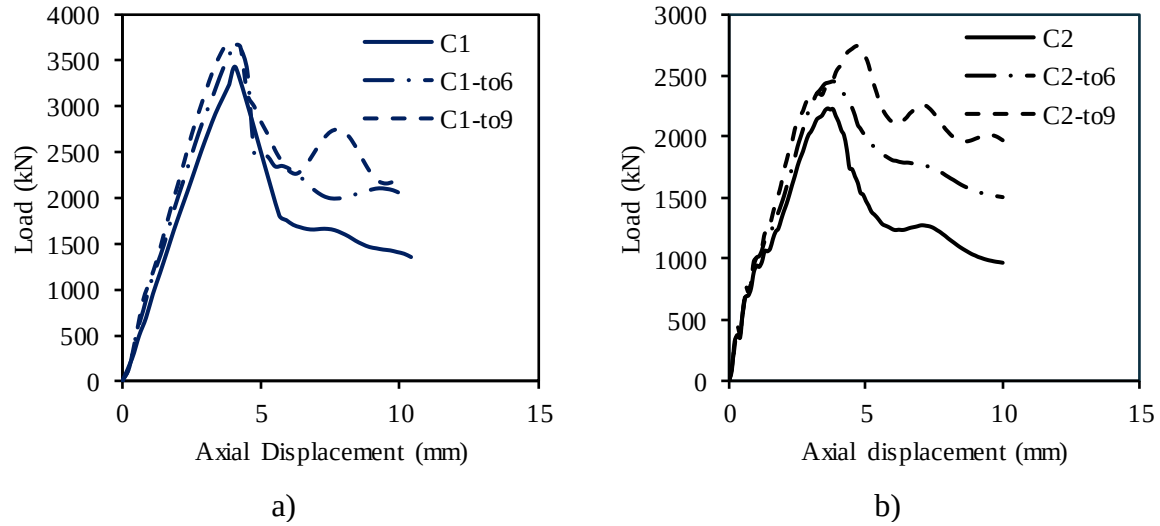
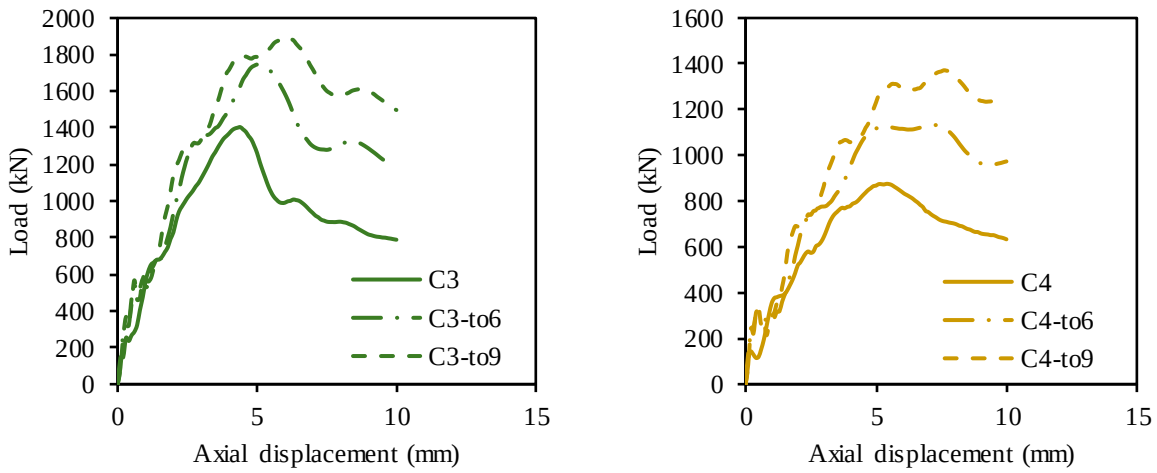


Fig. 20 load-axial displacement relationships for all columns of group one under different eccentricities a) e = 0; b) e = 30 mm; c) e = 60 mm; and d) e = 90 mm

Fig. 20 shows the load-axial displacement relationships for group one which has compressive strength variations. It can be clearly seen in Fig. 20(a) that reducing the compressive strength to 90 MPa and 60 MPa decreases the ultimate axial load by 19.66% and 33.87%, respectively, under pure axial load. However, the gap between the ultimate axial load and different compressive strengths has been reduced to 3.14% and 15.54% for 90 MPa and 60 MPa, respectively, for columns with an eccentricity of 90 mm. Therefore, the compressive strength influences the concentrically loaded columns more than columns under different eccentricities.

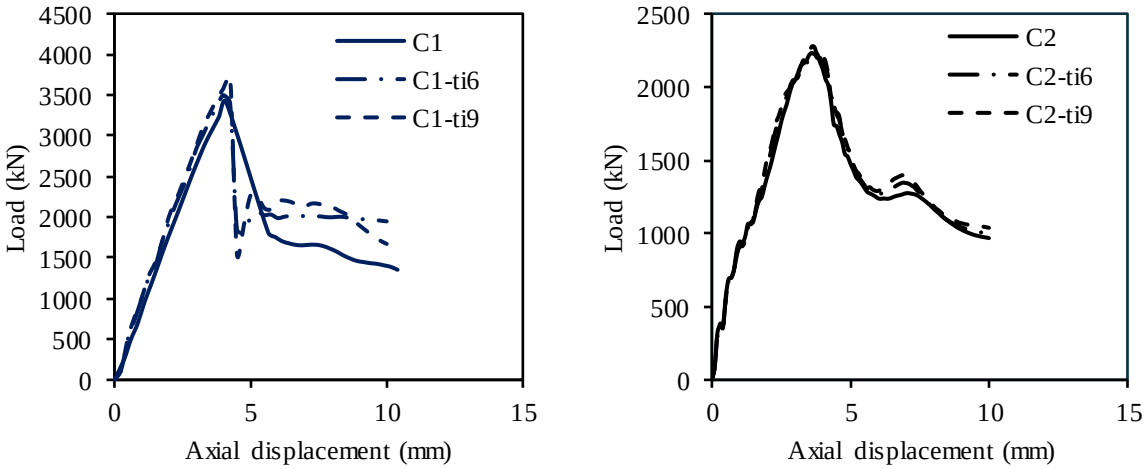




c) d)

Fig. 21 load-axial displacement relationships for all columns of group two under different eccentricities a) e = 0; b) e = 30 mm; c) e = 60 mm; and d) e = 90 mm

Fig. 21 illustrates the second group column results with variations in the outer tube thickness. Columns with thicker outer tubes exhibited higher axial load capacity for all columns under different eccentricities. Notably, increasing the eccentricity increased the difference between the control group and group two. Therefore, the higher thickness of the outer tube provided more confinement for columns that exhibited higher eccentricity. However, the effect of the thickness of the inner tube is shown in Fig. 22, which indicates that the inner tube thickness has less influence on the overall stiffness of the columns under different eccentricities as the inner tube lies far from the neutral axis of the columns which has suffered less strain compared to the outer tube. However, the thickness of the inner tube resulted in a slight increase in the axial load for higher eccentrically loaded specimens, as indicated in Fig. 22(d).



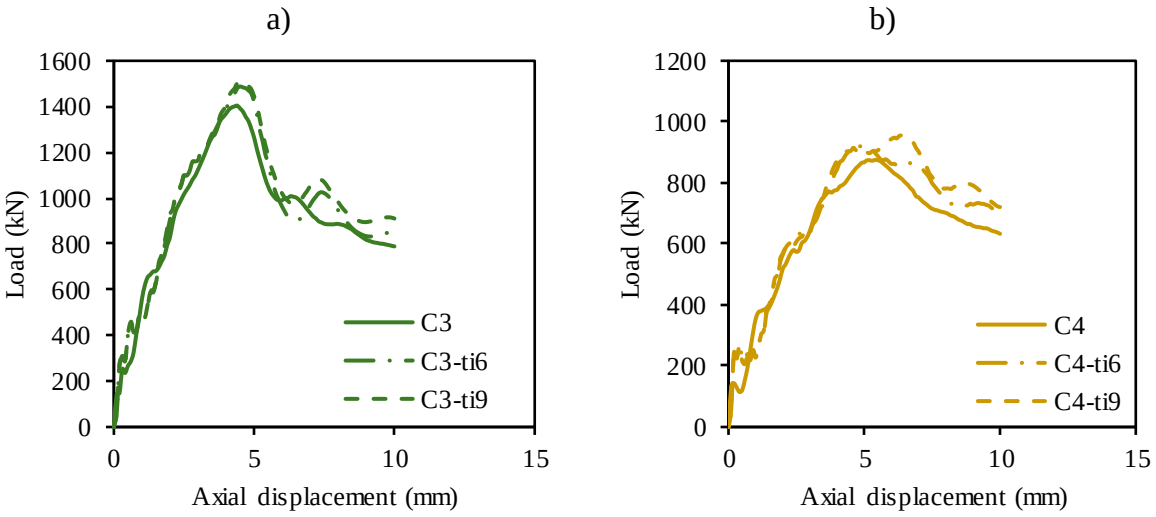
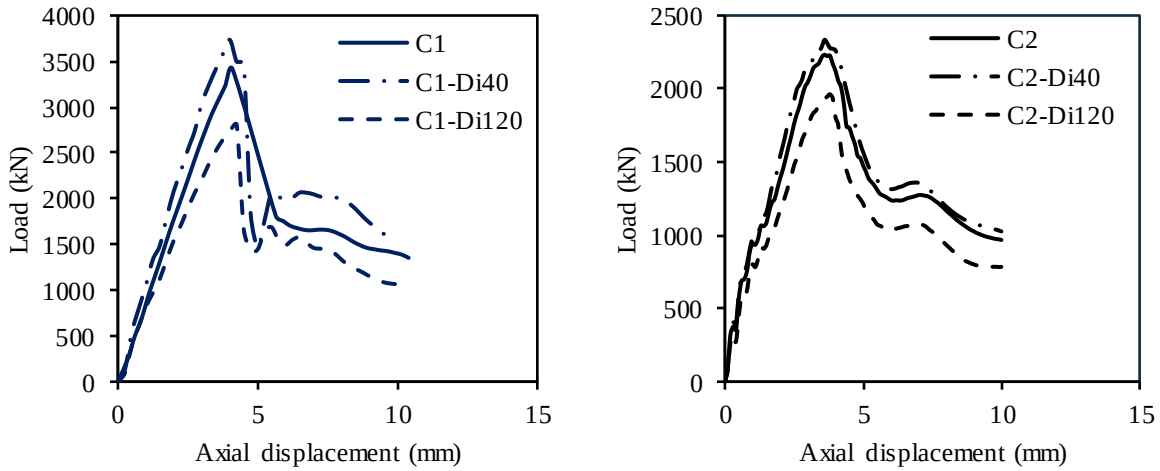
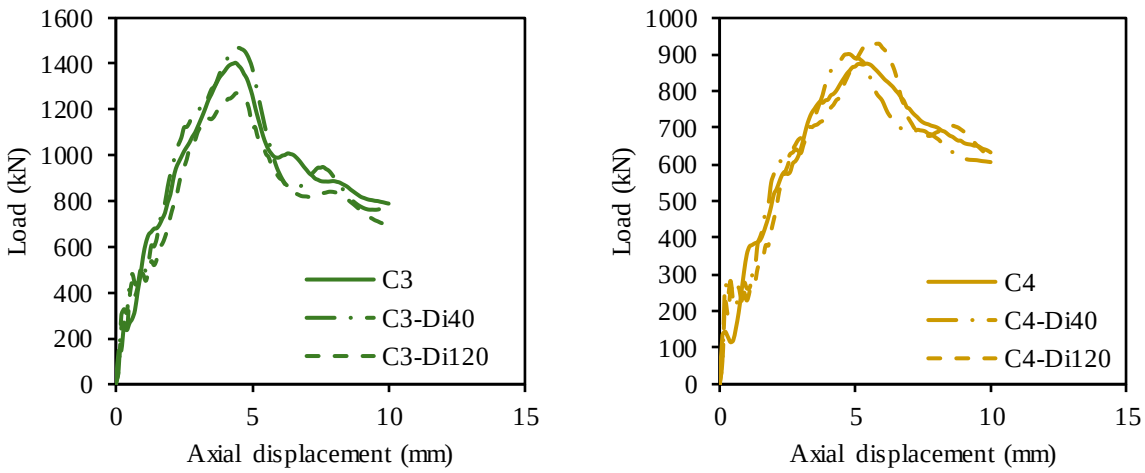


Fig. 22 load-axial displacement relationships for all columns of group three under different eccentricities a) e = 0; b) e = 30 mm; c) e = 60 mm; and d) e = 90 mm

The effect of the inner tube diameter (D_i) is illustrated in Fig. 23. As an increase in D_i influences the concrete area, a higher D_i exhibited the lower axial load capacity. It is noticed that the column with a high eccentricity of 90 mm shows almost similar results for different diameters. Thus, a higher diameter has a minor impact on the behaviour of the columns where the neutral axis lies far from the centroid of the section.





c) d)

Fig. 23 load-axial displacement relationships for all columns of group four under different eccentricities a) e = 0; b) e = 30 mm; c) e = 60 mm; and d) e = 90 mm

The P-M interaction diagram for all groups compared to the control group is presented in Fig. 24. Fig. 24(a) shows that the compressive strength has a very high impact on the columns under concentric load and low eccentricity while the effect gradually reduces toward the pure bending point. Moreover, the thickness of the outer tube exhibited similar behaviour while the impact on the pure bending point increased, as shown in Fig. 24(b). Additionally, the inner tube thickness has almost no effect on the overall P-M interaction diagram construction, as shown in Fig. 24(c). Furthermore, the effect of the diameter of the inner circular void is more pronounced for the columns under concentric load or loaded with a low eccentricity, while there is almost no effect on columns loaded under high eccentricity and the beam pure bending only. Overall, the compressive strength affects the concentrically loaded columns as well as the inner tube diameter, which changes the area of the concrete, while outer tube thickness has a significant impact on both concentrically and eccentrically loaded columns due to the anticipated confinement provided by the outer tube.

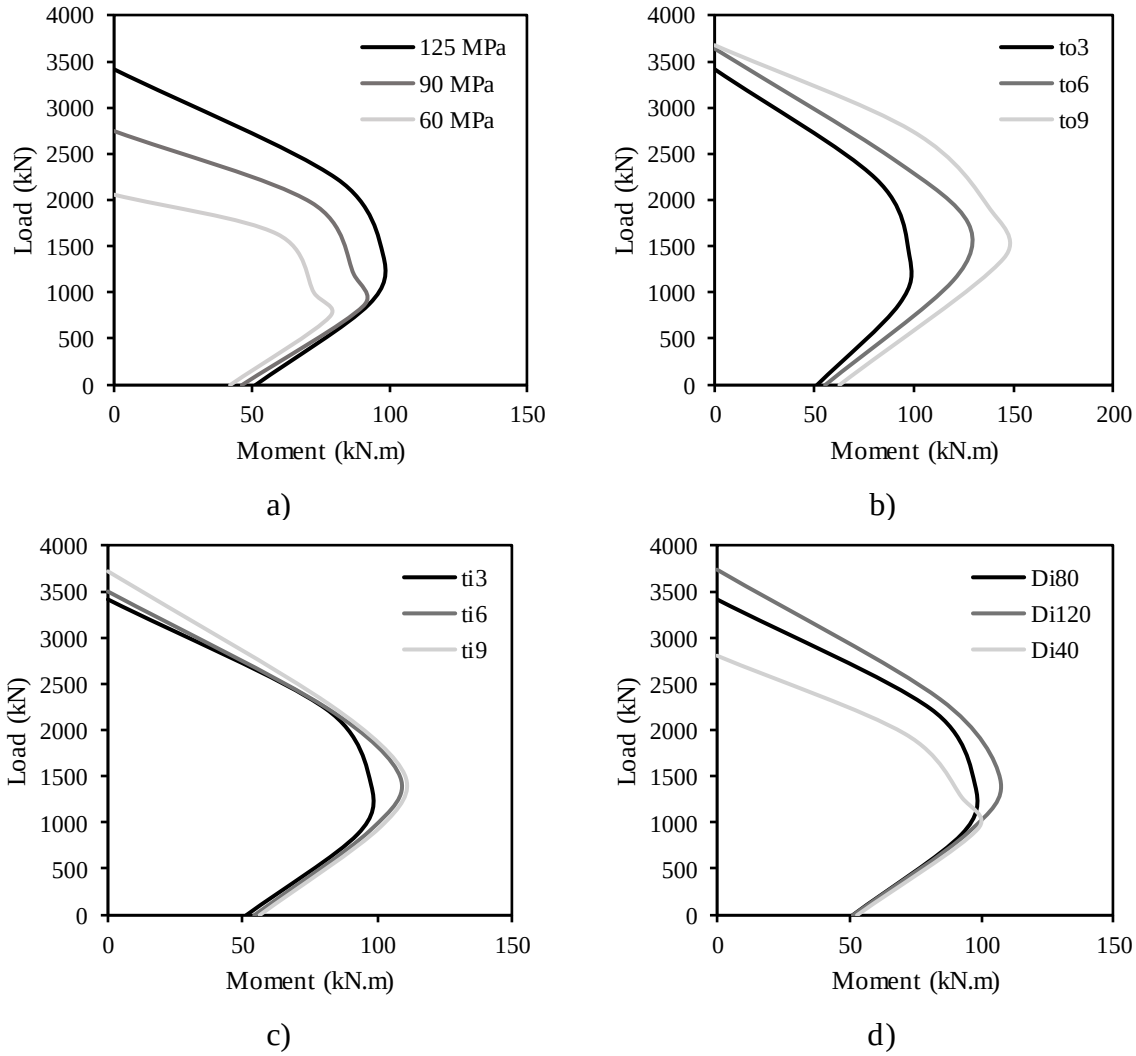


Fig. 24 P-M interaction diagrams for a) group one (strength effects); b) group two (outer diameter effects); group three (inner tube effects); and d) group four (inner diameter effects)

5 Conclusion

In this study, UHPC-FDAT composite which enhances the structural performance and resistance to corrosion required for long-term durability and structural integrity, particularly in marine and coastal structures, has been investigated both experimentally and numerically. The study involves testing columns and a beam under combined loading conditions (concentric, eccentric and four-point bending). Four full-scale columns and a beam were tested experimentally, and forty-five columns were modelled after validating the FEM model with the experimental results. Various parameters were considered, including the UHPC

compressive strength, inner tube thickness, outer tube thickness and inner diameter (hollow ratio ratio). The following conclusions can be made based on these investigations:

- Increasing the loading eccentricity leads to an increase in the lateral displacement at the mid-height of the columns with a decrease in the corresponding ultimate load.
- The predominant failure pattern at the compression face of the columns subjected to concentrically applied load is the local buckling failure associated with crushing of the sandwiched concrete, whilst the failure pattern changed when increasing the loading eccentricity by exhibiting a rupture of the outer aluminium tube at the tension face with an increase of cracking in the sandwiched concrete.
- The proposed numerical model correlates very well with the test results regarding the failure pattern, ultimate load, and axial displacement.
- The parametric study showed that the compressive strength of UHPC has the highest influence on the concentrically loaded columns. Moreover, the increase in the outer tube thickness achieved the highest ultimate load while increasing the corresponding loading eccentricity.

Acknowledgments:

The Australian Research Council grant number [DP 21001425] partially funded the research.

References

[1] E. Georgantzia, M. Gkantou, G.S. Kamaris, Aluminium alloys as structural material: A review of research, Eng Struct 227 (2021) 111372. https://doi.org/10.1016/j.engstruct.2020.111372.

[2] M. Latour, M. D'aniello, R. Landolfo, G. Rizzano, Experimental and numerical study of double-skin aluminium foam sandwich panels in bending, Thin-Walled Structures 164 (2021) 107894.

[3] M. Elchalakani, X.-L. Zhao, R. Grzebieta, Tests on concrete filled double-skin (CHS outer and SHS inner) composite short columns under axial compression, Thin-Walled Structures 40 (2002) 415–441. https://doi.org/10.1016/S0263-8231(02)00009-5.

[4] M. Ahmed, Q.Q. Liang, A. Hamoda, M. Arashpour, Behavior and design of thin-walled double-skin concrete-filled rectangular steel tubular short and slender columns with external stainless-steel tube incorporating local buckling effects, Thin-Walled Structures 170 (2022) 108552.

[5] S. Bin Ali, G.S. Kamaris, M. Gkantou, K.D. Kansara, Concrete-filled and bare 6082-T6 aluminium alloy tubes under in-plane bending: Experiments, finite element analysis and design recommendations, Thin-Walled Structures 172 (2022) 108907. https://doi.org/10.1016/j.tws.2022.108907.

[6] E. Georgantzia, S. Bin Ali, M. Gkantou, G.S. Kamaris, K.D. Kansara, W. Atherton, Flexural buckling performance of concrete-filled aluminium alloy tubular columns, Eng Struct 242 (2021) 112546. https://doi.org/10.1016/j.engstruct.2021.112546.

[7] S. Bin Ali, G.S. Kamaris, M. Gkantou, Flexural behaviour of concrete-filled double skin aluminium alloy tubes, Eng Struct 272 (2022) 114972. https://doi.org/10.1016/j.engstruct.2022.114972.

[8] Y. Zhao, J. Cao, S. Yang, Y. Zhu, Y. Zhang, X. Yang, Dynamic tensile behaviour of 7A04-T6 aluminium alloy at elevated temperatures, Structures 64 (2024) 106535. https://doi.org/10.1016/j.istruc.2024.106535.

[9] Z. Deng, J. Guo, J. Yu, B. Liu, Axial compression performance of coral concrete-filled aluminium tube (CCFAT) square stub columns, Case Studies in Construction Materials 15 (2021) e00697. https://doi.org/10.1016/j.cscm.2021.e00697.

[10] E. Georgantzia, S. Bin Ali, M. Gkantou, G.S. Kamaris, K. Kansara, W. Atherton, Structural response of aluminium alloy concrete filled tubular columns, 4 (2021) 614–620. https://doi.org/10.1002/cepa.1339.

[11] X. Zeng, C. Ning, W. Zeng, B. Xu, Numerical and experimental studies on bending behavior of circular aluminium-concrete-steel double skin tubular cross-sections and bending capacity design approach, Journal of Building Engineering 91 (2024) 109524. https://doi.org/10.1016/j.jobe.2024.109524.

[12] E. Georgantzia, M. Gkantou, G.S. Kamaris, Aluminium alloys as structural material: A review of research, Eng Struct 227 (2021) 111372. https://doi.org/10.1016/j.engstruct.2020.111372.

[13] S. Bin Ali, G.S. Kamaris, M. Gkantou, Flexural behaviour of concrete-filled double skin aluminium alloy tubes, Eng Struct 272 (2022). https://doi.org/10.1016/j.engstruct.2022.114972.

[14] S. Bin Ali, G.S. Kamaris, M. Gkantou, Flexural buckling behaviour of concrete-filled double skin aluminium alloy columns, Eng Struct 275 (2023). https://doi.org/10.1016/j.engstruct.2022.115316.

[15] F. Zhou, B. Young, Concrete-filled double-skin aluminum circular hollow section stub columns, Thin-Walled Structures 133 (2018) 141–152. https://doi.org/10.1016/j.tws.2018.09.037.
[16] D. Xu, J. Tang, X. Hu, Y. Zhou, C. Yu, F. Han, J. Liu, Influence of silica fume and thermal curing on long-term hydration, microstructure and compressive strength of ultra-high performance concrete (UHPC), Constr Build Mater 395 (2023) 132370. https://doi.org/https://doi.org/10.1016/j.conbuildmat.2023.132370.
[17] F. Lo Monte, L. Ferrara, Tensile behaviour identification in Ultra-High Performance Fibre Reinforced Cementitious Composites: indirect tension tests and back analysis of flexural test results, Mater Struct 53 (2020) 145. https://doi.org/10.1617/s11527-020-01576-8.
[18] M.G. Sohail, R. Kahraman, N. Al Nuaimi, B. Gencturk, W. Alnahhal, Durability characteristics of high and ultra-high performance concretes, Journal of Building Engineering 33 (2021) 101669. https://doi.org/https://doi.org/10.1016/j.jobe.2020.101669.
[19] A. Haidar, A. Fam, Behaviour of axially loaded UHPC-filled double skin steel tubular columns, J Constr Steel Res 220 (2024) 108811. https://doi.org/https://doi.org/10.1016/j.jcsr.2024.108811.
[20] J.-B. Yan, X. Yang, Y. Luo, P. Xie, Y.-B. Luo, Axial compression behaviours of ultra-high performance concrete-filled Q690 high-strength steel tubes at low temperatures, Thin-Walled Structures 169 (2021) 108419. https://doi.org/https://doi.org/10.1016/j.tws.2021.108419.
[21] V.I. Patel, Q.Q. Liang, M.N.S. Hadi, Numerical study of circular double-skin concrete-filled aluminum tubular stub columns, Eng Struct 197 (2019) 109418. https://doi.org/10.1016/j.engstruct.2019.109418.
[22] X. Yan, M. Ahmed, M. Hassanein, M. He, Performance analysis and design of circular high-strength concrete-filled double-skin aluminum tubular short columns under axial loading, Structural Concrete 24 (2023) 5677–5696. https://doi.org/10.1002/suco.202200768.
[23] X.-F. Yan, X. Yan, M. Ahmed, M. Ahmed, M.-N. He, M. He, Behavior and design of axially loaded high-strength concrete-filled circular aluminum tubular short columns, Structures 44 (2022) 357–371. https://doi.org/10.1016/j.istruc.2022.07.088.
[24] ASTM B221, Standard Specification for Aluminum and Aluminum-Alloy Extruded Bars, Rods, Wire, Profiles, and Tubes, ASTM International, West Conshohocken, PA, 2012. https://doi.org/10.1520/B0221-12.
[25] ASTM E8, Standard Test Methods for Tension Testing of Metallic Materials, ASTM International, West Conshohocken, PA, 2022. https://doi.org/10.1520/E0008_E0008M-22.
[26] Standards Australia, AS1012.9:2014 Methods of testing concrete Method 9: Compressive strength tests — Concrete , mortar and grout specimens, Standards Australia International Ltd, Sydney. (2014) 1–13.
[27] Dassault, Abaqus cae, (2017).
[28] P. Ayough, Z. Ibrahim, N.H.R. Sulong, P.-C. Hsiao, M. Elchalakani, M. Elchalakani, Numerical analysis of square concrete-filled double skin steel tubular columns with rubberized concrete, Structures 32 (2021) 1026–1047. https://doi.org/10.1016/j.istruc.2021.03.054.
[29] M. Elchalakani, V.I. Patel, A. Karrech, M.F. Hassanein, S. Fawzia, B. Yang, Finite element simulation of circular short CFDST columns under axial compression, Structures 20 (2019) 607–619. https://doi.org/10.1016/j.istruc.2019.06.004.

[30] M. Pagoulatou, T. Sheehan, X.H. Dai, D. Lam, Finite element analysis on the capacity of circular concrete-filled double-skin steel tubular (CFDST) stub columns, Eng Struct 72 (2014) 102–112. https://doi.org/10.1016/j.engstruct.2014.04.039.
[31] M.F. Hassanein, M. Elchalakani, A. Karrech, V.I. Patel, B. Yang, Behaviour of Concrete-filled Double-skin Short Columns Under Compression Through Finite Element Modelling: SHS Outer and SHS Inner Tubes, Structures 14 (2018) 358–375. https://doi.org/10.1016/j.istruc.2018.04.006.
[32] W. Ramberg, W.R. Osgood, Description of stress-strain curves by three parameters, 1943.
[33] H.N. Hill, Determination of stress-strain relations from" offset" yield strength values, 1944.
[34] J. Lubliner, J. Oliver, S. Oller, E. Oñate, A plastic-damage model for concrete, Int J Solids Struct 25 (1989) 299–326.
[35] J. Lee, G.L. Fenves, Plastic-damage model for cyclic loading of concrete structures, J Eng Mech 124 (1998) 892–900.
[36] Z. Hashin, A. Rotem, A fatigue failure criterion for fiber reinforced materials, J Compos Mater 7 (1973) 448–464.
[37] K.S. Al-Jabri, A. Seibi, A. Karrech, Modelling of unstiffened flush end-plate bolted connections in fire, J Constr Steel Res 62 (2006) 151–159.
[38] H. Yu, I.W. Burgess, J.B. Davison, R.J. Plank, Numerical simulation of bolted steel connections in fire using explicit dynamic analysis, J Constr Steel Res 64 (2008) 515–525.
[39] X.H. Dai, D. Lam, N. Jamaluddin, J. Ye, Numerical analysis of slender elliptical concrete filled columns under axial compression, Thin-Walled Structures 77 (2014) 26–35.
[40] M.F. Hassanein, V.I. Patel, Round-ended rectangular concrete-filled steel tubular short columns: FE investigation under axial compression, J Constr Steel Res 140 (2018) 222–236.
[41] X. Dai, D. Lam, Numerical modelling of the axial compressive behaviour of short concrete-filled elliptical steel columns, J Constr Steel Res 66 (2010) 931–942.
[42] M. Elchalakani, A. Karrech, M.F. Hassanein, B. Yang, Plastic and yield slenderness limits for circular concrete filled tubes subjected to static pure bending, Thin-Walled Structures 109 (2016) 50–64.
[43] M.F. Hassanein, M. Elchalakani, A. Karrech, V.I. Patel, B. Yang, Behaviour of concrete-filled double-skin short columns under compression through finite element modelling: SHS outer and SHS inner tubes, in: Structures, Elsevier, 2018: pp. 358–375.

Chapter 5

Background

the high-performance geopolymer concrete-filled double-skin stainless steel tube (HPGC-FDST) columns under concentric, eccentric and flexural loading conditions. For this, a rational orthogonal array approach was adopted to develop high-performance geopolymer concrete (HPGC) in a previous study. Then, the optimum HPGC mix design was combined with stainless steel tubes, which provides significant advantages in harsh marine environments in resisting both corrosion and chemical deterioration. Five specimens were constructed to be tested experimentally. Moreover, finite elements modelling (FEM) was conducted to simulate the fabricated columns in the experimental program. Furthermore, the interaction diagram was plotted analytically to assess the capabilities of existing models and predict the results accurately.

List of Manuscripts

Alameri, M., Mohamed Ali, M. S., Elchalakani, M., & Sheikh, A. (2024). "Investigation of high-performance geopolymer concrete-filled double-skin columns under combined loading conditions" Submitted to *Journal of Constructional Steel Research* (under review)

Statement of Authorship

Title of Paper	Investigation of high-performance geopolymer concrete-filled double-skin columns under combined loading conditions
Publication Status	☐ Published ☐ Accepted for Publication ☑ Submitted for Publication ☐ Unpublished and Unsubmitted work written in manuscript style
Publication Details	Alameri, M., Mohamed Ali, M. S., Elchalakani, M., & Sheikh, A. (2024). "Investigation of high-performance geopolymer concrete-filled double-skin columns under combined loading conditions" Submitted to Journal of Constructional Steel Research

Principal Author

Name of Principal Author (Candidate)	Mohammad Alameri		
Contribution to the Paper	Conceptualisation, methodology, and manuscript writing and revision		
Overall percentage (%)	80%		
Certification:	This paper reports on original research I conducted during the period of my Higher Degree by Research candidature and is not subject to any obligations or contractual agreements with a third party that would constrain its inclusion in this thesis. I am the primary author of this paper.		
Signature		Date	24-10-2024

Co-Author Contributions

Name of Co-Author	M.S. Mohamed Ali		
Contribution to the Paper	Supervision, conceptualisation, methodology, and manuscript revision (10%)		
Signature		Date	24-10-2024

Name of Co-Author	Mohamed Elchalakani		
Contribution to the Paper	Supervision, conceptualisation, methodology, and manuscript revision (5%)		
Signature		Date	28-10-2024

Name of Co-Author	Abdul Sheikh		
Contribution to the Paper	Supervision, conceptualisation, methodology, and manuscript revision (5%)		
Signature		Date	29-10-2024

Investigation of high-performance geopolymer concrete-filled double-skin columns under combined loading conditions

Mohammad Alameri[1,*], M.S. Mohamed Ali[1], Abdul Sheikh[1], Mohamed Elchalakani[2]

[1] *School of Civil, Environmental and Mining Engineering, The University of Adelaide, Adelaide, Australia*

[2] *Department of Civil, Environmental and Mining Engineering, The University of Western Australia, Perth, Australia*

[*] *Corresponding author E-mail: Mohammad.alameri@adelaide.edu.au*

Abstract

This study investigated the high-performance geopolymer concrete-filled double-skin stainless steel tube (HPGC-FDST) columns under concentric, eccentric and flexural loading conditions. For this, a rational orthogonal array approach was adopted to develop high-performance geopolymer concrete (HPGC) in a previous study. Then, the optimum HPGC mix design was combined with stainless steel tubes, which provides significant advantages in harsh marine environments in resisting both corrosion and chemical deterioration. Four short columns having a height of 900 mm were tested under different eccentricities to depth ratios (0, 0.06, 0.267 and 0.467) and a beam having a length of 1200 mm was also subjected to three-point flexural bending to complete the axial-moment interaction diagram experimentally. Additionally, finite elements modelling (FEM) was conducted to simulate the fabricated columns in the experimental program. The results showed an agreement between the numerical and experimental behaviour of the columns. Moreover, the interaction diagram was plotted analytically to assess the capabilities of existing models and predict the results accurately. The outcome also showed a good agreement between the experimental and analytical results.

Keywords: High-performance geopolymer concrete; Axial moment interaction diagram; Finite element model; Concrete-filled double skin steel tubes; durability

1 Introduction

Conventional ordinary Portland cement concrete (OPCC) and carbon steel are prone to rapid degradation due to the effect of corrosion, chemical attack, and chloride exposure. Thus, in Australia alone, the total bill for maintaining against corrosion costs is about $78 billion, which represents about 4.25% of the gross domestic product (GDP) [1]. Therefore, this implies the necessity for developing innovative concrete materials with superior durability characteristics and high load-bearing capacity.

Cement production accounts for approximately 5% of global greenhouse gas emissions, making it the third-largest industry producer of CO_2 [2]. Therefore, the initiation of geopolymer concrete (GPC) has revolutionised concrete technology, driving the industry toward more efficient and sustainable practices. Notably, GPC exhibits mechanical and durability characteristics comparable to conventional concrete [3], making it a viable alternative for sustainable construction. GPC relies on aluminosilicate precursors for binders, such as ground-granulated blast furnace slag (GGBS) [4], fly ash [5], and metakaolin [6], which are abundant in aluminosilicate sources that can be activated by alkali-activated materials [7]. However, it is important to note that most of the existing research has predominantly concentrated on the material properties of GPC, with less emphasis placed on its application in structural components.

Expanding the research field to include the investigation of the structural members made of GPC should be performed before starting to use GPC in real-life applications such as bridges and residential buildings. Multiple barriers prevent the wide use of GPC, such as the lack of appropriate standards and codes of practice [8], the complexity involved in handling GPC in situ [9], the special curing regime used [10], and the safety challenges [11].

Recently, the utilisation of GPC in the production of structural members has been explored to measure the applicability of replacing conventional concrete with GPC. One of the most

important structural members is the columns; Sumajouw et al. [12] have fabricated and tested twelve fly ash based geopolymer columns under eccentric loading conditions with two different compressive strengths of 40 MPa and 60 MPa. It was found that the design provisions for normal concrete prescribed by the design code of Australian standard AS3600 [13] and American Concrete Institute Building Code ACI 318-02 [14] can be applied conservatively. Moreover, Albitar et al. [15] constructed and tested fly ash based geopolymer short and slender columns under concentric and eccentric loadings and the failure mode was found to be similar to ordinary Portland cement concrete (OPCC) columns. Another finding is that the design provision contained in AS3600 has overestimated the interaction load-moment (P-M) curve by 25% for short columns and 30% for slender columns. Moreover, several experimental studies [16–20] have investigated the structural performance of the GPC columns, where mostly the columns failed in a brittle manner. Therefore, the confinement provided by the outer steel tube has been examined by Fang and Visintin [21]. In their study, eight circular and square concrete-filled tube columns were tested under combined axial-flexural loading conditions, and it was found that the brittle failure was prevented because of the provision of the outer steel tube, which enhanced both the strength and ductility of GPC. Additionally, increasing the ductility by incorporating fibres into the concrete matrix could alter the brittle behaviour of the GPC columns. Farhan et al. [22] have tested sixteen ambient cured steel fibre-reinforced geopolymer columns under different loading scenarios (concentric, eccentric, and four-point bending), where adding hybrid fibres has improved both the ductility and the axial peak load.

Concrete-filled double-skin tube (CFDST) members were formed by removing the central concrete of the concrete-filled tube (CFT) and replacing it with a hollow tube, which slightly contributed to the flexural strength [23]. CFDST has similar advantages to CFT but provides a lightweight configuration with higher bending stiffness [24]. CFDST can be constructed by forming different configurations, such as a combination of square and circular sections, as

shown in Fig. 1 [25–27]. Different concrete types have been used to fabricate CFDST columns such as normal concrete [24], high strength concrete [28], ultra-high strength concrete [29], and rubberised concrete [30]. These experimental studies showed that the CFDST columns are characterised by increased energy absorption and ductility with the benefit of being lightweight. Moreover, high-rise bridge piers in Japan are one of the implementations of wide applications of CFDST columns [31].

In several investigations, the normal steel tubes were replaced by stainless steel tubes as stainless steel provides superior durability, high ductility and improved fire resistance [32–34]. Note that although the initial cost of stainless steel is high, the life-cycle cost, which includes the initial cost and the maintenance cost during the structure's life span, makes it economical.

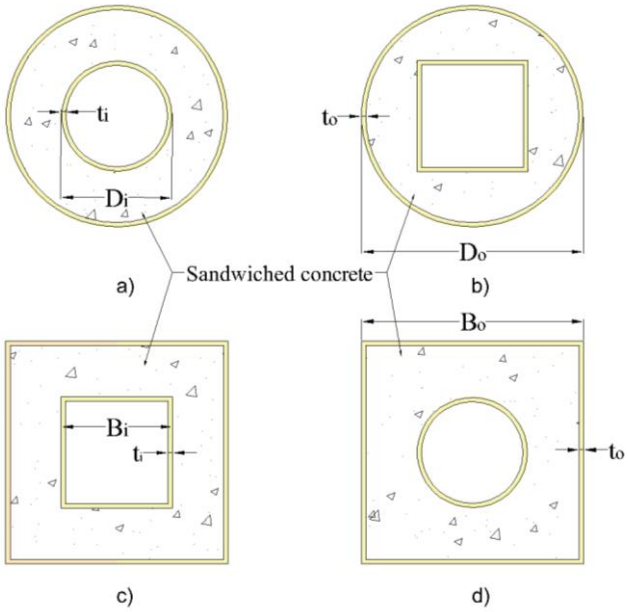


Fig. 1 Cross sections of most common CFDST

This study aims to experimentally investigate the construction of high-performance geopolymer concrete-filled double-skin stainless steel tube (HPGC-FDST) columns for more sustainable and cost-effective technology. Furthermore, GPC proposes enhanced durability due to its lower calcium content, reducing susceptibility to sulphate attacks, while the stainless-

steel jacket provides superior resistance to chloride-induced corrosion, making this combination ideal for marine environments. The columns will be investigated under concentric, eccentric, and three-point bending loading conditions. The target strength of the GPC is 60 MPa to be considered high-performance geopolymer concrete (HPGC). This experimental program concentrates on the load-deflection behaviour, stress-strain behaviour, and P-M interaction curve experimentally and theoretically, comparing the results with the existing provision and finally verifying the numerical models by the experimental results.

2 Methodology

2.1 Material properties

2.1.1 HPGC

2.1.1.1 Material used

The binder of the geopolymer mix was made of ground granulated furnace blast slag (GGBS) and silica fume (SF). This study used quartz sand (QS) with a diameter range of 0.075 mm to 1.18 mm and a subangular to round shape as fine aggregate. Table 1 shows the chemical composition of the binder and the fine aggregate. The potassium-based alkaline activator solution (AAS) is composed of potassium silicate (K_2SiO_3) which will be called (PS) and potassium hydroxide (KOH) which will be called (PH). The PS has a modulus of silicate (Ms) equal to 1.5 and the PH has a molarity of 13.95, wherein the PS to the PH ratio equals 3. Ace Chemicals Australia provided AAS in its liquid state. The total water is the free demineralised water as well as the water content in the potassium silicate which has 51.5% water content and the potassium hydroxide which has 53% water content. The total water also includes superplasticiser (SP), known as high range water retarder and 58.3% water content by mass. As shown in Table 2, two types of steel fibres have been utilised in this study to enhance the ductility performance of the GPC.

Table 1 Chemical compositions of the materials

	SiO_2	TiO_2	Al_2O_3	Fe_2O_3	MgO	CaO	Na_2O	K_2O	P_2O_5	SO_3
GGBS	35.10	0.57	13.59	0.98	5.36	41.52	0.14	0.33	0.04	0.10
SF	92.35	0.01	0.36	0.78	0.36	0.54	0.19	0.52	0.31	0.04
Quartz sand	93.48	0.04	0.06	0.06	0.03	0.02	0.039	0.02	0.01	0.01

Table 2 Physical properties of the steel fibres

	Length (mm)	Diameter (mm)	Aspect ratio (l/d)	Tensile strength (MPa)	Deformation	
0.2D	13	0.2	65	2500	Straight	
0.55D	35	0.55	64	1350	Hooked end	

2.1.1.2 HPGC mixing procedure

The mixing procedure significantly affects the fresh properties of the GPC, such as the setting time and workability, as revealed by Mahmood et al. [35]. The mixture design is illustrated in Table 3. Therefore, the mixing method was implemented as described by Alameri et al. [36]. The dry constituents (GGBS, SF, and QS) were mixed for 3 minutes to ensure a homogenous blend. 90% of free water and SP were added for 10 minutes to make the slurry. The fibres were added and mixed for one minute to distribute the fibres inside the slurry equally. Finally, the AAS was mixed with 10% of the free water and added for two minutes.

Table 3 Mix design of HPGC

Mix	Binder		Fine Agg. kg/ m^3	AAS/B	PS/PH	W/B ratio	SP kg/ m^3	Fibre%	
	GGBS kg/m^3	SF kg/m^3						0.55D	0.2D
HPGC	590	194	1098	0.38	3	0.28	0.03	0.167	0.083

Steel moulds were cleaned, oiled, and prepared prior to the mix so the mix can be poured immediately. For the columns, a special funnel was used to pour the mix smoothly and quickly inside the columns, as shown in Fig. 2. The specimens were sealed and stored in a fog room with a relative humidity of 100% until the day of testing.



Fig. 2 Columns before the mix with the funnels to ease the pouring process

2.1.1.3 Strength testings

Cubes (100 mm x 100 mm x 100 mm) were used to evaluate the compressive strength and tested according to the guidelines provided by ASTM C39 [37]. Three cubes were tested on the day of undertaking the test of the column.

Cylinders (diameter of 100 mm and length of 200 mm) were used to evaluate the modulus of elasticity according to the guidelines provided by AS1012 [38]. The stress-strain relationship was also obtained from the modulus of elasticity test. Three cylinders were tested on the day the column was tested.

2.1.1.4 HPGC Properties

The compressive strength (f_c')) results are presented in Table 4, along with the modulus of elasticity (E_c). As it can be seen from the figure consistent results were obtained from all pours. Pour one has only one column which is C1, whereas the other pours have two specimens per pour which are C2 and C3 for pour two and C4 and B for pour three; the details of pours and their corresponding specimens are presented in Table 5.

Table 4 Material properties for HPGC

Pour no.	Specimen ID	$f'_c(MPa)$	$f'_{c,avg}(MPa)$	Standard deviation	$E_{c,avg}$ (GPa)
1	P1-1	83.5	81.17	4.76	23.33
	P1-2	81.2			
	P1-3	78.8			
2	P2-1	78.8	80	5.63	26.9
	P2-2	83.3			
	P2-3	77.9			
3	P3-1	80.7	78.2	5.67	25.42
	P3-2	76.8			
	P3-3	77.1			

Table 5 Specimens details

Pour no.	Specimen ID	Column/Beam	Bo x to	Bi x ti	h	e/D*
1	C1	Column	150 x 3	75 x 3	900	0
2	C2	Column	150 x 3	75 x 3	900	0.066
	C3	Column	150 x 3	75 x 3	900	0.267
3	C4	Column	150 x 3	75 x 3	900	0.467
	B	Beam	150 x 3	75 x 3	1200	-

*e/D: eccentricity to depth ratio

2.1.2 Steel tubes

A stainless-steel tube grade 316 with a yielding strength f_y of 450 MPa and a modulus of elasticity Es of 193 GPa was used as the outer skin of the columns. Grade 304 with f_y of 450 MPa and Es of 195 GPa was used as the inner skin of the columns. More details about the cross-section dimensions are provided in Fig. 3. The cross-section of all columns and the beam was unified.

2.2 Experimental Program

2.2.1 Specimens

Four columns with a height of 900 mm were fabricated and prepared to be tested under concentric and eccentric axial loads. One beam with a length of 1200 mm was fabricated and prepared to be tested under a three-point bending load. The specimens were poured vertically, and a vibrator was used to distribute the mortar evenly between the steel tube skins. Also, a steel rod was used to compact the mortar, which was poured into multiple layers with each layer having approximately 300 mm in height. Then, the specimens were cured in a relative humidity of 100% in a controlled room temperature of 25ºC.

2.2.2 Instrumentations

All columns were instrumented with linear variable displacement transducer (LVDT) and longitudinal strain gauges. The test set-ups for the columns are shown in Fig. 3(a) and Fig. 3(b). Seven LVDTs were used for each column; three LVDTs were used to measure the lateral deflection of the columns, which can be used to obtain the deflection profile at any loading increment. Furthermore, two LVDTs were installed in the other direction, which can assist in determining any deviation perpendicular to the applied load. Additionally, two LVDTs were used to measure the axial displacement along the height of the columns. Moreover, four longitudinal strain gauges (one on each face) were glued to the surface at the mid-height of the columns.

Fig. 4(c) illustrates the test set-up for the beam. Laser LVDT was used underneath the mid-span of the beam to measure the deflection. Moreover, two strain gauges were glued on the top of the beam 75 mm from the middle point of the beam. In addition, four strain gauges were glued at the middle of the side of the beam to obtain the strain profile. Furthermore, one strain gauge was glued on the bottom at the middle of the beam.

2.2.3 Test Procedures

The columns were loaded axially with eccentricity variations, whereas the concentrically loaded column had 0 eccentricity; then, the e/D was changed for the other columns to 0.06, 0.267, and 0.467. Amsler machine with a capacity of 5000 kN, which has automotive software to collect the load and displacement data, was utilised to test the columns. The load was applied in increments of 30 kN/minute, and the loading continued after the failure occurred. A universal testing machine was used for the beam, which has a capacity of 500 kN and the load rate was 5 kN/minute.

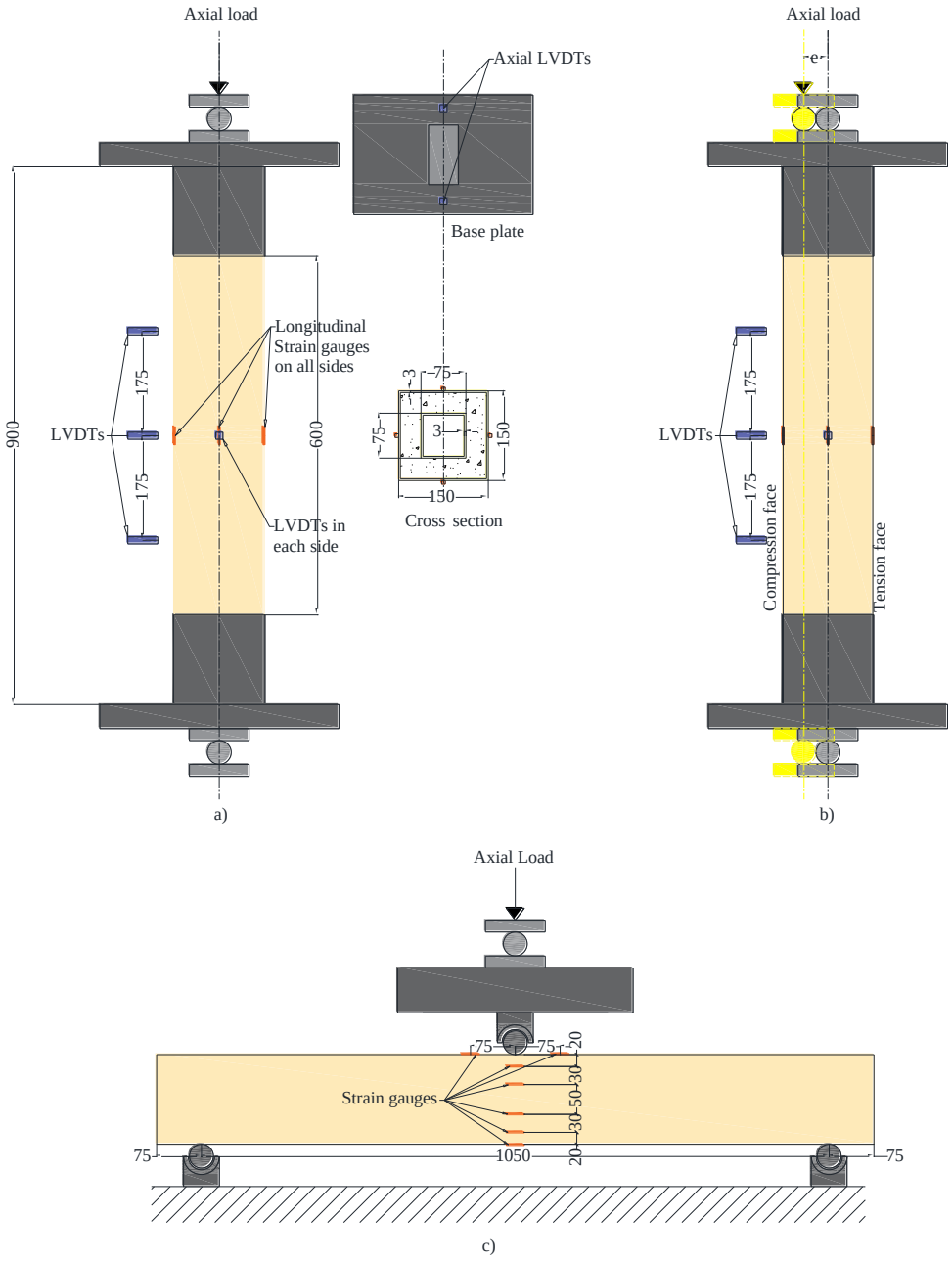


Fig. 3 Test set-up for a) the concentric column (with cross-section illustrated); b) under eccentric load; and c) under a three-point bending scenario of the beam

3 Results

All columns and the beam were tested until the failure occurred. The ultimate load (P_u), moment at the ultimate load (M_u), eccentricity, the mid-height lateral deflection at P_u ($\Delta_{u,mid}$),

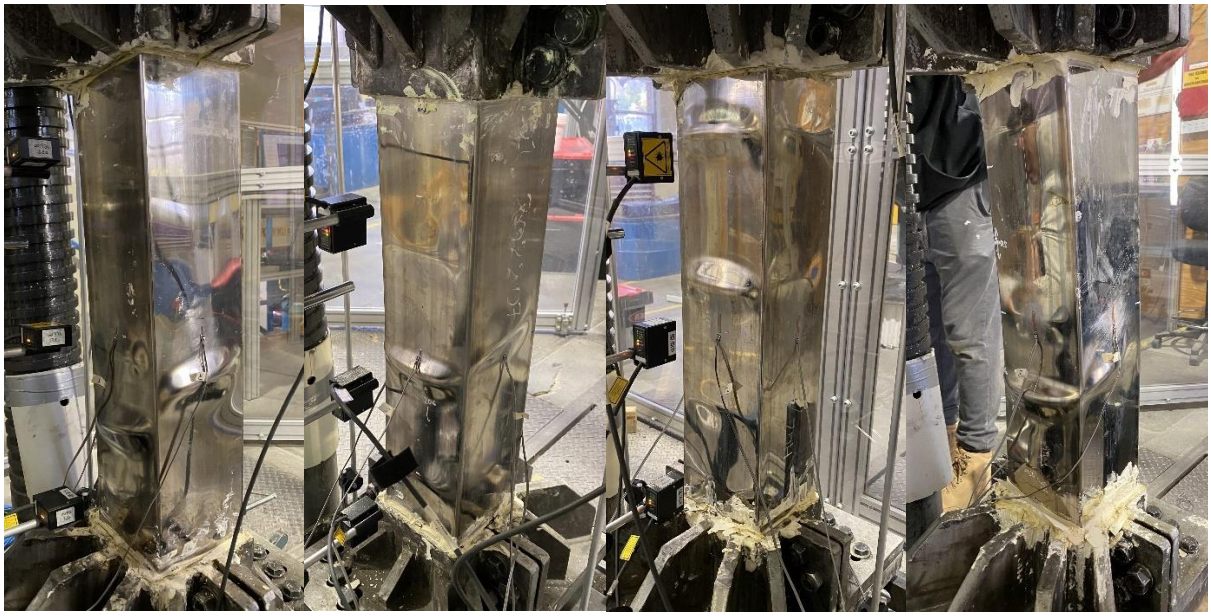
failure location from the middle of the specimen, axial strain (ε_u) at P_u (where the negative sign indicates compressive strain) and axial displacement at P_u ($\Delta_{u,axial}$) are presented in Table 6.

Table 6 Test results for all columns and the beam

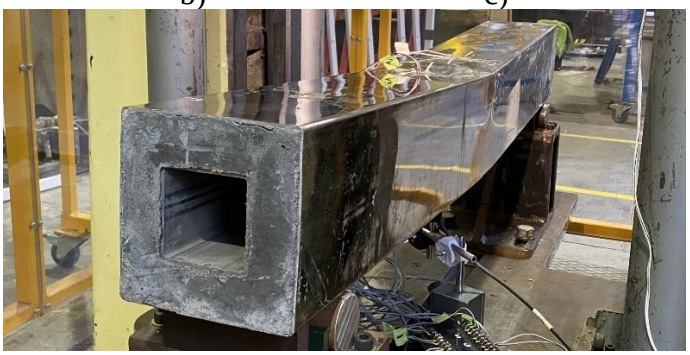
Specimen	P_u (kN)	e/D	$\Delta_{u,mid}$ (mm)	M_u (kN.m)	Failure location (mm)	ε_u	$\Delta_{u,axial}$ (mm)
C1	1700	0	-0.81	1.38	0 to -50 and -150 to -300	-0.00345	5.36
C2	1532.74	0.066	2.23	18.75	0 to -50	-0.00250	4.15
C3	972.69	0.267	7.58	46.28	0 to 100	-0.00917	5.23
C4	724.49	0.467	4.5	53.98	0 to 200	-0.00889	5.68
B	276.88	-	26.26	72.68	+75 to -75	0.019	26.26

3.1 Failure modes and ultimate bearing capacity

Fig. 4 shows the failure of all specimens. The local buckling of the columns in the steel tubes on different faces around the middle of the specimens has been observed consistently. Buckling occurred for all specimens towards the end of the test, which indicated the end of the test. For the concentrically loaded specimen C1, the shortening of the column vertically was observed with a crackling sound due to the bridging of the cracks by the steel fibres after the ultimate load, which was also observed for the eccentrically loaded specimens. For the eccentrically loaded specimens (C2-C4), the columns were bent during the elastic phase, followed by the local buckling toward the end of the test. For the beam, the local buckling at the compression face of the beam in the outer steel tube was observed after the load caused yield of the outer tube was attained and the beam continued to deform rapidly until the end of the test. Note that the specimens did not show any sign of an initial failure except for the shortening of the concentrically loaded column and the bending of the eccentrically loaded columns as well as the beam.



a) b) c) d)



e)

Fig. 4 Failure modes for specimens: a) C1; b) C2; c) C3; d) C4; e) B

3.2 Load-deformation relations

The ultimate axial load with the corresponding axial displacement of all columns is shown in Fig. 5. It can be seen that the increase of the eccentricity leads to a decrease in the ultimate axial load of 9.88%, 42.82% and 57.41% for e/D of 0.06, 0.267 and 0.467 respectively. Furthermore, the columns with higher eccentricity exhibited an increase in the axial displacement. Additionally, the failure behaviour for the axially loaded column C1 and relatively small e/D of 0.06 for C2 led to a sudden drop of the ultimate load by about 27% and 20%, respectively, indicating low ductility of the columns. However, the ductility has been increased significantly for C3 and C4 where in C3 the column exhibited a stabilisation of the ultimate load at 80% of P_u while in C4 the column exhibited the higher deflection with around 95% of P_u. This shows that the composite HPGC-FDST has efficiently provided both

confinements of the concrete and thus yielded a ductile failure mode with increasing eccentricity of the axial load.

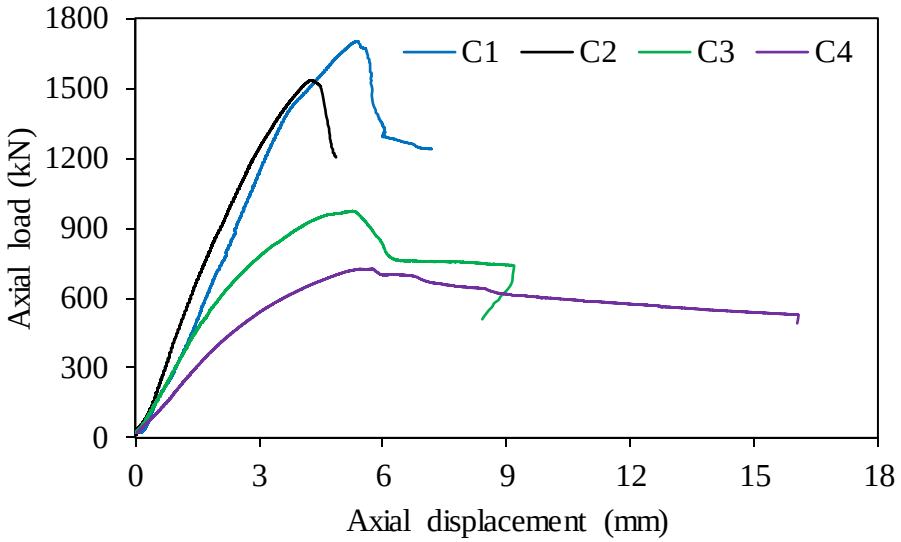


Fig. 5 Axial load vs axial displacement for the columns

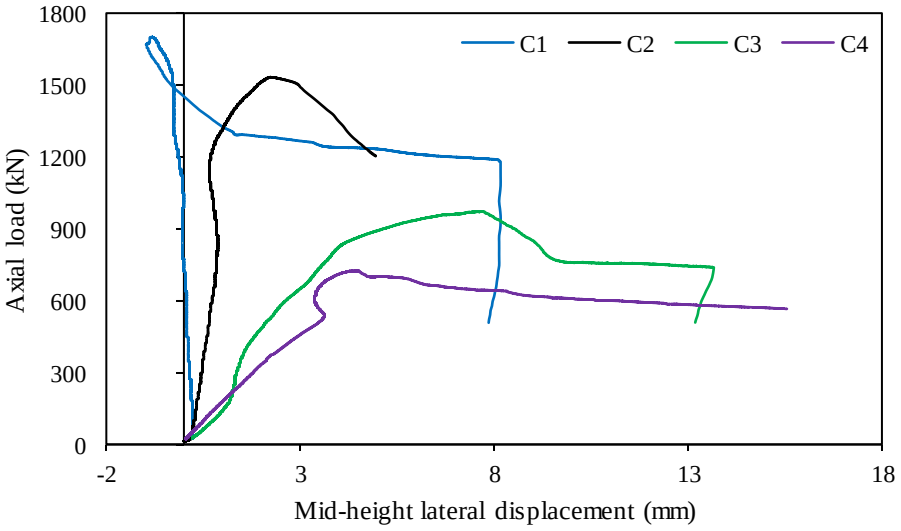
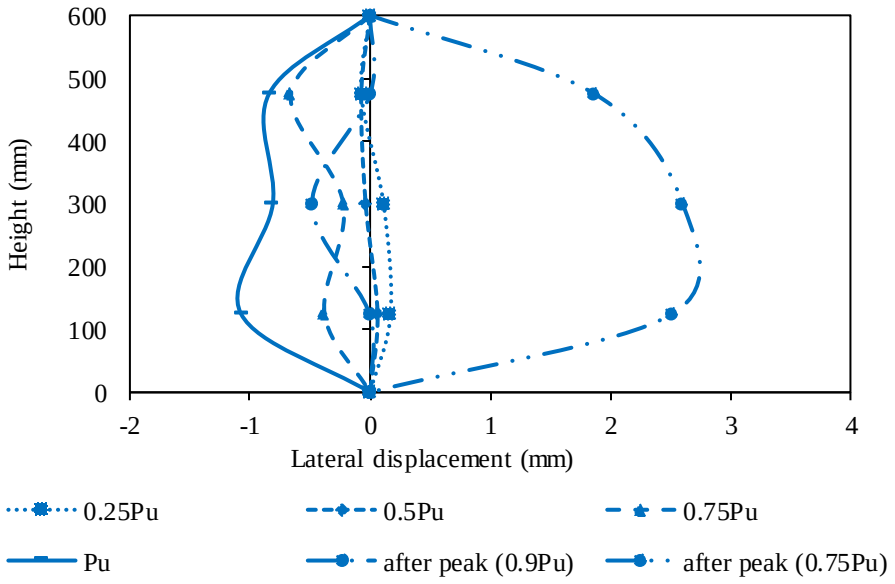


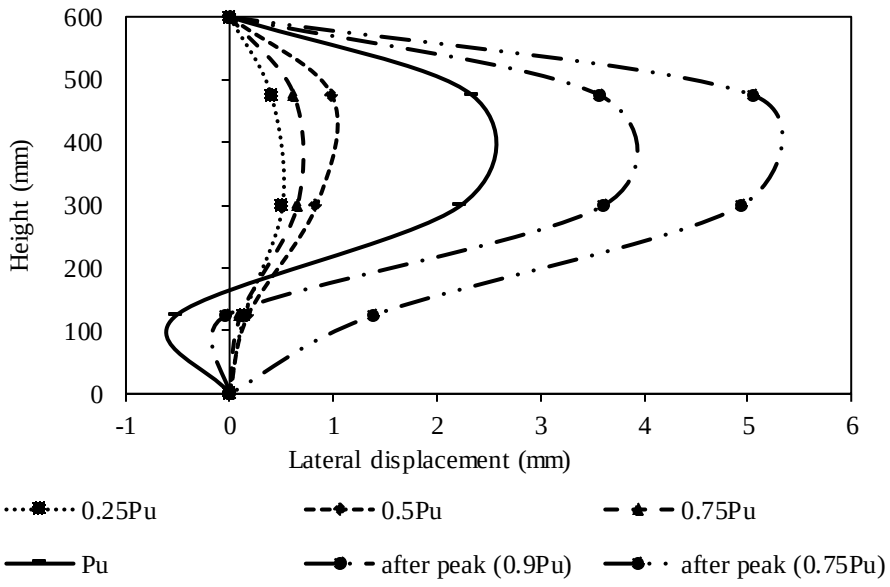
Fig. 6 Axial load vs mid-height lateral displacement

The ultimate loads for the columns with their corresponding mid-height deflection are presented in Fig. 6. Note that increasing eccentricity led to an increase in mid-height lateral displacement values. This was associated with decreased flexural stiffness (slope of the ascending branch of the curve) and the ultimate load of the columns.

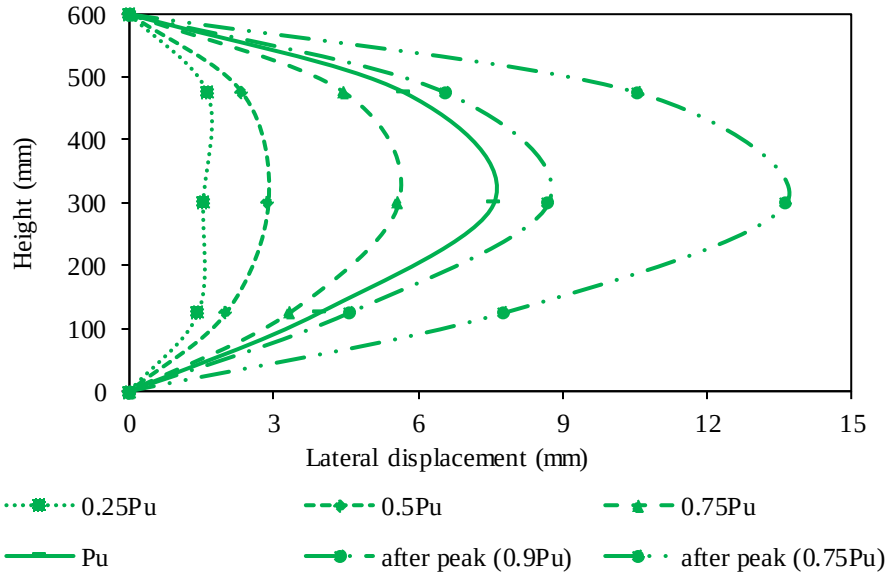
The deflection profile of the columns along their height is presented in Fig. 7. Note that the height of the columns is 900 mm but 150 mm in each end has been fixed from all sides to prevent any out-of-plane buckling during the loading stage. Fig. 7(a)-Fig. 7(d) shows the deflection profile of each column under different loads up to P_u and even after reaching P_u. The deflection profile under a concentric load exhibited a slight deformation of less than 1 mm before the ultimate load and then deformed significantly after reaching the ultimate load. C2 with e/D of 0.06 has behaved similarly to C1. However, increasing the eccentricity leads to a considerable deflection along the height of the column for C3 and C4 where they have e/D of 0.267 and 0.467, respectively. Additionally, the lateral deflection increased rapidly beyond the ultimate load for all columns.



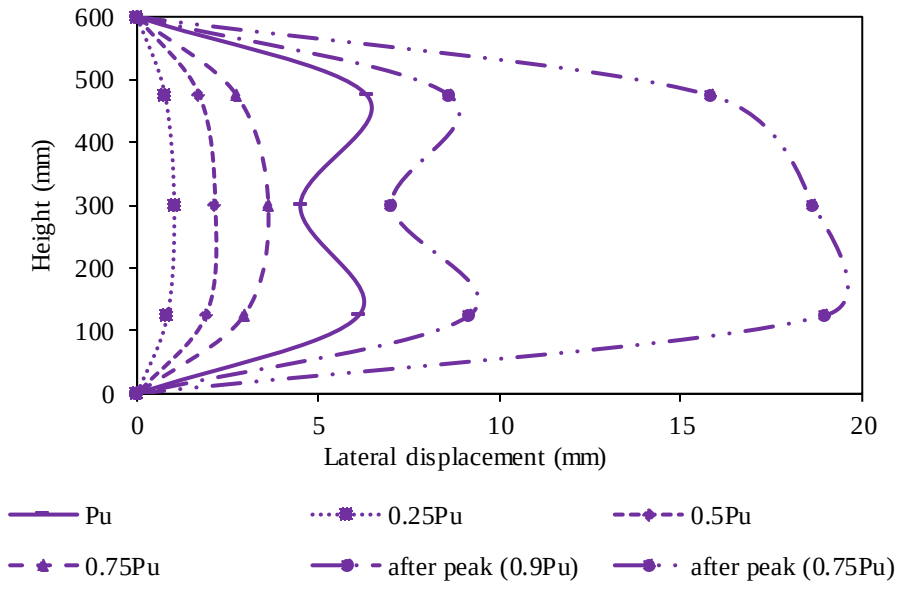
a)


600
500
400
300
200
100
0
Height (mm)
-1
0
1
2
3
4
5
6
Lateral displacement (mm)
0.25Pu
0.5Pu
0.75Pu
Pu
after peak (0.9Pu)
after peak (0.75Pu)

b)


600
500
400
300
200
100
0
Height (mm)
0
3
6
9
12
15
Lateral displacement (mm)
0.25Pu
0.5Pu
0.75Pu
Pu
after peak (0.9Pu)
after peak (0.75Pu)

c)



d)

Fig. 7 Deflection profile along the height of the columns a) C1; b) C2; c) C3; and d) C4

3.3 Load-strain relations

Fig. 8 displays the strain values on the compression and tension faces for all columns. Note that the continuous line represents the compression face and the dashed line represents the tension face. C1 with zero e/D has an unknown tension face and it can be seen that both faces exhibited compression behaviour of up to 80% of P_u, which is illustrated by the negative values of the strain. Hence, the outer tube yielded nearly at the P_u stage. Furthermore, the outer faces of the columns (compression and tension) exhibited a proportional increase in the strain values with the increase of the eccentricity. Thus, the eccentrically loaded columns experienced additional ductility due to the enhancement of the composite action by the steel tubes.

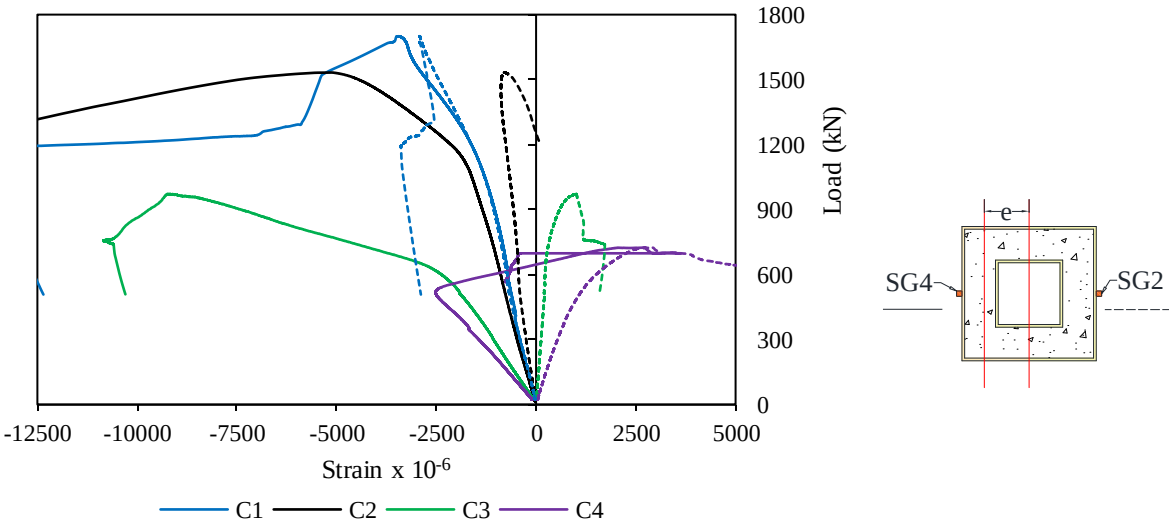


Fig. 8 Axial load vs strains on tension face (SG2) and compression face (SG4)

3.4 Beam test

The specimen has the same configuration as the columns except for a length of 1200 mm. Fig. 9 illustrates the load-deflection relationship in the mid-span for the beam tested under 3-point bending. It can be seen that the beam behaved elastically until 73% of the P_u and for the remainder of the test, it behaved inelastically. The long plateau of the P-Δ curve indicates the very high ductility exhibited by the composite HPGC-FDST beam. The beam achieved a peak load of P_u = 276.88 kN, corresponding to a maximum moment of M_u = 72.68 kN.m.

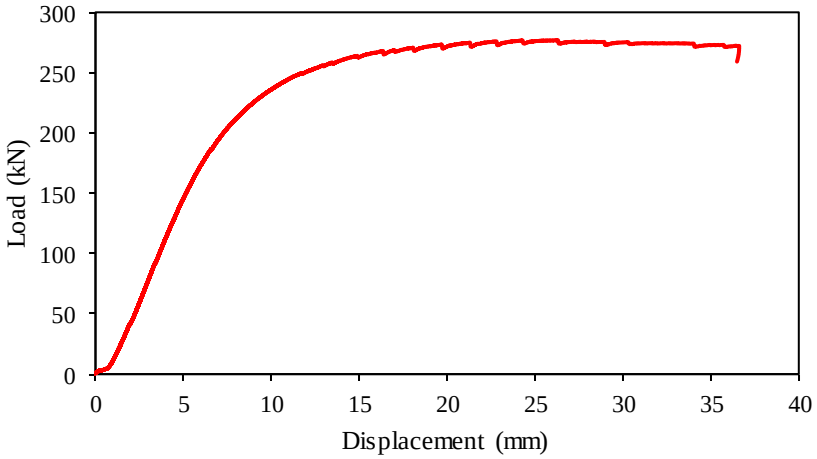


Fig. 9 Load vs deflection of the beam in the middle

The strain profile at different increments of the applied load along the depth of the beam is presented in Fig. 10. The beam exhibited a minimal change of the strain profile at 20% of P_u

which indicated the elasticity of the whole composite. Then, the gradual distortion of the strain started at 40% of P_u, which can be referred to as the cracking of the sandwiched geopolymer mortar wherein the steel had not yet yielded. The steel yielding of the tube occurred between the increment of 60% and 80% of P_u.

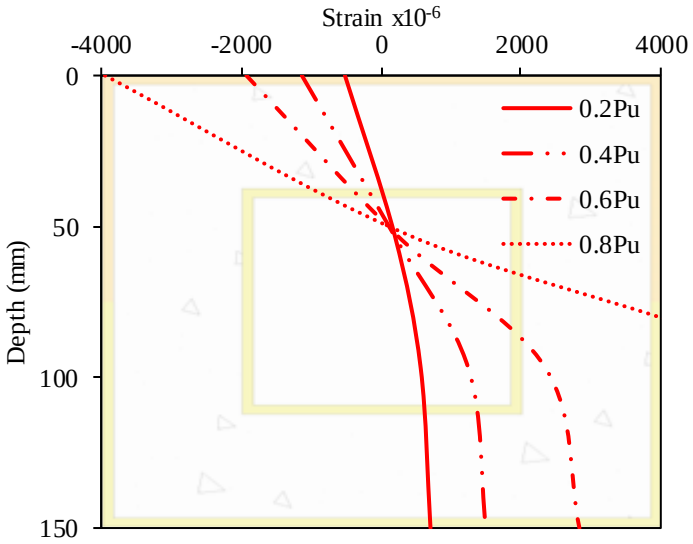


Fig. 10 Strain profile of the beam at different stages of the load along the depth of the beam where the 0 mark in the y-axis indicates the top of the beam

4 Finite-element modelling (FEM)

The finite element model (FEM) for each column has been built using the material properties obtained from the testing of the stainless steel and geopolymer composite. The aim of this section is to present the details of the numerical analysis of the columns under specific loading conditions using a well-regarded FEM code Abaqus [44] and to show its capabilities in simulating the columns accurately. This is motivated by some previous studies that have shown a very good performance of such FEM for the validation of double-skin columns under various loading conditions [39–42] A full non-linear analysis is conducted to estimate the ultimate axial load and the corresponding axial displacement as well as the mid-height displacement. Moreover, the failure pattern simulated by the model is compared with that observed in the actual test. Attentions are paid on various aspects associated with the building of the models in

Abaqus, which includes constitutive modelling of the materials, meshing, interactions of the components, boundary conditions, and loading.

4.1 Model geometry

Fig. 11 shows the model geometry along with meshing, generated within Abaqus, for a column along with the attachments at its two ends used for loading the column. Every component or part of the structural system have been created separately and combined in the assembly stage. The actual column has an inner and an outer steel tube while the gap between them has been filled with concrete that is sandwiched by these steel tubes. In order to safely transmit load at the top and bottom ends of the column with no damage in the experimental testing, steel caps have been used at the column ends to confine them properly. These caps have also been modelled to mimic the experimental program more realistically. The model has also considered steel plates used at each end of the steel caps where these plates helped to change the eccentricity of loading in the experimental work. As these plates performed elastically, they are simply treated as elastic parts to minimise the computational effort without affecting the column response as well as failure modes.

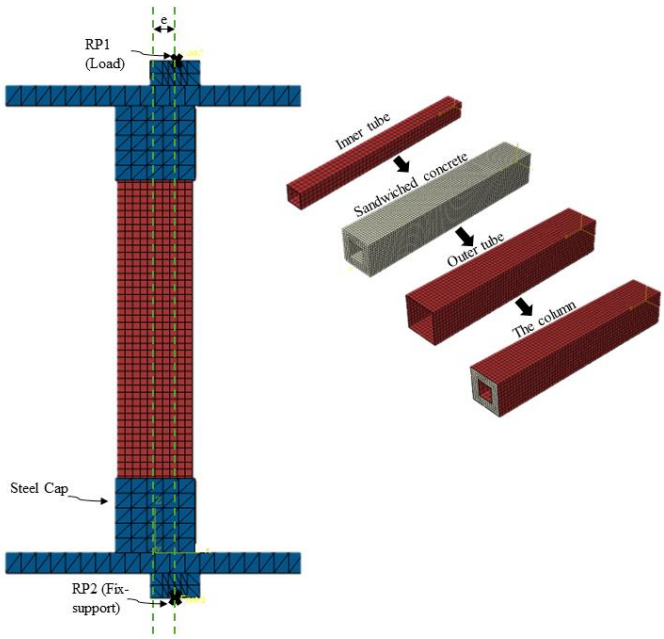


Fig. 11 Model geometry in Abaqus for the column and its loading attachments

4.2 Constitutive models of the materials

4.2.1 Stainless steel

The von Mises plasticity model with associated plastic flow and isotropic hardening rule has been used for the constitutive response of the outer and inner steel tubes under a multiaxial stress state. The results obtained from the uniaxial tensile tests of coupons made with the outer and inner steel tubes have been used to provide input to this material model. The material model needs inputs for the elastic modulus, Poisson's ratio and yield stress to simulate the elastic response of the material. Beyond the yield point of the stress-strain curve, the linear elastic behaviour switches to nonlinear response with plastic deformations, where the inputs for the variation of uniaxial stress have been given in terms of plastic strains.

4.2.2 HPGC

The concrete damage plasticity (CDP) model has been used to simulate the constitutive response of the HPGC [43]. The CDP model includes the effect of plasticity to capture irreversible permanent deformations of this concrete based material and the effect of damage to mimic the stiffness degradation due to micro-cracking where they are treated differently under compression and tension loading regimes as the behaviour of a concrete material. The model was further improved by Lee and Fenves [44] where the improved version of the model is available in Abaqus. These features help to capture the nonlinear inelastic behaviour of a concrete based material accurately which made the CDP model very popular. CDP has elastic property which includes the response of the elastic materials. The model possesses a pressure dependent yield surface as concrete based materials always demonstrate a pressure sensitive yielding behaviour. In order to properly simulate the dilation response of these pressure sensitive materials, the model used a non-associated flow rule taking a plastic potential different from the yield surface. A single yield function is used to capture both tensile and compressive stress states that helps to provide robustness in iterative based computational

algorithms. The functions used to represent the yield surface (F) and plastic potential (G) are expressed as follows:

$$F = \frac{1}{1-\alpha}\left(\bar{q} - 3\alpha\bar{p} + \beta\left(\tilde{\varepsilon}^{pl}\right)\left(\hat{\bar{\sigma}}_{max}\right) - \gamma\left(-\hat{\bar{\sigma}}_{max}\right)\right) - \bar{\sigma}_c\left(\tilde{\varepsilon}_c^{\,pl}\right) \leq 0 \quad (1)$$

$$G = \sqrt{(\zeta\sigma_{t0}\tan\varphi)^2 + \bar{q}^2} - \bar{p}\tan\varphi \quad (2)$$

$$\alpha = \frac{\frac{\sigma_{bo}}{\sigma_{co}} - 1}{2 \times \frac{\sigma_{bo}}{\sigma_{co}} - 1}; \quad 0 \leq \alpha \leq 0.5 \quad (3)$$

$$\beta = \frac{\bar{\sigma}_c\left(\tilde{\varepsilon}_c^{pl}\right)}{\bar{\sigma}_t\left(\tilde{\varepsilon}_t^{pl}\right)}(1-\alpha) - (1+\alpha) \quad (4)$$

$$\gamma = \frac{3(1-k_c)}{2k_c - 1} \quad (5)$$

where $\bar{q}$ is the von Mises effective stress, $\bar{p}$ is the hydrostatic effective stress or pressure, and $\hat{\bar{\sigma}}_{max}$ is the maximum principle effective stress, which is scalar quantities but computed during analysis using the multiaxial stress components. Similarly, $\tilde{\varepsilon}_c^{\,pl}$ and $\tilde{\varepsilon}_t^{pl}$ appeared in the above equations are accumulated plastic strains (scalar quantities) in compression and tension, respectively, which are computed during analysis using multiaxial plastic strain rate components accumulated over the load increments typically applied in a nonlinear analysis. The above equations also need input test data for the initial tensile strength σ_{t0} (i.e. initial yield stress) and the initial compressive strength σ_{co} while the initial biaxial compressive strength σ_{bo} is computed using the biaxial stress ratio (σ_{bo}/σ_{co}), which is taken as 1.16 for the present analysis based on the previous studies e.g. [45]. Similarly, the dilation angle φ appeared in Eq. (2) is taken as 39° while the ratio of second stress invariant on tensile and compressive meridians k_c in Eq. (5) is taken as 2/3 (usually varies from 0.5 to 1.0) in the present analysis. An eccentricity parameter ζ used in Eq. (2) controls the direction of plastic flow near lower pressure, which is taken as 0.1 in the present study (this parameter controls the rate of change

of curvature of the plastic potential function to approach the asymptote towards higher pressure region in compression). Beyond the initial yielding, the compressive and tensile strengths are evolved (increase or decrease through hardening or softening) as $\overline{\sigma}_c$ and $\overline{\sigma}_t$ (see Eqs. 1 and 4), which are computed using the accumulated plastic strains $\tilde{\varepsilon}_c^{\,pl}$ and $\tilde{\varepsilon}_t^{pl}$.

A typical illustration of the idealised CDP model response under uniaxial compression and tension is shown in Fig. 12, which should simply follow the stress-strain curves obtained in experimental testing concrete specimens under compression and tension. The figure shows an additive split of the total strains into pure elastic strains (ε_{0c}^{el}, ε_{0t}^{el}) and inelastic or cracking strains (ε_c^{in}, ε_t^{ck}), which have a portion of irrecoverable plastic strains ($\tilde{\varepsilon}_c^{pl}$, $\tilde{\varepsilon}_t^{pl}$) while the remaining portion is recoverable due to the stiffness degradation caused by the damage (d_c, d_t) initiated by the micro-cracking of the material. Thus, the pure elastic strains are the portion of strains recovered when a material undergoes pure elasto-plastic deformations with no damage while additional strains are recovered when the material also has damage which can be represented mathematically $(= \varepsilon_c^{in} - \tilde{\varepsilon}_c^{pl})$ in compression and $(= \varepsilon_t^{ck} - \tilde{\varepsilon}_t^{pl})$ in tension. The decomposition of the strains can be expressed as follows:

$$\varepsilon_c^{in} = \varepsilon_c - \varepsilon_{0c}^{el} = \varepsilon_c - \frac{\sigma_c}{E_0} \tag{6}$$

$$\varepsilon_t^{ck} = \varepsilon_t - \varepsilon_{0t}^{el} = \varepsilon_t - \frac{\sigma_t}{E_0} \tag{7}$$

$$\tilde{\varepsilon}_c^{pl} = \varepsilon_c^{in} - \frac{d_c}{(1 - d_c)} \frac{\sigma_c}{E_0} \tag{8}$$

$$\tilde{\varepsilon}_t^{pl} = \varepsilon_t^{ck} - \frac{d_t}{(1 - d_t)} \frac{\sigma_t}{E_0} \tag{9}$$

The damage parameters (d_c, d_t) are computed during the analysis at any load step using the updated values of σ_c, σ_t, and ε_c^{in} at that load step along with the undamaged elastic modulus E_0 and initial tensile strength σ_{t0} according to the following equations.

$$d_c = 1 - \left[\frac{\frac{\sigma_c}{E_0}}{0.2\varepsilon_c^{in} + \frac{\sigma_c}{E_0}}\right] \tag{10}$$

$$d_t = 1 - \frac{\sigma_t}{\sigma_{to}} \tag{11}$$

Note that the damage variables vary from zero to one, where zero represents an intact state with no damage and one represents complete damage.

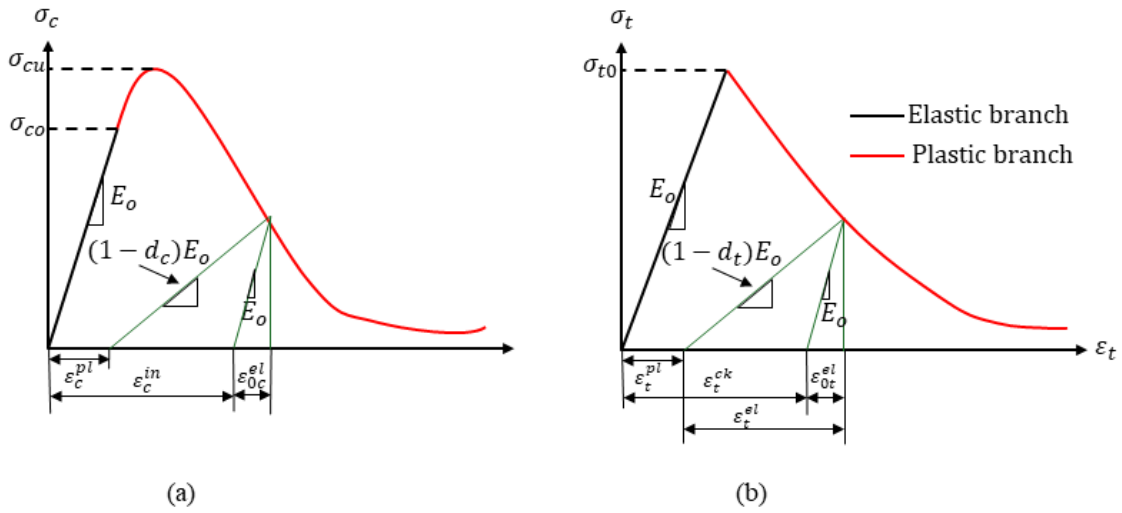


Fig. 12 A representation of the CDP model response under uniaxial a) Compression and b) Tension [46]

4.3 Details of the finite element modelling

The analysis has been conducted using an explicit dynamic solver to avoid convergence issues, which is frequently observed with an implicit static solver (iterative based) in solving a large set of complex nonlinear equations generated in modelling the inelastic behaviour of materials. The explicit solver was initially developed for solving dynamic problems but it was subsequently utilised with necessary adjustment for the inertia to solve quasi-static problems. Due to computational robustness, this modelling strategy has become very popular in complex damage and failure modelling, even under static loading. The explicit solver has also been used to model double skin columns under quasi-static loading in previous studies that proved its capability in producing accurate results [47,48] The benefit of the explicit solver is that it straightway computes the results without any iteration in each load step and moves forward to

the new step. A displacement control strategy has been adopted to impose the axial load on the columns where the value of the total displacement specified on each specimen is different as dictated by the experimental testing. In order to apply the load incrementally, an amplitude of 0.2 mm/s has been used for all specimens.

As the structural system has multiple components, the interaction between them has been established by using the general contact law applied to the column and the loading attachments. The contact property options utilised for that include tangential behaviour with a plenty friction coefficient of 0.35 and normal behaviour with hard contact. Furthermore, surface-to-surface based contact has been used to simulate the interaction between the outer face of the inner steel tube and the inner face of the sandwiched concrete material as well as the inner face of the outer steel tube with the outer face of the sandwiched concrete material. Moreover, two reference points have been created next to the ends of the steel cap, and the coupling interaction has been applied to connect each reference point to its nearest end plate. One of the reference points has been utilised to fix the column end to it while the second reference point is used to apply load to the other end of the column. Thus, all translation and rotational degrees of freedom of the first reference point have been restrained to impose fixed boundary conditions at the corresponding column end. The boundary condition at the other end of the column has been applied by restraining all degrees of freedom of the second reference point except the translation degrees of freedom along the column axis where a displacement of 20 mm has been applied to induce axial compressive load through load control mechanism. As stated in section 2.2, the same column specimen has also been tested under three-point bending. For this beam specimen, the same modelling techniques have been applied except for the value of the total displacement specified at the mid-span to induce the transverse load. In this case, the specified total displacement has been set to 40 mm which is a little higher than 35 mm as observed in the laboratory.

In this study, all components of the structural system have been modelled with 3D hexahedral solid elements having eight corner nodes with reduced integration capability (C3D8R), which is found to be used successfully in multiple studies, e.g. [49–51]. Due to the small thickness of the steel tubes, there is a natural tendency to use shell elements (e.g. S4R) for these steel tubes, as found in the literature. However, earlier studies conducted by Elchalakani et al. and Hassanein et al. [52,53] have shown the difficulty of imposing interactions between the concrete and steel tubes due to the placement of nodes inside the shell elements. Therefore, the solid element is also used to model the steel tubes for capturing their deflected shape properly. Initially, a convergence study has been made to identify a proper mesh size for the present analysis that has shown a meshing with a maximum element size of 20 mm for all components is an adequate size that has been employed for all specimens.

4.4 Results of FEM and validations

The results obtained from the numerical model have been validated by the experimental results produced in this study. The load-axial displacement relationship for all columns is illustrated in Fig. 13. The output of numerical models for all columns under different eccentricities showed an acceptable agreement with the experimental results for both the ultimate loads with their corresponding deflection. The variations between the numerical and experimental results were attained from the sensitivity of geopolymer concrete to the curing method where the confined composite by the steel skins functioned as a sealing curing for the geopolymer composite. Furthermore, the effect of steel fibre on bridging the cracks during the strain-hardening stage can be seen in the columns with eccentricities.

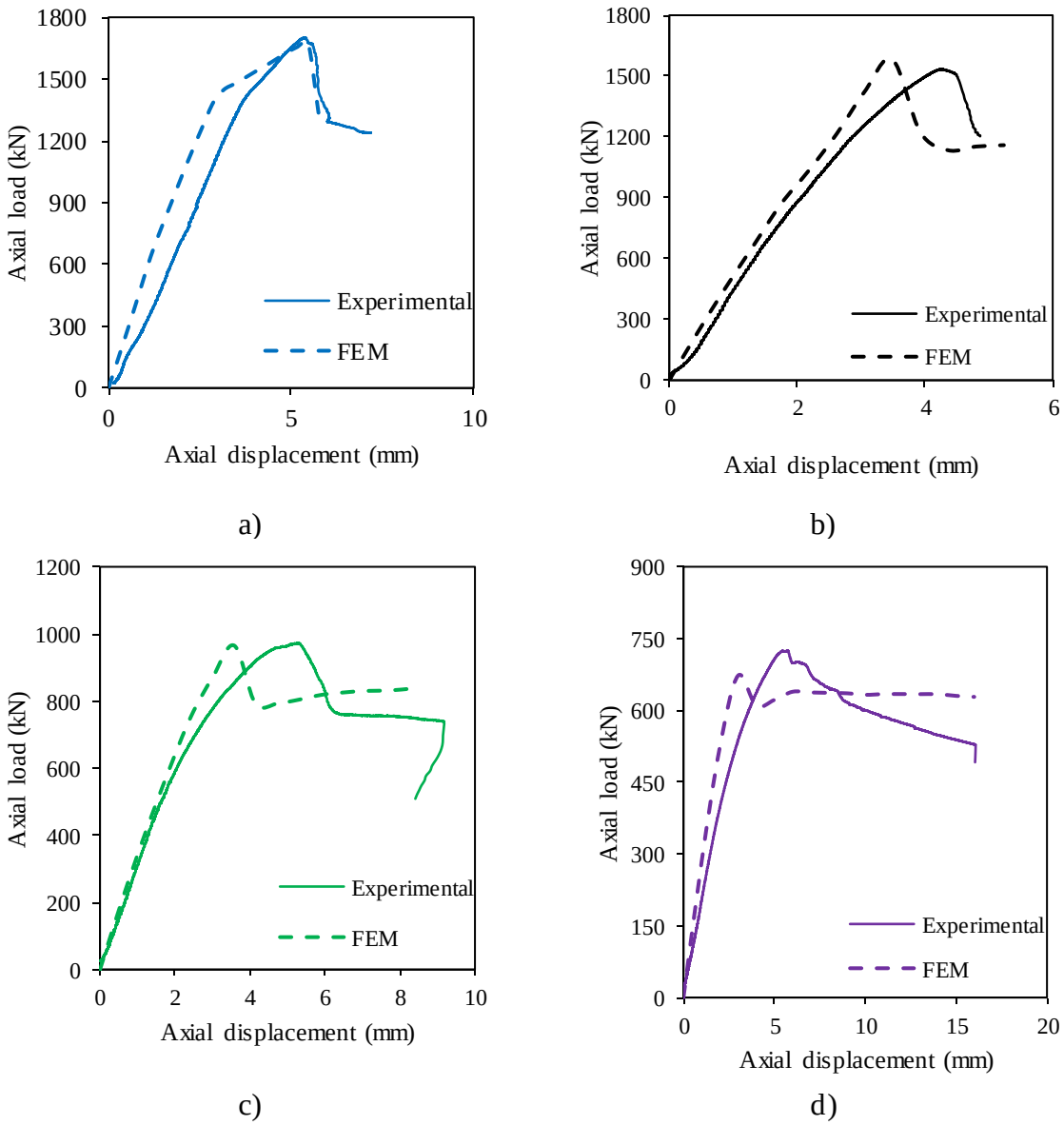


Fig. 13 Axial load-displacement for all columns: a) C1; b) C2; c) C3; and d) C4

Fig. 14 presents the mid-height lateral displacement for all columns against the axial load. Generally, a sudden drop in the load happens once the ultimate load is achieved and beyond this point the displacement increases linearly until the failure of the specimen. For C1, it can be noticed that there are two behaviours of lateral displacement due to the symmetricity of the load; therefore, the specimen may behave and fail on different sides. Moreover, the numerical model mostly followed the experimental results in the elastic branch.

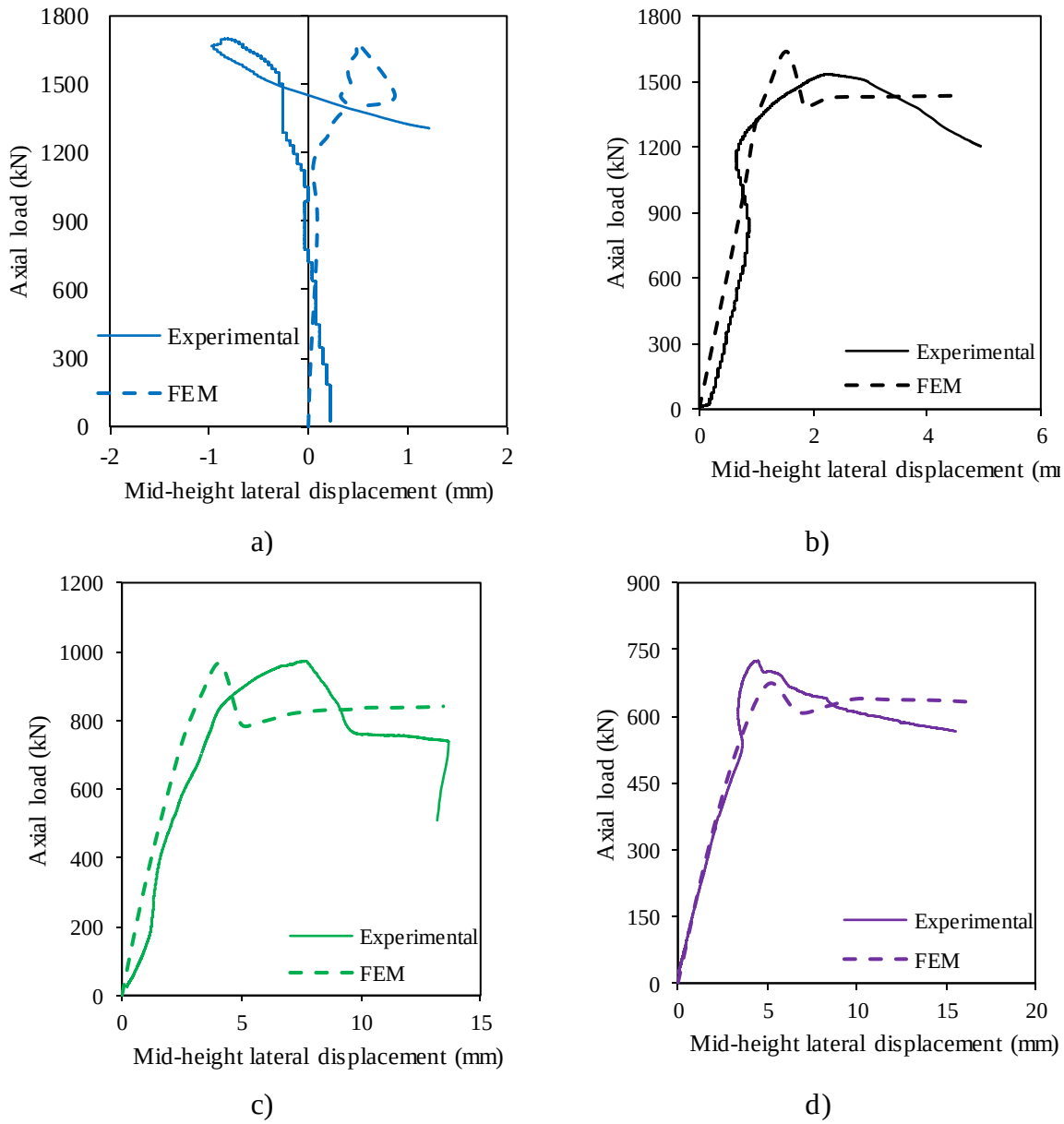


Fig. 14 Mid-height lateral displacement vs axial load for all columns: a) C1; b) C2; c) C3; and d) C4

Fig. 15 shows the failure pattern of the numerical model for all columns compared to the experimental failure for the specimens. The local buckling of the outer tube happened around the middle of the specimen for the concentric load specimen C1. The local buckling also occurred in the middle of the specimen for other columns in different locations. However, the global buckling appeared clearly with the increase in the eccentricity of the load for columns C2, C3, and C4. In general, the numerical model successfully simulated the failure of the experimental results due to the definition of the damage parameters in the model in terms of compression and tension as explained in Eqs. (10) and (11)

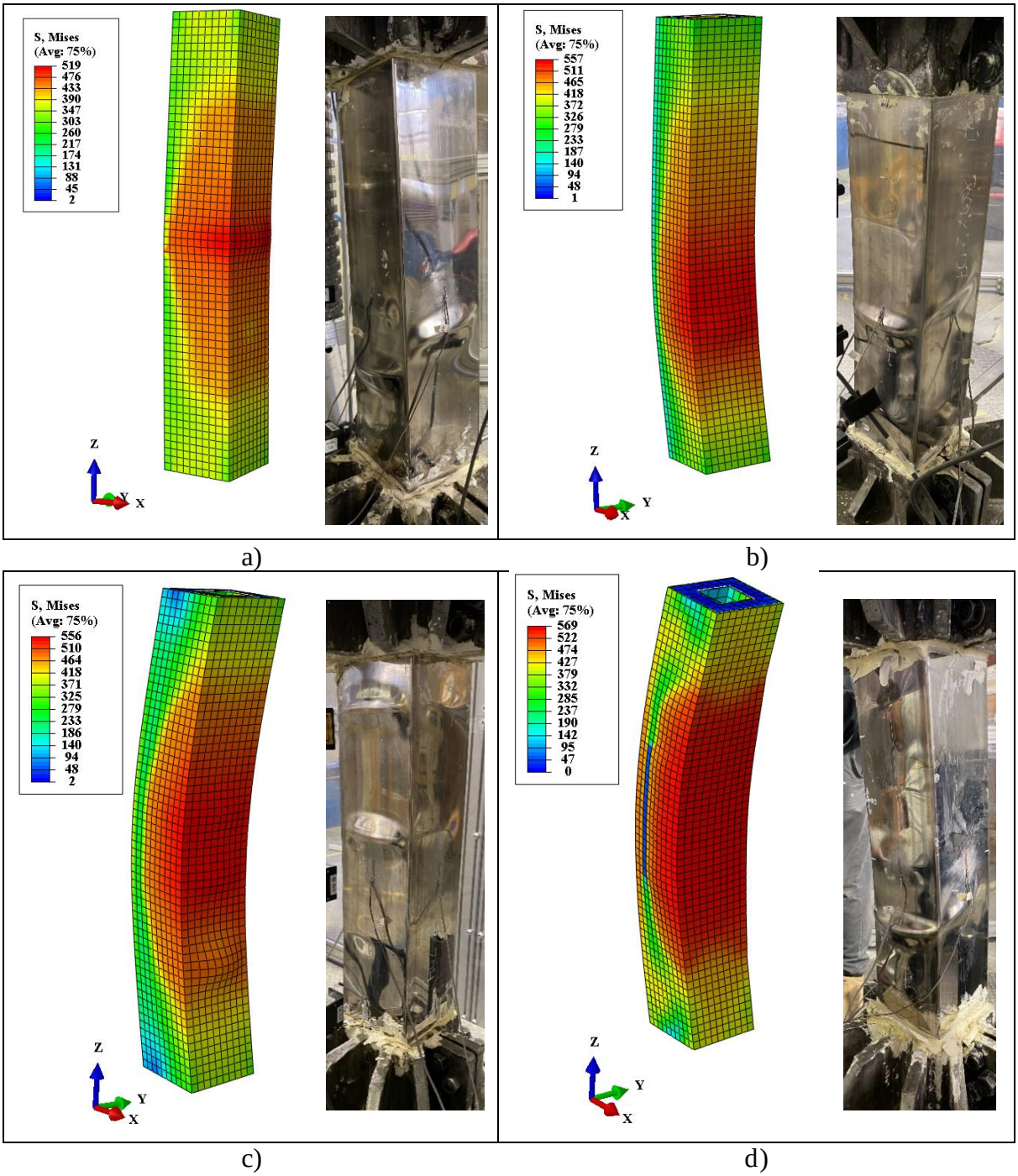
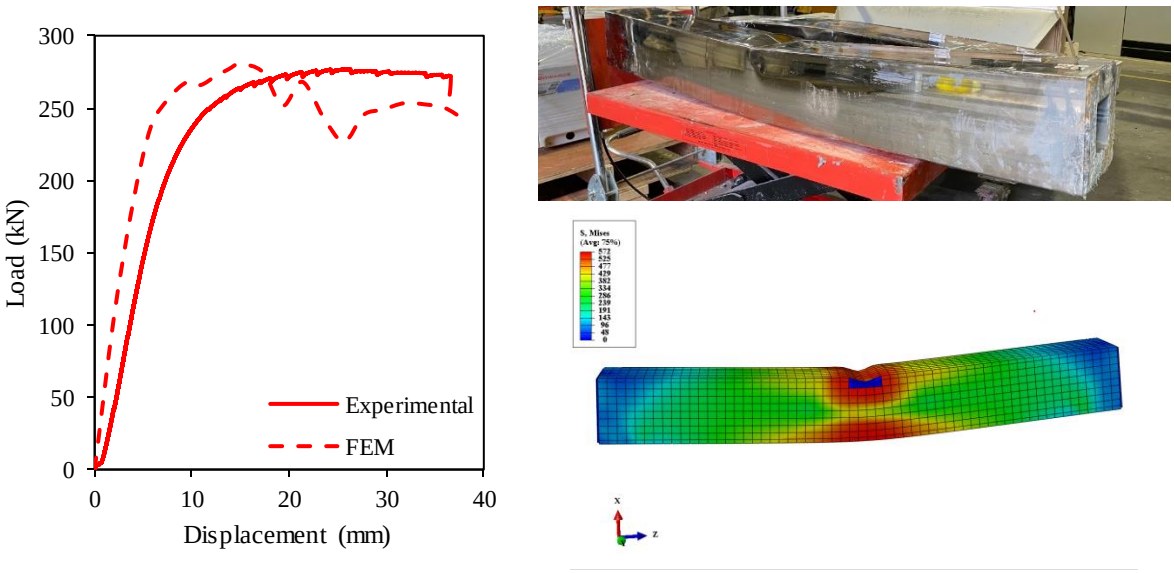


Fig. 15 Failure mode for all columns with the comparison between experimental and numerical results: a) C1; b) C2; c) C3; and d) C4

The beam failure pattern compared to the experimental one and the load-displacement relationship are illustrated in Fig. 16. For the load-displacement relationship, the numerical model has nearly followed the behaviour of the experimental results. The differences appeared in the strain-hardening region where the specimen in the experimental program was influenced by the presence of steel fibre which made the behaviour smoothly deviate from the strain-

hardening region until the specimen failed. However, the numerical model has achieved a higher accuracy in mimicking the experimental result up to the failure load. For the failure pattern, the local buckling occurred in the same region around the applied load for both results as well as the global buckling which occurred in the middle of the tension face of the specimen.



a) b)

Fig. 16 The comparison between experimental and numerical results for the beam a) Load-displacement relationship; and b) the failure pattern

Fig. 17 shows the axial-moment interaction diagram (P-M) for the experimental and numerical results. High accuracy of the outcomes of the numerical model compared to the experimental program where the ratio of the axial load ($P_{u,exp}$) to the axial load obtained from the numerical model ($P_{u,FEM}$) are 1.01, 0.97, 1.01 and 1.08 for C1, C2, C3 and C4 respectively. Furthermore, the ratio of the moment capacity for the beam numerically and experimentally is 1.01. Hence, the variation in the results could happen due to multiple causes such as the imperfections of the experimental program or any other human error.

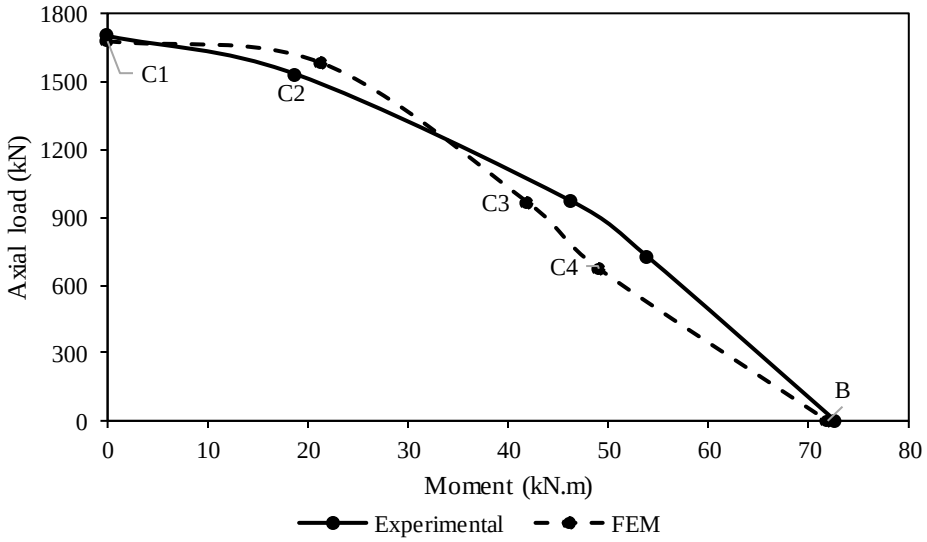


Fig. 17 Axial-moment interaction diagram for the numerical model with a comparison to the experimental results

5 Analytical procedure for developing P-M interaction diagram

The axial load – bending moment (P-M) interaction diagram is an essential analytical approach to predict the performance of the columns under combined axial and bending loads. Therefore, to generate P-M interaction diagram, an empirical procedure was developed in this study based on modifying and incorporating many aspects from previously published work. The equation to predict the ultimate axial load P_u was utilised for different cross sections such as rectangular by Ahmed et al. [54], and circular by Liang [55]. Therefore, the following equation was used to predict the P_u theoretically in this study

$$P_u = A_{so}\sigma_{0.2} + A_{si}f_{syi} + (\gamma_c f_c' + 4.1\, f_{rp})A_c \quad (12)$$

where A_{so} is the outer steel tube area (mm^2), $\sigma_{0.2}$ is the 0.2% proof stress (MPa), A_{si} is the inner steel tube area (mm^2), f_{syi} is the yield strength of the inner steel tube (MPa), γ_c is a reduction factor based on the size effect [56] which is taken as $1.85\, D_c^{-0.135}$ where

$D_c = B_o - 2\, t_o$, f_c' is the compressive strength of the concrete (MPa), A_c is the area of the sandwiched concrete and f_{rp} is the lateral stress as per this equation

$$f_{rp} = 1.35\xi + 0.61 \quad (13)$$

where ξ is the confinement factor which is calculated as

$$\xi = \frac{(A_{so}\sigma_{0,2} + A_{si}f_{syi})}{\gamma_c f_c' A_c} \quad (14)$$

The equations proposed by Han et al. [57] were used to obtain the ultimate moment (M_u) as follows

$$M_o = M_{osc,u} + M_{i,u} \quad (15)$$

where M_o is the pure bending moment, $M_{osc,u}$ is the ultimate moment for the combined outer tube and the sandwiched concrete and $M_{i,u}$ is the ultimate moment for the inner tube

$$M_{osc,u} = \gamma_{m1} W_{scm} f_{osc} \quad (16)$$

$$M_{i,u} = \gamma_{m2} W_{si} f_{syi} \quad (17)$$

where W_{scm} and W_{si} are the compound flexural modulus for the outer tube and sandwiched concrete and the inner tube respectively, γ_{m1} and γ_{m2} are the flexural bearing capacity factors as follows

$$\gamma_{m1} = 0.48\, ln\,(\xi + 0.1)\,(1 + 0.06\,\psi - 0.85\,\psi^2) + 1.1 \quad (18)$$

$$\gamma_{m2} = -0.02\,\psi^{-2.76}\, ln\,\xi + 1.04\,\psi^{-0.67} \quad (19)$$

where ψ is the hollow section ratio of the composite.

Then the interaction diagram is calculated according to the suggested formulas by Ahmed et al. [58] which is defined as

$$M_u = \alpha_s M_o \left[1 - \left(\frac{P_u}{P_o}\right)^{\alpha_m}\right] for\ P_u \geq 0.2P_o \quad (20)$$

$$M_u = M_o \left[1 - \frac{1}{5}\left(\frac{P_u}{P_o}\right)^{\alpha_n}\right] for\ P_u < 0.2P_o \quad (21)$$

where M_u is the maximum bending moment, P_o is the compressive load of the short columns and the following factors (α_s, α_m, and α_n) are the shape factors which depend on the length of the column L and the radius of generation r, defined in the following equations

$$\alpha_s = 1.223 - 0.005\left(\frac{L}{r}\right) \tag{22}$$

$$\alpha_m = 3.413 - 0.0119\left(\frac{L}{r}\right) \tag{23}$$

$$\alpha_n = 0.0001\left(\frac{L}{r}\right)^2 - 0.0336\left(\frac{L}{r}\right) + 2.2 \tag{24}$$

Both the experimental results obtained for HPGC-FDST columns and the corresponding theoretical results utilising the above-mentioned empirical equations are plotted in Fig. 18. The experimental to theoretical results exhibited a good correlation with relative difference between the experimental and theoretical results of 2.2% and 0.3% for C1 and C2, respectively. However, increasing the eccentricity causes an overprediction by the theoretical empirical equations of 10.7% and 16.9% for C3 and C4, respectively, because the actual compressive strength for the sandwiched composite is unknown and the strain behaviour and models of the geopolymer concrete are generally calculated or modelled as the conventional concrete one. Moreover, the premature failure at the top or the bottom of the columns causes this overprediction. Thus, it is suggested that the strain models be studied extensively to enhance and improve accuracy. For the beam under pure bending, the experimental and theoretical moment results demonstrated a high level of agreement, with a relative difference of only 0.97%.

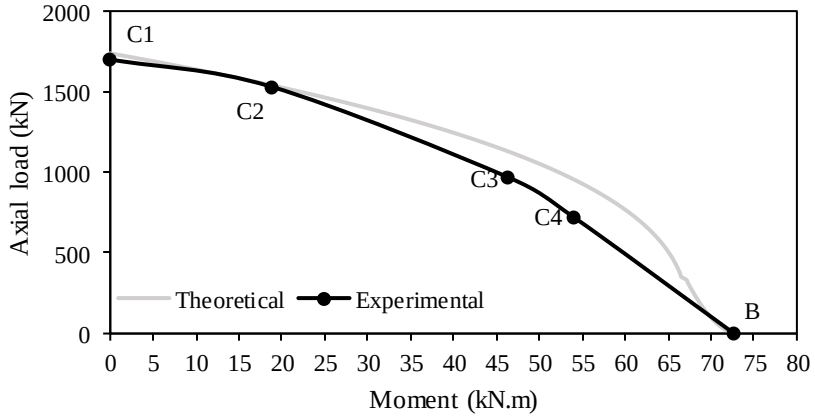


Fig. 18 P-M interaction diagrams experimentally and theoretically

6 Conclusion

This study investigated HPGC-FDST columns by utilising HPGC as a sandwiched concrete which has less calcium than OPCC hence fewer sulphate attacks. The stainless-steel tubes, providing resistant to chloride attack, were used to fully encase the HPGC. Therefore, this innovative composite provides high resistance to both corrosion and chemical attacks. These columns were subjected to different loading conditions (concentric, eccentric and flexural) which have been studied experimentally, numerically, and theoretically. The following conclusions can be drawn from this study:

- Increasing the eccentricity of the columns enhanced the axial deflection capacity of the columns.
- The mid-lateral deflection has been increased as well with the increase of the eccentricity.
- The columns exhibited similar failure patterns (local buckling around the middle of the columns).
- The axial load capacity decreased with the increase in the eccentricity.
- The FEM has been validated with the experimental results which indicated a high correlation in terms of deflection capacities and failure modes.
- The experimental and theoretical interaction diagram showed good agreement with the utilised empirical equations in this study.
- Finally, more studies are encouraged to enrich the database of the application of geopolymer concrete in the structural field.

Acknowledgement

The authors would like to acknowledge the financial support from the Australian Research Council (DP 21001425) for undertaking this research.

References

[1] NACE, International Measures of Prevention Application and Economics of Corrosion Technology (IMPACT), 15835 Park Ten Place, Houston, TX 77084, 2019.

[2] I. of U. S, Greenhouse Gas Emissions and Sinks: 1990–2017, (2019).

[3] B. Singh, G. Ishwarya, M. Gupta, S.K. Bhattacharyya, Geopolymer concrete: A review of some recent developments, Constr Build Mater 85 (2015) 78–90. https://doi.org/https://doi.org/10.1016/j.conbuildmat.2015.03.036.

[4] N. Li, C. Shi, Z. Zhang, D. Zhu, H.-J. Hwang, Y. Zhu, T. Sun, A mixture proportioning method for the development of performance-based alkali-activated slag-based concrete, Cem Concr Compos 93 (2018) 163–174. https://doi.org/10.1016/j.cemconcomp.2018.07.009.

[5] X.Y. Zhuang, L. Chen, S. Komarneni, C.H. Zhou, D.S. Tong, H.M. Yang, W.H. Yu, H. Wang, Fly ash-based geopolymer: clean production, properties and applications, J Clean Prod 125 (2016) 253–267.

[6] C. Tippayasam, P. Balyore, P. Thavorniti, E. Kamseu, C. Leonelli, P. Chindaprasirt, D. Chaysuwan, Potassium alkali concentration and heat treatment affected metakaolin-based geopolymer, Constr Build Mater 104 (2016) 293–297.

[7] J. Davidovits, Geopolymers: inorganic polymeric new materials, J Therm Anal Calorim 37 (1991) 1633–1656. https://doi.org/https://doi.org/10.1007/bf01912193.

[8] M.A. Ansari, M. Shariq, F. Mahdi, Geopolymer concrete for clean and sustainable construction–A state-of-the-art review on the mix design approaches, in: Structures, Elsevier, 2023: pp. 1045–1070.

[9] S. Akduman, R. Aktepe, A. Aldemir, E. Ozcelikci, B. Alam, M. Sahmaran, Opportunities and challenges in constructing a demountable precast building using C&D waste-based geopolymer concrete: A case study in Türkiye, J Clean Prod 434 (2024) 139976.

[10] M. Rabie, M.R. Irshidat, N. Al-Nuaimi, Ambient and heat-cured geopolymer composites: Mix design optimisation and life cycle assessment, Sustainability 14 (2022) 4942.

[11] Y.H.M. Amran, R. Alyousef, H. Alabduljabbar, M. El-Zeadani, Clean production and properties of geopolymer concrete; A review, J Clean Prod 251 (2020) 119679.

[12] D.M.J. Sumajouw, D. Hardjito, S.E. Wallah, B. V Rangan, Fly ash-based geopolymer concrete: study of slender reinforced columns, J Mater Sci 42 (2007) 3124–3130. https://doi.org/10.1007/s10853-006-0523-8.

[13] AS 3600, Concrete structures, Standards Australia, Sydney, 2018.

[14] ACI 318, Building Code Requirements for Structural Concrete, in: American Concrete Institute, 2014: pp. 1–524.

[15] M. Albitar, M.S.M. Ali, P. Visintin, Experimental study on fly ash and lead smelter slag-based geopolymer concrete columns, Constr Build Mater 141 (2017) 104–112.

[16] P. Visintin, M.S.M. Ali, M. Albitar, W. Lucas, Shear behaviour of geopolymer concrete beams without stirrups, Constr Build Mater 148 (2017) 10–21.

[17] M. Dong, M. Elchalakani, A. Karrech, T.M. Pham, B. Yang, Glass fibre-reinforced polymer circular alkali-activated fly ash/slag concrete members under combined loading, Eng Struct 199 (2019) 109598.

[18] Z. Huang, W. Chen, H. Hao, Z. Chen, T.M. Pham, T.T. Tran, M. Elchalakani, Flexural behaviour of ambient cured geopolymer concrete beams reinforced with BFRP bars under static and impact loads, Compos Struct 261 (2021) 113282.
[19] S. Kumar, P.K. Gupta, Mohd.A. Iqbal, Experimental and numerical study on self-compacting alkali-activated slag concrete-filled steel tubes, J Constr Steel Res 214 (2024) 108453. https://doi.org/https://doi.org/10.1016/j.jcsr.2024.108453.
[20] U. Katwal, T. Aziz, Z. Tao, B. Uy, D. Rahme, Tests of circular geopolymer concrete-filled steel columns under ambient and fire conditions, J Constr Steel Res 196 (2022) 107393. https://doi.org/https://doi.org/10.1016/j.jcsr.2022.107393.
[21] H. Fang, P. Visintin, Structural performance of geopolymer-concrete-filled steel tube members subjected to compression and bending, J Constr Steel Res 188 (2022) 107026.
[22] N.A. Farhan, M.N. Sheikh, M.N.S. Hadi, Behaviour of ambient cured steel fibre reinforced geopolymer concrete columns under axial and flexural loads, in: Structures, Elsevier, 2018: pp. 184–195.
[23] J.C.M. Ho, C.X. Dong, Improving strength, stiffness and ductility of CFDST columns by external confinement, Thin-Walled Structures 75 (2014) 18–29.
[24] M. Elchalakani, X.-L. Zhao, R. Grzebieta, Tests on concrete filled double-skin (CHS outer and SHS inner) composite short columns under axial compression, Thin-Walled Structures 40 (2002) 415–441.
[25] L.H. Han, Z. Tao, H. Huang, X.L. Zhao, Concrete-filled double skin (SHS outer and CHS inner) steel tubular beam-columns, Thin-Walled Structures 42 (2004) 1329–1355. https://doi.org/10.1016/j.tws.2004.03.017.
[26] L.-H. Han, Z. Tao, H. Huang, X.-L. Zhao, Concrete-filled double skin (SHS outer and CHS inner) steel tubular beam-columns, Thin-Walled Structures 42 (2004) 1329–1355. https://doi.org/10.1016/j.tws.2004.03.017.
[27] Z. Tao, L.H. Han, X.L. Zhao, Behaviour of concrete-filled double skin (CHS inner and CHS outer) steel tubular stub columns and beam-columns, J Constr Steel Res 60 (2004) 1129–1158. https://doi.org/10.1016/j.jcsr.2003.11.008.
[28] B. Zhang, J.G. Teng, T. Yu, Compressive behavior of double-skin tubular columns with high-strength concrete and a filament-wound FRP tube, Journal of Composites for Construction 21 (2017) 04017029.
[29] J.-J. Zeng, Y.-Z. Zheng, Y.-L. Long, Axial compressive behavior of FRP-concrete-steel double skin tubular columns with a rib-stiffened Q690 steel tube and ultra-high strength concrete, Compos Struct 268 (2021) 113912.
[30] M. Elchalakani, M.F. Hassanein, A. Karrech, B. Yang, Experimental investigation of rubberised concrete-filled double skin square tubular columns under axial compression, Eng Struct 171 (2018) 730–746. https://doi.org/10.1016/j.engstruct.2018.05.123.
[31] M. Sugimoto, S. Yokota, K. Sonoda, F. Yagishita, A basic consideration on double skin tube-concrete composite columns, in: Osaka City University and Monash University Joint Seminar on Composite Tubular Structures, Osaka, 1997.
[32] G. Gedge, Structural uses of stainless steel—buildings and civil engineering, J Constr Steel Res 64 (2008) 1194–1198.
[33] N.R. Baddoo, Stainless steel in construction: A review of research, applications, challenges and opportunities, J Constr Steel Res 64 (2008) 1199–1206.
[34] L.-H. Han, C.-Y. Xu, Z. Tao, Performance of concrete filled stainless steel tubular (CFSST) columns and joints: Summary of recent research, J Constr Steel Res 152 (2019) 117–131.

[35] A.H. Mahmood, S.J. Foster, A. Castel, Effects of mixing duration on engineering properties of geopolymer concrete, Constr Build Mater 303 (2021) 124449.
[36] M. Alameri, J. Joseph, M.S. Mohamed Ali, M. Elchalakani, A.H. Sheikh, Optimising GGBS-based ultra high-performance geopolymer mortar: an orthogonal array approach, Australian Journal of Structural Engineering (n.d.) 1–16. https://doi.org/10.1080/13287982.2024.2375468.
[37] Standards Australia, AS1012.9:2014 Methods of testing concrete Method 9: Compressive strength tests — Concrete , mortar and grout specimens, Standards Australia International Ltd, Sydney. (2014) 1–13.
[38] A. 1012.17, Methods of testing concrete : Determination of the static chord modulus of elasticity and Poisson ' s ratio of concrete specimens, Australian Standards 1997 (1997) 1–17.
[39] P. Ayough, Z. Ibrahim, N.H.R. Sulong, P.-C. Hsiao, M. Elchalakani, M. Elchalakani, Numerical analysis of square concrete-filled double skin steel tubular columns with rubberised concrete, Structures 32 (2021) 1026–1047. https://doi.org/10.1016/j.istruc.2021.03.054.
[40] M. Elchalakani, V.I. Patel, A. Karrech, M.F. Hassanein, S. Fawzia, B. Yang, Finite element simulation of circular short CFDST columns under axial compression, Structures 20 (2019) 607–619. https://doi.org/10.1016/j.istruc.2019.06.004.
[41] M. Pagoulatou, T. Sheehan, X.H. Dai, D. Lam, Finite element analysis on the capacity of circular concrete-filled double-skin steel tubular (CFDST) stub columns, Eng Struct 72 (2014) 102–112. https://doi.org/10.1016/j.engstruct.2014.04.039.
[42] M.F. Hassanein, M. Elchalakani, A. Karrech, V.I. Patel, B. Yang, Behaviour of Concrete-filled Double-skin Short Columns Under Compression Through Finite Element Modelling: SHS Outer and SHS Inner Tubes, Structures 14 (2018) 358–375. https://doi.org/10.1016/j.istruc.2018.04.006.
[43] J. Lubliner, J. Oliver, S. Oller, E. Oñate, A plastic-damage model for concrete, Int J Solids Struct 25 (1989) 299–326.
[44] J. Lee, G.L. Fenves, Plastic-damage model for cyclic loading of concrete structures, J Eng Mech 124 (1998) 892–900.
[45] Z. Hashin, A. Rotem, A fatigue failure criterion for fiber reinforced materials, J Compos Mater 7 (1973) 448–464.
[46] M. Singh, A.H. Sheikh, M.S. Mohamed Ali, P. Visintin, M.C. Griffith, Experimental and numerical study of the flexural behaviour of ultra-high performance fibre reinforced concrete beams, Constr Build Mater 138 (2017) 12–25. https://doi.org/10.1016/j.conbuildmat.2017.02.002.
[47] K.S. Al-Jabri, A. Seibi, A. Karrech, Modelling of unstiffened flush end-plate bolted connections in fire, J Constr Steel Res 62 (2006) 151–159.
[48] H. Yu, I.W. Burgess, J.B. Davison, R.J. Plank, Numerical simulation of bolted steel connections in fire using explicit dynamic analysis, J Constr Steel Res 64 (2008) 515–525.
[49] X.H. Dai, D. Lam, N. Jamaluddin, J. Ye, Numerical analysis of slender elliptical concrete filled columns under axial compression, Thin-Walled Structures 77 (2014) 26–35.
[50] M.F. Hassanein, V.I. Patel, Round-ended rectangular concrete-filled steel tubular short columns: FE investigation under axial compression, J Constr Steel Res 140 (2018) 222–236.
[51] X. Dai, D. Lam, Numerical modelling of the axial compressive behaviour of short concrete-filled elliptical steel columns, J Constr Steel Res 66 (2010) 931–942.

[52] M. Elchalakani, A. Karrech, M.F. Hassanein, B. Yang, Plastic and yield slenderness limits for circular concrete filled tubes subjected to static pure bending, Thin-Walled Structures 109 (2016) 50–64.
[53] M.F. Hassanein, M. Elchalakani, A. Karrech, V.I. Patel, B. Yang, Behaviour of concrete-filled double-skin short columns under compression through finite element modelling: SHS outer and SHS inner tubes, in: Structures, Elsevier, 2018: pp. 358–375.
[54] M. Ahmed, Q.Q. Liang, A. Hamoda, M. Arashpour, Behavior and design of thin-walled double-skin concrete-filled rectangular steel tubular short and slender columns with external stainless-steel tube incorporating local buckling effects, Thin-Walled Structures 170 (2022) 108552.
[55] Q.Q. Liang, Nonlinear analysis of circular double-skin concrete-filled steel tubular columns under axial compression, Eng Struct 131 (2017) 639–650.
[56] Q.Q. Liang, Performance-based analysis of concrete-filled steel tubular beam–columns, Part I: Theory and algorithms, J Constr Steel Res 65 (2009) 363–372.
[57] L.-H. Han, D. Lam, D. Nethercot, Design guide for concrete-filled double skin steel tubular structures, CRC Press, 2018.
[58] M. Ahmed, Q.Q. Liang, V.I. Patel, M.N.S. Hadi, Experimental and numerical studies of square concrete-filled double steel tubular short columns under eccentric loading, Eng Struct 197 (2019) 109419.

Conclusions and future recommendations

Conclusions

At the material level, this thesis discusses the development of a mix design for UHPC that includes an SAP to improve the cement's self-healing capacity. The thesis also discusses the development of a mix design procedure, and it uses the Taguchi method to statistically study the mix design and create UHPGC. Furthermore, the thesis presents a study that comprehensively develops and evaluates HPGC in terms of mechanical and durability characteristics using the Taguchi method. At the structural level, thin-walled columns were built using the mix design developed in this thesis. Regarding UHPC, UHPC-FDAT columns were tested experimentally and modelled numerically under combined loading conditions. Concerning HPGC, HPGC-FDST columns were tested experimentally, analysed based on available design recommendations and modelled numerically under combined loading conditions.

UHPC mixes with an SAP were investigated to evaluate their self-healing performance as well as the effect of the SAP on their mechanical and durability characteristics. Three mixes were made; two of them had SAP-to-binder ratios of 0.3% and 0.4%, while the control mix contained no SAP. The following major conclusions can be drawn:

- Adding an SAP to UHPC required increasing the W/B ratio to maintain the flowability of the mix, which led to a decrease in compressive strength.
- Adding an SAP did not decrease the flexural and tensile strength of UHPC due to the effect of the SAP on the internal curing of the specimens, which prevented microcracks.
- The load recovery of the notched specimens of the UHPC with the SAP was better than that of the control mix.

- The prisms made with the SAP–UHPC mix that were subjected to sustained tensile loading and wet and dry cycles exhibited self-healing after cracking, as was clearly indicated by the increase of stress with time.

To develop UHPGC, a new approach to the mix design was used based on the Taguchi method, which consisted of two trials with different variables and levels. The L9 array was utilised, and each trial included four parameters, with each parameter having three levels. The following major conclusions can be drawn:

- The second trial achieved a compressive strength of 126 MPa for the mix that had a W/B ratio of 0.28, a fibre volume of 3%, a SiC/B ratio of 0 and an SP/B ratio of 2%.
- The factor that contributed the most to the optimum mix was the W/B ratio (61.8%).
- The mathematical model used to predict compressive strength was validated by the proposed experimental program, with a coefficient of determination of 91.44%.

Furthermore, the Taguchi method was employed to assess the mechanical properties and durability characteristics of FRGCs. Using an L9 orthogonal array, mixes similar to those of the previous chapter were examined based on four parameters, with each parameter having three levels. Doing so made it possible to comprehensively assess the approach used in the previous chapter. The following conclusions can be drawn:

- The W/B ratio had the greatest influence on the mechanical properties and durability characteristics of the FRGCs. The lower level of the W/B ratio enhanced the compressive and flexural strength of the composites; the optimum level was 0.28.
- The fibre content had a greater impact on splitting tensile strength, with an optimum level of 2.5%.

- The contribution of each parameter was extracted by ANOVA, which confirmed the major effect of the W/B ratio on the outcome of the FRGCs.

Thin-walled applications were assessed by examining UHPC-FDAT columns under combined loading conditions. Five columns were evaluated experimentally. A numerical model was built in Abaqus to simulate the columns, and this model was validated by the experimental results. Forty-five columns were simulated to conduct a parametric study. The following conclusions can be drawn:

- The columns with increased loading eccentricity exhibited a decrease in the ultimate load and an increase in the mid-height lateral displacement.
- Local buckling in the compression face and rupture of the aluminium in the tension face were the typical failure patterns of the columns; with the increase in the loading eccentricity, the rupture extended to the concrete to create a major crack.
- The concrete damage plasticity model and the Ramborg and Osgood model were utilised to model the UHPC and the aluminium tubes, respectively, in Abaqus. These models achieved high accuracy in simulating the experimental results.
- The parametric study showed that the compressive strength impact was more obvious on the concentrically loaded specimens where increasing the outer tube thickness led to an increase in the ultimate load for the columns under high loading eccentricity.

FRGC-FDST columns were investigated experimentally, analytically and numerically. Five columns were tested under concentric, eccentric and four-point bending loading conditions. The proposed design model was compared to the experimental results. Furthermore, the numerical model was validated by the experimental results. The following conclusions can be drawn:

- The columns with increased loading eccentricity exhibited a decrease in the ultimate load and an increase in the mid-height lateral displacement.
- Local buckling around the mid-height of the columns was the typical failure pattern.
- The experimental (axial load–bending moment interaction diagram (P–M) and analytical P–M models exhibited very high agreement.

Future Research Directions

This thesis examined UHPC and FRGC both at the material and structural-response levels. Future studies of these two materials could focus on a variety of aspects, including the following ones:

1) The mechanisms of self-healing in UHPC can be further investigated by establishing a theoretical model that considers the impact of tensile creep.
2) Further studies on the use of waste materials could lead to the development of comprehensive recommendations for UHPGC and HPGC mix designs in order to take into account the most influential parameters. Moreover, machine learning approaches could improve the efficiency of producing GPC.
3) Enhancing the confinement of the aluminium tubes could improve UHPC-FDAT columns; this could be achieved by adding a fibre-reinforced polymer sheet at the mid-height of the structural member.
4) Few studies have been conducted on the use of GPC in structural members. Understanding the behaviour of GPC at the structural level is crucial before widely adopting this type of concrete as a replacement for conventional concrete. This kind of research can start with precast applications, which can be better controlled compared to cast-in-situ applications.

APPENDIX I

Conference paper (as published)

Alameri, M., Sadakkathulla, M. M., Sheikh, A. H., & Elchalakani, M. (2023). Self-healing Behaviour of Ultra-High-Performance Concrete Under Constant Load. In International Symposium of the International Federation for Structural Concrete (pp. 506-513). Cham: Springer Nature Switzerland.).

Self-healing Behaviour of Ultra-High-Performance Concrete Under Constant Load

Mohammad Alameri[1,2(✉)], Mohamed Mohamed Sadakkathulla[1], Abdul Hamid Sheikh[1], and Mohamed Elchalakani[3]

[1] School of Civil, Environmental and Mining Engineering, The University of Adelaide, Adelaide, Australia
Mohammad.alameri@adelaide.edu.au

[2] Faculty of Engineering and Islamic Architecture, Umm Al-Qura University, Mecca, Saudi Arabia

[3] Department of Civil, Environmental and Mining Engineering, The University of Western Australia, Perth, Australia

Abstract. Concrete technology has been developing remarkably in recent decades. One of the most significant developments is the invention of ultra-high- performance concrete (UHPC), which can cope with the higher level of demands associated with complex structures, such as long-span bridges. The strength and durability of this type of concrete are quite high. However, this kind of concrete needs a very low water-to-cement ratio (up to 0.2); consequently, the hydrated cement particles could not exceed 26%. Hence, the cracks may appear frequently due to the autogenous shrinkage. To overcome autogenous shrinkage, a superab- sorbent polymer (SAP) is used as an internal curing agent to subsequently increase the hydration of anhydrous cement particles. Much research has focused on induc- ing cracks under different curing conditions and observing the behaviour of the specimens when re-loaded, whether the cracks that had been induced had sealed during the curing time, and whether strength had been gained after re-loading. As such, in this research, a constant cracking load was applied to a pull-out specimen for 28 days under two different curing conditions (water curing and wet and dry cycles). The mix design for these specimens was UHPC with SAP of 0.3% and 0.4% of the total binder. Also, a reference UHPC mix has been used for compar- ison purposes. The results show that using SAP in the UHPC mix has the ability to boost the self-healing mechanism present in ultra-high-performance concrete. Additionally, tensile strength behaviour improved in the UHPC mix with 0.3% SAP.

Keywords: cracks · self-healing · superabsorbent polymer · ultra-high-performance concrete

© The Author(s), under exclusive license to Springer Nature Switzerland AG 2023
A. Ilki et al. (Eds.): *fib* Symposium 2023, LNCE 349, pp. 506–513, 2023.
https://doi.org/10.1007/978-3-031-32519-9_49

1 Introduction

During the last few decades, the improvement in concrete technology, namely, the capa- bility to form concrete into different shapes, has promoted a significant consumption of the material in the construction of high raised complex buildings. The high performance of concrete with a relatively low cost has led to its wide range of applications. As such, concrete technology has been extensively developed in various aspects to align with the unique demands placed upon it. One of the most prominent technologies is the devel- opment of ultra-high-performance concrete (UHPC). Durability and high compressive strength are best features of UHPC, which enhance the mechanical performance of struc- tural elements. UHPC has been used in many projects ranging from long span bridges to wind turbine towers [1–3]. However, there are still many challenges to overcome if UHPC is to be widely adopted.

Besides its considerable attributes, UHPC has an extremely low (water/cement) w/c ratio that can go up to 0.2. Consequently, the amount of hydrated cement can be limited to around 26% [4]. However, the low w/c ratio can cause high autogenous shrinkage leading to micro-cracking [5], which affects the safety and sustainability of the UHPC structural elements with pre-cracks. Even though collapse is less likely to occur due to micro-cracks, if they persist, it could lead to degrade the performance of these structural elements.

Cracks can be initiated due to loading or autogenous shrinkage, which affect the internal matrix of the concrete and pave the way for aggressive agents to enter inside the concrete. The increase of crack width leads to higher permeability for moisture and water flow [6] that accelerate the deterioration of concrete performance. Many design codes imposed a crack width limit; ACI 224R-01 [7] limits crack width up to 0.15 mm when concrete is exposed to wet and dry cycles. A traditional technique to limit crack widths is the use of adequate reinforcements as recommended by the design codes.

An improved hydration of cement particles within UHPC having an extremely low water/binder w/b ratio can be achieved by incorporating internal curing agents. The particles of these curing agents have a high water absorption capacity, which are released gradually. Light weight aggregates (LWAs) are often used in concrete without realising their ability for facilitating internal curing. Pre-saturated LWAs are found to be more effective than dried LWAs in terms of internally curing capability [8]. Henkensiefken [9] found that the pores in LWAs realise water to hydrate anhydrous cement particles at 96% of internal relative humidity (IRH); however, the water absorption capacity of LWAs is only about 5%–25% of their weight. This is contrary to superabsorbent polymers (SAPs), which have a much higher water absorption capacity that can reach up to 1000 times of their weight [10]. SAPs have mainly been used as internal curing agents to provide water to anhydrous cement particles after concrete is set [11–13]. SAP has also been investigated as an agent for forming sealing mechanisms in concrete [10, 11, 14].

Though SAP has been known to effectively reduce the autogenous shrinkage of UHPC, a limited number of experimental data exists on self-healing ability of UHPC using SAP [15]. Hence, the current study has aimed to investigate the effect of SAP particles in improving the healing capacity of concrete specimens under a constant load applied for 28 days.

2 Self-healing Technique

In this study, Portland cement, ground-granulated blast-furnace slag (GGBS), and silica fume were used in the concrete mix as the supplementary binder. Blended and dried sands with high silica contents (0.075 mm–1.18 mm) were utilised as fine aggregates, as they have sub-angular to rounded grains. In addition, tap water was used. A higher range of water reducer (HRWR) in the form of Polycarboxylates superplasticiser (SP), ViscoCrete-10 type, Sika, Australia was used to optimise the workability of the concrete. The HRWR used had 36% solid content by mass. Steel fibres (diameter: D = 0.2 mm, and length: L = 13 mm) having a tensile strength of 2500 MPa were used to reduce the crack opening through fibre bridging. The SAP used in the mix was Polyacrylate/Polyalcohol Copolymer that had the capability of water absorbing up to 60 g/g.

The details for the mix design of concrete are presented in Table 1 where UHPC refers to control mix, and S0.3 and S0.4 refer to mixes with two different proportions of SAPs. The proportion of water was adjusted to maintain the same level of workability as that of control mix. The workability was adjusted by increasing the amount of water and SP. Since SAP absorbs high quantity of water, a trial-and-error bases strategy was initially adopted to find the optimal mix prior to the full-scale of experimentation to achieve a proper level of workability by adjusting the content of SAP. For the preparation of concrete mix, the dry cementitious materials, sand, and SAP were first mixed at room temperature for 3 min. In next one minute, 90% of the water was added that is followed by mixing SP and remaining portion of water. The mixing continued for 25 min in wet state. Finally, the steel fibre was mixed for 3 min for a better distribution of the fibres.

Table 1. Proportions of concrete mix constituents

Mix ID	Binder		Silica fume (%) of binder	s/b	w/b	SAP (%)	Steel Fibre (%) (volume fraction)	SP (%)
	Cement (%)	GGBS (%)						
UHPC	85	15	25	1.1	0.166	0	1.5	4
S0.3					0.166	0.3		6
S0.4					0.17	0.4		6.5

Note: the binder contains the cement and GGBS only, s/b and w/b refer to fine aggregate to binder ratio and water to binder ratio, respectively, SAP (%) and SP (%) refer to the percentage with respect to the binder

2.1 Testing Methods

Determination of Mechanical Properties

The compressive strength of UHPC was evaluated according to AS 1012.9 [16] using cylindrical specimens. The modulus of elasticity was determined by attaching four strain gauges to the cylinders (two in the longitudinal direction and two in the

transverse direction [17]). Tensile strength was determined by direct tension test of dog bone test specimens [18]. The flexural strength was evaluated according to [19].

Testing of Specimen Under Constant Load Condition

Specimens having a length of 500 mm and a square cross-section (75 mm sides) were cast and kept under ambient curing conditions (25 °C) for 28 days before commencing of their testing. Figure 1 illustrates the set-up for testing of these specimens. The idea was adapted from long term creep testing [20] of specimens under sustained loading with some modifications, made to measure the cracks near the mid-length of specimens, where the cross-section was provided a groove. The cracking load was applied for 28 days under curing conditions involving water curing as well as wet and dry curing cycles of two days cycles where conditions were changed constantly. The crack was initiated in the grooved area where the linear variable displacement transducer (LVDT) was attached. A strain gauge was attached to the threaded rod to measure the strain and convert it to the induced stress or load.

First, the specimens were loaded with a steady and gradual increase of the load until the first crack appeared. The load was then reduced to 50%, 60%, or 70% of the maximum load and the reduced load was sustained. The load adjustments were made manually to avoid any possible premature failure. Table 2 presents the different levels of loads and stresses, which have been extracted from the tension test. These load values were configured using the material property of the M16 threaded rod.

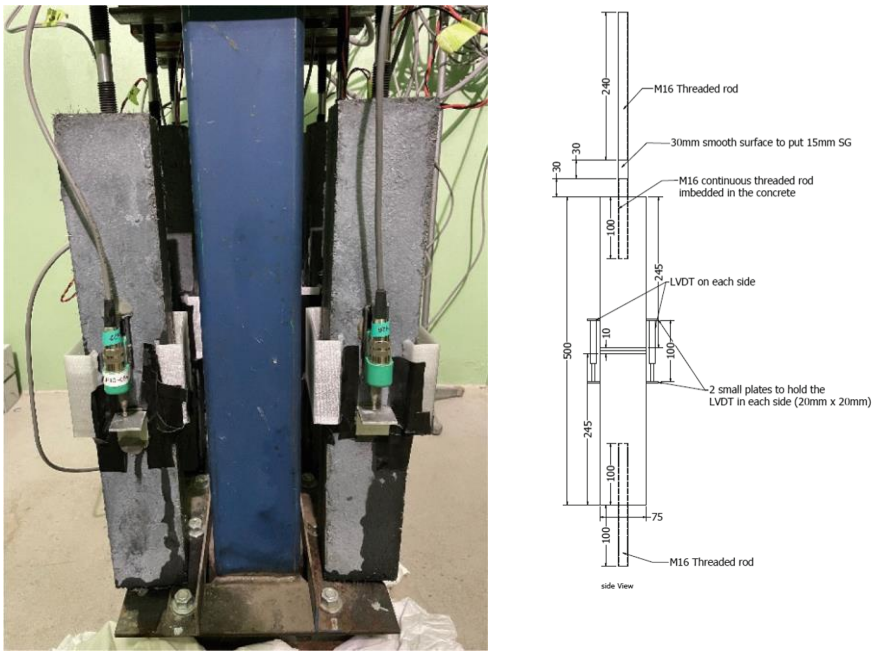


Fig. 1. Test set-up of specimens under constant loading

Table 2. Different levels of stresses and loads from tension test results

	UHPC	S0.3	S0.4
Stress at first crack (MPa)	4.50	4.90	3.84
Maximum stress (MPa)	4.62	5.10	4.14
Equivalent load from max stress (KN)	24.26	26.78	21.74
70% of the crack load (KN)	16.54	18.01	14.11
60% of the crack load (KN)	14.18	15.44	12.09
50% of the crack load (KN)	11.81	12.86	10.08

3 Results and Discussion

3.1 Mechanical Properties

Figure 2 has presented the influence of SAP on mechanical properties of UHPC as well as compressive strengths at 7, 28, 56, and 90 days for each concrete mix. The results show that the addition of SAP has negative influence on compressive strength in all cases. This effect was also reported in [21] and was linked to voids produced in the cement due to SAP. However, even though compressive strength was lower with the addition of SAP, it was found that the reduction in compressive strength at 7 days, which was about 13% lower than the control mix, was reduced to around 1% at 90 days.

The flexural and tensile strengths and modulus of elasticity values are also presented in Fig. 2 that shows S0.3% as the optimum mix, as it provided better results for the above- mentioned properties. Therefore, it can be stated that SAP has a positive effect on flexural and tensile strengths as well as elastic modulus that leads to stiffness enhancement of the mix. Similar findings were also reported in [22] for flexural and tensile strengths.

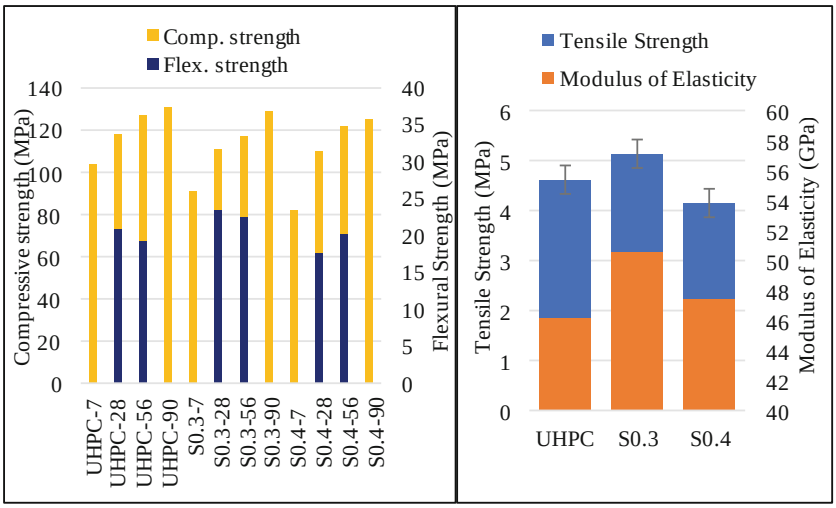


Fig. 2. Modulus of elasticity and compressive, flexural, and tensile strengths, the mix designated name is followed by number of days

3.2 Self-healing Under Constant Load Wet and Dry

Cycles

Figure 3 has presented time variations of displacements during wet and dry cycles where the displacement refers to the crack widening in the notched area. The average of two LVDT measurements was used to plot these results. For S0.4, the specimen was cracked on day 1. The stability of the curve (displacement or stress) means that there was no change in closing the cracks. For S0.3, the cracks were produced in a different area and the LVDTs couldn't record the crack widening. For the UHPC control mix, the load was applied slowly to avoid premature failure where the crack was produced in day 9. For all specimens except for the UHPC specimen, displacement remained relatively stable during the testing. The displacement of UHPC specimen increased slightly after day 7; the increase was attributed to the load applied occasionally to initiate cracks.

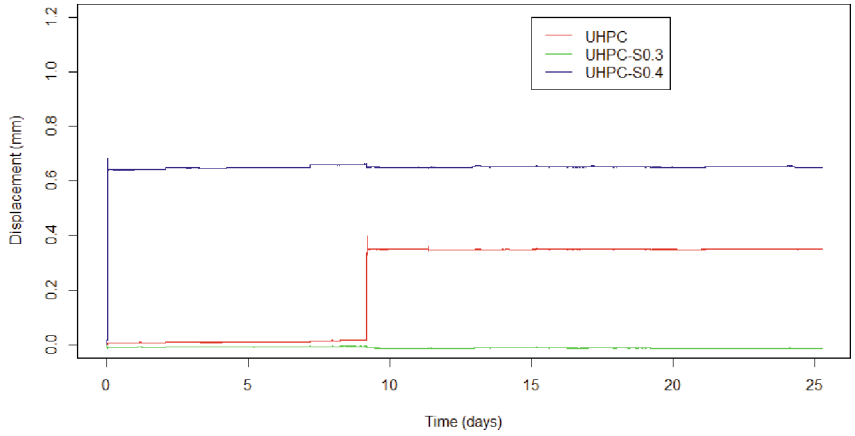


Fig. 3. Time variations of displacement during wet and dry cycles

Figure 4 has presented the time variations of stresses duration the test where the load was applied periodically to reach the cracking load. For S0.4, the stress was approxi- mately 8 MPa on day 1, which was then reduced to 2 MPa, i.e., 50% of the cracking load according to the tensile strength results. The stress was increased occasionally on days 1, 3, 5, 7, and 9. After day 9, the stress remained around 50% of the cracking load for 15 days. It is evident that the stress was increased during this period. The reason for this is the healing of S0.4 to the increase of stress rather than the decrease of displacement. For S0.3, the specimen was loaded up to 8 MPa to reach the cracking load on day 9. Subsequently, the failure occurred, and the measurements could not be taken, as mentioned earlier. For the UHPC control specimen, the load was boosted on the same days as that of S0.4, and the crack was initiated on day 9. The load was adjusted on day 12 to reach 50% of the cracking load. After day 12, the load remained constant, which means that the capacity of the specimen was not increased. As can be seen, S0.4 produced the best results in terms of crack healing and recovering stiffness at same displacement obtained from for the wet and dry cycles.

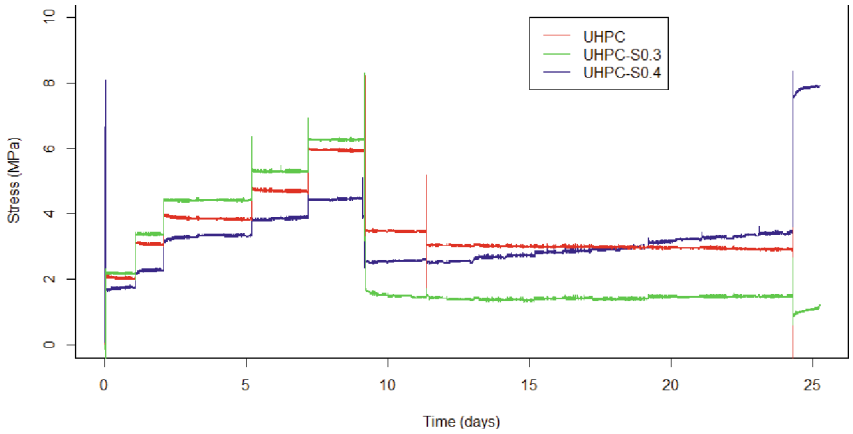


Fig. 4. Time variation of stress during wet and dry cycles

4 Conclusions

The UHPC control mix and mixes with addition of SAP having 0.3% and 0.4% of the binder were investigated. The mechanical properties of these mixes were first measured and processed before testing notched specimens under constant tensile loading during wet and dry cycles. Based on the experimental observations, the following conclusions can be made:

- The addition of SAP has insignificant effect on the compressive strength of UHPC but shows long-term improvement - reaching 99% of the strength of UHPC after 90 days.
- Flexural and tensile strengths were improved by adding SAP to the mix where S0.3 showed optimum improvement.
- For specimens under constant tensile load, S0.4% proved the best stiffness recovery by means of increase in the stress values.

This study employed a novel concept for testing the notched specimens under con- stant tensile loading that provided a wider range of valuable results. As can be seen, it also provided results that were more reliable as they can simulate real situations. For future studies, the same test procedure can be followed, but the curing conditions can be varied to simulate aggressive environments. It would also be of useful to study the long-term effects by increasing the duration of test up to 180 days, which would allow to investigate the effect of creep.

Acknowledgment. The authors would like to acknowledge the financial support received from Australian Research Council (DP 21001425) for undertaking this research.

References

1. Graybeal BA, Russel HG (2013) Ultra-high performance concrete: a state-of-the-art report for the bridge community
2. Schmitz GM (2013) Design and experimental validation of 328 ft (100 m) tall wind turbine towers utilizing high strength and ultra-high performance concrete 210
3. Hajar Z, Resplendino J, Lecointre D, Petitjean J, Simon A (2004) Ultra-high-performance concretes: first recommendations and examples of application. In: Proceedings of the fib symposium 2004 - concrete structures: the challenge of creativity, pp 242–243
4. Bonneau O, Vernet C, Moranville M, Aïtcin PC (2000) Characterization of the granular packing and percolation threshold of reactive powder concrete. Cem Concr Res 30(12):1861– 1867
5. Ji T, Chen CY, Zhuang YZ (2012) Evaluation method for cracking resistant behavior of reactive powder concrete. Constr Build Mater 28(1):45–49
6. Aldea CM, Shah SP, Karr A (1999) Permeability of cracked concrete. Mater Struct/Materiaux et Constr 32(5):370–376
7. Anon (1980) Control of cracking in concrete structures. Concrete International, American Concrete Institute, pp 35–76
8. Ma X, Liu J, Shi C (2019) A review on the use of LWA as an internal curing agent of high performance cement-based materials. Constr Build Mater 218:385–393
9. Henkensiefken R (2008) Internal curing in cementitious systems made using saturated lightweight aggregate. Purdue University
10. Jensen OM, Hansen PF (2001) Water-entrained cement-based materials - I. Principles and theoretical background. Cement Concrete Res 31(4): 647–654
11. Snoeck D, Van Tittelboom K, Steuperaert S, Dubruel P, De Belie N (2014) Self-healing cementitious materials by the combination of microfibres and superabsorbent polymers. J Intell Mater Syst Struct 25(1):13–24
12. Van Tittelboom K., De Belie N (n.d.) Self-healing in cementitious materials-a review. Materials 6 (6)
13. Rooij, M., van Tittelboom, K., Belie, N., and Schlangen, E. (2013) Self-Healing Phenomena in Cement-Based Materials: State-of-the-Art Report of RILEM Technical Committee. Springer,
14. Lee HXD, Wong HS, Buenfeld NR (2016) Self-sealing of cracks in concrete using superabsorbent polymers. Cem Concr Res 79:194–208
15. Justs J, Wyrzykowski M, Bajare D, Lura P (2015) Internal curing by superabsorbent polymers in ultra-high performance concrete. Cem Concr Res 76:82–90
16. AS 1012.9 (2014) Methods of testing concrete - compressive strength tests—concrete , mortar and grout specimens. Aust Stand, 1–13
17. A 1012.17 (1997) Methods of testing concrete : determination of the static chord modulus of elasticity and poisson's ratio of concrete specimens. Aust Stand, 1–17
18. Moreno DM, Trono W, Jen G, Ostertag C, Billington SL (2012) Tension-stiffening in rein- forced high performance fiber-reinforced cement-based composites under direct tension. In: Parra-Montesinos GJ, Reinhardt HW, Naaman AE (eds) RILEM Bookseries. Springer, Dordrecht, pp 263–270. https://doi.org/10.1007/978-94-007-2436-5_32
19. AS 1012.11 (2000) Methods of testing concrete -Determination of the modulus of rupture. Aust Stand, 1–9
20. Islam MMU (2021) Investigation of tensile creep for ultra-high-performance fiber reinforced concrete (UHPFRC) for the long-term. Constr Build Mater 305:124752
21. Ma X, Liu J, Wu Z, Shi C (2017) Effects of SAP on the properties and pore structure of high performance cement-based materials. Constr Build Mater 131:476–484
22. Liu J, Farzadnia N, Shi C, Ma X (2019) Shrinkage and strength development of UHSC incorporating a hybrid system of SAP and SRA. Cement Concr Compos 97:175–189